12-2016

A Characterization of Human Burial Signatures using Spectroscopy and LIDAR

Katie Ann Corcoran
University of Tennessee, Knoxville, kcorcor1@vols.utk.edu

To the Graduate Council:

I am submitting herewith a dissertation written by Katie Ann Corcoran entitled "A Characterization of Human Burial Signatures using Spectroscopy and LIDAR." I have examined the final electronic copy of this dissertation for form and content and recommend that it be accepted in partial fulfillment of the requirements for the degree of Doctor of Philosophy, with a major in Anthropology.

Amy Z. Mundorff, Major Professor

We have read this dissertation and recommend its acceptance:

Devin White, Dawnie Steadman, Budhendra Bhaduri

Accepted for the Council:
Carolyn R. Hodges

Vice Provost and Dean of the Graduate School

(Original signatures are on file with official student records.)

A Characterization of Human Burial Signatures using Spectroscopy and LIDAR

A Dissertation Presented for the

Doctor of Philosophy

Degree

The University of Tennessee, Knoxville

Katie Ann Corcoran

December 2016

DEDICATION

This dissertation is dedicated to all the missing and to the families who don't yet have the answers they need.

ACKNOWLEDGEMENTS

Completing a Ph.D. has been the most challenging and rewarding goal I've ever reached. As a graduate student, there were more moments than I can count where I was certain graduate school was the wrong choice. There was the lingering internal struggle over whether I could actually finish. There was imposter syndrome, there were both real and perceived road blocks and missteps. But, thankfully, there were even more moments where I felt innovative and rewarded for my work – where I felt that I was working toward something valuable to myself and to others. There was a persistent doctoral advisor, sympathetic friends, an understanding family, a couple of therapy cats, and an endlessly patient partner. No one finishes a Ph.D. alone, so I'd like to acknowledge the people who helped support me during the past five years.

First, I wouldn't have considered graduate school an option if not for my dear friend, Dr. Ian Ralby, who I met after I'd dropped out of college for the second time. Ian convinced me to re-enroll in college and work toward my first degree in anthropology, then later encouraged me to pursue an advanced degree. I'm forever grateful for Ian's friendship and for the many years of his sound advice and encouragement.

My doctoral advisor, Dr. Amy Mundorff, and my technical advisor, Dr. Devin White, have been outstanding mentors from start to finish. Amy and Devin are both wonderfully kind people who also happen to be two of the most respectable anthropologists in their fields. From Amy and Devin, I've learned not just practice, but patience ("Settle down, Frank!"). And thanks to Amy, after five years, I finally think scotch is tolerable.

I'd like to thank Drs. Dawnie Steadman and Budhu Bhaduri for serving on my dissertation committee, and for offering tremendously valuable feedback on the initial research design and later

drafts of the dissertation. I'd also like to express my sincere appreciation of Dr. Whitney Emch, Dr. Bruce Cook, Mr. Larry Corp, Mr. Tad Fickel, and Mr. Garold Warner for their support of this research and for maintaining an open line of communication throughout the study to ensure the best outcome for everyone involved. The research design and final dissertation were much improved as a result of everyone's active involvement.

As for my friends and family, I'm lucky to know each of them. My incredible family: the Corcorans, the Mazarins, Sam Watkins, and the Richardsons, for putting up with me as an always-anxious grad student. It's a good thing for me that they didn't have a choice. My wonderful friends: Liz Agosto, Janine Al-Aseer, Rachel Canfield, Matt and Jackie Kerr, Robert Lassen, Amanda Reinke, Kristen and Nick Savell, Greg Simpson, Tyler Sonnichsen, and Sam Williams. There was yelling and laughter, but in the end, almost everyone had a cat. And my partner, model cat-dad, and the person to which I'm most deeply indebted: Stewart Richardson – an infinitely generous person who really believes in leaving the world better than he found it.

Finally, I'd like to acknowledge the various sponsors and partners that supported both me as a researcher and the larger project. This study would not have been possible if not for the support of the National Geospatial-Intelligence Agency, the US Department of Defense, the US Geospatial-Intelligence Foundation, P.E.O. International, the Goetz Instrument Support Program, the DigitalGlobe Foundation, Walter Leitner and his family, the William M. Bass Endowment, the Naval Postgraduate School Remote Sensing Center, Oak Ridge National Laboratory, and the UT Forensic Anthropology Center.

Thank you.

Disclaimer: This research was sponsored by the U.S. Army Research Office and the Defense Forensics and Biometrics Agency and was accomplished under Cooperative Agreement Number W911NF-14-2-0089. The views and conclusions contained in this document are those of the authors and should not be interpreted as representing the official policies, either expressed or implied, of the Army Research Office, DFBA, or the U.S. Government. The U.S. Government is authorized to reproduce and distribute reprints for Government purposes notwithstanding any copyright notation hereon.

Disclaimer: This work was created in the performance of a Cooperative Research and Development Agreement with the National Geospatial-Intelligence Agency (CRADA #HM1583-CR-FY13-004). The Government of the United States has a royalty-free government purpose license to use, duplicate or disclose the work, in whole or in part and in any manner, and to have or permit others to do so, for government purposes.

ABSTRACT

This study is an analysis of terrestrial remote sensing data sets collected at the University of Tennessee's Anthropology Research Facility (ARF). The objective is to characterize human burial signatures using spectroscopy and laser scanning technologies. The development of remote human burial detection methodologies depends on basic research to establish signatures that inform forensic investigations. This dissertation provides recommendations for future research on remote sensing of human burials, and for investigators who wish to apply these technologies to case work.

Data used in this study include terrestrial spectra, aerial hyperspectral imagery, satellite multispectral imagery, terrestrial light detection and ranging (LIDAR), and aerial LIDAR. In February 2013, ten individuals donated through the Forensic Anthropology Center body donation program were buried in three differently sized graves at the ARF. The graves contain one, three, and six bodies, respectively. An empty experimental control grave was also created. Terrestrial data collections were made from two-days pre-burial to 21-months post-burial. Aerial data were collected from 19 to 27-months post-burial. Satellite imagery was collected from six-months pre-burial to 23-months post-burial. Analytical emphasis is placed on the terrestrial data sets, which are of the highest spatial and spectral fidelity. Results of terrestrial data analysis reveal separable spectral and topographic signatures between the disturbed locations and surrounding undisturbed area. Aerial and satellite data were used to attempt validation of terrestrial data analysis findings, but findings were inconclusive.

This study demonstrates that live vegetation spectral samples can be correctly classified as disturbed or undisturbed groups at rates from 52.0 – 78.3% using statistically-based classification models. Additionally, this study documents localized elevation change at burial surfaces as a result

of initial digging activity, subsequent soil settling and subsurface decomposition. The findings of this research are significant to both researchers and practitioners. It is the first study to compare live vegetation spectra associated with human burials and is the first to document burial elevation change using LIDAR. This work contributes to a collective understanding of human burial signatures that can be used together or with other geophysical methods to assist in locating unmarked human burials.

TABLE OF CONTENTS

LIST OF TABLES

LIST OF FIGURES

LIST OF FREQUENTLY USED ACRONYMS

AAAS	American Association for the Advancement of Science
AGL	Above Ground Level
AP	Additional Protocol (to the Geneva Conventions)
ARF	Anthropology Research Facility
BLR	Binary Logistic Regression
CONADEP	*Comisión Nacional sobre la Desaparición de Personas*, the National Commission on the Disappearance of Persons
DFA	Discriminant Function Analysis
DPAA	Defense POW/MIA Accounting Agency
EAAF	*Equipo Argentino de Antropología Forense*, the Argentine Forensic Anthropology Team
ENVI	Environment for Visualizing Images
FAC	Forensic Anthropology Center
FBI	Federal Bureau of Investigation
FWHM	Full Width at Half Maximum
GC	Geneva Convention(s)
GPR	Ground Penetrating Radar
GPS	Global Positioning System
GSD	Ground Sample Distance
GSFC	Goddard Space Flight Center
HSI	Hyperspectral Imaging/Imagery
ICC	International Criminal Court
ICMP	International Commission on Missing Persons
ICP	Iterative Closest Point
ICRC	International Committee of the Red Cross
ICTY	International Criminal Tribunal for the former Yugoslavia
IHL	International Humanitarian Law
JHUAPL	Johns Hopkins University, Applied Physics Laboratory
LIDAR	Light Detection and Ranging
MRENDVI	Modified Red Edge Normalized Difference Vegetation Index
MRESRI	Modified Red Edge Simple Ratio Index
MSI	Multispectral Imaging/Imagery
NASA	National Aeronautics and Space Administration
NDVI	Normalized Difference Vegetation Index
PCA	Principal Components Analysis
PLS	Partial Least Squares
RENDVI	Red Edge Normalized Difference Vegetation Index
REPI	Red Edge Position Index
ROI	Region of Interest
SAM	Spectral Angle Mapper
SGI	Sum Green Index
SID	Spectral Information Divergence
SIPI	Structure Insensitive Pigment Index
UN	United Nations

VIP	Variable Importance, or Variable Influence on Projection
WV2	WorldView-2
WV3	WorldView-3

CHAPTER 1: INTRODUCTION

Unmarked burials containing human remains are often difficult to locate due to natural environmental processes or deliberate concealment. Such burials, and any associated contextual evidence, are valuable to communities searching for missing loved ones, to investigators who are building cases for criminal prosecution, and for post-conflict accounting of missing persons (Gassiot and Steadman 2008; Skinner 2002). If located, unmarked burials can be excavated to help establish an accurate narrative of events (Wright 2010). If graves are located and subsequently excavated, the victims' remains can be returned to their next of kin or communities, if that is desirable, so the living can perform culturally specific funerary rituals (Eppel 2014). Without knowledge of burial locations, victimized family or community members can endure significant distress over the unknown status of their missing family members (Rosenblatt 2015; Stover et al. 2003; Wagner 2008). Moreover, without a body or other evidence of their crimes, perpetrators may benefit from impunity (Wright 2010). Therefore, a reliable method to locate unmarked human burials is important for addressing these significant problems.

Unmarked burials are difficult to find because, after a period of time, they can appear the same as their undisturbed surroundings. Natural processes, such as vegetation regrowth or organic debris accumulation obscure burials over time (Bevan 1991; Owsley 2001). Moreover, individuals will sometimes deliberately conceal a burial by attempting to mimic these natural processes as camouflage (Hanson 2012; Hunter and Simpsons 2007). Yet, the presence of buried human remains fundamentally changes the immediate environment, leaving subtle clues of their existence. Understanding the effects of human burials on the nearby environment is foundational to developing methodologies for their detection after they have become difficult to identify (Gaffney et al. 2015).

Environmental responses to human burial decomposition processes can inform the study of burial detection. Timing of human decomposition within a burial is widely variable due to environmental factors, such as precipitation and temperature (Mann et al. 1990; Rodriguez and Bass 1985; Schotsman et al. 2011). Eventually though, reduction of buried mass (the body), and subsequent redistribution of soil into those voids, may be observable at the ground surface as an elevation change or as modified plant chemistry. As a result of this subsurface activity, burial depressions can form at the surface. However, surface depressions are not always obvious and may not persist indefinitely, so they are easily overlooked by search parties (Killam 2004; Morse et al. 1983; Owsley 2001; Steadman 2009). Additionally, human decomposition below the surface is known to influence above ground vegetation. Throughout the decomposition process, nutrients are released into the soil and are absorbed by surface vegetation (Mundorff et al. 2014). Such changes in nutrient levels influence plant chemistry, but much like surface depressions, may not always be visible to humans.

Surface elevation change and vegetation spectra are potential indicators of burial presence, but few studies have attempted to observe these relationships. Most researchers use spectral analysis to visualize non-human burials, and have attempted burial detection before first establishing a characteristic burial signature (Kalacksa and Bell 2006; Kalacska et al. 2009; LeBlanc et al. 2014; Snirer 2013). Far fewer studies have evaluated the use of elevation measurements for visualizing burial surfaces, conducting synchronic studies, rather than diachronic studies of elevation change (Weitman 2012). Not all burial surfaces express topographic relief (i.e., small mounds or depressions), but those that do may appear consistent with surrounding topography at any single point in time. Therefore, diachronic observations may be the

more advantageous approach by measuring the *range* of activity throughout time – activity that likely does not occur at undisturbed locations subject to the same environmental conditions.

Many other approaches to burial detection have been attempted, with varying degrees of reliability. Unmarked burials can and have been located through pedestrian survey (i.e., systematically walking the landscape), ground probing to gauge relative soil mixture and compaction, exploratory excavation, or the use of more involved geophysical techniques. Geophysical technologies can include ground penetrating radar (GPR), electrical resistivity, or magnetometry – all of which record sub-surface observations. These ground-based methods, however, require people and sensors to operate in close proximity – if not at the precise location – of the burial, a requirement that remote sensing technologies do not necessarily demand. Moreover, many of these ground-based methods are time-limited, as established through controlled research experiments (Salsarola et al. 2015). The success of remote sensing technologies may also be time-dependent, which this dissertation attempts to address. However, it is important to note that no single technology is expected to locate all unmarked burials, including the technologies tested in this study, but continued experimentation will help determine how new technologies can be used in combination with others for a more comprehensive approach to burial detection.

Prior to developing additional methodology capable of assisting with unmarked burial detection, the relationship between burials and their immediate environment must be understood. Research and testing will help characterize burial signatures that are unique to a specific methodology. Once these signatures are identified, they can be applied to the interpretation of landscapes, presumably containing unmarked human burials (Gaffney et al. 2015). However, since the nature and extent of the effects of human burials on surface topography and surface vegetation

is not well understood, forensic remote sensing researchers have not been successful outside experimental scenarios.

1.1 Research Objectives

The purpose of this research is to characterize burial signatures using high fidelity terrestrial (i.e., ground-based) data that may be used for the development of a remote sensing human burial detection method. The goal of this research is to examine whether spectral and ground surface signatures can be used to separate burials from non-burials, and aims to achieve three objectives:

1. Statistically separate burial and non-burial vegetation spectra.

   Terrestrial data: Live vegetation reflectance spectra associated with human burials, a control unit (disturbed ground without human remains, herein after referred to as a "control"), and undisturbed ground will be statistically evaluated to determine if vegetation groups are spectrally separable, and if so, which wavelengths are best suited for their classification.

2. Measure and compare burial and non-burial elevation change.

   Terrestrial data: Surface elevation measurements throughout the study area, including over human burials, a control, and undisturbed areas will be compared over time to establish the extent of net elevation change at those surfaces.

3. Evaluate potential scalability of terrestrial findings in airborne/satellite data.

   Guided by Objectives 1 and 2: Statistical models derived from terrestrial spectra will be applied to spectral imagery collected from airborne and satellite sensing platforms to determine if the same separation is achievable at lower spatial and spectral resolution. Elevation change measurements observed in terrestrial LIDAR data will

help determine whether ongoing elevation change activity is also observable at lower spatial resolution.

The analysis of two data types, spectra and elevation change, to characterize multiple burial signatures may prove to be an advantage over using any single data type that might only provide partial information about a burial (Kvamme et al. 2006). Moreover, because the optimal timeframes for observing signatures have not yet been established – assuming signatures exist and are measurable – multiple data sets may improve the likelihood that at least one signature will be observed during the data collection period.

The analytical emphasis for this research is on high resolution terrestrial data to establish whether burial signatures exist and are measurable (Objectives 1 and 2). High resolution data are necessary for preliminary research because human burials may only slightly modify their immediate environment so that vegetation spectra or elevation change measurements do not significantly differ from their non-burial counterparts. If burial signatures only represent a small deviation from the mean distributions of either data set, the results may not be statistically significant. Such small differences could be diluted by sensors with low spatial or spectral resolution (e.g., satellite imagery), or be nested within a sensor's normal functioning error range (van der Meer and de Jong 2011). Terrestrial data sets possess higher spatial and spectral resolution than aerial or satellite data and represent the highest spatial and spectral resolution of all data collected for this study. The instruments used to collect the terrestrial data sets have specifications of accuracy, precision, and signal-to-noise ratios that offer the best chance to position any potential burial signals outside the sensors' error range. If a signature can be established, the next step will be to search for that signature in airborne or satellite data collections (Objective 3).

This study addresses research questions that focus on the relationship between human burials and their immediate environment. The established relationship between soil nutrient concentrations and vegetation spectra (Sims and Gamon 2002; Yoder and Pettigrew-Crosby 1995) present the foundation upon which to observe and understand the influence of human body decomposition processes on nearby vegetation. Additionally, human decomposition and the subsequent reduction of body mass leads to redistribution of mass within a burial, providing an opportunity to observe the overall trend of burial surface elevation changes (Mann et al. 1990; Owsley 2001; Rodriguez and Bass 1985).

Among the rules of international humanitarian law, the right of families to know the fate of the missing, in particular, is legally supported by customary law (i.e., general practice accepted as law) (ICRC 2016), in addition to three international treaties: the Geneva Conventions IV (Article 26)/Additional Protocol I (Article 32), the African Charter on the Rights and Welfare of the Child (Article 19:3), and the Convention on Enforced Disappearances (Article 24). However, the ability for any organization or agency to enforce such a right in practice is limited by current technology, economic resources, political motivations, and the survival needs of the living. This study represents the first attempt to use existing sensing technologies to characterize vegetation and elevation change signatures specific to human burials. This study is a necessary step to understanding these signatures for the purpose of developing a reliable burial detection methodology. The findings of this research may be used by anyone with proper training to assist in the location of unmarked human burials.

1.2 Research Questions and Hypotheses

This study addresses three central research questions: 1) Do human burials influence nearby vegetation spectra, and if so, how? 2) Does burial surface elevation change over time, and

if so, how? 3) If spectral and elevation changes are separable, are the differences unique to human burials or indicative of similar disturbance without interred human remains? The following hypotheses are framed by these research questions.

This study focuses on the effects of human decomposition within a burial on nearby vegetation and surface elevation. Considering these relationships, this research tests four hypotheses:

1. Vegetation associated with disturbed ground containing human remains (human burials), disturbed ground containing no remains (control unit), and undisturbed ground are statistically separable groups as indicated by differences in reflectance spectra.

2. Ground surfaces at burials, the control unit, and undisturbed locations exhibit differences as measured by net elevation gain or loss.

3. Vegetation associated with burials, the control unit, and undisturbed areas exhibit spectral separability for the duration of the study.

4. Ground surfaces associated with burials, the control unit, and undisturbed locations exhibit differences in elevation change for the duration of the study.

Findings in *full* support of the first or second hypotheses would reveal differences between all three comparison samples (i.e., burial, control, undisturbed). Full support of the first and second hypotheses would suggest that the combined effects of ground disturbance and body decomposition processes influence burial signature differences. Findings in *partial* support of the first and second hypotheses would reveal no difference between human burials and the control

unit. However, this scenario would indicate a difference between the undisturbed sample and both of the disturbed samples. Partial support of the first and second hypotheses would suggest that spectral and/or topographic differences are influenced by non-specific ground disturbance.

Findings that do not support the first hypothesis would suggest that vegetation is not measurably affected by ground disturbance or body decomposition and may be interpreted as having no influence on vegetation nutrient uptake or nutrient storage processes. Findings that do not support the second hypothesis would suggest that elevation changes are not the result of buried human remains, but are instead a uniform and natural change in elevation throughout the study area. Moreover, findings that reveal no differences in high resolution terrestrial data between burial, control, or undisturbed vegetation spectra or elevation change can be interpreted as a lack of support for the scalability of those effects to airborne or satellite data.

Findings in support of the third and fourth hypotheses would suggest that differences are independent of temporal factors, such as seasonality, plant phenology (i.e., growth cycles), or the human body decomposition process. Support for these hypotheses would suggest that such factors do not influence the timing of initial divergence, maximum difference, or final convergence of burial and non-burial signatures. Findings that do not support the third and fourth hypotheses would suggest that these temporal factors do influence the timing of initial divergence, maximum difference, or final convergence of burial and non-burial signatures, and the timing of those expressions will inform optimal data collection windows in future research.

1.3 Dissertation Organization

This dissertation contains eight chapters. Chapter 2 is a discussion of unmarked burials, and reviews factors that contribute to the challenges of locating unmarked buried remains. Chapter 3 introduces the science of remote sensing, and describes two types of remote sensing technology

used in this research – passive and active. Chapter 4 provides a comprehensive overview and critique of existing ground-based and remote sensing methods used to locate unmarked burials. Chapter 5 details the study's data sets and presents the analytical methods applied to each data set to attempt characterization of burial signatures. Chapter 6 presents the results of this study. Chapter 7 discusses the results and how they relate to the phenomenology that drives each signature, including the potential application of findings to forensic casework and future research as it relates to refining burial detection methods. Chapter 7 also discusses research limitations, potential future research directions, and revisits the research questions to draw final conclusions.

CHAPTER 2: UNMARKED BURIALS

This chapter focuses on the social, political, and environmental challenges of unmarked burials and the benefits of locating them. It begins with a brief introduction to international humanitarian law as it relates to two complementary concepts, 1) the legal rights of families of the missing and 2) the responsibilities of parties to conflict to search for and recover the dead. This chapter also explores human remains as evidence, to establish an accurate historical narrative or as a means of truth-seeking. The final section describes the varied anthropogenic and environmental factors that contribute to the challenges of locating unmarked burials.

Humans bury their dead for a myriad of reasons. However, the geophysical qualities of burials exist independent of the context, or reason for interment. Context, for the purpose of this discussion, refers to the combination of timing and burial location, and circumstances leading to death. Context can inform a burial location investigation, such as defining search parameters, but context does not influence the geophysical signatures of a human burial. For example, the geophysical signatures of a burial created with the intention of hiding a body would not vary from the geophysical signature of a documented burial in a cemetery. While the first burial would be considered a forensic context and the latter would not, the burial signatures would be identical, regardless of the intent behind each burial's creation. This statement is true if all other parameters except context are equal, such as if the bodies were interred at the same time, in the same location, and buried in the same manner (i.e., without a coffin, same depth, same soil or other conditions). This distinction is important because, as the science of burial detection develops, incidental or non-forensic burials may be identified. However, while geophysical signatures of a burial exist independent of context, a hidden burial is often associated with a context that drives an investigation for its location. The scope of this dissertation includes unmarked burials that are not

documented or are deliberately concealed. Burials that were once documented, but are now "lost" may potentially share similar geophysical signatures with other unmarked burials for the reasons stated above, but fall outside the contextual scope of this research.

2.1 International Humanitarian Law as a Legal Foundation for the Current Study

International humanitarian law (IHL) is comprised of treaty law and customary international law, made up of military manuals, national legislation and case-law, UN resolutions, or other protocol and general practice of states accepted as law. In the context of international and non-international armed conflict, IHL establishes the families' right to know the fate of their missing relatives and the obligation of parties to the conflict to search for and recover the dead (Petrig 2009), providing a legal foundation for the application of remote sensing to unmarked burial detection.

When bodies are deliberately hidden or burial locations are not documented, communities and families of the missing often have unanswered questions. In both domestic and international scenarios, the living often chooses to locate unmarked burials to recover the remains (Stover et al. 2003). Preferences for how to facilitate peace and reconciliation vary among communities, so the need or desire to recover the remains of the missing is not universal (Stover and Shigekane 2002; Wagner 2008). Regardless of preference, the rights of family members to know the fate of their missing relatives is codified under the combined protections known as Rule 117, Section D, or the right of families to know the fate of their relatives (Henckaerts 2005; Petrig 2009), hereafter in this dissertation as the "right to know." The international treaties that establish the legal right to know are the 1949 Geneva Convention IV (Article 26) and 1977 Additional Protocol I (Article 32), the 1990 African Charter on the Rights and Welfare of the Child (Article 19), and the 2006 Convention on Enforced Disappearance (Article 24). A breadth of instruments and protocol that make up

customary IHL exist for this purpose, as well (ICRC 2016). The families' right to know is described throughout IHL and customary international law as the right to know the fate of missing relatives in circumstances such as conflict, displacement, or forced disappearance.

IHL also establishes Rule 112, which states that, "whenever circumstances permit, and particularly after an engagement, each party to the conflict must, without delay, take all possible measures to search for, collect and evacuate the dead without adverse distinction" (Henckaerts 2005). This protection is interpreted such that parties having a direct or indirect role in the conflict must, to the extent that available resources will allow, search for and recover the dead, without preferential treatment (ICRC 2016; Petrig 2009). The international treaties that establish the parties' responsibility to search for and collect the dead are the 1929 Geneva Convention (Article 3), the 1949 Geneva Convention I (Article 15), 1949 Geneva Convention II (Articles 18 and 21), 1949 Geneva Convention IV (Article 16), 1977 Additional Protocol I (Articles 17 and 33), and 1977 Additional Protocol II (Article 8). Additionally, several instruments make up customary IHL for this purpose (ICRC 2016). Enforcing the right to know through the search and recovery of remains is not straightforward, as circumstances may prove logistically difficult where wartime resources are limited, and the needs of the living must take priority (Petrig 2009). Additionally, the parties responsible for accounting for the dead are often the parties responsible for the loss of life in the first place, sometimes contributing to complicated post-conflict political circumstances that make implementation difficult.

The right to know and the recovery of the dead are closely linked concepts. Searching for and recovering the physical remains of the deceased is a *sine qua non* in the process of ensuring the families' right to know, if that right is to be met through direct evidence of an individual's death (Henckaerts et al. 2005; Petrig 2009). Under IHL, parties to conflict are shouldered with the

responsibility of recovering the missing as a result of international or non-international armed conflict, and that parties "shall be prompted mainly by the right of families to know the fate of their relatives" (AP I/Article 32). Therefore, where search and recovery yields a lack of evidence, families are effectively denied their right to know.

International humanitarian law is designed to protect wartime cemeteries, but extends to formally establish legal responsibility of parties in the context of armed conflict. The breadth of IHL protections suggests that there is a wide range of circumstances that can lead to death during conflict, leading to the spectrum of possibilities for human body disposition. In the case of burials, human remains can be buried in unmarked graves following conflict with an opposing party, but they can also be buried under different circumstances related to conflict (Hunter and Simpson 2007; Rugg 2000). Community or family members may bury a dead body they have discovered out of respect for the dead, for environmental or hygienic reasons, or to prevent desecration of bodies caused by necroviolence, animal scavenging, or weathering (DeLeon 2015; Eppel 2014; Hunter and Simpson 2007). Hastily buried remains, even those interred by the victim's family or community, can be equally challenging to locate after the conflict has officially ended, particularly if the location is not marked.

Given the challenges of locating unmarked burials, which will be discussed later in this chapter, the families' right to know is difficult to guarantee. Confounding these challenges are the negative effects of conflict, such as a depressed economy (Collier 2000) and weakened infrastructure limiting progress (Addison and Bruck 2008). Continued rule by offending governments hinders investigations (Gassiot and Steadman 2008), and the welfare of survivors will, and should, take priority over recovery of the dead (Brinkerhoff 2005; Petrig 2009). However, as each of these complicating factors is introduced, guaranteeing the right to know becomes easier

to delay, which effectively denies families their right. For these reasons, the involvement of independent international organizations is often necessary to search for and recover the physical remains of missing persons. Few organizations are equipped to support such an endeavor, but with technology-assisted search efforts on the rise, the recovery of human remains may soon become less costly and more efficient, rendering the process less demanding of the limited resources that are available in a post-conflict environment.

There are social, political, and environmental obstacles in areas where bodies have been interred that hinder search and recovery. Former conflict zones often continue to pose safety hazards, even after conflict has officially ended, preventing investigators' safe access to burial sites. Skinner and colleagues (2003) report that some workers in the former Yugoslavia were exposed to armed grenades and other unexploded ordnance at grave sites, and also comment on the danger of traveling to and from the field. The Guatemalan Forensic Anthropology Foundation team members and their families have received death threats and have been targets of other types of harassment for their involvement in forensic investigations of state violence (Lloyd 2002). Moreover, the physical safety of investigators is sometimes in question through gestures that imply risk, such as when armed officers were sent by government officials to an Andalusian cemetery to prevent the previously approved exhumations of Spanish Civil War dead from an already exposed grave (Gassiot and Steadman 2008). Such scenarios pose real physical and psychological threats to workers on the ground that must be balanced with efforts to meet the responsibilities of parties and ensure the families' right to know.

Physical safety concerns are not only limited to investigators. Witnesses, too, can receive threats to physical safety, as well as constant political pressure, so surviving witnesses may have reservations about coming forward with information about the location of human remains. Eppel

(2014) describes a witness account from Zimbabwe, where a woman was killed by soldiers for hiding schoolgirls to protect them from rape. The soldiers forced the witness to bury the woman's body in an unmarked grave near a tree. Following the burial, the witness marked the tree with a shovel so he could keep track of the burial location over time. The witness was afraid to tell the victim's relatives about her fate until other excavations and reburials had begun, at which time he came forward with the location of the burial and the woman's remains were recovered and reburied by investigators (Eppel 2014).

Forensic investigations are also political. Gassiot and Steadman (2008) describe obstacles that have prevented investigators from adequately addressing human rights violations that occurred in Spain during the Civil War. The extent of political influence on the investigation has included forced amnesia where powerful stakeholders promote a culture of forgetting. Moreover, inconsistent government policies can cause confusion between agencies and hinder investigations (Gassiot and Steadman 2008). For example, Kovras (2008) outlines a dilemma over the exhumation of the famous poet and playwright, Federico Garcia Lorca, who was executed and buried in an unmarked mass grave during the Spanish Civil War. Lorca's family initially rejected the idea of exhumation, as they felt it would disturb his remains. However, some argue that not exhuming his remains would serve to "forgive and forget" past offenses during the conflict. Proponents to exhumation believe inaction diminishes the government's repressive role in the conflict (Kovras 2008). Navigating the politics of burial exhumations is not always straightforward, though Gassiot and Steadman (2008) argue that the political nature of investigations is often what dictates where and when they can occur. Logistical and political challenges often prevent parties of conflict from fulfilling their responsibilities to account for the

dead. These often unavoidable obstacles subsequently affect the families' right to know the fate of their missing relatives.

2.2 Human Remains Recovery as a Form of Truth-Seeking

Truth-seeking approaches to justice can focus on the past and on accountability, or on the future and community recovery or reintegration. The two perspectives are not mutually exclusive, but researchers are often divided on whether victims and perpetrators should be encouraged to agree on past events. A dead human body is evocative, so some argue that backwards-looking perspectives on reconciliation, which could include the exhumation of human remains, may dredge up mutual feelings of resentment and promote renewed conflict (Mendelhoff 2004; Thoms et al. 2010). Conversely, others argue that an exclusively forward-looking perspective on reconciliation ignores past offenses, passively legitimizing the oppressive actions of the perpetrator (Kovras 2008). However, communities are not homogenous, and individual opinions vary on which approach to take. Moreover, post-conflict recovery through truth-seeking can be complicated by the fact that some victims of conflict were also perpetrators compelled to act violently against members of their own community and, therefore, represent both groups (Nwogu 2010), such as the many cases of child soldier abductees in Uganda (Veale and Stavrou 2007). Acknowledging that conflict is complicated and communities are heterogeneous, some argue against blanket approaches to truth-seeking and recovery, instead focusing on individuals directly affected by violence (i.e., victims and perpetrators) to truly understand the conflict and how best to promote reconciliation (Nwogu 2010).

Acknowledging the circumstances of death by recovering physical remains is an important element for meeting the needs and legal rights of families during post-conflict recovery. Post-conflict recovery often includes truth-seeking efforts focused on establishing accountability for

past offenses and correcting a false narrative of events with an aim to prevent recurring conflict (Gonzalez and Varney 2013). In circumstances that are amenable to exhumation, recovering the dead can be a valuable avenue for truth-seeking, but may include complex and sometimes conflicting narratives and agendas. Seeking truth through the recovery of human remains is rarely straightforward, and may even compete with social norms, evoking controversy and mixed emotions. For example, in 1941, hundreds of Jews were killed in Jedwabne, Poland, and for many years it was accepted that Nazi occupiers were responsible for the deaths (Rosenblatt 2015). However, a book published by Gross (2001) contested that widely held belief, arguing that the Jews were killed by Polish members of their own community – an unpopular idea met with criticism. Polish anthropologists working for the Polish Institute of National Remembrance, along with Dr. William Haglund, performed exhumations at two mass graves from the massacre. The anthropologists found evidence supporting Gross's claim that the Polish townspeople played a crucial role in the premeditated violence, but also found evidence of German involvement (Ignatiew 2002), sparking contentious debate (Rosenblatt 2015). Exhumations were stopped by Orthodox Jews who claimed the digging disturbed the dead bodies, and any further exhumations would violate Jewish law. Ultimately, the extent of Polish and German involvement and the number of people killed will remain unknown because religious law forbids further exhumations. Recovering the dead through exhumations may not always be the best method of truth-seeking because, as in the case with Jedwabne, family or community members may object to exhumation for its potential to disturb the dead or linger on past offenses (Kovras 2008; Rosenblatt 2015).

Coordinated efforts aimed at guaranteeing the right to know, such as organized truth and reconciliation commissions, generally assume all participants want the truth, and that everyone wants to arrive at that truth at the same time (Mendelhoff 2004; Thoms et al. 2010). Truth

commissions are usually established with general goals of truth-seeking in mind – truths that are believed to set the record straight or lead to additional knowledge, but these efforts are sometimes made in the immediate wake of violence, possibly before survivors are ready to share their realities of conflict (Hayner 1996; Shaw 2007). Truth and reconciliation commissions can also encourage reconciliation that is focused on mutual peace-building efforts in coordination with efforts aimed at holding the accused accountable for perceived wrongdoing. Truth-seeking efforts can aim to restore peace and guarantee the families' right to know using incentives to promote information gathering. For example, Colombia's Justice and Peace Law (JPL) offers reduced sentences to paramilitaries in exchange for a commitment to demobilize and provide confessions containing valuable information about the fate of missing relatives, including – if bodies were buried – the locations of human graves (CCC 2005, 2006). The JPL, however, has been criticized for its lenient penalties for violent crimes, while supporters argue the law promotes reconciliation, and is consistent with international law (Garcia-Godos and Lid 2010). Reconciliation is a debated concept in post-conflict studies, however, as there is an apparent lack of consensus about what reconciliation means, what are its goals, and can parties to conflict ever actually agree on those ideas (Skaar 2012). Tied to this debate is the matter of whether the recovery of human remains is an essential step toward reconciliation, particularly if the families' right to know can be satisfied through other means. Aronson (2011) argues that in post-Apartheid South Africa the justice process has focused on social and political reconstruction, but if individuals are to benefit from the process of truth-seeking, which included the search for and recovery of missing persons, survivors of conflict should first be consulted. With pressure, and not without challenges, reconciliation efforts can still result in apologies, commemorations, or formal peace agreements, sometimes as a complement to amnesty or prosecution (Olsen et al. 2010).

Some researchers see truth-seeking efforts, including the recovery of human remains, as posing potential obstacles to reconciliation efforts between recently opposing parties (Shaw 2007), while others see truth-seeking as an opportunity to facilitate reconciliation (Wierzynska 2004). During the genocide in Rwanda, which has been called an "intimate genocide" (Staub and Pearlman 2001: 206), neighbors and people in ethnically mixed families turned on each other, and in some cases killed their own children (des Forges 1999; Mamdani 2002; Staub 2006). Death toll estimates include over 700,000 Tutsis and 50,000 Hutus, resulting in more Rwandans left affected by this event than unaffected (des Forges 1999; Mamdani 2002; Prunier 1995). The scale of the Rwandan genocide meant that no court system could feasibly prosecute every perpetrator (Stover and Shigekane 2002), and attempting to do so would overburden an already weakened economy (Wierzynska 2004). To address the sheer scale of the genocide, the Gacaca court – a community justice system based on traditional Rwandan values – was formed to bring together perpetrators, victims, and the government as active participants in their own post-conflict reconciliation (Wierzynska 2004). Human Rights Watch (2011) has reported that the Gacaca process has had a positive effect on some genocide survivors' lives (Connor 1996; Haglund et al. 2001). For example, the Gacaca system created a forum for families to learn the truth about the fate of their missing relatives, which involved the exhumation of missing persons in unmarked graves, allowing families to perform burials according to their own customs (HRW 2011).

Locating and exhuming human remains has been often described as a way to help establish an accurate historical record. History is sometimes revised or blatantly denied by the perpetrators (Wright 2010). The continued existence of deliberately hidden bodies can contribute to a legacy of denial and impunity, perpetuating the existing tensions between perpetrators and victims (Gassiot and Steadman 2008). Locating unmarked burials may facilitate access to physical

evidence contained within a burial, substantiating victims' claims on history (Klinkner 2008; Sanford 2006; Stover 1995). For example, during the early stage of his war crimes trial, former Serbian President Slobodan Milošević invoked his nation's right to self-defense – referring to his effort and the effort of his people as "heroic" (Milošević 2002) – against perceived terrorists posing a threat to his people stating, "here the struggle against terrorism in the heart of one's own country, one's own home, is considered to be a crime" (Milošević 2002).

Milošević's account was a powerful message of ethnic nationalism that was widely embraced and unquestioned by many of his supporters at the time (Gagnon 1994). If left unchallenged, this fictional narrative may have suppressed accurate historical accounts, further marginalizing the victims. Fortunately, developments in the forensic investigation and subsequent legal proceedings revealed that Milošević had been jointly responsible for the targeted killing of many thousands of people including women and children found executed in mass graves (ICTY 2004). Women and children do not fit into the militarized narrative presented by Milošević at his trial. These actions were, by their sweeping nature, characteristic of war crimes, not self-defense. Milošević died before his trial concluded, so a verdict was never rendered. However, the presentation of forensic evidence at the International Criminal Tribunal for the former Yugoslavia (ICTY) overwhelmingly supported Milošević's involvement in the coordinated actions carried out by Serbs against non-Serbs during the conflict. This evidence directly influenced the 2016 conviction of Radovan Karadzic, who was found guilty of genocide, war crimes, and crimes against humanity, resulting in a 40-year prison sentence (ICTY 2016).

2.3 The Benefits of Locating Human Remains

In cases where missing persons are believed to be deceased, the absence of physical remains to confirm death or perform funerary rites can bring about significant and lasting

economic, emotional, or spiritual distress for families (Eppel 2006; Stover et al. 2003; Wagner 2008). Attempts to locate human remains may ameliorate the uncertainty felt by family members and friends of the missing (ICRC 2016; Rosenblatt 2015). For example, following the disappearance of their husbands during the 1995 – 2006 Maoist insurgency, Nepalese women are neither widows nor wives and face severe social stigmas (Robins 2011). Typically not self-sufficient, Nepalese women live with their husband and his family. However, the wife of a disappeared man is viewed as an economic burden to his family if she stays on without him present, or as disloyal to her husband and his family if she chooses to leave and remarry. Men are the primary income earners in Nepalese society, so it is uncommon for women to independently support themselves or their children. Robins (2011) emphasizes the particular importance of either recovering the physical remains or having "absolute evidence of death in order to complete rituals," (2011:87) in the form of a definitive test, such as a DNA comparison. Such evidence serves two purposes; absolute evidence of death enables families to carry out funerary rituals and evidence of death helps resolves ambiguity about the social status of the wives of deceased men (Robins 2011).

Eppel documented the benefits of locating and recovering the physical remains of missing persons following years of state violence in Zimbabwe, reporting that "reburials had transformative outcomes at the individual, family and community levels" (Eppel 2014:2). The Argentine Forensic Anthropology Team conducted burial exhumations in Zimbabwe from 1999 to 2001, resulting in the reburial of exhumed remains. Collaboration with EAAF also provided a training opportunity for local Zimbabweans to learn forensic anthropological techniques. Eppel's follow up with the communities in 2014 revealed through interviews with community members that the recovery effort encouraged witnesses to share information, which provided details about locations of the dead. In Zimbabwe, wandering spirits are credited with family hardship, but spirits

cannot be appeased until burial rituals are appropriately performed, which includes burying the body in a carefully selected location (Eppel 2006; Eppel 2014). The ambiguity of a disappeared person's status and the disrespectful nature in which remains are disposed of during conflict are difficult traumas to overcome and, therefore, disrupt the normal psychological and cultural processes of grieving (Eppel 2014). Recovery, identification, and reburial of physical remains are credited with resolving family conflict "linked to unresolved grief, displaced anger and fear" (Eppel 2014:8), and provide a burial site for families to visit and commemorate their deceased relatives. Following reburial, hardships experienced by families are no longer attributed to the wandering spirits, but to other causes, and most families claimed they had been healed by the reburials (Eppel 2014). Community members now attribute their hardships to God disowning the government that is overrun with poor leadership. In Zimbabwe, the outcome of reburial, then, is one of healing, and if hardship still exists it can be separated from the existence of poorly treated dead bodies (Eppel 2014).

Conflict has far-reaching and often immeasurable effects on living individuals, communities, and entire societies. Affected individuals include victims, perpetrators, or people who represent aspects of both groups simultaneously. Victims and perpetrators may be directly or indirectly affected by conflict in more than one way, whether economically, physically, emotionally, or spiritually in both the short and long-term. Post-conflict recovery is a complex process that involves many stakeholders who may have different motivations and expectations that are often shaped by their experiences with conflict. Coordinated efforts to move past conflict, which may or may not include searching for missing persons buried in unmarked graves, should be guided by the input of people directly involved in the conflict. This input can be supplemented

by the guidance and resources of the international community (Aldana 2006; Antkowiak 2011; Lundy and McGovern 2008).

2.4 Accounting for the Dead

Many different governmental bodies or non-governmental organizations exist for the purpose of accounting for the dead. Some are managed at the international level, addressing multiple conflicts in different regions of the world, while others are run at national, state, or local levels focusing on individual conflicts. This section focuses on three well-known organizations that facilitate recovery efforts in various countries, as well as a brief description of the domestic agencies that search for missing persons in the United States.

2.4.1 Missing Persons Accounting Organizations

Several organizations exist for post-conflict casualty accounting, including the Defense POW/MIA Accounting Agency (DPAA), the Argentine Forensic Anthropology Team (*Equipo Argentino de Antropología Forense*, or EAAF), and the International Commission on Missing Persons (ICMP). While these organizations are independent of each other and embody very different scopes of work, each was established with missions to account for missing persons, and each with a unique contextual and geographic scope. The history of formal US post-conflict accounting dates back over 40 years. The DPAA mission is to account for the remains of nearly 42,000 recoverable (i.e., those not lost at sea) missing US service personnel lost between 1941 to 2010, usually as ground burials or aircraft crash sites in former US conflict zones throughout the world (DPAA 2016). The DPAA finds burial sites through survey or reconnaissance either when an artifact or other evidence is turned in without association to a specific site or through local knowledge of a likely burial site (DPAA 2016). The DPAA reports on finding the remains of

missing US service personnel in unmarked burials located in Cambodia, North Korea, Germany, France, and most other territories having strategic geographic significance in World War II, the Korean, Vietnam, and Cold Wars, and more recent conflicts in the Middle East (DPAA 2016).

The National Commission on the Disappearance of Persons (CONADEP) was formed in 1983 by then-recently inaugurated Argentine President Raúl Alfonsín to investigate over 8,000 forced disappearances, or *desaparecidos* from what is known as Argentina's "Dirty War" (1976 – 1983). In 1984, CONADEP released, "Nunca Más" (Never Again), a public report detailing the accounts of torture, disappearances, and killings by the Argentine military forces against political dissidents during the period of the Dirty War. The following year, CONADEP committee members and the Grandmothers of the Plaza de Maya, who were searching for their missing grandchildren, requested assistance from the Science and Human Rights Program at the American Association for the Advancement of Science (AAAS). A delegation of scientists, including renowned forensic anthropologist Dr. Clyde Snow and then-director of the AAAS Science and Human Rights Program, Eric Stover, traveled to Argentina to assist with the investigation and documentation of human rights violations. Dr. Snow returned to Argentina during the following years to train a cohort of anthropologists, archaeologists and medical professionals in forensic anthropological and archaeological techniques, thus helping to form the EAAF. The team is credited with finding and identifying the remains of hundreds of *desparacidos* throughout Argentina (EAAF 2016). The EAAF now operates globally, assisting other countries with post-conflict missing persons recovery efforts and training other national teams to perform recoveries, such as in Guatemala, Peru, and Chile (EAAF 2016).

The ICMP was formed as part of the 1996 Dayton Peace Agreement that formally ended the conflict in the former Yugoslavia. The four-year conflict resulted in over 40,000 missing

persons (ICMP 2016). Since 1996, the ICMP has recovered and identified over 27,000 missing persons, but nearly 30% have still not been found (ICMP 2016). The ICMP has since expanded operations to serve countries across five continents, which includes offering DNA expertise for responding to human rights violations, armed conflict, and disaster victim identification (ICMP 2016). The ICMP continues to locate unmarked burials throughout the western Balkans, but the rate of recovery has rapidly decreased because, according to ICMP Director General Kathryne Bomberger (2015), burials are "getting harder to find" and additional resources, such as remote sensing, may soon become necessary to locate the remaining clandestine graves.

Unmarked burials have been a central focus of investigation for each of these organizations, but such burials are not an exclusively international or post-conflict problem. Local, state, and federal law enforcement agencies in the United States attempting to locate and identify missing persons face similar challenges (Christensen et al. 2009; Harrison and Donnelly 2009; Schultz and Dupras 2008). As of year-end 2013, over 84,000 people in the United States were considered missing persons (FBI 2016), many of whom were thought to have disappeared involuntarily or who went missing under circumstances indicating they were in physical danger at the time of their disappearance (FBI 2016). An unknown percent of these missing persons are likely to be deceased, and of the deceased, even fewer are buried in clandestine graves. However, domestic missing persons buried in unmarked graves are no less challenging to find than graves located in an international or post-conflict context.

2.4.2 Evidence-based vs. Humanitarian Investigations

Families of the missing, communities, governments, tribunals, or international organizations may attempt to search for and recover the dead, or they may choose to enlist the help of trained forensic specialists. Recovery efforts by trained professionals may serve a legal purpose,

where bodies and associated grave contents are exhumed in a systematic manner, usually following the Minnesota Protocol (UN 1991), to preserve the integrity of the evidence. In rare instances, bodies may be exhumed for the sole purpose of repatriation. Indeed, the two approaches are compatible, as evidence can be preserved for prosecution with repatriation in mind, even if that is not the initial focus.

While excavations can have humanitarian or evidence-based goals, they are not mutually exclusive – although their approaches may differ, the two overlap quite often. Regardless of the mandate, archaeological techniques are well suited for systematically exposing, documenting, recovering, and preserving buried evidence, including human remains. In 2005, the Minnesota Protocol was created to establish the best-practices for conducting investigations of violent or suspicious death, which includes possible extra-legal, arbitrary, and summary executions. These non-binding guidelines outline methods for carrying out investigations under standards of competence, thoroughness, promptness, and impartiality (UN 1991). Created by the Minnesota Lawyers International Human Rights Committee, with input from other notable human rights experts, including Eric Stover, Dr. Clyde Snow, and Dr. Karen Burns, the Minnesota Protocol includes valuable guidelines on identifying victims, recovering and preserving evidence, identifying witnesses, determining the circumstances of death, identifying individuals involved in the death, and bringing perpetrators before a court. Many of these standards rely on the strengths of impartial forensic experts, where their vetted techniques are applied within a legal framework. Internationally, evidence-based investigations following conflict have led to legal proceedings against perpetrators of war crimes, genocide, crimes against humanity, and other grave breaches of IHL. For example, members of the Guatemalan Forensic Anthropology Foundation (FAFG) used the Minnesota Protocol as a guide for documenting evidence and providing expert witness

testimony during the trial of José Efraín Ríos Montt, the former military general and President of Guatemala during the Guatemalan Civil War. The evidence and expert witness testimony helped build a strong case against Ríos Montt, resulting in his conviction on charges of genocide and crimes against humanity (Stuesse 2013).

Forensic investigators document and recover evidence and other material associated with a grave. Forensically significant evidence includes clothing, which may identify individuals to a specific protected group; blindfolds, ligatures, and bullet casings possibly indicating cause or manner of death; or other items, such as identifying building material, which has been used to link the execution location with the buried victims (Cheetham and Hanson 2009). Evidence also includes features within the grave, such as tool marks or digging scars left by heavy machinery on the grave walls. In court, prosecutors have used this type of evidence to illustrate how a grave was created (Skinner et al. 2003). Digging scars from heavy machinery can also be evidence of the effort put forth by the perpetrators to conceal a crime or may indicate premeditation. Forensic evidence can help establish a sequence of events, contribute to victim identification or group affiliation and provide indications of cause and manner of death. Forensic evidence recovered from within a grave can indicate that a body has been moved postmortem, assist with crime scene reconstruction, link a grave to a crime scene, or a perpetrator, and – as clearly illustrated during crime scene investigation and recovery in the former Yugoslavia – can link primary, secondary, and tertiary graves to one another (Cheetham and Hanson 2009).

Forensic anthropological techniques also offer a rigorous approach to humanitarian projects. Humanitarian investigations are those that actively promote the welfare of surviving families and community members by encouraging participation in their own recovery process, or participating on their behalf. Family and community participation can take many forms,

including providing witness testimony, selecting sites for commemoration, or even acting as co-plaintiffs with the prosecution (Crettol and La Rosa 2006). Additionally, burial excavations can and do involve family members, such as in Guatemala where anthropologists with the Guatemalan Foundation for Forensic Anthropology worked alongside family members who observed many of the excavations (Lloyd 2002; Stover and Shigekane 2002). In both Guatemala and Argentina, some family members even participated as workers in burial excavations (Doretti and Fondebrider 2002; Juhl and Olsen 2006; Stover and Shigekane 2002). The successful outcome of an investigation is not necessarily dependent on families actively participating in the recovery of human remains, but it is important to maintain an open dialogue between investigators and communities to ensure that efforts meet the needs of the people they are intended to help.

Addressing the needs of the living and accounting for the dead means striking a balance between short-term and long-term goals of individuals, families, communities, and nations. Families of the missing may want their relatives' remains returned immediately after the conflict ends, but they may also want criminal prosecutions. Hastily conducted excavations, by inexperienced persons in Iraq and Cambodia, resulted in long-term problems for both evidence-based and humanitarian investigations (Klinkner 2008; Stover et al. 2003). Following conflicts in those regions, untrained individuals opened graves in an attempt to find the remains of their missing family members. In Iraq, bodies were exhumed with heavy machinery, resulting in recovery-induced trauma to the skeletal remains that was unrelated to the cause of death (Stover et al. 2003). Moreover, the manner in which excavations were conducted induced commingling of skeletal remains from multiple individuals, further challenging the identification process (Klinkner 2008; Stover et al. 2003).

Where resources allow, investigations can simultaneously meet evidence-based and humanitarian goals, although this may not be the initial approach. For example, in 1999, ICTY Deputy Prosecutor Graham Blewitt explained the primary goal of investigators was to establish patterns to prove command responsibility of President Slobodan Milošević by linking sites of mass civilian death to each other (Abrahams et al. 2002). Teams of forensic scientists working in the former Yugoslavia had begun mass grave exhumations with the goal of establishing categorical identification (e.g., ethnic or religious groups), as opposed to individual identifications. Their mandate was set by the newly created ICTY, to demonstrate an "intent to destroy, in whole or in part, a national, ethnic, racial or religious group," in accordance with the Convention on the Prevention and Punishment of the Crime of Genocide (Article 2). Thousands of bodies were exhumed from clandestine graves, then released to Bosnian authorities who, instead of identifying and repatriating the remains, disposed of them in an abandoned tunnel and in storage containers (Stover and Shigekane 2002). This evidence-focused process effectively ignored a large segment of the families' humanitarian needs (Stover and Shigekane 2002) until they demanded that the identification and repatriation of their relatives was equally as important as evidence gathering for criminal prosecution. In 2000, the ICMP established a number of facilities to better manage the human remains and address the needs of the living (Stover and Shigekane 2002). Ultimately, the families of the missing influenced policy change.

Deliberately hidden or undocumented burials deny the living the right to know the fate of the missing and limit the investigator's capacity to search for and recover the remains of missing persons. If a grave cannot be located, investigators are also limited in their capacity to collect evidence. Despite the demand for locating unmarked burials, the challenges are significant, and will be discussed in the following section.

2.5 Unmarked Burials

This section describes the reasons for marking burials, the visual transformation of burials as a result of natural and deliberate concealment, and examples of factors that contribute to the difficulty of locating unmarked burials.

The energy invested in marking and maintaining a burial or a cemetery can be an expression of respect, and often one that is embedded in cultural tradition. For example, fences or walls may delineate the perimeter of a family cemetery, while stones are often placed at surfaces of historic and archaeological burials. In managed cemeteries, graves are often conspicuously marked and their surfaces and surroundings well maintained (Rugg 2000). Marking and maintaining burial sites can also be a gesture of commemoration (Bevan 1991). Marked burial grounds, such as Holocaust cemeteries in Europe and the Srebrenica Genocide Memorial, are important symbols of community loss and are places for survivors and visitors to commemorate the dead (Francaviglia 1971; Rugg 2000). Therefore, burial markers serve two intertwined purposes: 1) to mark the location of a burial for future reference, to ensure that people are able to successfully locate the same burial site each time they visit, and 2) to name and commemorate the dead and their families.

The disposal or deliberate concealment of a body can be as straightforward as covering the remains with debris, or it may involve more effort, such as planting vegetation over the surface of buried remains to disguise the location (Hunter and Simpson 2007). For example, in Branjevo State Farm, Bosnia and Herzegovina, perpetrators planted corn to disguise the new burial as agricultural disturbance (Hanson 2012). Perpetrators also dispose of bodies in remote locations, such as caves and ravines, to avoid accidental discovery (Hunter and Simpson 2007).

The 1995 Srebrenica massacre resulted in over 8,000 disappeared persons in a few days; a devastating event nested within a larger conflict that ultimately led to over 40,000 missing persons (ICMP 2016). The disposal of bodies was both organized and haphazard. Thousands of bodies were buried in mass graves, hundreds were disposed of in caves, ravines, and wells, and countless others were left on the ground surface to decompose in plain view (Wagner 2008). Upon learning of an international investigation, the perpetrators attempted to hide the bodies buried in mass graves by exhuming and moving the remains to secondary and tertiary gravesites (ICMP 2004; Skinner et al. 2001). This act destroyed evidence and commingled remains and other material evidence to such a degree that victim identification continues to be a challenge (Skinner et al. 2001; Wagner 2014).

When digging a grave the displaced soil is usually set aside until it is used to cover the body and backfill the pit. Typically, the surface of a newly constructed burial appears mounded, due to additional interred body mass and loosened soil (Steadman 2009). The mound may be reduced manually or with heavy machinery at the time of interment by compressing or distributing the soil (Steadman 2009). Unless the overlying sod is preserved and replaced back on top of the grave, this process typically results in a scar of exposed soil with the original vegetative cover mixed into the backfill matrix. Therefore, a new burial appears markedly different from its surroundings, particularly if exposed soils are surrounded by vegetation (Steadman 2009). However, such stark visual differences (i.e., upturned soil among vegetation) do not persist indefinitely. If the mound is not manually compacted, or compacted using heavy machinery, it will settle naturally over time. Eventually, vegetation will begin to regrow, blending the burial surface with the surrounding vegetation (Bock and Norris 1997; Carter and Tibbett 2003; Steadman 2009), effectively making the burial difficult to discern from the surrounding environment (Bevan 1991).

This rate of visual transformation at a burial's surface varies considerably. Some of the factors that influence how quickly or slowly a burial surface heals include the time of year of interment, the natural environment in which the interment occurred, the burial's physical dimensions and bodily contents, vegetation species present, precipitation, and amount of available sunlight (Anderson et al. 2013; Bock and Norris 1997; Carson and Barrett 1988; Carter and Tibbett 2003). The visible degree of transformation may be affected by vegetation growth rate differences attributed to changes in burial soils driven by the body decomposition process (Anderson et al. 2013; Meyer et al. 2013). In addition, opportunistic plant species may populate the burial surface differently than surrounding areas (Caccianiga et al. 2012; Callahan 2009; France et al. 1992; Hunter et al. 1996; Killam 2004; Watson and Forbes 2008). Further camouflaging a burial is dry leaf litter and other debris that accumulates at the surface naturally over time (Owsley 2001).

Witness testimony can facilitate locating unmarked burials that have become camouflaged. Yet, witness testimony can be fraught with complicating factors. Aside from false testimony or an ulterior motive, a reliable witness may feel intimidated if there is reason to believe their reputation, physical safety or the safety of their relatives and friends might be at risk (Trotter 2012). As witnesses age, they may have difficulty recalling or describing specific details of an event, including the burial location (Wald 2002), which can be further complicated by changing landscapes. In some instances, there are no witnesses to an event, or the witness has passed away before sharing information (Larson et al. 2011). Where witness testimony is available and reliable, the information can be invaluable to an investigation. Reliable witness testimony can help clarify event timelines, lead investigators to unmarked burial locations, and provide estimates on the number of buried victims (Larson et al. 2011; Schmitt 2001; Stover 2011; Wald 2002). In El Salvador, the El Mozote massacre resulted in the deaths of hundreds of civilians at the hands of

the Salvadoran Army (Danner 1993). Estimates of the number of people killed during the massacre range from approximately 200 to over 900. The lower number is based on the number of people thought to be living in El Mozote at the time. However, a witness who escaped during the massacre claims that, in the days preceding the violence, people in the area were warned of impending conflict with the guerrillas by a member the Salvadoran Army. According to the witness, at the time of the attack, El Mozote was overwhelmed with people who traveled from nearby villages believing that El Mozote would provide shelter from the impending conflict because it did not support the guerrillas and would, therefore, be passed over by the Salvadoran Army. In addition to the minimization – or outright denial – of violence stemming from various political agendas, the failure to consider the movement of people within the region has resulted in a continually debated death toll. In 1993, less than a week after the Truth Commission for El Salvador published its report, estimating over 500 people were killed in El Mozote and surrounding villages during the massacre, Salvadoran legislature passed a blanket amnesty law preventing prosecution of anyone responsible. While the remains of over 100 victims were recovered by forensic anthropologists, the law effectively put a stop to investigations, including the search for and recovery of the remaining victims (Danner 1993).

The political and logistical challenges of unmarked burial location and human remains recovery can be significant. These challenges often limit what can be done in the field, so forensic professionals have begun investigating the potential for remote technologies to help narrow down areas of interest and remotely monitor sites by adopting technologies developed for other disciplines, which are discussed in the following chapter.

CHAPTER 3: REMOTE SENSING

This chapter focuses on the science of remote sensing. The following discussion explores different types of remote sensing and the strengths and limitations of each with respect to scalability of each type, as well as respective environmental compatibilities. The term "remote sensing" refers to a general approach to data collection, where sensors record observations without making physical contact with an object. This chapter discusses two types of sensing systems: passive and active. These two types of remote sensing technology are scalable, meaning instrumentation can be designed for operation at one of three scales: terrestrial (ground-based), aerial (aircraft-based), and orbital (satellite-based), with distance and data resolution sharing in inverse relationship. Specifically, the discussion of sensing technologies focuses on the strengths and limitations of each sensing type and the influence of scale on overall data fidelity for each. The review concludes with an explanation of how the successful application of any sensing configuration (i.e., combinations of sensor type and scale) may be affected by different landscapes.

3.1 Passive Sensing

Passive sensing instruments record electromagnetic energy, such as sunlight, that is naturally available to a sensor (Schott 2007). Examples of passive sensors are common cameras (without flash) and multi-channel spectrometers. A natural example of a passive optical sensor is the human eye, which collects naturally available light. The sun's constant incident energy stream interacts with Earth's atmosphere and with objects at Earth's surface as absorption, emission, transmission, or reflection. Absorbed energy is the transformation of energy to another type of energy, (e.g., light to heat), where heat is energy emission. Transmission is the transfer of energy through one material to another, (e.g., light passing through transparent glass). Reflection is energy that is returned in the general direction from which it originated; its direction dependent on an

object's surface properties, such as texture or curvature. Passive sensors in this study are used to measure reflected energy in the visible and near infrared regions of the electromagnetic spectrum, and are discussed in Chapter 5.

Because solar geometry (i.e. the sun's position in the sky) and atmospheric light scattering are variables that influence the magnitude and direction of incident sunlight, the sun's reflected energy is most reliably measured and compared to other data as a *percentage* of incident energy; the unit-less value of reflectance (Goetz et al. 1985; Schott 2007). Reflectance is calculated by dividing the amount of measured reflected light from a surface by the total amount of measured incident sunlight. This process normalizes measurements of energy to help control for the effects of solar geometry and atmospheric scattering, allows for data collection in sub-optimal lighting and atmospheric conditions, and allows for comparisons of spectra collected under different lighting and atmospheric conditions (Goetz et al. 1985; Schott 2007).

Spectral data sets are commonly referred to as "data cubes," and can be thought of as a stack of images, where each image in the stack is sensitive to a narrow region of light and each image pixel contains the reflectance value at a geographic location on the ground. The collection of all reflectance values at a single pixel location down through all images is referred to as a "spectral profile." This research makes use of four different spectrometers that are discussed in Chapter 5.

3.2 Active Sensing

Active sensing instruments operate in much the same way as passive sensors, but rather than rely on naturally available energy, they provide their own constant energy source (Schott 2007). Examples of active sensing technologies are common cameras (*with* flash), Sound

Navigation and Ranging (SONAR), and Light Detection and Ranging (LIDAR); each designed to emit an energy pulse away from the sensor. Ranging instruments emit pulses that are intended to interact with objects in the environment, and then return to the sensor as reflected energy. When a pulse returns, the instrument measures distance between the energy source and surrounding objects as a function of the time it takes for the signal to return. Object distance, combined with the known direction of the emitted pulse, allows the instrument to calculate the object's position in the environment as a three-dimensional data point.

LIDAR data sets are commonly referred to as "point clouds," and are dense collections of millions of three-dimensional points that represent the location coordinates of pulse-object interaction. This research makes use of three different LIDAR systems that are discussed in Chapter 5.

3.3 Data Resolution and Scale

The visibility of differently sized features in data is largely determined by data quality and available analytical tools (Schott 2007). Since LIDAR is an active sensing technology, multiple fly-overs can help build up the ground point density that contributes to final data resolution. In contrast, the optical parameters, altitude, and viewing geometry of an imaging spectrometer drives image resolution, which determines the minimum visible feature size in airborne spectral imagery. While many existing remote sensing technologies perform exceedingly well in a variety of industries and sciences, most image processing and analytical methods have been developed for scientific disciplines concerned with identifying relatively large or high contrast surface features like buildings, roadways, or geologic features. However, even the most rigorous analytical methods cannot compensate for a feature not captured by a sensor, or a small signature nested

within the normal operating error range of a sensor. To achieve desired results, both data quality and analytical tools must be appropriate for the application.

Spectroscopy

Spectrometers are designed for operation at one of three scales: terrestrial (ground-based), aerial (aircraft-based), and orbital (satellite-based). While the technological concepts of spectroscopy are scalable, the actual sensors designed for operation at a specific scale are not scalable due to wide ranging configurations of the detector, such as field of view and array size, that determine the image size (Weng 2014). For spectral data, data resolution includes spatial and spectral resolution, which should both be taken into consideration when selecting data for any application.

Spatial resolution refers to the amount of area on the ground that fills each image pixel, where higher resolution spectral images appear sharp and features well-defined, and lower resolution images appear blurry or pixelated. Spatial resolution of spectral data is determined by sensor altitude (i.e., scale), viewing geometry, and the sensor's optical configuration, including detector size and focal length (Weng 2014). In terms of sensor scale, the spatial resolution of data collected by a spectrometer is inversely related to the distance between the sensor and its target (e.g., Earth's surface), so as distance increases, spatial resolution decreases. Ground-based spectrometers are operated in close proximity to an object of interest, yielding the highest spatial resolution data at up to a centimeter or less (PANalytical; Spectra Vista Corp.), but cover only as much area as a sensor operator can reach in-person. Satellite-based spectral sensors provide the most rapid data collection and produce imagery containing large areas due to swath widths ranging from 13 km (WorldView-3, DigitalGlobe, Inc.) to 185 km (Landsat missions, NASA/USGS), at nadir. The best commercial or public imaging satellites orbit Earth at approximately 500 km

altitude or higher, resulting in spatial resolution of image bands ranging from approximately 1.2 m to over 1000.0 m. This range includes the WorldView-3 sensor at 1.2 m (DigitalGlobe, Inc.), the Landsat and Hyperion instruments at 30 m, the Visible/Infrared Imager Radiometer Suite (VIIRS) system at 750 m (NASA), and the Moderate Resolution Imaging Spectroradiometer (MODIS) at 1000 m (NASA). Airborne sensors, however, cover a greater amount of area than ground-based spectrometers and, because flight altitude is variable, airborne spectrometers can generate higher spatial resolution imagery than satellite sensors can provide, ranging from 0.5 m resolution at 150 m flight altitude (G-LiHT, NASA-GSFC, unmanned aerial systems) to approximately 20.0 m at 11 km altitude (AVIRIS, NASA-JPL).

Spectral resolution refers to the number of spectral bands and the sensitivity of each band to variations in radiation within an instrument's spectral range. Imaging spectrometers typically cover a spectral range of visible (400 – 750 nm) and near infrared (750 – 1400 nm) wavelengths, but some sensors will also cover the shortwave infrared wavelengths (1400 – 2500 nm). Spectral response functions for each spectral band typically follow Gaussian distributions and are measured by their full width at half the maximum wavelength response (FWHM), also known as bandwidth (Weng 2014), where lower FWHM values indicate higher spectral sensitivity. Ground-based spectrometers have the highest spectral resolutions with hundreds or thousands of bands with FWHM ranging from 3.0 – 10.0 nm (PANalytical; Spectra Vista Corp.). Satellite sensors have the lowest spectral resolution, with 4 – 220 bands with FWHM ranging from approximately 10 - 100 nm. This range includes sensors such as GeoEye-1 which contains four bands (DigitalGlobe, Inc.), MODIS which contains 36 bands (NASA), and Hyperion which contains 220 bands (USGS). Similar to spatial resolution, airborne spectrometers provide a compromise for spectral resolution,

with hundreds of bands with FWHM ranging from 7 – 16 nm (G-LiHT, NASA-GSFC; AVIRIS NASA-JPL). Data resolutions for each spectrometer used in this study are discussed in Chapter 5.

LIDAR

LIDAR data are collected from terrestrial or aerial platforms. For LIDAR data, spatial resolution refers to the density of a point cloud, where high point density helps generate accurate surface elevation images. Density of LIDAR point data is primarily driven by the pulse rate and the number of scans performed (Weng 2014). Because LIDAR is an active sensing technology, data sets are cumulative and each new scan increases overall point density. Point cloud density can be increased by scanning an area multiple times from different positions to fill in data gaps. Multiple scans can be merged to create a single, high density point cloud that can be filtered to include only a specific type of point (e.g., ground points). Once filtered, points are used to create surface images, where the more points, the higher the spatial resolution of the image. Data resolutions for each LIDAR scanner used in this study are discussed in Chapter 5.

3.4 Landscape Considerations

Landscapes exhibit varying levels of complexity that influence the effectiveness of some remote sensors in certain environments or circumstances. For example, spectrometers require an unobstructed line-of-sight to a surface to measure its reflectance (Weng 2014). Objects that restrict an airborne or satellite sensor's line-of-sight can include tall buildings and tree canopy. Foreground objects may themselves be visible and measurable, but they obstruct the surfaces behind or beneath them, keeping those background surfaces from being observed. The challenge of vertical obstructions blocking a ground surface may be exacerbated by off-nadir viewing geometry, where an oblique image is captured by a sensor that is not positioned directly overhead and aimed

perpendicular to the ground surface. Additionally, visible but shaded surfaces (e.g., areas inside a shadow cast by a building or tree) reflect more scattered light than reflected incident sunlight needed to measure reflectance, which is effectively a data noise measurement that cannot be used in analysis. These challenges can be overcome by capturing images from different viewing positions or at different times of day to avoid objects and shadows, but unconditionally obstructed surfaces such as ground beneath tree canopy are not so easily observable from airborne or satellite sensor platforms, no matter the viewing geometry (Pu and Gong 2011).

LIDAR scanners are well suited for complex environments in that data sets are cumulative, and multiple scans from different positions can fill in data gaps behind obstructions, such as buildings. Additionally, since naturally reflected light is not a requirement for LIDAR systems, which supply their own energy, shaded and unshaded areas are equally measurable (Shan and Sampath 2006). LIDAR pulses can pass through narrow spaces between canopy leaves and branches that would otherwise limit light that is naturally reflected at the ground surface from reaching a spectrometer's detector. This capability permits LIDAR scanners to overcome certain obstructions that spectrometers cannot, and in general requires that a direct pulse path exist between a surface and a sensor, even if through a small space. For this reason, active sensors are used by archaeologists in densely forested areas to simultaneously measure the ground and canopy surfaces (Chase et al. 2011), while imaging spectrometers are used to measure canopy reflectance spectra (Saturno et al. 2007) – applications that are discussed in Chapter 4.

Whether a sensor is passive or active, or designed for use at a particular scale, remote sensing technologies are able to record observations rapidly and in a non-destructive manner. Instruments mounted on aerial or orbital platforms have the added advantage of collecting data over large swaths of land, making remote sensing one of the most time-wise efficient data

collection methods available. In the right environment, remote sensing holds the potential to augment existing data collection approaches without interfering in them and can be used in addition to, rather than as a replacement for, existing burial detection methods.

CHAPTER 4: CURRENT METHODS FOR LOCATING HUMAN BURIALS

This chapter focuses on current methods used to locate unmarked burials. The strengths and limitations of existing ground-based survey methods will be followed by a review of remote survey methods used in both archaeological and contemporary contexts.

Defining the search area is one of the first priorities for locating an unmarked burial. To define a search area, investigators may rely on witness or perpetrator testimony or other types of documentary evidence (Areh and Umek 2004; Komar 2008; Larson et al. 2011; Schmitt 2001). Selecting which search method or combination of methods to start with depends on a number of factors such as available witness testimony, resources, and access to the search area. In preparation, search areas may be narrowed down using other types of documentation such as maps, plans, and records, or by applying models developed from other known burials in cases of patterned violence (Congram 2010; Komar 2008). However, without such information, searches can prove significantly more challenging.

4.1 Ground-based Survey Methods

Ground-based survey methods require people and/or equipment to be present at the approximate, if not precise, location of inspection. Pedestrian survey is used in a defined search area to acquire the lay of the land and identify areas of interest, such as surface-scattered human remains or evidence of disturbed ground. In practice, a team of individuals spaced equally apart will systematically move across the landscape, searching for signs of disturbance or other evidence indicative of human activity. The team will attempt to identify signs of digging, such as exposed soil, a remnant backfill pile or changes in the appearance of the ground surface (Christensen et al. 2014; Killam 2004). Cadaver dogs trained to identify the scent of human decomposition may be

incorporated at this phase to augment the investigation if the post mortem interval is not extensive (Lasseter et al. 2003). However, the success of ground-based surveys depends on accessible surface evidence and relies on the ability of search party members to recognize evidence or signs of disturbance. Taphonomic processes may camouflage evidence or obscure disturbance activity, diminishing the effectiveness of a pedestrian survey.

When a search area is defined, ground probing may be used to identify potentially disturbed soil. Systematic probing assesses soil consistency, identifying areas with loosened soil relative to surrounding compact soil (Christensen et al. 2014; Killam 2004, Owsley 1995). A probe is inserted into the ground at shallow depth to gauge near surface soil compaction. A methodically slow and tedious process, probing can offer valuable subsurface information not discernable during conventional pedestrian survey (Owsley 1995). Probing should be performed on a grid pattern, where probe holes are created at pre-defined intervals. The coarseness of this method is a clear disadvantage in that a burial could be missed, or worse – impacted by the tip of the probe, mimicking or obscuring trauma or other types of evidence. This type of investigative artifact can cause evidentiary problems during trial (Boyd 1979). Moreover, the method relies on the presence of loose soil and on the ability of each person using a probe to correctly assess the soil compaction at each location.

When pedestrian survey or probing fails to provide sufficient evidence, investigators may attempt a more invasive approach, such as soil cores, shovel test pits or surface scraping (Ubelaker 1999). Eventually, systematic excavations, ranging from shallow hand-dug test units or large trenches using heavy machinery may be attempted (Bass 1963; Bass & Birkby 1978; Owsley 1995; Ubelaker 1999). Any type of systematic excavation may expose patterns in soil stratigraphy indicating a natural soil profile (undisturbed) or otherwise. An undisturbed, natural soil profile

typically exhibits one or more intact layers containing mostly homogenous soil types that share similar pigments and textures (Holliday 2004). Undisturbed layers may appear discrete with clear boundaries or a continuous gradient of change, depending on the natural formation processes. A disturbed soil profile will lack any patterned stratigraphic quality, and may even contain evidence of commingled soil types and textures, or plant material that would otherwise be found at the ground surface. Mixed soil stratigraphy is a sign of general ground disturbance activity, not just caused by a burial interment, but through any process necessitating removal and replacement of soil for any purpose (Holliday 2004). While excavation is the only method to definitively confirm the presence or absence of a burial, it is time and labor-intensive and destructive by the nature of the process. Therefore, caution is advised when employing this method as an exploratory measure, rather than as a method for verification.

4.2 Geophysical Techniques

Ground-based sensing technologies like ground penetrating radar (GPR) (Barone et al. 2015; Bladon et al. 2011; Buck 2003; Schultz 2012), electrical resistivity (Nero et al. 2016; Scott and Hunter 2004), and magnetometry (Dalan et al. 2010) have assisted with subsurface human burial detection (Büyüksaraç et al. 2013; Cheetham 2005; Christensen et al. 2014; Clark 2000; Cox et al. 2008; Killam 2004). A GPR instrument emits microwave radiation into the ground. As the energy leaves the instrument, it interacts with material boundaries or buried objects, where a portion of the signal is returned to the sensor (Barone et al. 2015; Bladon et al. 2011; Buck 2003; Schultz 2012). Electrical resistivity survey is a method of detecting subsurface anomalies, where an electrical current is delivered through the soil using shallow probes. Features that are buried in uniformly resistant soil will either attract or repel the current, depending on its own resistance. Measurements of electrical current are interpreted as relatively low or high density. GPR and

electrical resistivity survey anomalies are interpreted as generic features until excavation can verify their material properties (Nero et al. 2016; Scott and Hunter 2004). Similarly, magnetometers are used to record the strength of a magnetic field, including disturbances caused by disturbed soils (Dalan et al. 2010).

For all three of these geophysical approaches, subsurface materials are not specifically identifiable solely from signal strength or quality, but their location can be marked as anomalous for follow-up investigation, usually through excavation. Researchers are beginning to explore potential time limitations for applying GPR to human burials and have learned that, after buried remains have skeletonized, signals are noticeably diminished and eventually indistinguishable (Salsarola et al. 2015). Electrical resistivity and magnetometry tend to result in poor spatial resolution, where individual graves may be too small to detect using these techniques. The advantages to these methods are that they are non-destructive and non-intrusive, so buried evidence is not disturbed due to their application. The equipment necessary for applying each technique is specialized, but fairly common, and therefore easy to obtain. While these approaches are useful for isolating the presence of potential subsurface anomalies in environments and circumstances that permit access to areas of interest, they share two common disadvantages: 1) the techniques are associated with high omission and commission errors (i.e. false negatives and false positives) as they are sensitive to certain soil types (Christensen et al. 2014) and 2) they require a trained instrument operator to have a somewhat precise idea of where to collect data, since these instruments must be placed on the surface directly above the burial to sense it (Christensen et al. 2014; Clark 2000; Cox et al. 2008; Killam 2004).

4.3 Remote Survey Methods

Remote survey methods are those that do not require people or equipment to be present at the location of a burial, but at a point approximately overhead – either from an unmanned or piloted aircraft, or from an orbiting satellite. These methods include aerial and satellite photography, multispectral or hyperspectral imaging, or laser scanning. These methods are useful for instances where ground-based methods cannot be applied due to inaccessibility or have proven unsuccessful, or where only limited information exists to narrow the general location of a burial. Aerial and satellite photography are among the most commonly used remote survey methods since archived remote photography is sometimes created to serve other, unrelated purposes, such as land use mapping or natural resource management, and is often stored in public archives like those curated by the U.S. Geological Survey, the Bureau of Land Management, or even local and regional agencies.

Remote photography offers a wide view of landscapes, allowing the viewer to observe patterns that are sometimes difficult for investigators to make sense of from a ground-based vantage point. Some features, such as gradients in vegetation greenness or exposed ground features surrounded by overgrown vegetation, are more visible from above, where contrasting features stand out against surroundings. Remote photography can reveal recent or past changes to the landscape that may indicate soil or vegetation disturbance, or other isolated or patterned features that are most visible from a distance (Christensen et al. 2014; Killam 2004). Interpretation of aerial and satellite photography, however, is somewhat subjective and relies on surface anomalies being visible in red/green/blue (RGB) or color infrared images and unobstructed from overhead view.

Most photographic cameras employ light filters to capture and display broadband red, green, and blue wavelengths as a composite color image. While independent inspection and

reordering of image data for image analysis and interpretation are possible, photographic cameras are not usually designed for scientific application, and light filters do not provide the reliability of a calibrated radiometric measurement instrument. However, the usefulness of remote photography is expanded if collections are made at times of day that present shadows revealing topographic relief (France et al. 1992). Additionally, stereo images – two or more overlapping images taken near simultaneously – can be used to photogrammetrically reconstruct three-dimensional surfaces (Wolf et al. 2014). For example, CORONA satellite stereo image pairs have been used by archaeologists to visualize archaeological features, including burial mounds, using photogrammetry (Goossens et al. 2006). Unfortunately, because aerial and satellite photography are passive sensing technologies, they are limited to environments with clear line-of-sight to the target, thereby reducing the applicability of remote photography to very specific environments and conditions. Moreover, limiting image collection to include only broadband or only visible light is to miss potentially useful information about a landscape. Valuable information may be observed as signals in narrow spectral wavelengths or the invisible infrared region. Ignoring this spectral information can result in false negatives at locations where anomalies might have been observed at high spectral resolution or outside the normal spectral range.

Multiple published reports describe examples of aerial and satellite photography and multispectral imaging for helping to visualize sites of suspected human burials as a result of large scale violent conflict, usually in tandem with witness testimony. Among the best known examples, aerial photography was captured by the United States in the days following the disappearance of several thousand men in Srebrenica, Bosnia and Herzegovina. The imagery was of high enough spatial resolution to reveal heavy machinery, an open grave pit, and a nearby pile of elongated features that were interpreted as human bodies. The images were used to demonstrate the

systematic violence in Bosnia, and prompted Western nations to add pressure to the Bosnian Serb leadership to end the conflict. The images were later used as evidence by the ICTY in the trial of Slobodan Milošević (Willum 2000; Marx and Goward 2013). The imagery was significant in that it helped demonstrate the effectiveness of remote sensing as a technology capable of identifying and combating human rights violations.

In a similar application of remote sensing for corroborating witness testimony, the Harvard Humanitarian Initiative developed the Ground Reporting through Imagery Delivery (GRID) methodology. The methodology provided a way for witnesses of the crisis in Darfur to participate in the process of identifying potential areas containing evidence of mass atrocities in remotely sensed data (Card and Baker 2014; Satellite Sentinel Project 2011). Through the process, witnesses were shown high-resolution satellite imagery collected before an event took place, to avoid the visual influence of physical anomalies that might be present in the "after" image. Once the witness provided the general location of an area where they recalled a mass grave location, higher resolution imagery was sent to help narrow down a more precise location. After a more precise area was identified and confirmed by the witness, the researchers performed change detection analyses to reveal disturbed earth consistent with the location and timeframe of the event reported by the witness – in this case, the creation of an unmarked mass grave (Card and Baker 2014; Satellite Sentinel Project 2011). While these examples demonstrate the effectiveness of remote sensing for documenting evidence of human rights violations, the successful application of remote imagery has relied heavily on eyewitness accounts, such as the aerial images in Bosnia and the satellite images in Sudan used to confirm the locations of mass graves. The imagery itself is most commonly used as a tool to confirm existing information, rather than as a tool to lead investigators to new information.

Remote imagery can be valuable tool for visualizing suspected burial sites within the context of their larger environment if the disturbance is recent enough for the scars to still be visible. The technology, however, has limitations that are attributable to instrument capability, vantage point, and time-of-day. Surveying a landscape from an overhead platform will have drawbacks due to a potentially limited line-of-sight and increased observation distance, resulting in lowered spatial resolution. However, aerial and satellite platforms can offer a tremendous advantage to investigators by covering large areas of land compared to ground-based technologies, and have potential to allow investigators to narrow areas of interest for more efficient and well-informed ground-based follow up investigations.

4.3.2 Archaeological Remote Sensing

The closest conceptual neighbor to forensic remote sensing is archaeological remote sensing, where the differences between burial targets of interest are context and time-depth. Contextually, forensic burials bear inherent legal relevance to an active investigation, while archaeological burial sites do not. With respect to timing, forensic sites are more contemporary than archaeological sites. While archaeological and forensic targets may differ in these two respects, remote sensing technologies were first adopted by archaeologists and later used as a forensic tool. Since the use of remote sensing in archaeology is well established, the forensic community has much to draw from the archaeological literature.

The scope of archaeology is much wider than the scope of a forensic investigation, in that the time-depth of archaeology is greater and objects of interest include a wider range of features, but there is some overlap. Remote sensing has been used by archaeologists to attempt to locate anthropogenic features, which can include features associated with human body interments, such as burials, burial mounds, and tombs. The time difference between archaeological and forensic

targets may not be comparable, but the collection, processing, and analysis of remotely sensed data for both applications are similar. Finally, since the geophysical qualities of human burials are context-independent, a review of key archaeological remote sensing studies provides a foundation for discussing remote sensing as a technology for locating forensically-relevant human burials. Archaeologists have used different types of remotely sensed data, including multispectral and hyperspectral imagery, and light detection and ranging (LIDAR).

Multispectral and hyperspectral instruments are sensitive to a range of visible and infrared wavelengths that are recorded in multiple discrete channels. This capability provides an advantage over conventional cameras that are sensitive to a broad range of visible or near infrared light. Due to this advantage, spectral imaging is a discovery technology used by professionals in a wide variety of disciplines, including archaeology. The scientific appeal for archaeologists is that spectral imaging has the potential to reveal objects that reflect light differently from their surroundings as anomalous features that require increased sensitivity to observe them. Such objects might otherwise appear consistent with their surroundings in broad range imagery or across an invisible region, rendering them unidentifiable to broadband cameras and to the human eye.

Archaeologists adopted spectral imaging as a tool in the 1970s, when the technology was still relatively new (NASA 2011). At the time, archaeological applications were still limited by poor data quality, as well as the high cost for imagery (Gumerman and Lyons 1971; Miller et al. 1974). The continually improving quality and accessibility of spectral imagery now allows for its use as a common archaeological tool. Archaeology is currently well supported by the public and private sectors, with a large selection of spectral imaging platforms offering a wide range of spectral and spatial resolutions. These platforms include low-altitude unmanned aerial vehicles (UAVs), piloted aircraft, and Earth-orbiting satellites. Using remote sensing technologies,

archaeologists investigate features of varying size and spectral qualities, ranging from expansive continuous landscapes to small discrete objects. Features can include remnant structures, such as roads or paths (White 2007), house mounds (Johnson and Haley 2011), or evidence of terraforming (Evans et al. 2016). Features can also include mortuary structures, such as burial mounds or tombs (Artz et al. 2013; Riley 2009; Sobotkova and Ross 2010).

Visualizing archaeological features using remotely sensed data typically takes one of two general directions before following more specific analytical workflows. The first approach is somewhat exploratory, highlighting generic anomalies by making general, but informed, assumptions about archaeological features (unsupervised approach). This approach does not account for spectral signatures of known features. The second is an *a priori* approach that searches for spectra that closely match a reference spectrum belonging to a known archaeological feature (supervised approach). Both approaches are met with advantages and disadvantages and neither is without some degree of error. Therefore, despite the increasing quality of imagery and the growing body of analytical techniques available to users, it still remains important for archaeologists to perform ground-based investigations to verify the existence of archaeological sites and associated features predicted using remote sensing. Validation will be equally important for forensic remote sensing surveys, as remote sensing is a supplemental tool, not a replacement, for fieldwork.

In one of the earliest applications of hyperspectral analysis for archaeology, White (2003) attempted both unsupervised and supervised approaches to site prediction using 224-band Airborne Visible/Infrared Imaging Spectrometer (AVIRIS, JPL) imagery to identify archaeological pithouses lacking surface relief in Arizona. The unsupervised approach, which assumed archaeological sites were spectral endmembers (i.e., *n*-dimensionally clustered), was unsuccessful. However, the supervised approach, which involved extracting spectral data from

known, verified features, did produce promising results. The supervised approach made the assumption that archaeological features contain mixtures of natural material that are slight spectral deviations from their surroundings, but are spectrally consistent with other features of the same type – an assumption that also can be applied to human burial environments because human burials and the materials used to disguise their surfaces are mixtures of rearranged organic material. By applying the Mixture Tuned Match Filtering (MTMF) tool in ENVI to the known site spectra, White (2003) was able to locate all of the pithouses to within 70 m of their known locations. Additionally, several other locations were identified through this process that may be unrecorded sites or false positives that, in either case, require follow up fieldwork. While these sites are not funerary in nature, White's study (2003) is relevant to the current research since the pithouses present no surface expression and are otherwise not visible to observers.

Sobotkova and Ross (2010) took a similar supervised approach, using QuickBird satellite multispectral imagery to identify burial mounds in Bulgaria. The authors used the normalized difference vegetation index (NDVI) to simplify imagery analysis. Terrestrial spectra were collected simultaneously at anomalous locations in imagery to confirm the presence or absence of archaeological sites, and to provide immediate feedback of imagery analysis. The terrestrial spectra allowed for a supervised classification, where locations and spectral signatures were known, resulting in the positive identification of 107 burial mounds in the QuickBird imagery. The study reports 117 misclassified burial mounds and further states that the method failed for burial mounds with a height and radius of less than 0.5 m and 10 m, respectively. However, the authors reiterate that the technology is low-cost and the study demonstrates the technology's usefulness as a preliminary aid to site prospection (Sobotkova and Ross 2010).

Spectral imaging in archaeology has become so pervasive that several edited volumes are available on the topic. Among the best-known volumes are Remote Sensing in Archaeology, by Wiseman and El-Baz (2007), Satellite Remote Sensing: A New Tool for Archaeology, by Lasaponara and Masini (2012), and Mapping Archaeological Landscapes from Space, by Comer and Harrower (2013), each presenting several case studies in archaeological remote sensing. For example, in the Wiseman and El-Baz (2007) edited volume, Saturno and colleagues hypothesized that spectral change in vegetation are observable at the Maya archaeological site of San Bartolo in Guatemala. The authors suggest that these changes may be the result of humans using limestone and lime plasters as building material, which continues to influence the moisture and nutrition levels of the immediate environment. Under this assumption, the authors took an unsupervised approach by displaying the 4-band visible and near infrared IKONOS satellite multispectral imagery as near infrared, green, and blue rather than the default red, green, and blue. Their approach resulted in bright features in the imagery that, through follow up fieldwork, corresponded to previously undocumented archaeological sites. The authors acknowledged that the moisture and nutrient modifications, likely causing high contrast spectral anomalies in the near infrared band, are not yet proven and may be difficult to apply in other environments with different site formation characteristics. However difficult it may be to scale these results to different environments for the same application, their work illustrates the larger idea that is relevant to the current research, that anthropogenic modifications to the environment can influence canopy vegetation spectra.

These studies, and dozens more like them, illustrate the utility and limitations of applying remote sensing to anthropological questions. Archaeologists have adopted remote sensing technology, and use data collected with sensors not specifically designed for this application, which is a testament to the resourcefulness of archaeologists and to the power of remote sensing

technology. Throughout the archaeological literature (Masini and Lasaponara 2009; Saturno et al. 2007; White 2003), researchers demonstrate that natural materials used by ancient peoples to modify their landscapes are spectrally similar to the surrounding area from which those materials originated, and therefore difficult to visually separate. In modified environments that contain commingled natural materials, a spectral anomaly can represent an observation of human activity, but may not always provide a distinctive signal to make spectral imaging a reliable indicator of anthropogenic site modification. As a result, archaeologists are sensitive to the scientific and technical challenges of isolating features that tend to be reconfigurations of natural materials in an image scene. These studies demonstrate that unsupervised approaches that are successful in one environment may be difficult to scale to other areas (Saturno et al 2007). Therefore, if data resources allow for supervised approaches to site prospection, *a priori* data should be incorporated into the research methodology to enhance results (Sobotkova and Ross 2010; White 2003).

Active sensors, such as LIDAR scanners, provide their own energy source. As such, LIDAR scanners can take advantage of gaps in dense vegetation through which pulses pass to measure the positions of solid features underneath. This capability provides an advantage over passive sensors that measure only unobstructed, solar illuminated objects in direct view of the sensor. LIDAR technology is used by professionals in a variety of disciplines, including archaeology. The appeal for archaeologists is that LIDAR has the potential to reveal objects that are located underneath dense vegetation, such as tree canopy, allowing for the visualization of surface features by digitally removing the canopy. Such objects may be otherwise completely obscured by tree cover during certain seasons or year-round, effectively limiting the opportunities for observing forest floors or other difficult environments.

Archaeologists adopted LIDAR for site prospection in the early 2000s, after the technology had been well established for several decades. Given the limited availability and great expense of LIDAR systems, data were difficult to come by until the cost of collection was reduced. Data become even more available as web-based public archives, such as Open Topography, USGS Earth Explorer, NOAA Digital Coast, and as various state-level data repositories have become more prevalent. Much like airborne spectral imagery, LIDAR data can be collected specifically for archaeological survey, or it can be collected for another purpose and stored for public use. While the cost of collection remains the primary barrier of entry for guaranteeing detailed coverage, the availability of LIDAR data has increased, so its use as an archaeological tool has and will continue to become more common.

LIDAR can reveal subtle elevation changes and is used by archaeologists to digitally remove physical obstructions, such as trees, to identify underlying morphological anomalies in a landscape. Among the best examples of landscape archaeology, Chase and colleagues (2011), conducted an aerial LIDAR survey of Caracol in Belize to visualize the Maya archaeological landscape beneath the dense canopy. Their data revealed a larger and more detailed archaeological site than previously documented by ground-based mapping surveys. Moreover, their analysis revealed individual structures, causeways, and agricultural terraces, some of which exhibited topographic relief as low as 5 – 30 cm – features that are potentially similar in topographic relief to human burials. Their study highlights the advantage that LIDAR data provide researchers hoping to learn more about modifications to obstructed ground surface, possibly including human burials. Chase and colleagues demonstrate that, in addition to large prehistoric monuments, relatively small anthropogenic features situated under dense tree canopy can be visualized using airborne LIDAR technology (2011).

Archaeologists have also used LIDAR to locate and map human burials, in particular, burial mounds. Artz and colleagues (2013) and Riley (2009) have used LIDAR to help map known burial mounds and predict the locations of unknown burial mounds to facilitate archaeological site preservation efforts. Riley (2009) developed an automated model for detecting conical burial mounds in Iowa with 86% success for mounds known at the time, indicating there is a degree of morphological predictability to burial mounds in the Midwest. Riley's approach potentially identified two previously unrecorded mounds that require follow up investigation for confirmation. Artz (2013) performed a larger scale, but manual inspection of imagery for identifying burial mounds in Minnesota using hillshading and contour lines to emphasize topographic features. While only 36% of recorded burial mounds were identifiable using LIDAR, an additional 118 locations of potentially unrecorded burial mounds were also documented. Clearly, the range of performance depends on the analytic approach taken, but Artz (2013) argues that certain burial mounds will be more difficult to discern in LIDAR data because they exhibit decreased topographic relief as a result of erosion or human tampering. Artz (2013) found that, since hillshading and contour lines were used to aid human image interpretation, mound size was the greatest contributing factor to mapping a mound. Riley (2009) concluded that poor results corresponded with the presence of dense vegetation, which can be difficult to automatically filter out from LIDAR point clouds. Forensic investigators will face similar challenges when attempting to locate clandestine burials, affecting the longer-term performance of remote sensing for human grave detection.

Weitman (2012) conducted a LIDAR survey to map two historic cemeteries in Georgia, (US) which were in use between the years 1813 and 2011. According to Weitman (2012), the abundance of low-lying vegetation at the burial surfaces obstructed the emitted laser pulse,

resulting in insufficient information to determine burial locations. However, Weitman's LIDAR data collection is limited to only one day for each cemetery, so the data are synchronic. Yet, she remarks on the presence of burial surface depressions in areas lacking grave markers (2012), which indicates that an elevation change study complete with multiple LIDAR collections may reveal localized net elevation losses that persist for an unknown period of time after a burial is created and vegetation has regrown at the surface.

The successful application of using remote sensing in archaeology demonstrates that anthropogenic change is spectrally and topographically measurable, setting a precedent for other anthropological applications. However, using remote sensing to identify archaeological mortuary features, even burial mounds, is different from its application in a contemporary context. Features that tend to be the focus of discussion in the archaeological remote sensing literature are often discrete objects with vertical relief that might be considered anomalous for the environment (e.g., pyramids, house mounds, burial mounds). These features may have low relief, but span a large area or may be identifiable by their linear qualities (e.g., buried walls, agricultural fields). It is still uncertain whether spectral imaging technologies or LIDAR can help identify smaller discrete features, such as an unmarked burial, with low topographic relief and possessing spectral or topographic qualities approximating their undisturbed surroundings.

4.3.3 Forensic Remote Sensing

Remote sensing is well established in archaeology, however, our understanding of more contemporary and small-scale human changes to the earth surface is still lacking. To date, most studies exploring the potential benefits of airborne hyperspectral imagery in forensic contexts rely on exposed soil to separate spectral signatures of non-human buried remains (Kalacska and Bell 2006; Kalacksa et al. 2009; LeBlanc et al. 2014; Snirer 2013). Exposed soil following a recent

interment is a temporary state before vegetation regrowth and other surface changes take place. Moreover, high contrast anomalies such as exposed soil may not provide enough information to narrow a search area, particularly if a landscape's vegetation cover is highly variable or if a burial is truly hidden among materially similar surroundings. Even more problematic is the lack of established signatures in association with burials, specifically, or ground disturbance, generally.

Kalascka and Bell (2006) observed experimental cattle burials in Costa Rica as spectral samples collected using a portable field spectroradiometer and spectral imagery collected using the MODIS/ASTER (MASTER) airborne simulator. They compared ground-based spectra from the cattle burials to empty control units at one and five-months post-burial. From these data, the authors assert spectral separability between the control and cattle burials using forward feature selection and pattern classification techniques. Comparisons between the control and cattle burials using airborne MASTER image pixels from one-month post-burial reveal that separability was achieved using the infrared bands, but there is no report on comparisons made between each burial and surrounding spectral samples of undisturbed vegetation or soil. Further, the authors note that vegetation failed to regrow at both disturbed surfaces by the five-month mark. In the same study, the authors also tested their approach using an archived six-band ASTER satellite multispectral image of a known human mass burial thought to contain up to 96 bodies buried in 1982, but spectral resolution was deemed too low for successful detection.

Kalacska and colleagues (2009) also collected ground-based visible to shortwave infrared spectra and HyMap airborne hyperspectral imagery in an attempt to classify the cattle burial and the control containing no cattle. Similar to their earlier work, the authors do not report on whether they made comparisons of either group to surrounding undisturbed spectra. Using forward feature selection, they reduced ground-based spectra from 500 bands to 10, 20, and 30 band sets for

analysis. Separation was then determined using three nonparametric methods: a binary decision tree, a multilayer neural network, and the k-nearest neighbor (k-NN) classifier. Data were divided equally into training and validation datasets and the band sets of 10, 20, and 30 were evaluated in all three models. The authors do not elaborate on which bands comprise each of the 10, 20, or 30 band sets, but do present the results of simultaneous Bhattacharrya's tests indicating spectral regions with greatest separability between groups, which shift from visible to infrared wavelengths throughout the course of the study.

The authors were not able to separate the burial and control immediately after interment using any of the classifiers (Kalacska et al. 2009). One-month post-burial the authors were able to separate the two groups using a neural network and 10 bands, reporting greatest separability in the visible region from 400 – 550 nm and greater than 850 nm. At five-months post-burial the control surface presented more than 50% vegetation regrowth, but the cattle burial had none; increasing separation performance as a direct result. The authors report separation in peaks around 450 and 550 nm, but also note that these differences are characteristic of visible differences between soil and vegetation. At sixteen months, the two features are reported as perfectly separable from each other above 700 nm using all classifiers (Kalaksca et al. 2009), however, the authors acknowledge that the exposed soil still covered 30% of the burial surface.

The presence of exposed soil is not an experimental design flaw, and the rate of natural vegetation regrowth is not within the researchers' control, but material composition affects spectral response and must be recognized as a contributor to the results and interpretation. The presence of soil will influence the mean spectral response of a vegetation feature (Gibson 2013). It is also possible that exposed soil renders a burial poorly matched for remote sensing survey, particularly if a traditional pedestrian might have accomplished as much without the financial investment. Cost

is a limiting factor for law enforcement agencies and piloted-aircraft remote sensing campaigns are expensive. The studies by Kalacksa and colleagues (2006; 2009) reveal discernible differences in the spectral signatures between burials with 100% vegetation regrowth and burials with 70% vegetation regrowth; a difference that investigators may be able to visualize without the assistance of advanced remote sensing technologies. Truly clandestine burials are often obscured by vegetation or other deliberate camouflage and appear, to the naked eye, no different from non-burials or undisturbed areas.

Kalacksa's studies lay important groundwork for future forensic remote sensing research by establishing that recent disturbance with some exposed soil can be visualized as a high contrast material anomaly in aerial hyperspectral imagery. Their studies confirm that additional research is needed to understand the differences between like-materials as part of a vegetation-specific or soil-specific burial study, and also how burials and similar disturbance (control unit) are spectrally different from each other and from undisturbed surroundings. Only when these two phenomena are better understood should the scientific community promote remote sensing as a tool for predictive modeling and monitoring of human burial locations. Paradoxically, it appears they attempted grave detection without first characterizing unique burial signatures and, therefore, may be unable to deliberately search for those signatures in non-experimental burial scenarios.

Norton (2010) followed previous work by conducting a lab-based pilot study to determine whether burial soils were spectrally separable from non-burial soils. Using principle component analysis (PCA), Norton concluded that soil spectra associated with buried minced beef were separable from untreated control soil as distinctive component clusters by six-days post-burial. Norton (2010) also determined that these results were not solely attributable to an increase in soil moisture, but likely directly associated with buried matter decomposition (2010). The pilot phase

of Norton's study involved the use of wooden boxes containing soils, some with buried minced beef and some without. The lab-based nature of the experiment indicates that all soils were inherently disturbed, and therefore, spectral comparisons were made between disturbed soils with and without decomposing matter; no comparisons were made between the disturbed soil samples and undisturbed or completely unaffected soils.

Norton found mixed results when attempting to validate her lab results in the field (2010). Due to U.K. legislative restrictions on the use of human remains for scientific research, Norton was limited to collecting soil spectra from burials in modern cemeteries, in which human remains are enclosed in biodegradable caskets – an atypical scenario for conflict related graves. Clustering was less structured for the cemetery burial soil spectra and the author reasonably concludes that more research is necessary to better understand the relationship between burial age and spectral separability (2010).

Norton's work (2010) is the first forensic remote sensing study to evaluate spectral separation of comparable materials, (i.e., burial soil versus non-burial soil), associated with decomposing matter before attempting separation in a field setting. However, using non-human remains and not performing comparisons to undisturbed soils limits the application of Norton's findings. In addition, Norton does not indicate which wavelengths or wavelength regions contribute most to the separation of the experimental soil groups, rendering the interpretation of nutrient influence or other factors on overall spectral signatures somewhat challenging.

Snirer (2013) observed chemical and spectral properties of pig grave soils and vegetation in an open grassy field in Canada. More specifically, Snirer evaluated vegetation pigments, terrestrial spectra of soil and vegetation, and airborne hyperspectral imagery of twelve individual pig burials of various depths, six surface depositions, six empty control units, and undisturbed

ground. Analytical methods for pigment and spectral data were the one-way analysis of variance (ANOVA), a *t*-Test, and eight classifiers. The pigment analysis resulted in separation between disturbed and undisturbed vegetation, but no separation between disturbed vegetation types (i.e., pig graves and control units). Terrestrial soil and vegetation spectra separated surface placements from disturbed areas, but proved unreliable for separation of disturbed group types. The results were scaled to airborne HSI to reveal similar results – separation of disturbed areas from undisturbed areas, but no discernable difference between disturbance types. Snirer's work is a clear contribution to forensic science in that it will undoubtedly help narrow down areas of potential disturbance. A potential drawback, however, is that during analysis, terrestrial vegetation spectra were reduced from 451 spectral bands to sixteen pre-established spectral indices, effectively limiting the analysis to include a small fraction of available data without first testing them for significance. The inherent problem with this approach is that, while the spectral indices used in Snirer's study were developed for vegetation spectral research, they were each developed for broad application (e.g., vegetation stress or health) rather than to identify specific anomalies, such as human burials. While these spectral indices may still reveal differences between groups, unmarked burials are a nuanced type of disturbance that likely influence vegetation uniquely, due to subsurface body decomposition and the subsequent redistribution of nutrients to the soil. However, none of the spectral indices used in Snirer's study help fully characterize burial, or generally disturbed, vegetation spectral signatures. It is also important to note that Snirer does not clarify whether surface vegetation regrowth was complete when the HSI collections were acquired. Additionally, outside of the spectral indices, which follow pre-established calculations with prescribed wavelengths, there is no mention of individual wavelength contributions to group separation, so the work will be difficult to independently validate.

LeBlanc et al. (2014) report a 100% success rate for pig burial detection using airborne visible to shortwave infrared hyperspectral imaging. They conducted a blind test in an undisclosed location in Canada, where they were able to identify two unmarked pig burials. Their analysis relied on the presence of exposed soil and included reflectance data at 2200 nm to isolate hydroxyl (OH^-), a spectral indicator of clay. In addition to this signature, three spectral indices – Normalized Difference Vegetation Index (NDVI), Sum Green Index (SGI), and Structure Insensitive Pigment Index (SIPI) – were used together to identify common anomalous pixels using a Bayesian model. The authors reported finding three anomalous features, two of which were pig burials and the third a possible false positive. The possible false positive suggests their model excels at isolating exposed soil features, which may be characteristic of unmarked burials in certain – but not well camouflaged – scenarios.

4.4 Rationale for Human Burial Remote Sensing Research

Relying on non-human remains as proxies for humans in burial research is problematic throughout forensic studies. Pigs and other animals differ from humans in body plan, diet, skin thickness and other factors that influence decomposition. Recent research shows that decomposition rates and patterns between animals and humans are highly variable (Dautartas et al. 2015; Dautartas et al. 2016; Steadman et al. 2016). These results further confound the fact that individual burials differ from one to the next, depending on location, number of interred bodies, depth of interment, environment, and many other variables (Jessee and Skinner 2005; Mann et al. 1990). Therefore, when designing experimental research, it is important to minimize as many confounding variables as possible, such as interring human bodies instead of animal remains.

There are only a few published studies on the application of remote sensing to burial detection, limiting the research community's overall understanding of the topic. Yet there is an

emergent demand for an efficient and reliable human burial detection methodology. This demand may directly contribute to the premature application of remote sensing technology to the challenges of human burial detection. Despite LIDAR's overwhelming success as an archaeological survey tool, there are no systematic studies evaluating its use for measuring human burial surface changes. Before non-experimental unmarked human burials can become targets for detection, the measurable characteristics that render them separable must first be established and the underlying phenomenology understood by conducting more basic research. Only after establishing human burial signatures will researchers have the opportunity to reliably separate burials from their surroundings or from other anomalous features with greater confidence.

CHAPTER 5: MATERIALS AND METHODS

This chapter describes the experimental study site, anticipated burial signatures, and data sets. Additionally, this chapter presents the detailed data collection, processing, and analytical strategy used to address the research questions and hypotheses presented in Chapter 1. Results are presented in Chapter 6.

This study investigates a group of experimental human burials in a controlled study area, rather than non-experimental human burials. An experimental approach to the research was taken to limit the effects of environmental variables, as well as control for the effects of differences in burial depths and burial ages found at non-experimental sites. While natural vegetation and topographic relief exists within the experimental study site and between experimental burials, mimicking non-experimental sites, using a known, experimental site can minimize additional confounding effects. If not controlled, these effects could influence the magnitude and timing of potential burial signatures, thereby complicating direct comparisons between sites and the direct application of experimental findings to non-experimental sites.

5.1 The Experimental Study Site

The study area is contained in a newly fenced portion of the outdoor Anthropology Research Facility (ARF), managed by the University of Tennessee's Forensic Anthropology Center (FAC), in Knoxville, TN (**Figures 5.1-1** and **5.1-2**). The ARF is located on the south bank of the Tennessee River and is surrounded by two security fences. The experimental graves were created in a relatively level area away from rainwater flows; all burials are exposed to equal gross environmental conditions (e.g., precipitation, temperature). The experimental graves are located minimally 10 m from other forensic experiments and foot traffic near the research site is limited

Figure 5.1-1: The study area in relation to Knox County, TN.

Figure 5.1-2: The study area, adjacent to the William M. Bass Forensic Anthropology Building (west) and the Tennessee River (northeast).

by fencing. The study area is densely populated with mixed tree, underbrush, and grass species of both native and non-native origins. The soils are primarily topsoil (0 – 10 cm below surface) and red clay (10+ cm below surface). During Spring and Summer seasons, the dense tree canopy obscures the study area view from above. During Autumn and Winter seasons, the study area is visible from above, but decomposing leaves cover all ground surfaces.

5.1.1 The Experimental Human Graves

During 13 – 15 February 2013, four grave units were hand-dug at the experimental study site with shovels and pickaxes, each to approximately 0.70 m in depth and at least 2 m apart from each other (**Figures 5.1-3** and **5.1-4**). To assist with the mapping of body placement, and to ensure consistency between units, a datum was set in the southwestern-most corner of each unit, along with pins in the remaining three corners. String was tied to each datum or pin to delineate grave boundaries. In cooperation with another research study, the surface layer of sod on each grave unit surface was removed and set aside before excavation. The horizontal dimensions of each grave unit are a) 1 x 2 m, b) 2 x 2 m, c) 2 x 4 m, and d) 2 x 4 m. The volume of displaced soil for each grave unit is approximately a) 1.4 m^2, b) 2.8 m^2, c) 5.6 m^2, and d) 5.6 m^2. The interred bodies are individuals whose remains have been self- or family-donated to the FAC for forensic research. On 14 February 2013, one male individual was placed inside the 1 x 2 m grave unit and three individuals (one female, two males) were placed inside the 2 x 2 m grave unit. On 15 February 2013, six individuals (two females, four males) were placed inside one of the 2 x 4 m grave units. The combined body mass interred in the one, three, and six-person burials is 178, 403, and 618 lbs., respectively. The second 2 x 4 m grave unit serves as an experimental control for the effects of disturbance without interred human remains.

Table 5.1-1: The experimental units by number of bodies, dimensions, and total body mass.

	Control	Grave-1	Grave-3	Grave-6
# Donated Human Bodies	0	1	3	6
Horizontal Dimensions (m)	2 x 4	1 x 2	2 x 2	2 x 4
Depth (m)	0.70	0.70	0.70	0.70
Total Body Mass (lbs)	0	178	403	618

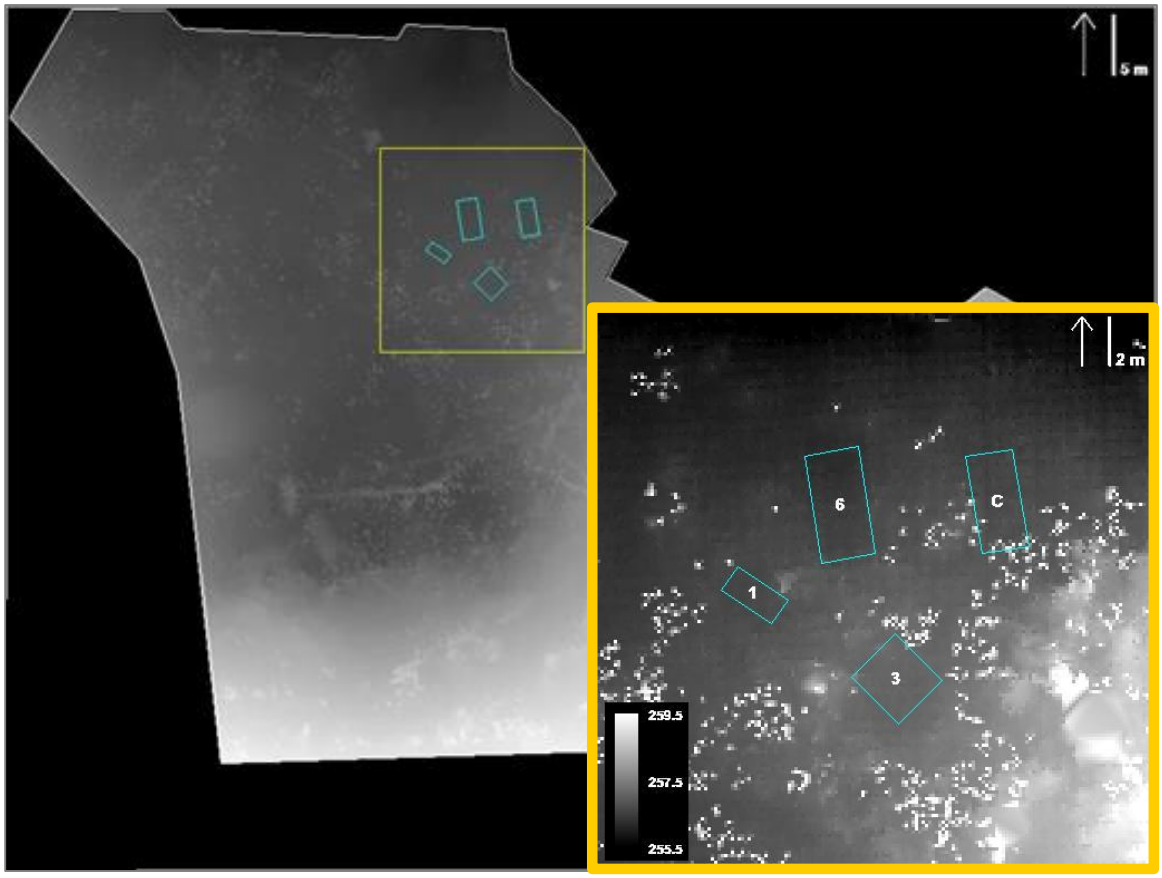

Figure 5.1-3: The study area extent (main), with burial locations (inset); Numbers indicate the number of buried bodies in each grave, C indicates 'Control'.

Figure 5.1-4: The author helping dig the 2 x 2 m grave unit; 13 February 2013.

The bodies were placed in the graves without coffins or other type of protective boundary. Hands and feet were wrapped in durable plastic mesh to prevent commingling of small skeletal elements. Additionally, a piece of thin plastic mesh was placed between overlapping bodies. To simulate an actual forensic scenario, some bodies were partially clothed and/or bound with ligatures and material artifacts such as bullet casings, keys, gloves, and other personal effects were added to the soil matrix. The units were backfilled with the removed soil and the grass sod was replaced on each unit (**Figure 5.1-5**). All interments and backfilling were completed on 15 February 2013 (**Figure 5.1-6**).

5.1.2 Anticipated Burial Signatures

This research investigates potential burial signatures using two types of remotely sensed data collected at the experimental study site: 1) reflectance spectra sampled from live vegetation and 2) ground surface elevation measurements derived from LIDAR point clouds.

Vegetation Reflectance Spectra

Plants depend on many different nutrients to thrive, such as carbon, nitrogen, and potassium. However, this section focuses on the relationship between human burials, nitrogen, and vegetation spectra for two reasons. The first reason is that nitrogen is currently the only vegetation nutrient to be studied in a forensic context using human remains (Mundorff, et al. 2014). The second reason is that nitrogen has a strong link to chlorophyll production and overall plant health (Blankenship 2014), which is supplemented by a large body of existing spectroscopic research to support the findings of this study.

Figure 5.1-5: The author helping backfill the 2 x 4 m control unit soil while A. Mundorff takes photos; 15 February 2013.

Figure 5.1-6: Eastward-facing image of burial surfaces on 15 February 2013; six bodies (foreground); control unit (background).

The Relationship between Nitrogen and Chlorophyll

The anticipated effect of human burials on vegetation reflectance spectra depends on the existing relationship between soil and vegetation. Soils contain naturally occurring nutrients that rooted plants use to fuel photosynthesis (Blankenship 2014). Through photosynthesis, a plant produces the chlorophyll that allows it to absorb light and is associated with green, healthy vegetation. Chlorophyll concentration is directly affected by the presence or absence of certain soil nutrients, and abnormal levels of nitrogen, oxygen, or other nutrients can impose changes to chlorophyll concentration in plants. Specifically, the relationship between nitrogen and chlorophyll concentration is observed as a positive curvilinear relationship, ranging from r^2=0.43 in maples leaves (Yoder and Pettigrew-Crosby 1995) to r^2=>0.96 in coffee leaves (Netto et al. 2005), where higher nitrogen concentration drives higher chlorophyll concentration, the magnitude depending on plant species. Following this logic, the nutrients released from decomposing human remains, such as nitrogen, are redistributed to nearby soils.

Nitrogen Uptake in Burial Vegetation

Vegetation naturally absorbs nutrients that are present in the soil. Within a grave, available nutrients are elevated by decomposing human remains. The effect of human decomposition on soil nutrient enrichment, particularly nitrogen, is poorly understood. However, non-human decomposition research demonstrates that soil nitrogen concentrations become elevated over natural soil nitrogen values (Benninger et al. 2008; Carter et al. 2007; Hopkins et al. 2000). Given that humans are tertiary consumers (i.e., highest on the food chain) we typically have higher levels of nitrogen concentration than do primary or secondary consumers, such as pigs (Carter et al. 2007), buried human bodies are likely to influence the relationship between soil and vegetation chemistry in a similar and measurable way.

A recent study by Mundorff and colleagues (2014) supports the phenomenon of elevated soil nitrogen concentration as a result of *human* decomposition. The authors demonstrate significantly elevated nitrogen isotope ($\delta^{15}N$) values from vegetation sampled at the surface of a recent human burial compared to values from the surrounding off-burial vegetation. Moreover, this difference persists for several years post-burial, including in current data from ongoing collections made six years into the study (Mundorff et al. forthcoming). Similar analyses of nitrogen isotope values from other non-burial enriched environments, such as farms and archaeological middens within ancient Norse settlements, reveal that elevated plant nitrogen isotope values can persist hundreds of years (Commisso and Nelson 2008; 2010). Anthropogenic disturbance has a demonstrated, if general, effect on vegetation nitrogen content. However, given that Mundorff and colleagues' (2014) study observes a contemporary human burial and Commisso and Nelson's (2008; 2010) studies observe non-burial archaeological features, it is still unclear if the same long-term elevated nutrient signature persists in live vegetation that is specifically associated with human burials.

Nitrogen, Chlorophyll, and Vegetation Spectra

The positive curvilinear relationship between plant nitrogen and chlorophyll (Netto et al. 2005; Yoder and Pettigrew-Crosby 1995) provides the basis for vegetation studies that use spectrometers to estimate nutrient and pigment concentration in leaves. Reflectance spectra are not a direct measurement of vegetation nitrogen or chlorophyll content in leaves, but visible spectral wavelengths between 400 – 700 nm (Sims and Gamon 2002; St.-Jacques and Bellefleur 1991; Tsay et al. 1982; Yoder and Pettigrew-Crosby 1995) and infrared wavelengths between 2000 – 2200 nm (Yoder and Pettigrew-Crosby 1995) share a relationship with nitrogen and chlorophyll concentration. For example, leaf pigments – such as chlorophyll – are widely used in spectral

research to estimate the effects of plant stress, such as over or under-fertilization. Leaf stress caused by nitrogen fertilization in crops is observable as anomalous reflectance values in the visible region of the spectrum, where at 540, 610, and 700nm, which are nitrogen-correlated wavelengths, an increase in nitrogen results in a decrease in reflectance (St.-Jacques and Bellefleur 1991; Tsay et al. 1982; Yoder and Pettigrew-Crosby 1995). Chlorophyll concentration can be similarly estimated in the visible region, due to the co-correlation of nitrogen and chlorophyll, but correlations between chlorophyll and spectra tend to be stronger than for nitrogen (Knipling 1970; Yoder and Pettigrew-Crosby 1995). The effects of nutrient levels on plant health, then, can be observed and interpreted as variations of chlorophyll or nitrogen concentration across the reflectance spectrum (Knipling 1970; Rouse et al. 1973; Sims and Gamon 2002).

The vegetation nitrogen isotope research by Commisso and Nelson (2008; 2010) and Mundorff et al. (2014), combined with current understandings of the relationship between chlorophyll, nitrogen, and plant spectra (St.-Jacques and Bellefleur 1991; Tsay et al. 1982; Yoder and Pettigrew-Crosby 1995) supports an investigation of vegetation spectral responses in this experimental human burial study. Previous forensic and plant science research suggests the most promising spectral wavelengths in this research may be those that correlate with nitrogen and chlorophyll. Decomposing human bodies act as fertilizer, supplying nitrogen and other nutrients to surrounding soil, which are subsequently taken up by nearby vegetation. Therefore, vegetation reflectance spectra may reveal the effects of buried human decomposition on vegetation chlorophyll and nitrogen concentration.

Ground Surface Elevation

Digging Activity and Body Decomposition Effects on Surface Topography

The anticipated effect of buried human remains on ground surface elevation will depend on the decomposition process and the redistribution of the buried mass. Topographic changes are an unavoidable consequence of creating a human burial. During the interment process, soil is first displaced, creating enough space for a body or bodies. Excavations can be done manually and/or using shovels or heavy machinery. Human remains are then deposited within the grave pit and the soil is usually replaced over the body. Backfilling can sometimes result in a temporary mound due to the effects of excess mass (the body) in the ground, leaving less room to replace the once-compacted and now loosened soil (Steadman 2009). To date, no published studies document localized elevation activity at burial surfaces to investigate the immediate elevation changes as a direct result of interment.

Eventually, gravitational forces and precipitation cause the backfilled soil to settle, sometimes visible lower than the surrounding undisturbed soil. After this initial settling, the burial surface will continue changing, depending on environmental factors. Buried bodies undergo varied decomposition processes influenced by environmental conditions, such as precipitation and soil composition (Mann et al. 1990; Rodriguez and Bass 1985). In Knoxville, TN active decomposition has been shown to begin anytime from one to ten weeks after interment (Rodriguez and Bass 1985), followed by a more gradual decomposition phase lasting approximately one year (Mann et al. 1990). Subsurface decomposition processes may result in observable surface elevation changes, as redistribution of body mass and soil takes place. Once a body skeletonizes, soil matrix fills the voids created where soft tissue once existed (Rodriguez and Bass 1985). This secondary settling may result in a depression, localized over the buried remains, which is discernable from the

generalized settling over the entire disturbed area following backfilling (Killam 2004; Morse et al. 1983; Owsley 2001; Steadman 2009; Weitman 2012).

The forensic archaeological literature describes burial surfaces as depressions (Owsley 2001; PHR 1998), but these descriptions are anecdotal and not all burials exhibit depressions at their surfaces (Davenport and Harrison 2011). If a depression develops following interment, it may not be visible indefinitely due to accumulation of organic debris over time. To isolate a burial surface depression, or mound, researchers must first understand the range of elevation change at the surface, measurable as net elevation gains or losses over time.

Topographic Activity and Change Detection

Active Light Detection and Ranging (LIDAR) systems generate three-dimensional models of environments, where each data set can contain millions of points (point clouds) that can be filtered to visualize obstructed surfaces, including the ground surface beneath some vegetation. Multiple terrestrial LIDAR collections made over time are commonly used by researchers to compare surfaces to each other and measure topographic change over time, such as estimating volumetric changes of beaches or hillsides before and after storms or landslides (Schürch et al. 2011; Zeibak and Filin 2007). Change comparisons are useful because the topographic variation of any landscape can range from subtle to conspicuous. An example of the former, an unmarked burial may blend in to its immediate surroundings, appearing at any given time an unremarkable feature in a naturally variable landscape. Moreover, outdoor environments are dynamic and undergo change as a result of natural taphonomic processes, such as erosion or accumulation of organic debris (Harris 2014). However, the extent of elevation change at a burial surface may be expressed over a period of time as localized gain or loss that is independent of the apparent natural processes acting on the entire environment. In the case of burials, such localized change could be

attributable to the decomposition process, to soil settling, or to both. Point cloud data collected from research grade terrestrial LIDAR systems can be compared to each other to measure such localized surface changes over time, if they exist.

Data Sets

Five remote sensing data sets are evaluated in this study; three spectral and two LIDAR. The remote sensing data sets used to observe the study area were collected from multiple scales; terrestrial (spectral and LIDAR), aerial (spectral and LIDAR), and satellite (spectral only). Passive sensors (spectrometers) recorded each data point (e.g., leaf surface or image pixel, depending on sensor scale) as a reflectance spectrum, as described in Chapter 3. Active sensors (LIDAR) recorded each data point as a discrete three-dimensional coordinate to model the study area topography, also as described in Chapter 3. Data collection, processing, and analytic strategies specific to each data set are described in the following sections.

The analytical emphasis of this dissertation is on the high fidelity terrestrial spectra and terrestrial LIDAR data that are used to characterize vegetation reflectance and surface elevation change signatures, respectively. Aerial hyperspectral images (HSI), aerial LIDAR data, and satellite multispectral images (MSI) were used to assess the potential scalability of the terrestrial data analysis findings, but are not the central focus of this study.

5.2 Terrestrial Spectra

This section describes the methodologies employed to collect, process, and statistically analyze terrestrial vegetation spectral samples. Terrestrial vegetation spectra were collected to address Hypotheses 1 and 3:

1. Vegetation associated with disturbed ground containing human remains (burials), disturbed ground containing no remains (control unit), and undisturbed ground are statistically separable groups as indicated by differences in reflectance spectra.

3. Vegetation associated with burials, the control unit, and undisturbed areas exhibit spectral separability for the duration of the study.

The terrestrial spectral analysis addresses Hypothesis 1 by separating vegetation spectra into human burial and non-burial comparison groups, where the non-burial group included the control unit and undisturbed ground. Hypothesis 3 is addressed by further separating those vegetation spectra into two temporal groups.

High fidelity spectral data help characterize vegetation properties by measuring reflectance and can assist with the interpretation of airborne and satellite spectral imagery by providing a "ground-truth" observation (Schott 2007; Yoder and Pettigrew-Crosby 1995). Due to the portability of field instruments, ground-based spectrometers can collect data beneath dense canopied environments, such as the study area, which is problematic for overhead airborne and satellite sensing instruments that cannot overcome such line-of-sight obstructions. As discussed in Chapter 3, spectrometers are passive sensing instruments that record only naturally available energy that reaches the detector, meaning any visual obstructions will influence data. For this reason, terrestrial spectra are not intended to perfectly simulate spectral observations made by airborne or satellite imaging spectrometers. Instead, a terrestrial spectrometer is used in this study to characterize burial signatures, which may then be applied to remote imagery in search of similar signatures in more open environments. The terrestrial spectral findings may prove difficult to scale to airborne or satellite spectral images, due to the dense tree canopy that obstructs overhead line-of-sight. However, understanding the general spectral characteristics of human burial vegetation

at high spectral and spatial resolution is necessary to advance future research in unmarked human burial detection. The challenges of scalability will be significant, to be sure, but establishing a human burial reference spectrum will be valuable as future research expands to different locations, environments, and sensing platforms.

5.2.1 Terrestrial Spectral Collection and Processing

Vegetation reflectance spectra were collected in the field using a FieldSpec® 4 Standard-Res Spectroradiometer (PANalytical, Boulder, CO). The portable sensor is designed for collecting spectra on the ground, and covers a spectral range from 350 – 2500 nm in 2151 1 nm spaced spectral bands. Sensor accuracy is reported to be ±0.5nm across all bands. The Noise Equivalent Delta Radiance (NEdL), or signal-to-noise ratio, for the instrument in a known light-source setting is 1.0 x 10^{-9} W/cm^2/nm/sr at 700 nm, 1.2 x 10^{-9} W/cm^2/nm/sr at 1400 nm, and 1.9 x 10^{-9} W/cm^2/nm/sr at 2100 nm. The reported spectral resolution is 3 nm at 700 nm and 10 nm at 1400/2100 nm (PANalytical). The default sensor fiber optic field of view (FOV) is 25˚, but a 5˚ lens was used during collection to achieve a more focused sample that minimizes the possibility of spectral mixture with non-plant materials.

Samples (spectra) were collected over the course of two one-month collection windows: 24 March to 25 April 2014 ("Spring") and 17 October to 21 November 2014 ("Autumn"). Spectra were recorded mid-day to benefit from as much direct sunlight as possible within the densely vegetated study area. Only leaves that received direct sunlight were sampled. The effects of atmospheric scattering were minimized by calibrating the sensor using a 3.62 in. diameter Spectralon® white reference panel at approximately ten-minute collection intervals, as recommended by PANalytical.

Live vegetation reflectance spectra were collected throughout the study area. Each vegetation spectrum is associated with a categorical feature: human burial, control unit, or undisturbed. For vegetation near the edge of a disturbance feature (i.e., a burial or control), the plant soil/stem location was first verified as being associated with the disturbance feature or undisturbed ground before sampling; if an origin was uncertain, no sample was taken. During the Spring collection period, the burial containing three bodies lacked enough surface vegetation to provide enough data for reliable comparison on its own (n=1), due to lack of direct sunlight, but is included as part of the combined human burial dataset. During the Autumn collection period, the control surface received minimal direct sunlight, limiting the data collection opportunities for control vegetation (n=5).

Collections of spectra were sorted by categorical group and stored as spectral libraries and ASCII text files. For all data, the full 2151 bands were reduced to 1803 bands, omitting wavelengths surrounding 1400 and 1900 nm that are associated with spectral noise or light-scattering atmospheric water: 1331 – 1439 nm and 1801 – 1989 nm (Goetz et al. 1985). Remaining bands retain their original spectral resolution. Spectral sample sizes are presented in **Tables 5.2-1** and **5.2-2.** Mean spectral signatures of each live vegetation group are presented in **Figures 5.2-1 – 5.2-3.**

5.2.2 Terrestrial Spectral Analysis

Analyses included live vegetation samples because those samples contain the pigment necessary to attempt separation potentially influenced by human burials, or similar disturbance (Yoder and Pettigrew-Crosby 1995), as described in Section 5.1.2. Moreover, the ability to differentiate human burial, generally disturbed (control), and undisturbed live vegetation spectra has been one of the most understudied questions in published forensic remote sensing research

Table 5.2-1: Sample sizes for live vegetation FieldSpec samples from Spring 2014; N=154.

Category	Live Vegetation Spectra Sample Size
Single burial (G1)	n = 16
Three-person burial (G3)	n = 1
Six-person burial (G6)	n = 36
All Human	**n = 53**
Control	n = 17
All Disturbance	**n = 70**
Undisturbed	**n = 84**

Table 5.2-2: Sample sizes for live vegetation FieldSpec samples from Autumn 2014; N=133.

Category	Live Vegetation Spectra Sample Size
Single burial (G1)	n = 11
Three-person burial (G3)	n = 8
Six-person burial (G6)	n = 30
All Human	**n = 49**
Control	n = 5
All Disturbance	**n = 54**
Undisturbed	**n = 79**

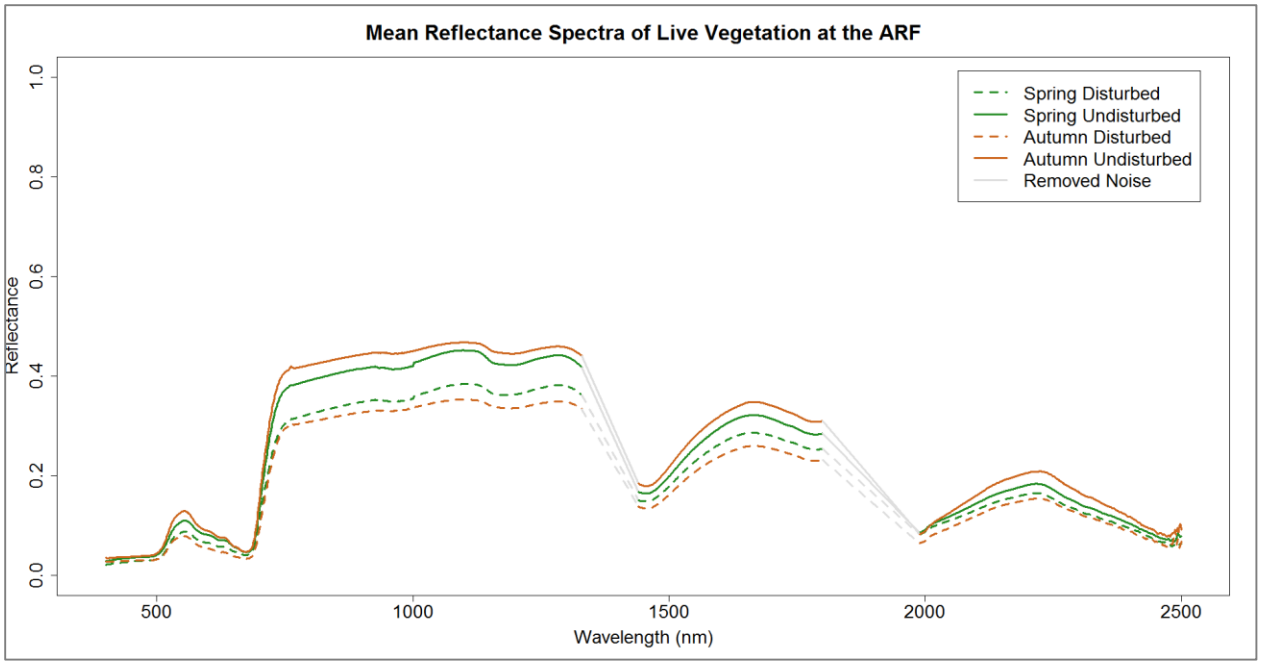

Figure 5.2-1: Mean spectral signatures of disturbed and undisturbed live vegetation during Spring and Autumn 2014 collection periods; 400 – 2500 nm.

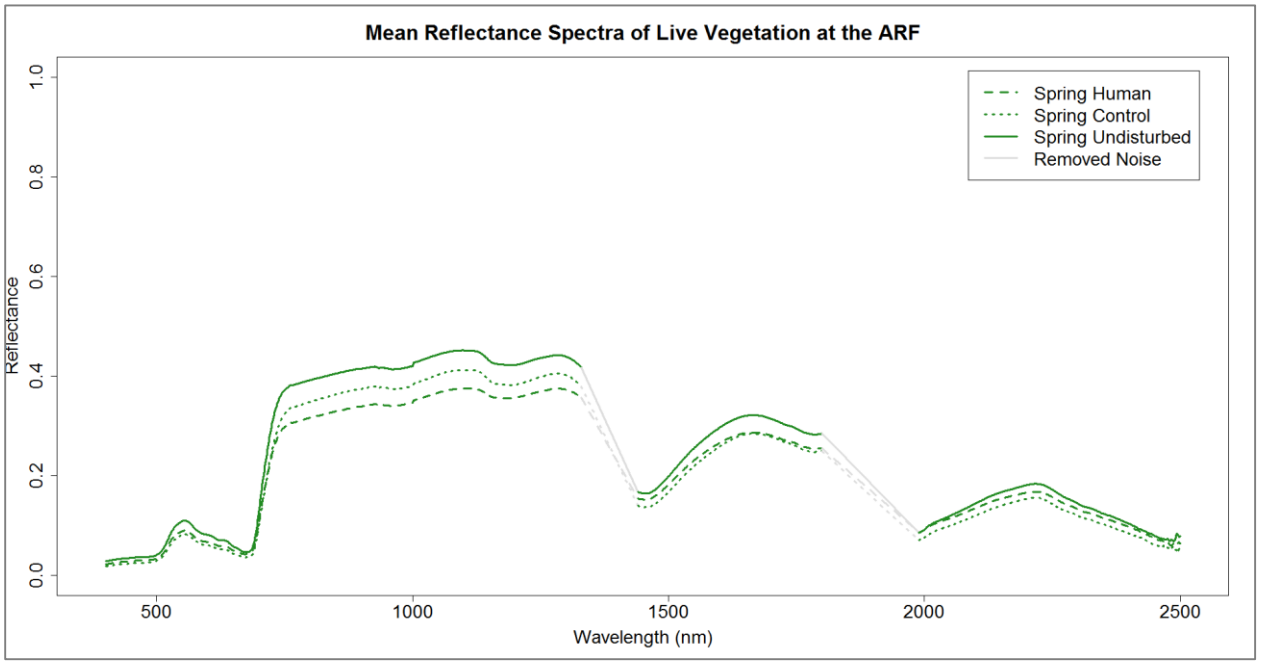

Figure 5.2-2: Mean spectral signatures of live vegetation groups during the Spring 2014 FieldSpec collection period; 400 – 2500 nm.

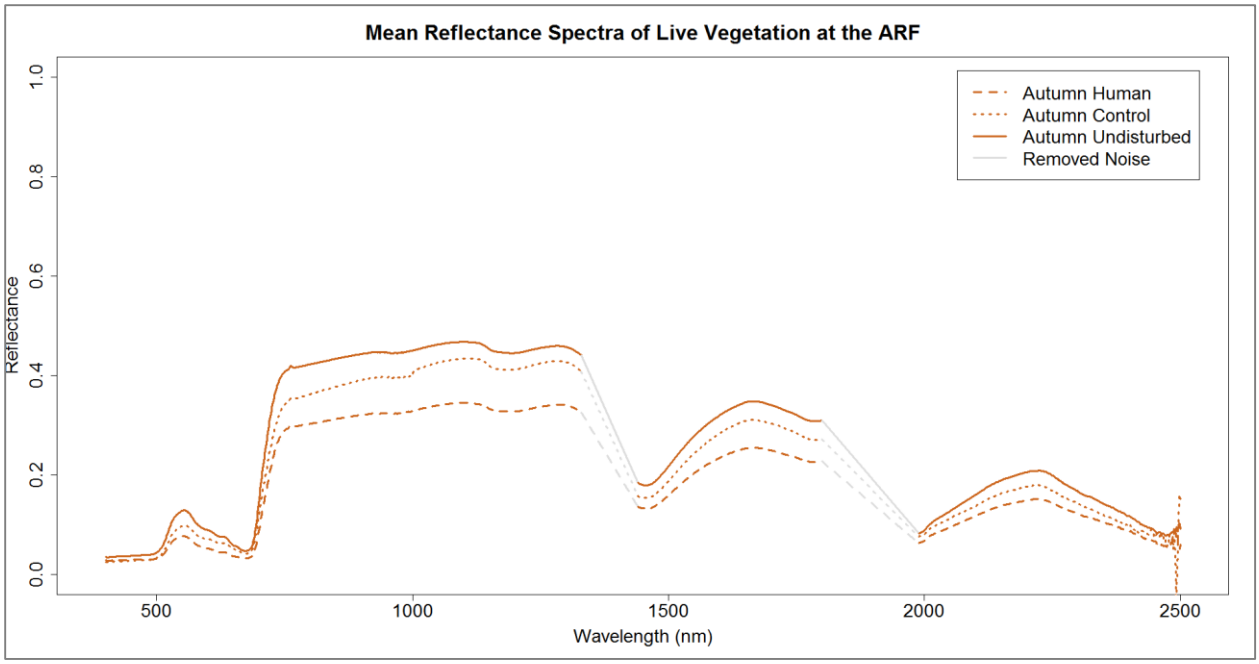

Figure 5.2-3: Mean spectral signatures of live vegetation groups during the Autumn 2014 FieldSpec collection period; 400 – 2500 nm.

(Kalacska and Bell 2006; Kalacska et al. 2009; LeBlanc et al. 2014; Norton 2010).

To enable temporal comparisons and maximize inter-season comparisons, spectral samples were separated by season (Spring and Autumn) and grouped in four ways: 1) combined human burial vegetation (spectra from all three human burials), 2) control unit vegetation, 3) combined disturbed vegetation (spectra from all three human burials and the control unit), and 4) undisturbed vegetation. Depending on the requirements of each method, group comparisons were made as a) the combined human burial group (all human burials) and the undisturbed group, b) the combined disturbance group (all human burials and the control unit) and the undisturbed group, and c) the combined human burial group, the control group, and the undisturbed group. Respective comparisons are explained in each section. Combining data into these groups was necessary because, due to uneven sunlight throughout the study area caused by the tree canopy, some sample sizes are too small for separate analysis.

Spectra were first analyzed in ENVI using the Spectral Angle Mapper (SAM) tool and the Spectral Information Divergence (SID) tool to establish quantitative support for separating dependent variables into discrete categories for statistical analysis. Statistical analyses between those groups include binary logistic regression (BLR) and discriminant function analysis (DFA) in SPSS (IBM, Inc.) and partial least squares regression (PLS) using the 'plsdepot' package (Sanchez 2012) in R (R Core Team 2015), for selecting wavelengths to differentiate between two or more dependent variables. For both Spring and Autumn live vegetation datasets, 70% of the cases are used to train each BLR and DFA model, and 30% are used to validate their performance. For PLS, 100% of the data are used to confirm the contribution of variables selected by the BLR and DFA statistical methods.

Multiple analyses were performed to triangulate results because the spectral data include over 1800 independent variables and are too highly dimensional for most statistical tests to adequately manage. Additionally, there are more independent variables than dependent variables and most independent variables are collinear; data qualities for which there is no perfect-fit statistical test.

5.2.2.1 Spectral Angle Mapper and Spectral Information Divergence

Spectral Angle Mapper (SAM) is an analytical tool in ENVI (Harris Corp.) that treats each spectral signature like a vector in *n*-dimensional space, where *n* equals the number of spectral bands along each signature. The program calculates the angle between two vectors and reports the measurement in radians where smaller values indicate spectral similarity, and larger values indicate difference (Kruse et al. 1993). Remote sensing convention tends to treat two spectra with SAM values ≥ 0.10 radians as two distinct classes, though there is no available documentation to account for the significance of this threshold (Schwarz and Staenz 2001), so values are simply treated as relative difference for this study.

Spectral Information Divergence (SID) is a tool that calculates the probability that each spectral signature is equal to that of a reference spectrum. Probability distributions are used to calculate overall similarity between groups where, like Spectral Angle Mapper, smaller divergence values indicate spectral similarity and larger values indicate greater spectral divergence (Du et al. 2004). Similar to SAM, convention states the SID classification threshold value is ≥ 0.05, but this value is not empirically supported (Schwarz and Staenz 2001).

For SAM and SID, *individual* vegetation reflectance spectral profiles from a) combined human burials (all three burials) and b) general disturbance (all burials and control) were compared to the *mean* undisturbed spectrum. Separate comparisons were made for Spring and Autumn data

sets, and each comparison was made by its full spectrum (400 – 2500, 1803 bands) and as spectral regions: blue (400 – 500 nm), green (500 – 600), red (600 – 750 nm), near infrared (750 – 1330 nm), and shortwave infrared (1440 – 1800, 1990 – 2500 nm).

5.2.2.2 Binary Logistic Regression

Binary logistic regression (BLR) is a statistical method for using independent variables to estimate the probability of membership of a binary categorical group, or dependent variable. The test measures the relationship between a dependent variable and one or more independent variables using a logistic function (Menard 2002), and has been used for predictive modeling of prehistoric human land use using multivariate geospatial data, including remotely sensed data (Vaughan and Crawford 2009). The logistic regression model is different from a linear regression model in that it will tolerate categorical dependent variables. All 1803 variables (bands) were entered stepwise, and are each evaluated based on their contribution to the overall model. If a wavelength significantly improves the model, it is retained; if a wavelength does not significantly improve the model, it is removed.

For both Spring and Autumn live vegetation reflectance data sets, comparisons were made between a) the combined human burial group (all human burials) and the undisturbed group, and b) the combined disturbance group (all human burials and the control unit) and the undisturbed group. Models were trained using wavelengths in the full spectral range (400 – 2500 nm) and wavelengths within a spectral subset that includes only the spectral range of the airborne hyperspectral sensor used to collect imagery in this study (418 – 919 nm). Using this strategy, six possible models for each season were evaluated, for a total of twelve possible models. For all BLR comparisons, 70% of the samples were used to train each model, and 30% were used to validate the model's performance.

The results of training a logistic regression model produce a constant and one or more variable coefficients that are applied to reflectance values at specific wavelengths. Regression **Formula 5.2-1** is used for validation sample classification, where α is a scalar coefficient and λ is the reflectance value of an associated wavelength. Applying this formula to a reflectance spectrum results in a value ranging from 0.0 – 1.0, where values ≥ 0.50 are classified as a burial or general disturbance, depending on the model, and values < 0.50 are classified as undisturbed.

Formula 5.2-1: $p = 1/1+e^{-(\text{Constant} + \alpha 1*\lambda 1 + \alpha 2*\lambda 2 + \ldots + \alpha n*\lambda n)}$

5.2.2.3 Discriminant Function Analysis

Like logistic regression, discriminant function analysis (DFA) is a statistical method for predicting membership of two or more categorical groups. The procedure generates functions that maximize group differences by creating linear combinations of independent variables (Quinn and Keough 2002). The maximum number of functions is equal to *n*-1 groups or *n* predictor variables, whichever is less. All 1803 wavelength variables are entered stepwise, and evaluated based on their contributions to the overall model. If a wavelength significantly improves the model, it is retained; if a wavelength does not significantly improve the model, it is removed.

For both Spring and Autumn live vegetation reflectance data sets, comparisons were made between a) the combined human burial group (all human burials) and the undisturbed group, b) the combined disturbance group (all human burials and the control unit) and the undisturbed group. A separate attempt was made to produce a three-class model using the combined human burial group, the control unit, and the undisturbed group, which instead produced a binary result that is presented in Chapter 6. Models were trained using wavelengths in the full spectral range (400 – 2500 nm) and wavelengths within a spectral subset that includes only the spectral range of the airborne hyperspectral sensor used to collect imagery in this study (418 – 919 nm). Using this

strategy, six possible models for each season were evaluated, for a total of twelve possible models. For all comparisons, 70% of the samples were used to train each model, and 30% were used to validate the model's performance.

The training procedure generates two sets of coefficients that are both used in **Formula 5.2-2**: 1) discriminant function coefficients for each category, which produce a binary result for each validation sample (True/False), and 2) classification function coefficients, which produce a continuous result for each 'True' binary result.

Formula 5.2-2: $D = \text{Constant} + \alpha 1 * \lambda 1 + \alpha 2 * \lambda 2 + \ldots + \alpha n * \lambda n$

The two sets of discriminant function coefficients are applied to each new spectrum in the 30% validation sample. Each spectrum is classified depending on whichever of the two results is largest. For instance, if a model is designed to separate between human burial vegetation and undisturbed vegetation, two equations are applied to each test case – D_1 (human burial vegetation) and D_0 (undisturbed vegetation). If the result of applying equation D_0 to a reflectance spectrum is greater than that produced by applying equation D_1 to the same reflectance spectrum, then the spectrum is classified as undisturbed vegetation. If the opposite is true, then the spectrum is classified as human burial vegetation. This formula is used to first make a binary classification, followed by the application of a separate set of discriminant function coefficients applied only to the spectra classified as D_1, revealing variation among spectra that have been classified as either human burial vegetation or generally disturbed vegetation.

5.2.2.4 BLR and DFA Model Development Workflow

The BLR and DFA model development workflows are the same (**Figure 5.2-4**), where 70% of Spring and Autumn data sets are used to train binary statistical models and the remaining

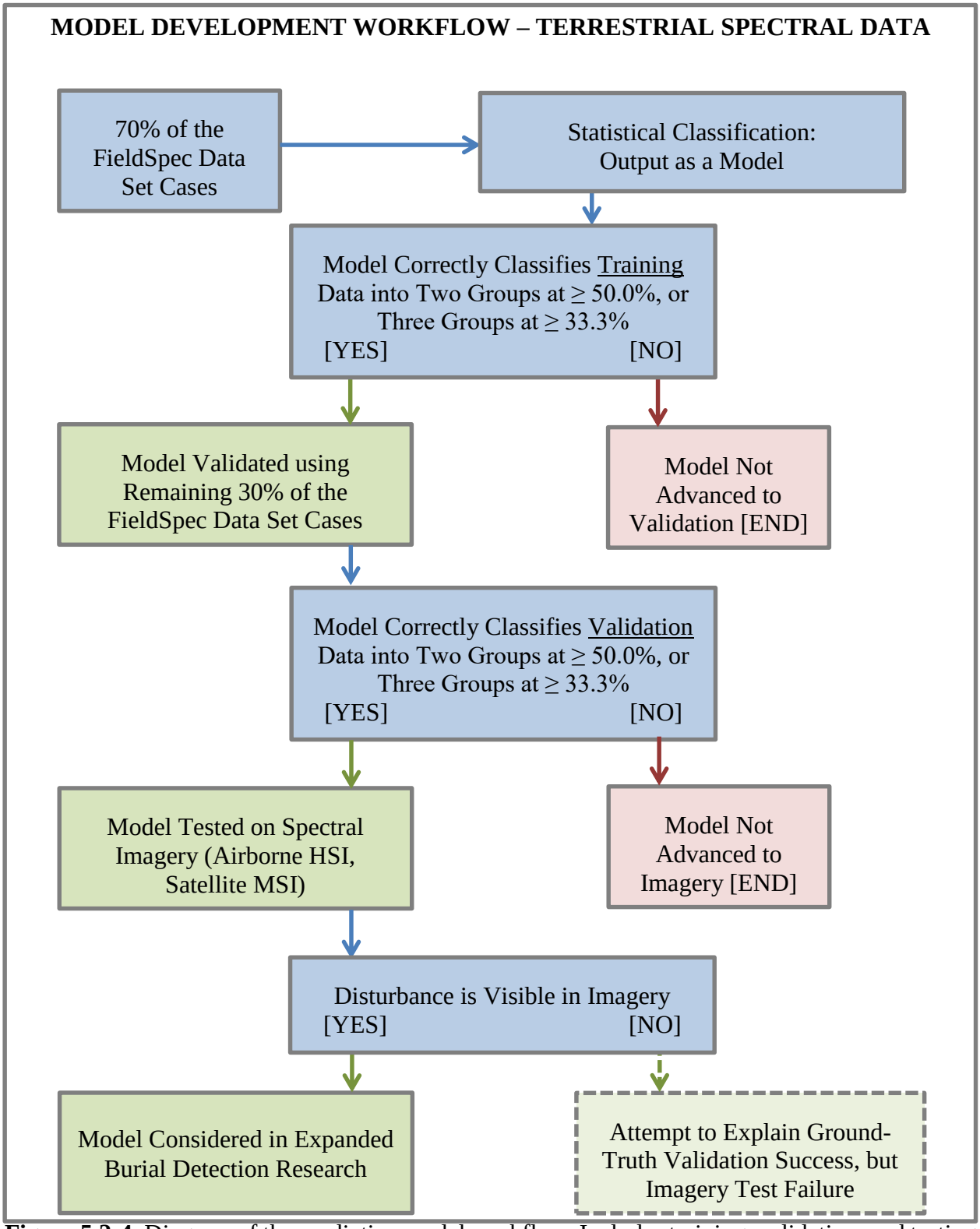

Figure 5.2-4: Diagram of the predictive model workflow. Includes training, validation, and testing of FieldSpec data.

30% are used to validate the same models. If a model correctly classifies the 70% training data set for both groups at ≥ 50.0%, the model is advanced to the remaining 30% validation sample. Successful validation requires meeting the same ≥ 50.0% performance standard for the 70% sample as well as the 30% sample. Successfully validated models are later advanced to spectral imagery as a preliminary assessment of terrestrial model scalability to canopy spectra.

5.2.2.5 Partial Least Squares Regression

When data contain a large number of predictor variables, traditional regression methods are likely to develop a model that fits training data perfectly, but performs poorly at predicting new data; an issue known as *over-fitting*. Additionally, regression methods are often intolerant of multicollinearity among predictor variables, where each variable is highly correlated with each other. Partial Least Squares Regression (PLS) is a useful approach for evaluating datasets that contain more independent variables than recorded samples (high dimensionality), but most importantly, in scenarios where independent variables are collinear. These advantages make PLS a popular method to support spectral research, as spectral data usually violate the statistical assumptions of multicollinearity and high dimensionality. PLS also permits dependent variables to be categorical. PLS combines concepts of principle components analysis and linear regression by reducing both dependent and independent variables to a smaller set of uncorrelated factors, to which PLS performs a least squares regression (Geladi and Kowalski 1986; Hoskuldsson 1988).

The PLS routine explains variance within data by constructing new independent variables, known as factors, as linear combinations of the original variables. PLS factors consider the relationship between dependent and independent variables by explaining data variability for both variables (Geladi and Kowalski 1986; Hoskuldsson 1988). Principle component analysis (PCA), which is another common analytical approach, only explains variability of independent variables

and largely ignores the dependent variable, which is why PCA is not used in this study. As a result, PLS factors can model the dependent-independent variable relationship with fewer factors than would PCA (Maitra and Yan 2008).

For both Spring and Autumn live vegetation reflectance data sets, comparisons were made between a) the combined human burial group (all human burials) and the undisturbed group, b) the combined disturbance group (all human burials and the control unit) and the undisturbed group, and c) the combined human burial group, the control unit, and the undisturbed group. PLS factors were derived using wavelengths in the full spectral range (400 – 2500 nm) and wavelengths within a spectral subset that includes only the spectral range of the airborne hyperspectral sensor used to collect imagery in this study (418 – 919 nm), for a total of twelve comparisons. For all comparisons, 100% of the samples were used to derive each PLS factor.

A PLS analysis generates values of variable importance (or variable influence on projection, VIP) where the first factor VIP tends to explain the most variance in the data set. PLS output was limited to a set of four factors for each test, where in all tests the first factor explained at least 83.4% data variance. It is convention to exclude variables with a VIP score less than 1.0 since this value is the mean of squared VIP scores, though this approach still retains a large number of predictor variables (wavelengths). Since PLS is used in this research to support BLR and DFA variable inclusion, rather than as the sole method for wavelength selection, the focus of PLS results and discussion is on the extent of agreement between ≥ 1.0 VIP values and BLR and DFA model variables.

5.3 Airborne Hyperspectral Imagery

While the analytical emphasis of this dissertation is on terrestrial data sets, this section discusses the methodology used to collect, process, and analyze airborne hyperspectral imagery (HSI) to address Objective 3, which is to evaluate the potential scalability of terrestrial findings in airborne data. Airborne hyperspectral imagery was collected by the NASA Goddard Space Flight Center (GSFC) using the Headwall Hyperspec (Headwall Photonics, Inc.) is an imaging spectrometer in Goddard's LIDAR, Hyperspectral, and Thermal Imager (G-LiHT) airborne sensing system (Cook et al. 2013).

The spatial resolution of HSI is largely determined by aircraft altitude, but at any altitude, resolution is still lower than that of the ground-based point spectra, such as the data collected using the FieldSpec® 4 Standard-Res Spectroradiometer (PANalytical, Boulder, CO). The primary advantage of HSI over ground-based sensors, however, is that it permits rapid collection of large swaths of land and does not necessarily require personnel to physically operate on the ground. The relative disadvantage of HSI, compared to ground-based spectra, is a lower spectral resolution, which is discussed below.

5.3.1 Airborne Hyperspectral Imagery Collection and Processing

The Hyperspec sensor is designed for aircraft-mounted overhead collections, and covers a spectral range from 418 - 919 nm in 114 resampled spectral bands each spaced at approximately 4.5 - 5 nm (**Figure 5.3-1**). Images were collected as at-sensor radiance within one hour of solar noon on 23 March, 17 April, and 07 May 2015 and delivered by NASA-GFSC at 1.0 m pixel ground sample distance (GSD) for March and April collections and 0.5 m resolution for the May collection. All images were georeferenced by NASA using GPS/INS flight data and align with

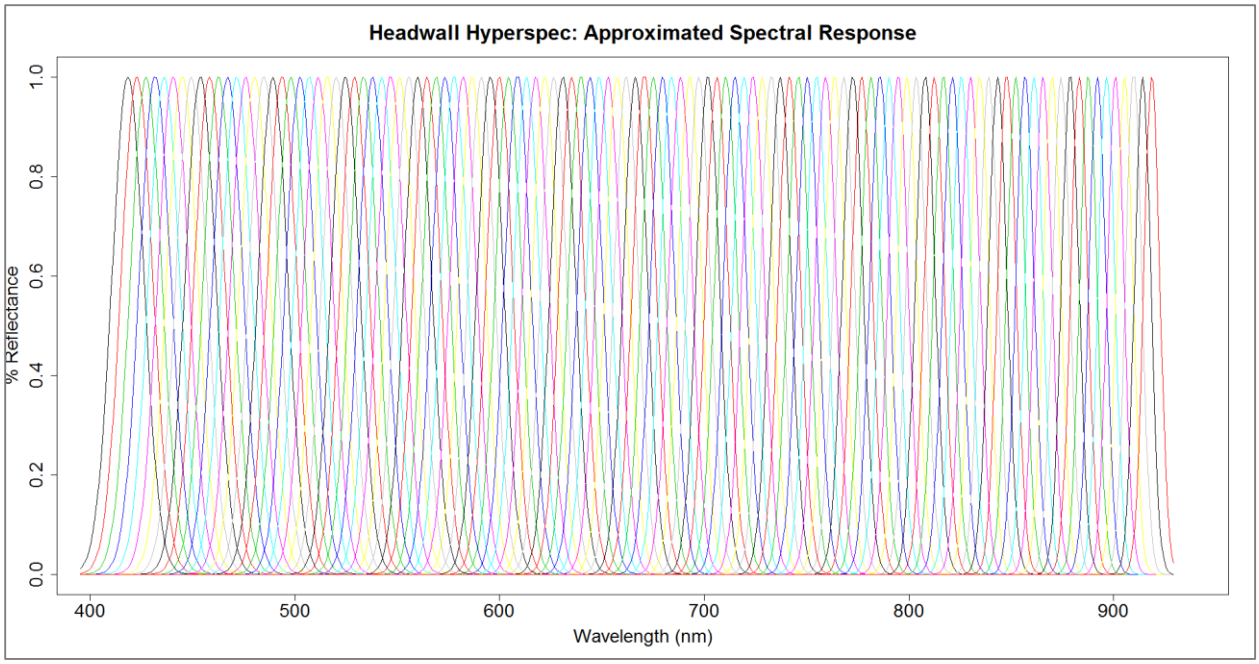

Figure 5.3-1: The approximated spectral response for the Headwall Hyperspec imaging spectrometer. Wavelength centers and bandwidths at full-width at half-maximum (FWHM) were fitted to Gaussian curves for each of the 114 bands to demonstrate the instrument spectral resolution, which is lower than terrestrial spectra and higher than the satellite multispectral imagery used in this study.

each other to maximum of approximately one-meter spatial offset. Timing of data collection was constrained by the availability of NASA resources and personnel on short notice due to an unforeseen change in data partners. Under different circumstances, planned collections would likely have been distributed more evenly through the calendar year. The effects of atmospheric scattering were minimized by collecting reflectance spectra of airport tarmac ground targets, both before take-off and after landing, for each flight. These reflectance spectra were used to apply an empirical line correction that converted at-sensor radiance to surface reflectance. A standard resolution FieldSpec 4® spectroradiometer was used for this purpose, and was calibrated immediately before each data collection using a 3.62-inch diameter Spectralon® white reference panel.

5.3.2 Airborne Hyperspectral Imagery Analysis

Hyperspectral imagery analysis involved two separate approaches. First, the two scalable DFA models developed using FieldSpec data were applied directly to HSI using ENVI. The second approach uses the built-in ENVI spectral index function to calculate seven vegetation indices. A third approach, where tree canopy directly above the known burial locations is defined as a fixed region of interest (ROI) to be compared to a nearby known undisturbed ROI, was considered but not performed. This step was omitted because of the ambiguity in the association between area canopy tree roots in relation to burials, resulting in further uncertainty in whether a user-defined ROI will align with a potentially affected canopy sample.

5.3.2.1 Statistical Models

Seven statistical models were developed using field spectra: two binary logistic regression (BLR) models and five discriminant function (DFA) models. Of the seven models, only DFA models 4 and 9 can be applied to hyperspectral imagery because their wavelength variables are all

contained within the 418 – 919 nm spectral range of the Hyperspec imagery. The remaining five models incorporate shortwave infrared bands that are not covered by the HSI sensor and, therefore, cannot be testing using HSI. DFA models 4 and 9 were input as ENVI Band Math expressions (**Formulas 5.3-1** and **5.3-3**) and applied to each full reflectance image. Binary results are then used as an image mask when applying the second set of formulas (**Formulas 5.3-2** and **5.3-4**) to reveal continuous variation among image pixels classified as human burials or general disturbance.

DFA Model 4:
Binary (TRUE/FALSE, 1/0) Human Burial Classification, if:

Formula 5.3-1: $D_1 = -1.866 + 19.252*R_{707} > D_0 = -4.335 + 33.926*R_{707}$

Continuous Among TRUE (1) Results from **Formula 5.3-1**:

Formula 5.3-2: $D = -2.258 + 12.570*R_{707}$

DFA Model 9:
Binary (TRUE/FALSE, 1/0) Disturbance Classification, if:

Formula 5.3-3: $D_1 = -2.004 + 19.555*R_{708} > D_0 = -4.294 + 32.412*R_{708}$

Continuous Among TRUE (1) Results from **Formula 5.3-3**:

Formula 5.3-4: $D = -2.260 + 12.078*R_{708}$

5.3.2.2 Vegetation Indices

Spectral indices can be used to emphasize vegetation anomalies (e.g., stress) in airborne or satellite imagery. Vegetation indices have been developed for the purpose of monitoring vegetation by estimating concentrations of pigments correlated with vegetation health (Curran et al. 1995; Penuelas et al. 1995) or estimating vegetation nutrient concentration (Rouse et al. 1973; Sims and Gamon 2002). Indices vary in their rationale and complexity, but they generally play at least one

band known to be associated with a specific vegetation phenomenon against a different band that is not.

Dozens of vegetation indices are used in vegetation health studies, so to maintain the scope of this analysis, indices applied to HSI are limited to those that incorporate a spectral wavelength within ±5 nm of a wavelength included in a statistical model derived using terrestrial spectra, and indices used in published forensic remote sensing work. Leblanc et al. (2014) used three indices – NDVI, SGI, and SIPI – in a study evaluating remote sensing to identify clandestine pig burials. In addition to these indices, their results depend on shortwave infrared spectral data to isolate a clay signature. However, shortwave infrared spectra are not available for this dissertation research and, therefore, cannot be evaluated at this time. The seven vegetation indices evaluated in the current study include NDVI, SGI, and SIPI, which are presented in **Table 5.3-1**.

5.4 Satellite Multispectral Imagery

This section discusses the methodology use to collect, process, and analyze satellite multispectral imagery to evaluate the potential scalability of terrestrial findings in satellite data (Objective 3). Much like airborne hyperspectral imagery (HSI), satellite multispectral imagery (MSI) is used to determine whether spectral anomalies observed in terrestrial data are also observable using long-range sensors. Satellite images are among the most cost-effective remote sensing data sets, and are often collected and delivered to consumers within a day or two. An added benefit of incorporating MSI in this study is that archived baseline data are usually available. Companies that own imaging satellites tend to collect and archive imagery even if there is no current demand, because many researchers who work with satellite imagery use MSI for landscape change comparison.

Table 5.3-1: Spectral indices used to estimate vegetation health in HSI collections; (*) denotes indices used by Leblanc et al. (2014). Formulas for calculating vegetation indices from reflectance spectra are available in **Appendix D, Tables D.1 – D.3**.

Index	Abbreviation	Estimates
Normalized Difference Vegetation Index	NDVI*	Vegetation Health
Red Edge NDVI	RENDVI	Vegetation Health
Modified Red Edge Simple Ratio Index	MRESRI	Vegetation Health
Modified Red Edge NDVI	MRENDVI	Vegetation Health
Sum Green Index	SGI*	Vegetation Pigment
Red Edge Position Index	REPI	Chlorophyll
Structure Insensitive Pigment Index	SIPI*	Carotenoid Pigment

The primary advantage of MSI over ground-based or airborne sensors is that it provides the most rapid collection rate. Additionally, orbiting sensors are not subject to the same degree of spatial error caused by turbulence that aircraft-based sensors must account for during a flight. The significant disadvantage of using MSI is that the spatial and spectral resolutions cannot compete with that of either terrestrial or airborne collections. The best performing commercial satellite multispectral scanners offer up to 1.24 m ground sample distance (GSD, or pixel size), and eight spectral bands.

5.4.1 Satellite Multispectral Imagery Collection and Processing

Four multispectral satellite images are used in this study that span from July 2012 – March 2015 (**Table 5.4-1**). Two satellite sensors are used to collect imagery for this study: WorldView-2 and WorldView-3 (DigitalGlobe, Inc.). Both sensors are sun- synchronous, meaning that image collections by each sensor are made at approximately the same local time. Consistency of image acquisition time helps limit variation between images collected at different dates with the same sensor due to solar geometry. WorldView-2 and WorldView-3 are 8-band multispectral scanners

that orbit Earth at 770 and 617 km, respectively. These altitudes result in respective 1.84 and 1.24 m multispectral GSD, at nadir.

Sensor specifications for WorldView-2 are presented in **Table 5.4-2** and **Figure 5.4-1**, and for WorldView-3 in **Table 5.4-3** and **Figure 5.4-2**. In addition to the four images included in this analysis, several more satellite images were made available for this work, but they were either collected during poor atmospheric/weather conditions or collected within days of the images that are included in this study. Images with the best atmospheric conditions and viewing geometry were selected from contemporaneous collections. MSI scenes were radiometrically calibrated, then corrected for the effects of atmospheric scattering and converted to reflectance using the Fast Line-of-Sight Atmospheric Analysis of Hypercubes (FLAASH) tool in ENVI. Reflectance images were orthorectified using scene-specific rational polynomial coefficients (RPCs).

5.4.2 Satellite Multispectral Imagery Analysis

5.4.2.1 Vegetation Index

The two DFA models developed using terrestrial spectral data were not applied to MSI because the Red Edge band is too wide (40 nm) to isolate the narrow spectral feature located at 707/708 nm. Also due to the width of MSI spectral bands, only one vegetation index (Normalized Difference Vegetation Index) among the seven indices performed using HSI, can also be performed using MSI, so the analysis is limited. The image co-registration process yielded poor results, with spatial offset between images at 1m or more. Therefore, MSI images were not compared to each other as part of a change comparison due to a lack of confidence in the alignment of burial location pixels.

Table 5.4-1: Satellite imagery used in this dissertation research, chronological; dashed line indicates boundary between baseline and post-burial collections.

Acquisition Date	Sensor
30 Jul 2012	WorldView-2
29 Nov 2012	WorldView-2
04 Mar 2013	WorldView-2
25 Mar 2015	WorldView-3

Table 5.4-2: WorldView-2 sensor spectral and spatial specifications; 770 km altitude.

WV-2 Band	Spectral Range (nm)	Spectral Center (nm)	GSD at Nadir (m)
Panchromatic	450 – 800	-	0.46
Coastal	400 – 450	427.00	1.84
Blue	450 – 510	478.50	1.84
Green	510 – 580	546.00	1.84
Yellow	585 – 625	608.00	1.84
Red	630 – 690	659.00	1.84
Red Edge	705 – 745	724.00	1.84
NIR1	770 – 895	833.00	1.84
NIR2	860 – 1040	949.50	1.84

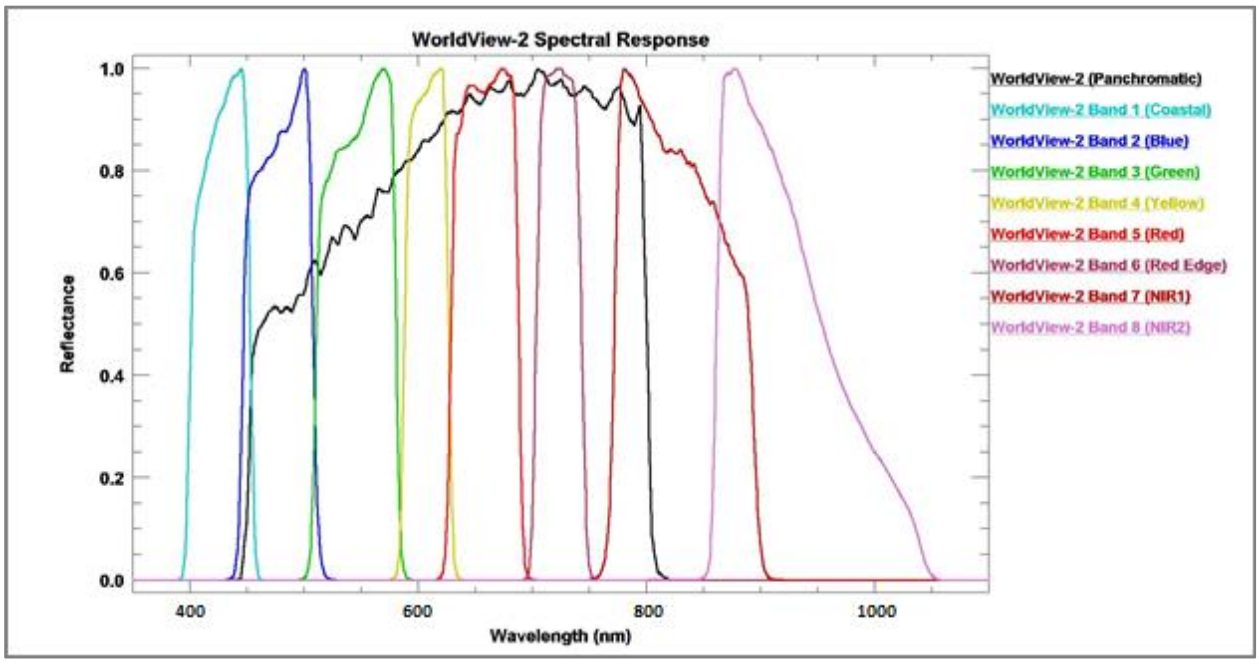

Figure 5.4-1: WorldView-2 spectral response for each band.

Table 5.4-3: WorldView-3 sensor spectral and spatial specifications; 617 km altitude.

WV-2 Band	Spectral Range (nm)	Spectral Center (nm)	GSD at Nadir (m)
Panchromatic	450 – 800	-	0.31
Coastal	400 – 450	425.50	1.24
Blue	450 – 510	481.00	1.24
Green	510 – 580	546.50	1.24
Yellow	585 – 625	604.50	1.24
Red	630 – 690	661.00	1.24
Red Edge	705 – 745	723.50	1.24
NIR1	770 – 895	832.00	1.24
NIR2	860 – 1040	948.00	1.24

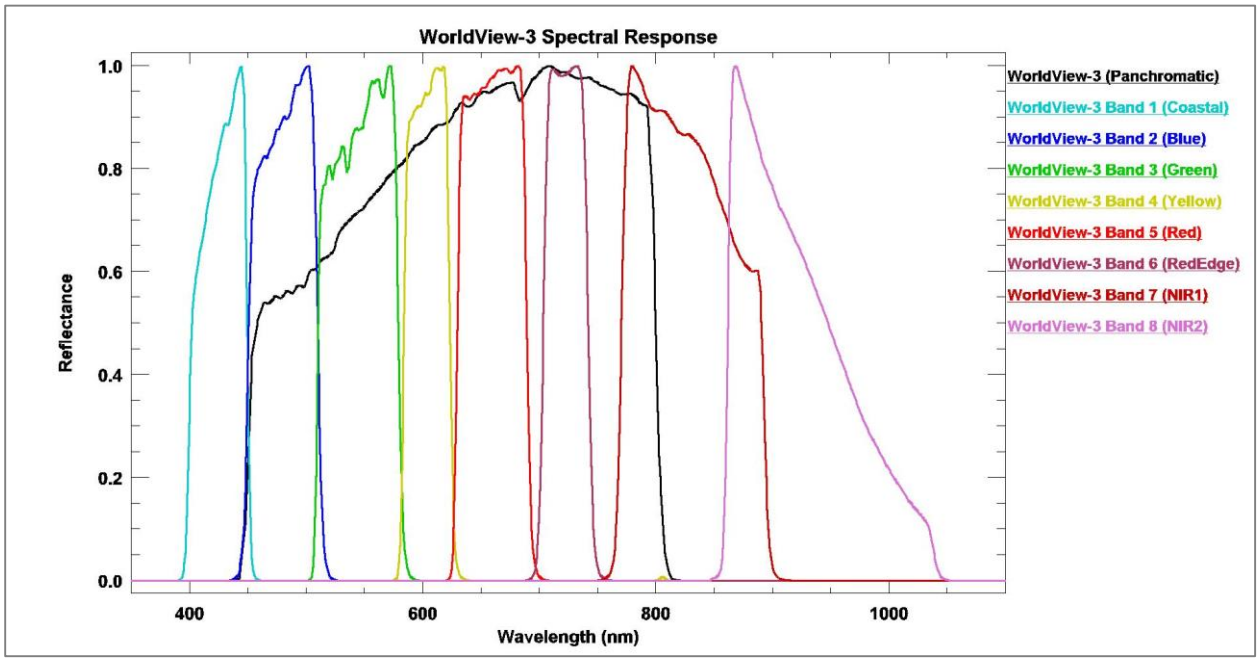

Figure 5.4-2: WorldView-3 spectral response for each band.

5.5 Terrestrial LIDAR

This section discusses the methodology used to collect, process, and analyze terrestrial light detection and ranging (LIDAR) elevation data. The terrestrial LIDAR analysis addresses Hypotheses 2 and 4 by evaluating human burial and non-burial surface elevation change over time. Specifically, hypotheses 2 and 4 state:

> 2. Ground surfaces at burials, the control unit, and undisturbed locations exhibit differences as measured by net elevation gain or loss.
>
> 4. Ground surfaces associated with burials, the control unit, and undisturbed locations exhibit differences in elevation change over a 21-month period.

Terrestrial light detection and ranging (LIDAR) is used in this study to establish a localized pattern of elevation change at the surfaces of each experimental burial and the control unit. Terrestrial sensors are operated on the ground within the study area environment. The most accurate terrestrial LIDAR data are collected using stationary scanners tied to a known geographic location. The tripod-mounted scanner rotates horizontally, emitting pulses that reflect off object surfaces within the environment. Upon encountering objects, pulses are returned to the sensor. The precise positions of those interactions are recorded as three-dimensional point data, and are calculated as a function of pulse direction and travel time.

The orientation of terrestrial LIDAR scanners results in a point cloud with an uneven point distribution where point density decreases as distance from the sensor increases. Uneven point distribution can be overcome by performing scans from multiple positions throughout the environment to densify the point cloud and fill in data gaps behind solid objects in the scene that interrupt pulse paths. Multiple scans can be aligned to each other to produce a larger point cloud

that represents the entire environment. The advantage of a multi-scan terrestrial LIDAR strategy is that unlimited scans can be performed to generate a point cloud as dense as is desirable for any practical application. This study took advantage of that capability to generate sub-centimeter point density at each burial surface to monitor surface elevation changes over time. Terrestrial LIDAR data are used to address the question of whether burial surface elevation change exists, and if so, whether change is localized (burial surfaces only) or generalized (entire study area).

5.5.1 Terrestrial LIDAR Data Collection and Processing

Terrestrial LIDAR data were collected using a Riegl VZ-400 tripod-mounted laser scanner (Riegl USA, Orlando, FL). The sensor is designed to collect three-dimensional points in panoramic fashion as it rotates horizontally on a stationary platform. Scanner accuracy and precision are reported to be ±5 mm and ±3 mm, respectively, for measurements up to 600 m at a rate of up to 122,000 measurements per second at 1550 nm. The scanner's vertical and horizontal fields-of-view are 100˚ (+60˚/-40˚ off-horizon) and 360˚, respectively. Beam divergence is 0.35 ($1/e^2$), and corresponds to an increase of 35 mm in beam diameter per 100 m distance.

For clarity, this section will discuss entire *point clouds* that are collections of individual *scans* made from different *scan positions*. LIDAR data collections and point cloud sizes are presented in **Table 5.5-1**. A terrestrial laser scanner was placed in at least three positions throughout the study area for each data collection, **Figure 5.5-1**, with all scan positions keeping at least one experimental human burial in the sensor's field-of-view. Cylindrical reflectors were placed throughout the study area, with a minimum of three in view of the scanner at all scan positions. Reflectors help tie scans to each other through triangulation so they can be later merged into one comprehensive point cloud. Additional steps are taken to more precisely align scans to

Table 5.5-1: Point cloud sizes for each terrestrial LIDAR data collection.

Collection Date	# Points, Entire Cloud	# Points, Limited to Fence Line/ <1m AGL
12 February 2013	44,809,070	33,277,648
15 February 2013	56,111,989	31,975,234
03 June 2013	40,838,607	11,168,278
20 November 2014	119,214,901	40,143,940

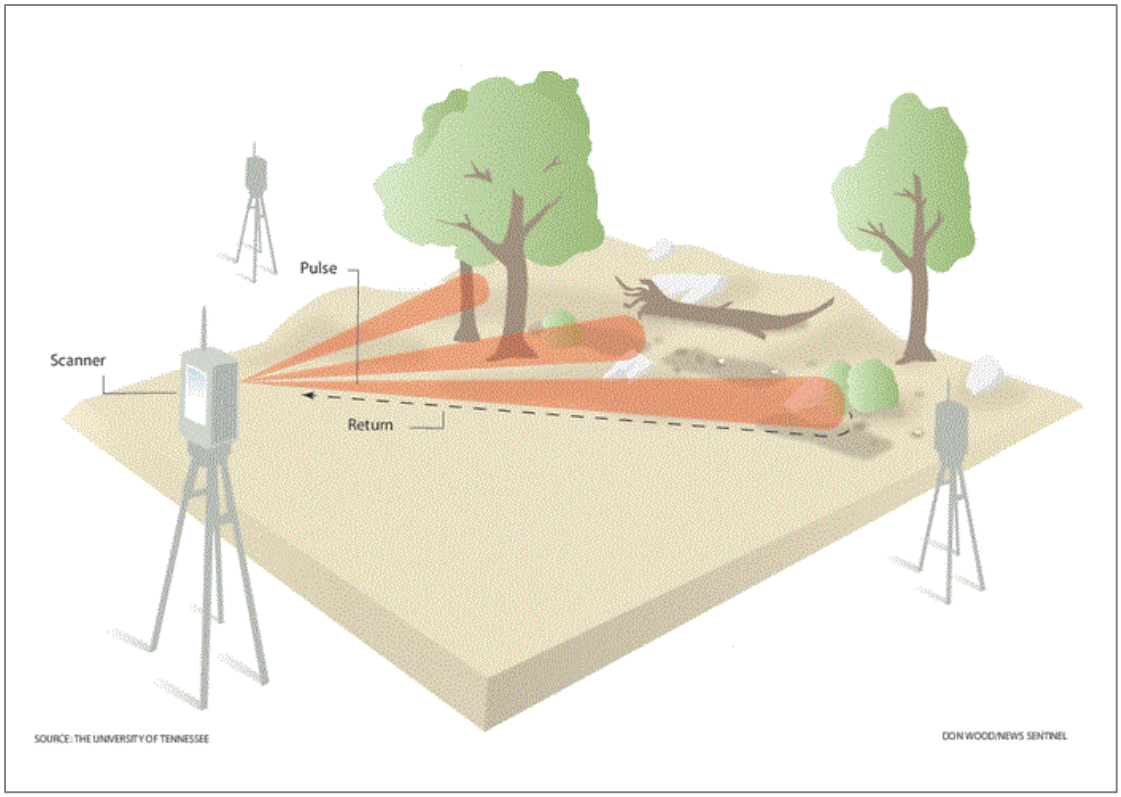

Figure 5.5-1: Diagram of a hypothetical terrestrial LIDAR survey; multiple scan positions to fill in 3-D data behind obstructions. (Image credit: Don Wood/Knoxville New Sentinel, modified by the author, used with permission).

each other using the Iterative Closest Point (ICP) point cloud registration algorithm, where this initial correction is inadequate.

Under optimal field conditions, GPS data can be collected to register point clouds to global coordinate space. To ensure precise registration, it is best to allow the GPS system to gather data for several hours then directly relate those data to the sensor. Due to time and weather constraints, only the baseline collection was tied to coincident GPS data, which means that all subsequent collections are manually co-registered, or aligned, to that first collection. Alignment algorithms perform well enough to reconcile the remaining collections with a high degree of confidence, and are described in this section.

5.5.1.1 Point Cloud Alignment

Scans made from the same position are well-aligned to each other, but scans between scan positions often need a 'nudge' to precisely align them. Alignment, or point co-registration, is important because if there is an offset to one scan, the subsequent ground point filtering process will be intolerant of that offset. For instance, in the case of a vertical offset, filtering algorithms will classify an artificially elevated blanket of ground points as non-ground points, unnecessarily removing hundreds or thousands of useful points that are representative of the ground surface. Point registration is performed using the Iterative Closest Point (ICP) algorithm (Besl and McKay 1992) in CloudCompare (**Figure 5.5-2**).

To align point clouds, one point cloud is treated as a reference for the remaining point clouds that will require a rigid transformation. The first scan of the baseline collection is registered to a global coordinate system using coincident GPS data, and the others are not, therefore the subsequent scans are registered to the first scan. The ICP algorithm assumes all objects in a scene are stationary and rigid, but wind at the study area causes objects in the scene to move and must

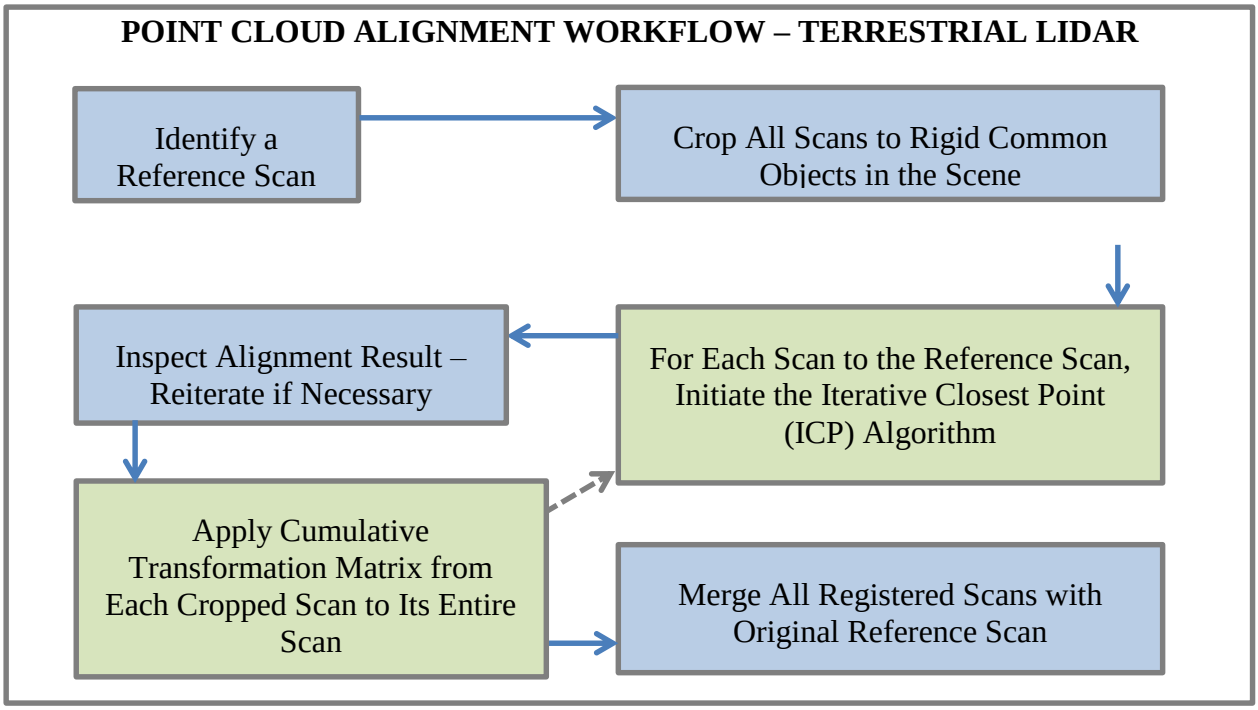

Figure 5.5-2: Diagram of the point alignment workflow.

be temporarily removed, or they will result in poor overall point cloud alignment. Point cloud subsets containing only rigid and stationary objects in the scene are used to calculate transformation matrices. A transformation matrix is calculated by measuring the distances between points within point cloud subsets and relating them to the point distances measured in the reference point cloud (CloudCompare). Transformations include translation, rotation, and scale. If subset alignment is satisfactory, the transformation matrix is applied to the entire point cloud. If results need improvement, further iterations are performed. The results of this process produce well-aligned scans that can be merged as one point cloud.

5.5.1.2 Point Filtering

Laser scanners emit millions of pulses per scan that are returned – in full or in part – to the scanner upon encountering objects in their path. In the study area, objects can be any physical material such as a tree, rock, or fence. The sensor does not recognize these materials by category; it records the three-dimensional coordinates at the location of pulse/object interaction. For this reason, sensor geometry becomes important for determining point classification. Differing geometries of terrestrial and airborne LIDAR datasets are a central point of interest for this study because most ground point filtering methodologies rely on assumptions of point-to-scanner orientation or the number of times a pulse is returned to the sensor. For stratified environments, a first return to an aircraft-based sensor is usually canopy and a last return is usually ground. Unlike in airborne LIDAR, returns in terrestrial LIDAR are less useful than location values because any return can be a ground point if a pulse travels parallel, rather than perpendicular, to terrain.

There is a lack of comprehensive terrestrial LIDAR filtering tools available to the public. Of those that do exist, few are sufficiently concerned with removing low-lying vegetation, which is a significant problem for this application because vegetation obscures burial surfaces. In

response to the lack of adequate filtering tools, an existing Block Minimum algorithm originally developed for airborne LIDAR data (Wack and Wimmer 2002) was modified slightly for use with terrestrial LIDAR data in this research. After all point clouds are aligned, filtering is performed to reduce them to mostly ground points (**Figure 5.5-3**). Before filtering begins, the point cloud is cropped to remove points located outside the horizontal boundary of the study area fence line. QT Modeler is then used to approximate an initial ground surface by selecting the lowest point in each 2 m grid cell, which is reduced from 9 m due to increased point density. Points located at a height greater than 1 m above this surface are removed, a modification that eliminates most of the large vegetation and fencing in the scene and narrows the range of elevation values for more accurate surface approximations in later steps. To adapt the Block Minimum algorithm for terrestrial data, remaining points are thinned using LAStools (rapidlasso) to produce a point cloud that includes only the single lowest elevation point in every 5 cm grid cell. Since point density is highest in the circular area immediately surrounding a terrestrial scanner, thinning simulates a more even point distribution seen in airborne collections.

The thinned point cloud is then used to approximate a new ground surface at 50 cm GSD. Approximating a new surface is performed because the thinned point cloud now contains a higher proportion of ground points than the original point cloud, meaning the new approximated surface is more reliable for filtering than the first. Height statistics for the new surface are calculated and used to remove points with height values greater than the remaining point cloud's own statistical mean, plus one standard deviation. The point cloud is then visually inspected to verify that no obvious non-ground points remain in the data set and no large data gaps were created during the process. Generally, the method performs well after the first iteration, but the process can be

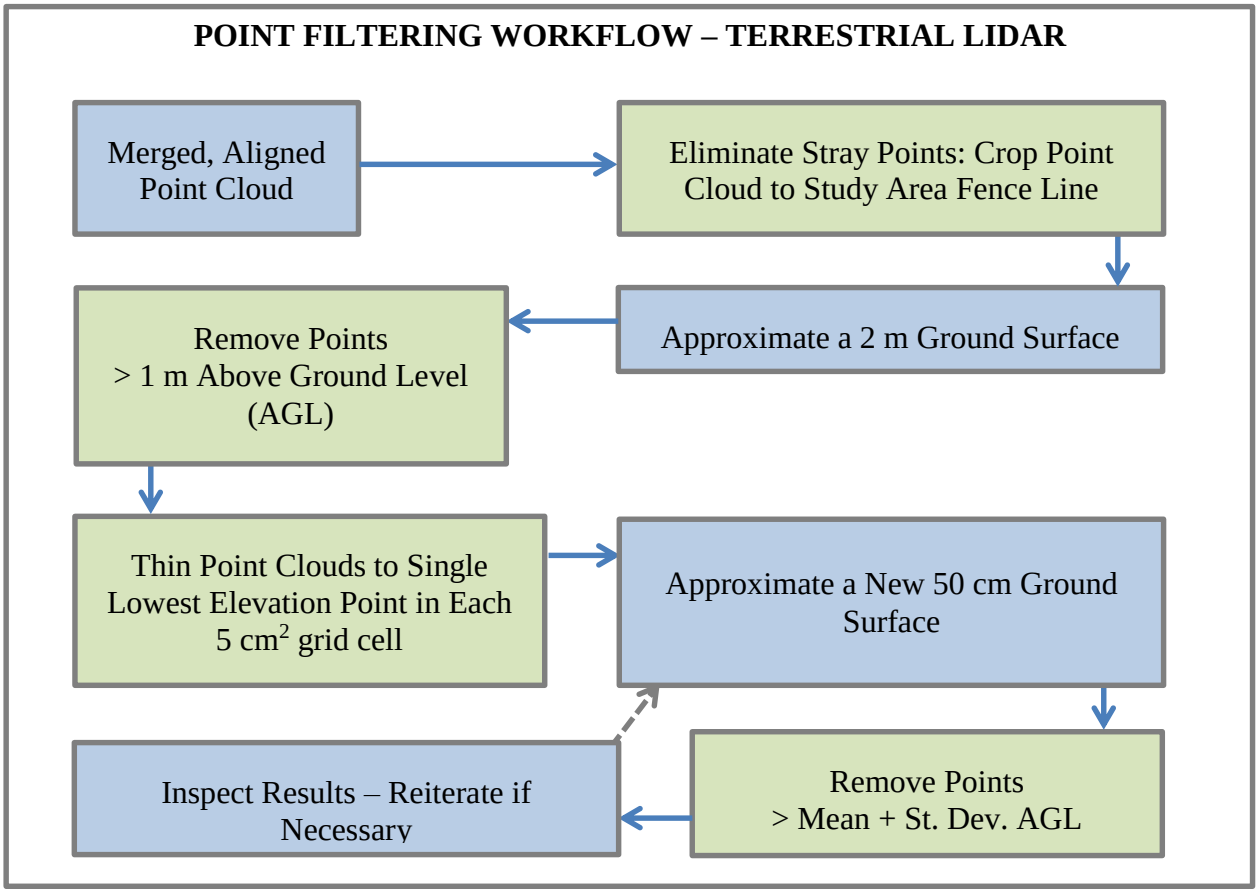

Figure 5.5-3: Diagram of the Block Minimum point filtering workflow.

repeated if needed. The modified algorithm is straightforward, performs well for removing low-lying vegetation, is independent of return values, and its geometric assumptions can be applied to terrestrial and airborne point cloud data.

5.5.2 Terrestrial LIDAR Data Visualization

The experimental burials are presented as images in two forms: 1) as absolute elevation measurements at each of four collection dates, and 2) as elevation changes over time (**Figure 5.5-4**), where each of the absolute elevation images are subtracted from each other to reveal net changes between each collection date. Elevation images and change images were run through the Sky-View Factor surface visualization tool (Kokalj et al. 2011; Zaksek et al. 2011), which excels at highlighting subtle features in variable terrain. The method measures the percentage of sky that is visible from each pixel location and accounts for visual obstructions within a user-specified radius. The radius used for this research is 2.25 m, to allow all burial surface pixels to 'see' beyond their respective burial extents in as many directions as possible. The hypotenuse of the largest burial feature is 4.47 m. Therefore, the radius is set to approximately one half that length so the visibility of the centermost pixels of the largest features reach their own burial surface extents where relevant topographic outliers would be anticipated, if they exist.

Localized elevation changes are emphasized using density slicing, a tool in ENVI that allows the user to highlight pixels within user-specified value ranges. Density slicing is used in this research strictly as a visualization tool to emphasize distinctive spatial clustering at disturbance feature locations. Values used to define ranges of elevation change at these locations are extracted from change images at regions of interest (ROI), i.e., control unit and burial surfaces, and the same values are highlighted throughout each image. Density slices help illustrate that change values

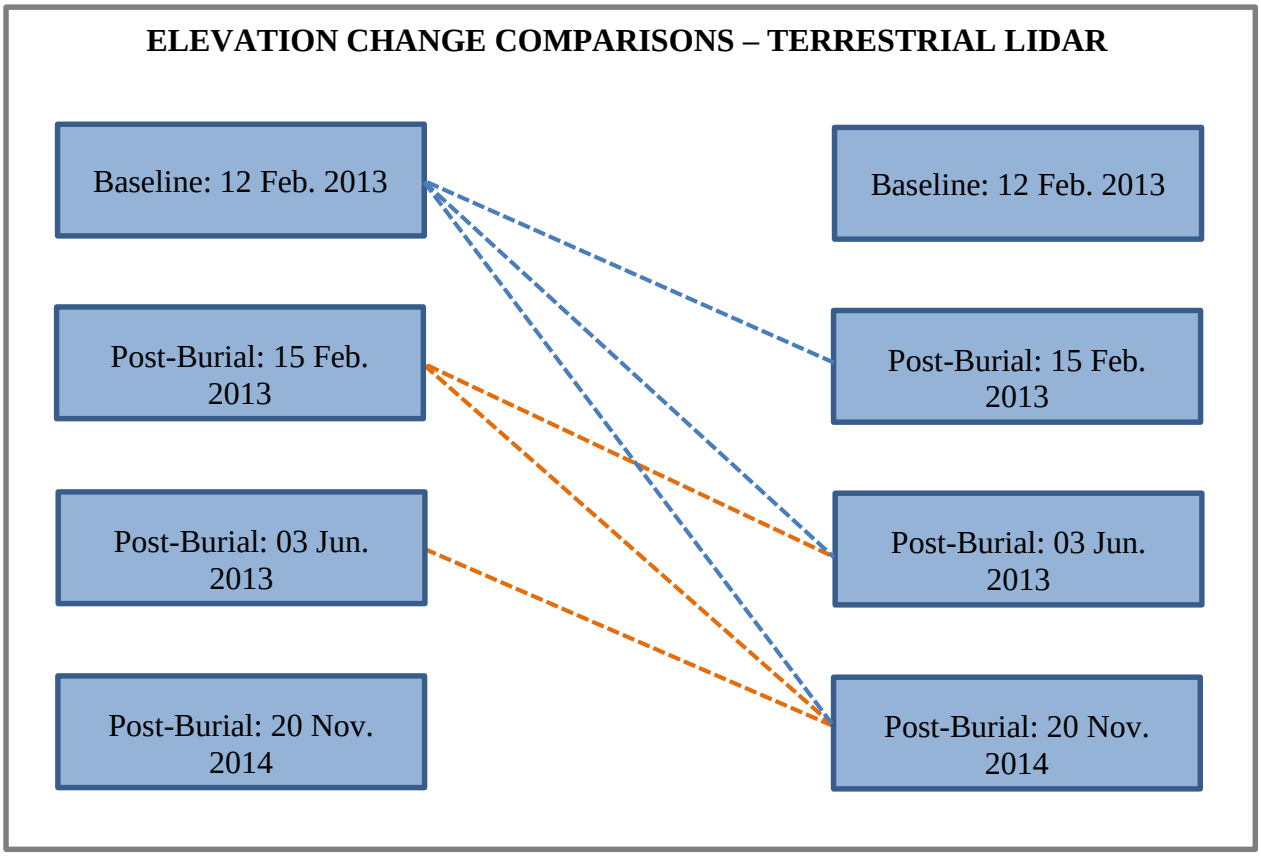

Figure 5.5-4: Elevation change comparisons, terrestrial data set pairings; blue comparisons make a baseline data availability assumption, orange comparisons do not.

present at burial surfaces are unique to those specific locations and are not the result of uniform site processes.

The 15 February 2013 elevation data set analysis focuses on the control unit and the single and triple graves. At the time the scans were taken, the grave containing six-bodies had not been completely backfilled.

5.6 Airborne LIDAR

While the analytical emphasis of this dissertation is on terrestrial data sets, this section discusses the methodology used to collect, process, and analyze airborne LIDAR data. Airborne LIDAR data are used to address Objective 3, which is to evaluate the potential scalability of terrestrial findings in airborne data.

If the terrestrial LIDAR dataset establishes that burial surfaces undergo spatially clustered elevation changes that are observable at the ground surface at different times, then airborne LIDAR can be used to help determine whether those elevation change patterns are also observable using more remote sensors. The geometry of airborne LIDAR is inherently different from that of terrestrial LIDAR because the airborne sensor is positioned overhead for perpendicular viewing from a mobile platform, rather than panoramic viewing from a stationary platform. However, like the terrestrial LIDAR approach, multiple scans can help densify an airborne LIDAR point cloud. Since LIDAR pulses can pass between gaps in dense tree canopy, attempts were made to accumulate a dense ground point cloud across the entire study area to observe the clustered elevation change patterns, if observed, in terrestrial LIDAR.

5.6.1 Airborne LIDAR Data Collection and Processing

The airborne LIDAR data set includes four data collections (**Table 5.6-1**). The first collection was made by the Johns Hopkins University Applied Physics Laboratory (JHUAPL). The remaining three collections were made by NASA Goddard Space Flight Center (GSFC) Goddard's LIDAR Hyperspectral and Thermal Imager (G-LiHT) system to specifically accommodate this research. JHUAPL's survey used an Optech Gemini (Teledyne Optech) laser scanner and GSFC used an Riegl VQ-480i (Riegl USA) laser scanner. Instruments are mounted to the underside of a piloted aircraft, and record three-dimensional points by rapidly scanning laterally as the aircraft passes overhead. The Optech Gemini, operated by JHUAPL, is a scanner with reported accuracy of ± 5 – 35 cm, depending on operating parameters. Dual beam divergence is 0.25 mrad (1/e) or 0.8 mrad (1/e). The Riegl VQ-480i is a scanner with reported accuracy of ± 20 mm at 150 m range. Beam divergence is 0.3 mrad ($1/e^2$).

The airborne LIDAR data analysis is limited to points contained within the study area fence, within which, points range from ground surface to canopy. The difference in tree canopy density at the time of each airborne collection is the primary driver of ground point density. For

Table 5.6-1: Sample sizes for aerial LIDAR data collections; based on a study area of 3493 m^2.

Collection Date	# Points, Limited to Fence Line/ <1m AGL	# 'Ground' Points	# Ground Points per m^2
18 September	971,349	172,352	49.34
23 March 2015	437,753	227,631	65.17
17 April 2015	661,258	132,405	37.91
07 May 2015	358,257	64,744	18.54

instance, the March 2015 collection contains the most ground points because canopy is at its lowest density, so more pulses could pass through to the ground surface. By contrast, April and May 2015 collections contain the least ground points because canopy is at its highest density, and fewer pulses could pass through to the ground surface. The airborne LIDAR data sets include empty data patches at the ground surface throughout the study area for the September 2014 and April and May 2015 collections. Despite making eight overhead passes from eight directions, there are few ground points – in some cases, zero – at the burial surfaces for the April and May collections, which means comparisons between full canopy collections and the minimal canopy March 2015 collection are effectively made between interpolated and actual elevation data.

5.6.1.1 Point Cloud Alignment and Filtering

Airborne LIDAR data were subjected to the same alignment process described for terrestrial LIDAR, using CloudCompare (**Figure 5.5-1**). The iterative point filtering process is the same as that used for terrestrial LIDAR, where a ground surface is approximated using the full cloud with QT Modeler (Applied Imagery, Inc.) and points above a statistically-defined height above that surface are removed using QT Modeler (**Figure 5.5-2**).

5.6.2 Airborne LIDAR Data Visualization

The study area is presented as images in two forms: 1) as elevations measurements at each of four collection dates, and 2) as elevation changes over time (**Figure 5.6-1**), where each of the absolute elevation images are subtracted from each other to reveal net changes between each collection date. Due to the low density of ground points at the burial surfaces in three of the four airborne LIDAR collections, neither Sky-View Factor nor density slices were used to visualize them, as those surfaces include interpolated, rather than actual, elevation values.

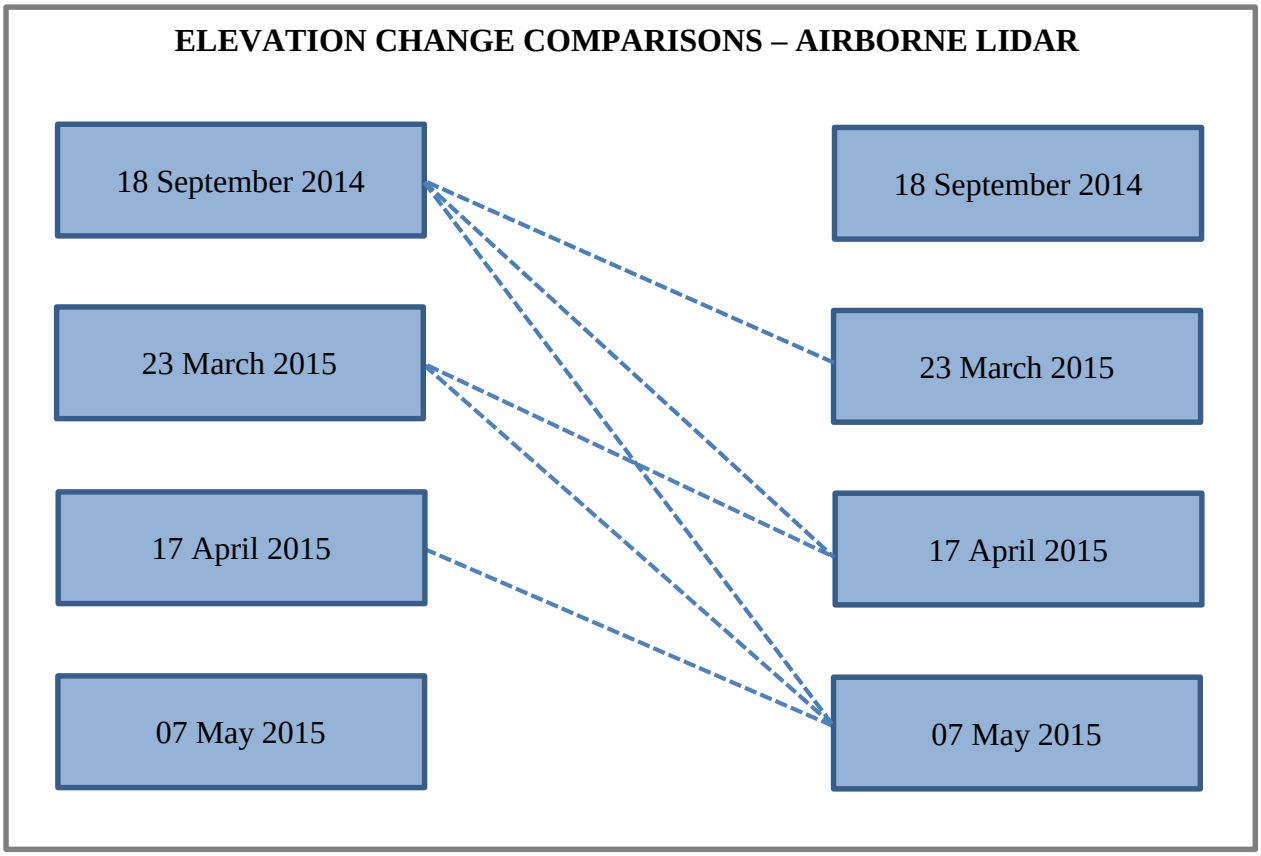

Figure 5.6-1: Elevation change comparisons, airborne data set pairings.

CHAPTER 6: RESULTS

This chapter presents the results of all five remote sensing data sets analyses described in Chapter 5. Analytical emphasis is on the terrestrial spectra and terrestrial LIDAR data, which are used to establish vegetation reflectance spectral signatures and ground elevation change activity patterns.

Results for terrestrial spectral analysis include support for separating vegetation groups into categorical dependent variables using the Spectral Angle Mapper (SAM) and the Spectral Information Divergence (SID) tools in ENVI. SAM and SID results presented in this chapter are limited to combined human burial spectra (all three burials), combined disturbance spectra (all human burials and the control unit), and undisturbed spectra. Detailed SAM and SID results, including those of individual burials and the control, are presented in **Appendix A**. Results for statistical analysis of categorical dependent variables include models developed using binary logistic regression (BLR) and discriminant function analysis (DFA). Detailed statistical model development results are presented in **Appendix B**. Results also include a post hoc analysis of wavelength variables using partial least squares regression (PLS) to confirm variable inclusion in validated BLR and DFA models. Partial Least Squares results between additional pair comparisons that do not correspond with validated BLR or DFA model are presented in **Appendix C**.

The results of terrestrial spectral analyses are applied to airborne hyperspectral imagery (HSI), as were seven vegetation indices. One vegetation index was applied to satellite multispectral imagery (MSI). Each result is presented in this chapter using color ramping. Detailed vegetation indices and their calculations are presented in **Appendix D**.

Terrestrial LIDAR results include absolute ground elevation images and elevation change images. Absolute elevation images are presented using traditional color ramping of elevation values and of Sky-View Factor results. Sky-View Factor is a tool that measures the percentage of sky that is visible from each pixel in a user-defined radius. Elevation change images are presented using traditional color ramping of elevation values and of Sky-View Factor results. Mean elevation changes for each burial and control are presented in **Appendix E**, which establish ranges for density slicing, a feature enhancement tool in ENVI that is used in this research to highlight image pixels that fall within a user-defined range to emphasize spatial clustering of specific values.

All terrestrial LIDAR images are presented at 5 cm GSD. Data resolutions of terrestrial LIDAR images ranging from 10 – 50 cm GSD are presented in **Appendix F**. All airborne LIDAR elevation images presented are 10 cm GSD. Results presented in this chapter are interpreted and discussed in Chapter 7.

6.1 Terrestrial Spectra

6.1.1 Spectral Angle Mapper and Spectral Information Divergence

Spectra were analyzed in ENVI using the Spectral Angle Mapper (SAM) tool and the Spectral Information Divergence (SID) tool to support the validity of separating vegetation groups into discrete categories for statistical analysis. For SAM and SID, *individual* vegetation reflectance spectral profiles from a) human burials and b) general disturbance (burials and control) were compared to the *mean* undisturbed vegetation spectrum. Separate comparisons were made for Spring and Autumn data sets, and each comparison was made by its full spectrum (400 – 2500) and as spectral regions: blue (400 – 500 nm), green (500 – 600), red (600 – 750 nm), near infrared (750 – 1330 nm), and shortwave infrared (1440 – 1800, 1990 – 2500 nm). The results of those

comparisons are presented in **Figures 6.1-1 – 6.1-12**. Individual bars in each figure represent the results of those comparisons; four total, one set of results for each season.

While the SAM and SID comparisons (each bar) are intended to be interpreted independently to support sorting the dependent variable into discrete categories, additional patterns are observable in comparisons between bars. For **Figures 6.1-1 – 6.1-12**, *within* and *between* seasonal comparisons of each set of four bars offers a cursory assessment of the spectral differences between burial and general disturbed vegetation (within seasons), as well as the potential effects of seasonality or burial age (between seasons). However, any apparent differences between SAM and SID results do not necessarily indicate a causal relationship between features or age/season and spectral difference.

SAM results for Burial and Undisturbed Spring vegetation spectra include an overall difference of 0.0965 radians across the full spectrum (**Figure 6.1-1**), with regional differences ranging from 0.0396 radians in the near infrared region (**Figure 6.1-5**) to 0.0885 radians in the red region (**Figure 6.1-4**). Results for Disturbed and Undisturbed Spring vegetation spectra include an overall difference of 0.0893 radians across the full spectrum (**Figure 6.1-1**), with regional differences ranging from 0.0356 radians in the near infrared region (**Figure 6.1-5**) to 0.0880 radians in the red region (**Figure 6.1-4**). Results for Burial and Undisturbed Autumn vegetation spectra include an overall difference of 0.0914 radians across the full spectrum (**Figure 6.1-1**), with regional differences ranging from 0.0228 radians in the near infrared region (**Figure 6.1-5**) to 0.1245 radians in the shortwave infrared region (**Figure 6.1-6**). Results for Disturbed and Undisturbed Autumn vegetation spectra include an overall difference of 0.0934 radians across the full spectrum (**Figure 6.1-1**), with regional differences ranging from 0.0241 radians in the near infrared region (**Figure 6.1-5**) to 0.1250 radians in the shortwave infrared region (**Figure 6.1-6**).

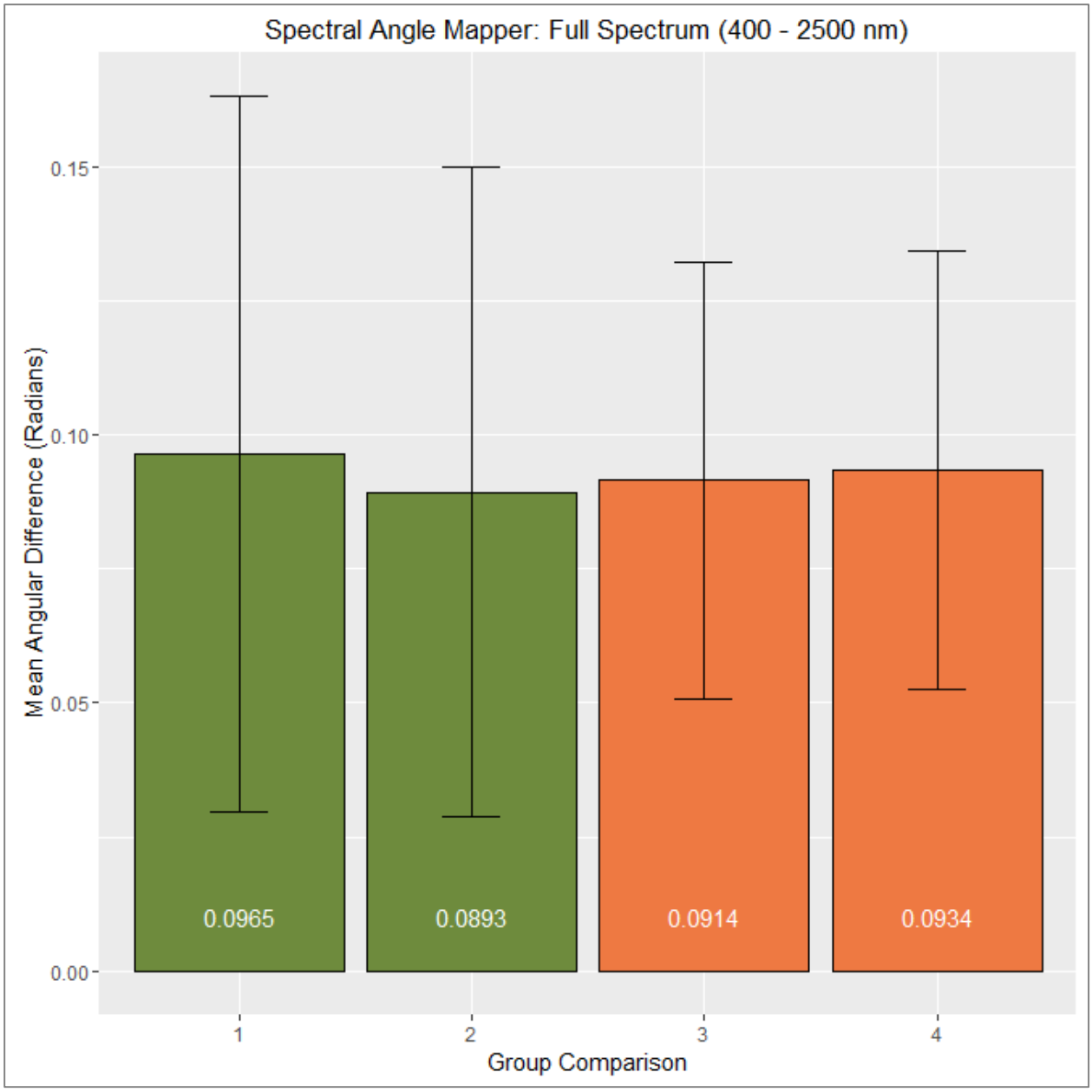

Figure 6.1-1: SAM results of full spectrum comparisons between 1) Burial vs. Undisturbed vegetation, Spring, n=137; 2) Disturbed vs. Undisturbed vegetation, Spring, n=154; 3) Burial vs. Undisturbed vegetation, Autumn, n=128; and 4) Disturbed vs. Undisturbed vegetation, Autumn, n=133. Larger values indicate greater spectral difference between vegetation groups in each comparison. The conventional arbitrary discrete classification threshold for SAM is 0.10.

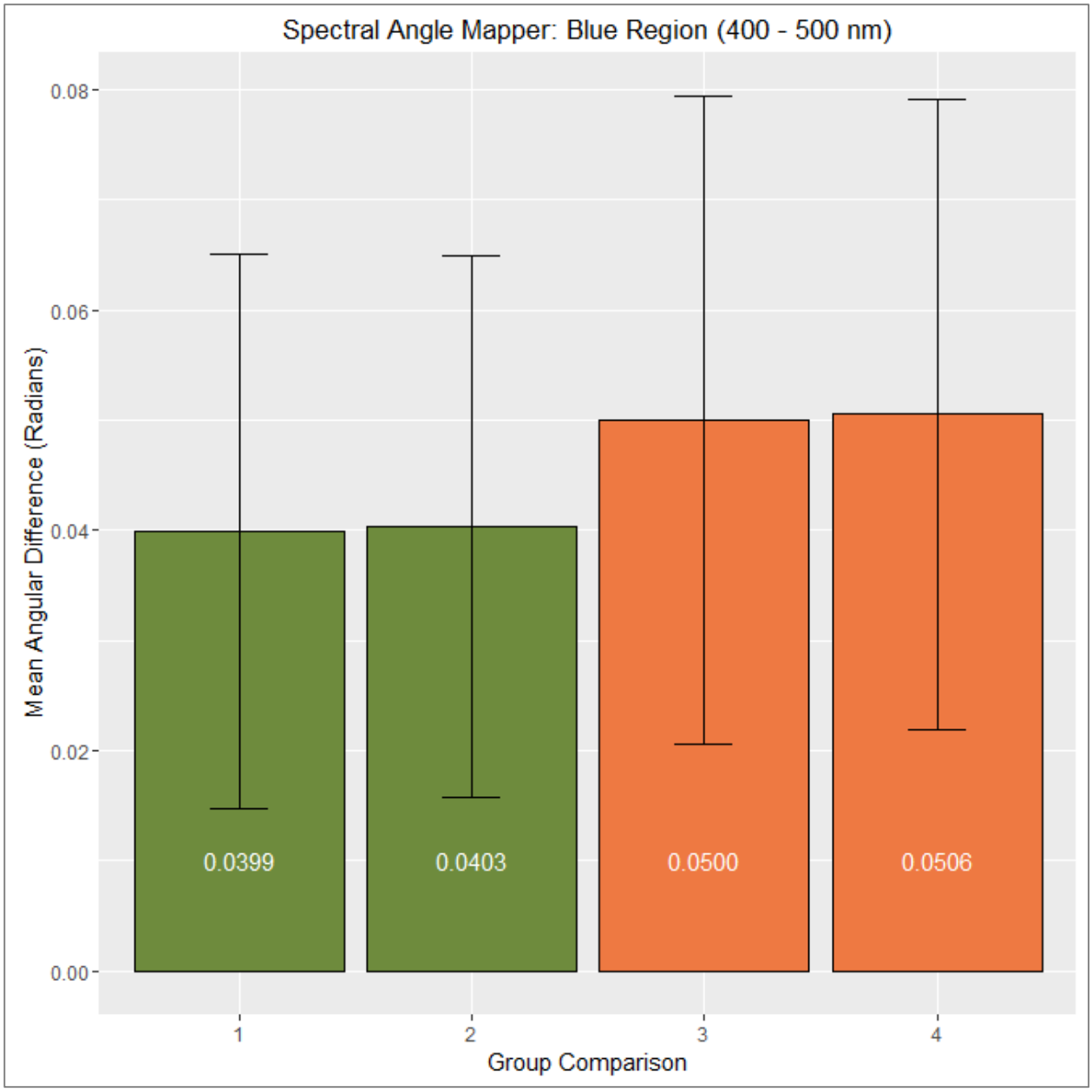

Figure 6.1-2: SAM results of blue region comparisons between 1) Burial vs. Undisturbed vegetation, Spring, n=137; 2) Disturbed vs. Undisturbed vegetation, Spring, n=154; 3) Burial vs. Undisturbed vegetation, Autumn, n=128; and 4) Disturbed vs. Undisturbed vegetation, Autumn, n=133. Larger values indicate greater spectral difference between vegetation groups used in each comparison. These results demonstrate a greater mean spectral difference in the blue region between Autumn samples (3 and 4) than Spring samples (1 and 2). The conventional arbitrary discrete classification threshold for SAM is 0.10.

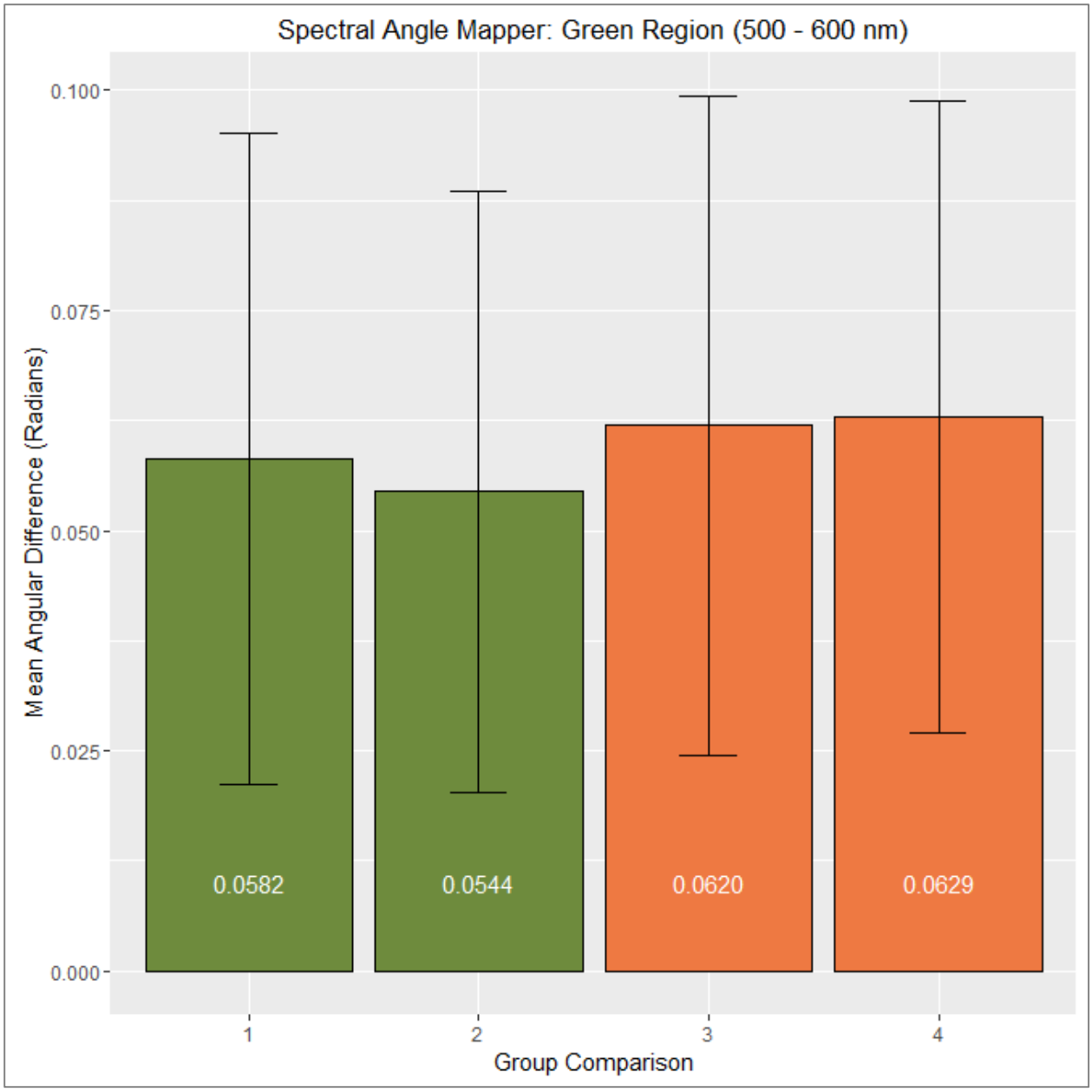

Figure 6.1-3: SAM results of green region comparisons between 1) Burial vs. Undisturbed vegetation, Spring, n=137; 2) Disturbed vs. Undisturbed vegetation, Spring, n=154; 3) Burial vs. Undisturbed vegetation, Autumn, n=128; and 4) Disturbed vs. Undisturbed vegetation, Autumn, n=133. Larger values indicate greater spectral difference between vegetation groups used in each comparison. These results demonstrate a greater mean spectral difference in the green region between Autumn samples (3 and 4) than Spring samples (1 and 2). The conventional arbitrary discrete classification threshold for SAM is 0.10.

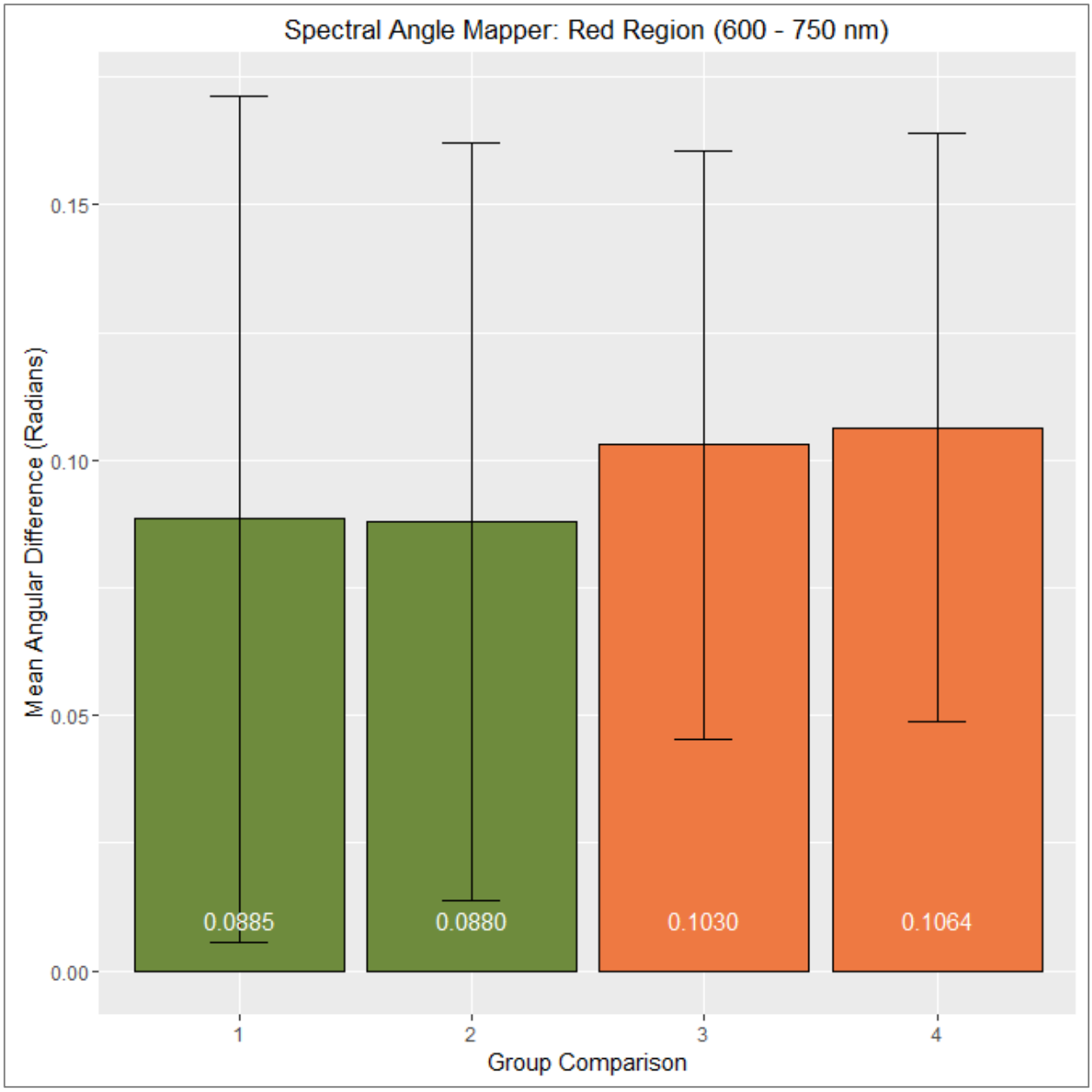

Figure 6.1-4: SAM results of red region comparisons between 1) Burial vs. Undisturbed vegetation, Spring, n=137; 2) Disturbed vs. Undisturbed vegetation, Spring, n=154; 3) Burial vs. Undisturbed vegetation, Autumn, n=128; and 4) Disturbed vs. Undisturbed vegetation, Autumn, n=133. Larger values indicate greater spectral difference between vegetation groups used in each comparison. These results demonstrate a greater mean spectral difference in the red region between Autumn samples (3 and 4) than Spring samples (1 and 2). The conventional arbitrary discrete classification threshold for SAM is 0.10.

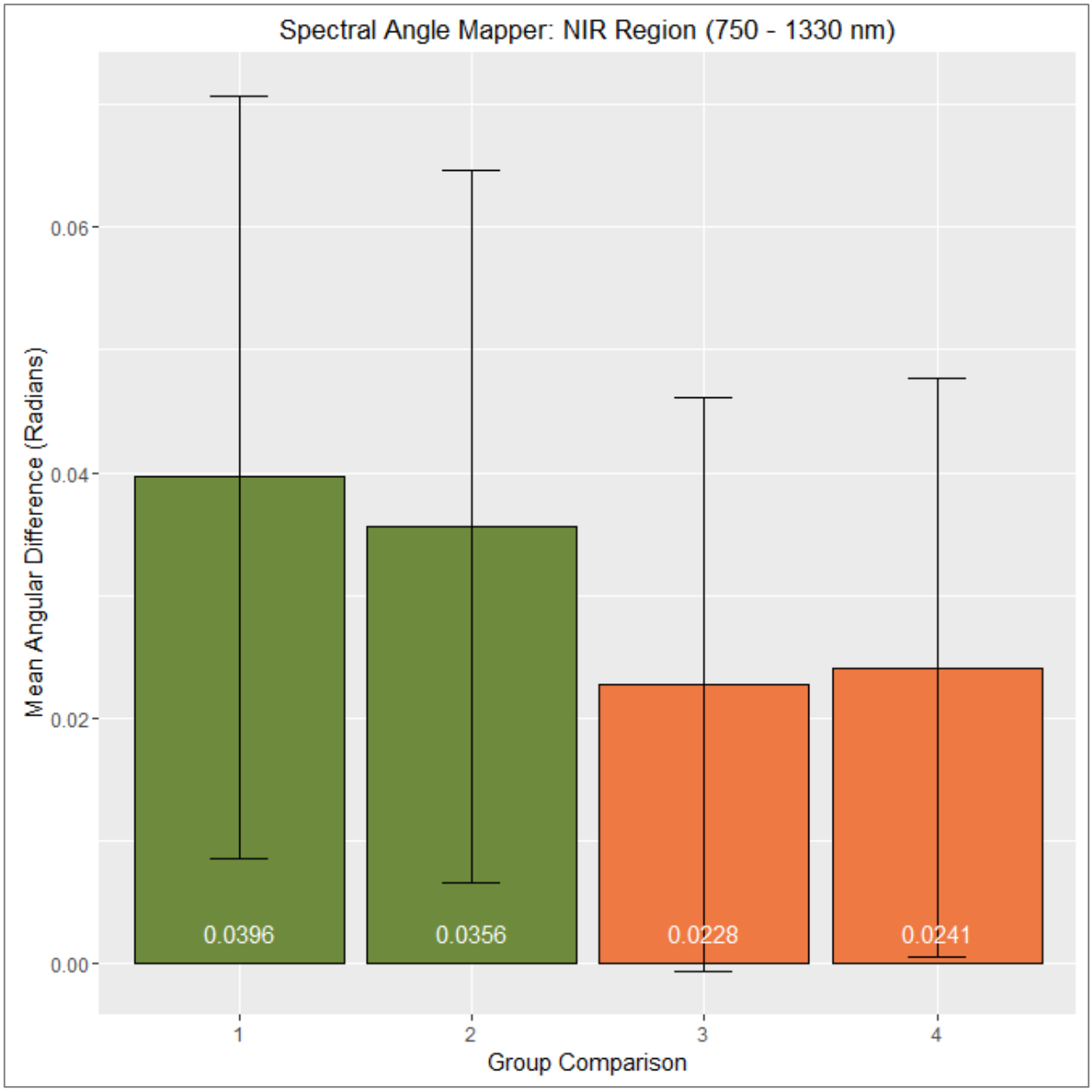

Figure 6.1-5: SAM results of near infrared region comparisons between 1) Burial vs. Undisturbed vegetation, Spring, n=137; 2) Disturbed vs. Undisturbed vegetation, Spring, n=154; 3) Burial vs. Undisturbed vegetation, Autumn, n=128; and 4) Disturbed vs. Undisturbed vegetation, Autumn, n=133. Larger values indicate greater spectral difference between vegetation groups used in each comparison. These results demonstrate a greater mean spectral difference in the near infrared region between Spring samples (1 and 2) than Autumn samples (3 and 4). The conventional arbitrary discrete classification threshold for SAM is 0.10.

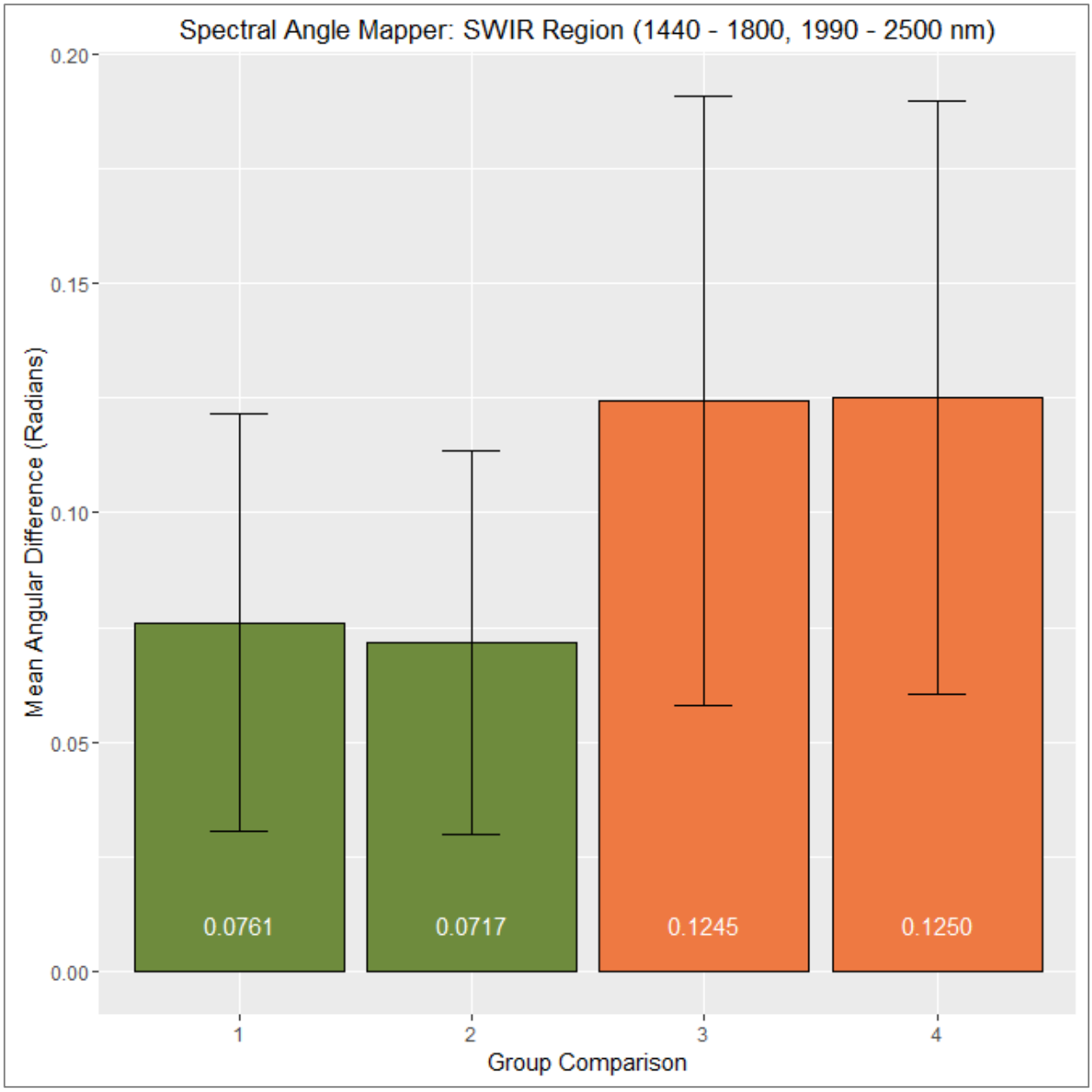

Figure 6.1-6: SAM results of shortwave infrared region comparisons between 1) Burial vs. Undisturbed vegetation, Spring, n=137; 2) Disturbed vs. Undisturbed vegetation, Spring, n=154; 3) Burial vs. Undisturbed vegetation, Autumn, n=128; and 4) Disturbed vs. Undisturbed vegetation, Autumn, n=133. Larger values indicate greater spectral difference between vegetation groups used in each comparison. These results demonstrate a greater mean spectral difference in the shortwave infrared region between Autumn samples (3 and 4) than Spring samples (1 and 2). The conventional arbitrary discrete classification threshold for SAM is 0.10.

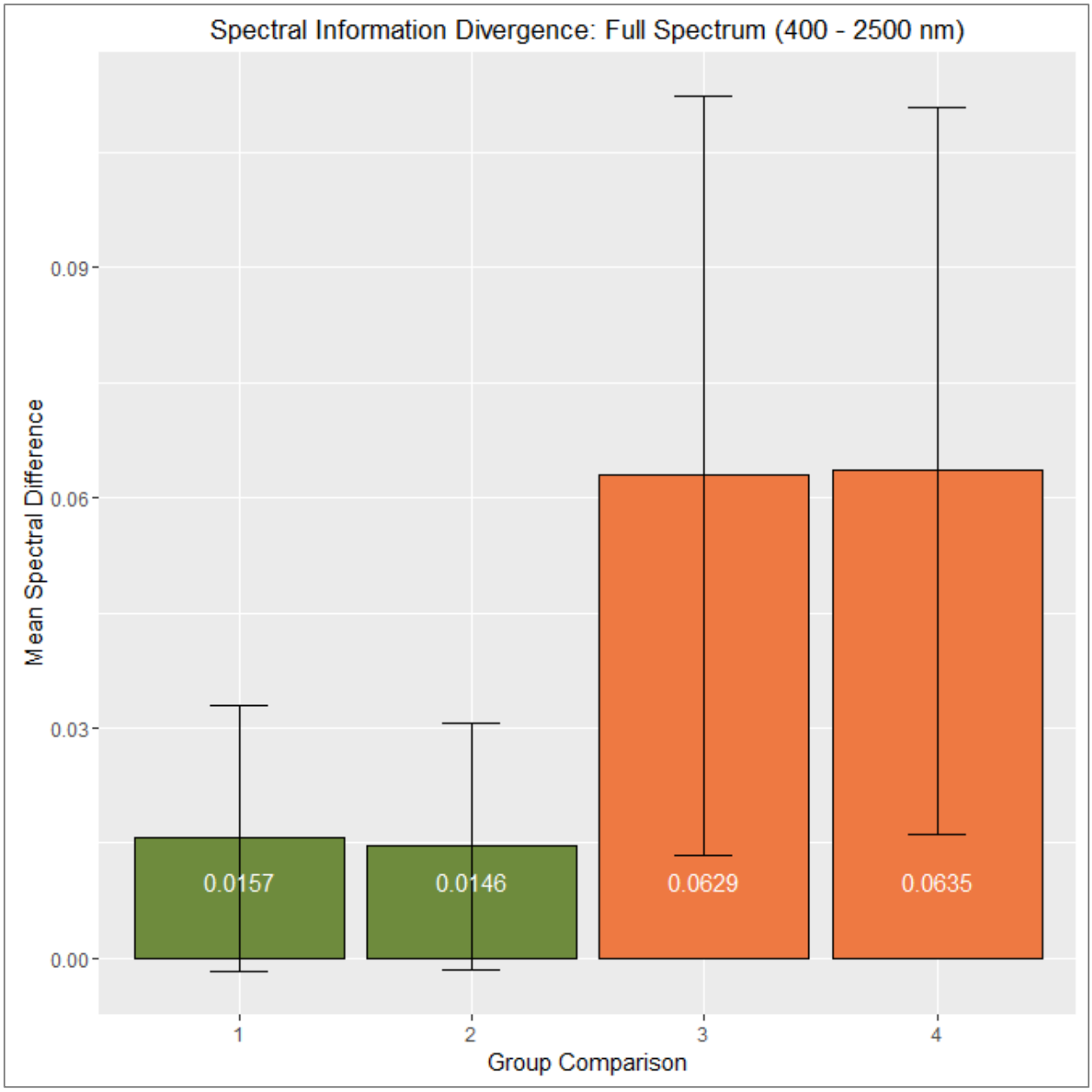

Figure 6.1-7: SID results of full spectrum comparisons between 1) Burial vs. Undisturbed vegetation, Spring, n=137; 2) Disturbed vs. Undisturbed vegetation, Spring, n=154; 3) Burial vs. Undisturbed vegetation, Autumn, n=128; and 4) Disturbed vs. Undisturbed vegetation, Autumn, n=133. Larger values indicate greater spectral difference between vegetation groups used in each comparison. These results demonstrate a greater mean spectral difference across the full spectrum between Autumn samples (3 and 4) than Spring samples (1 and 2). The conventional arbitrary discrete classification threshold for SID is 0.05.

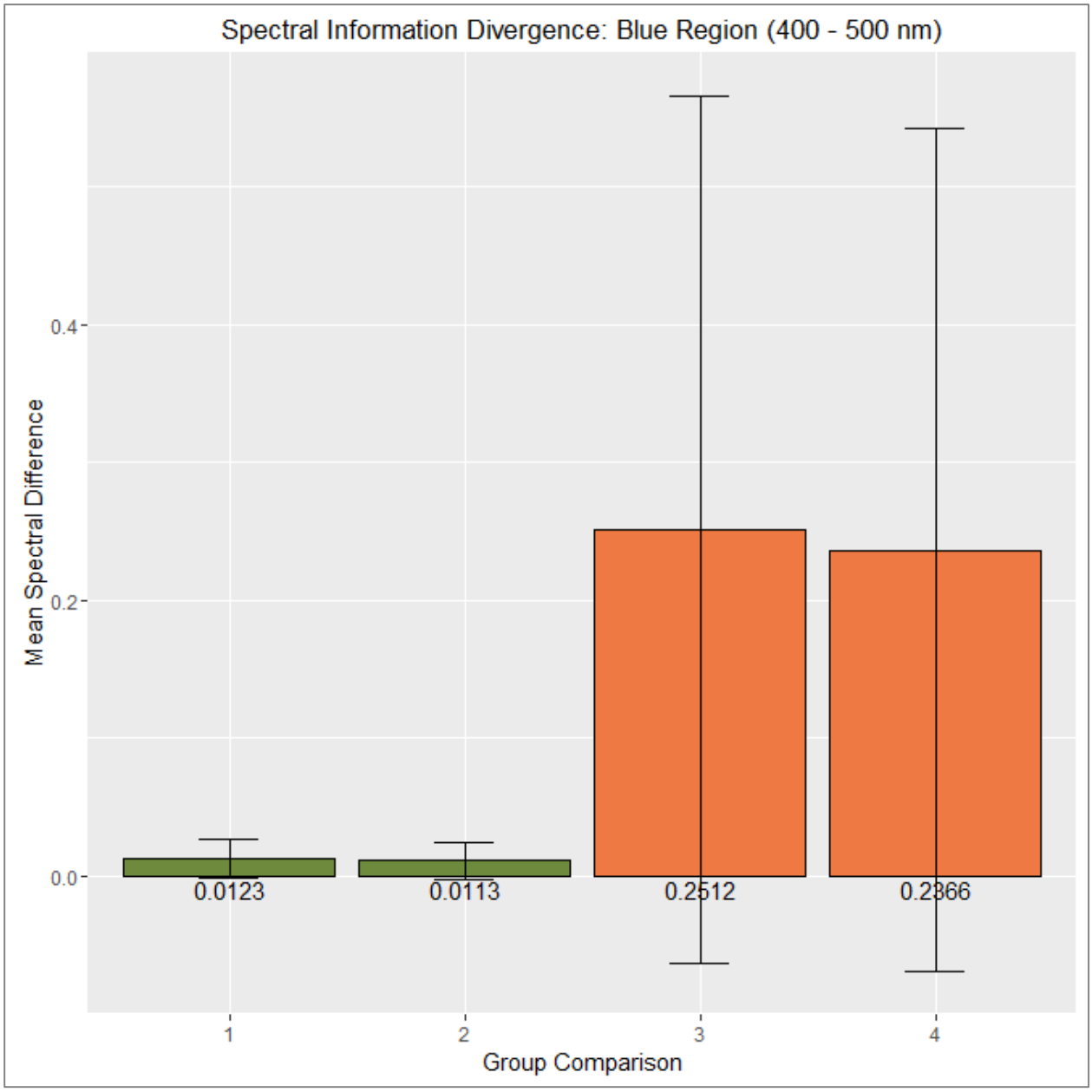

Figure 6.1-8: SID results of blue region comparisons between 1) Burial vs. Undisturbed vegetation, Spring, n=137; 2) Disturbed vs. Undisturbed vegetation, Spring, n=154; 3) Burial vs. Undisturbed vegetation, Autumn, n=128; and 4) Disturbed vs. Undisturbed vegetation, Autumn, n=133. Larger values indicate greater spectral difference between vegetation groups used in each comparison. These results demonstrate a greater mean spectral difference in the blue region between Autumn samples (3 and 4) than Spring samples (1 and 2). The conventional arbitrary discrete classification threshold for SID is 0.05.

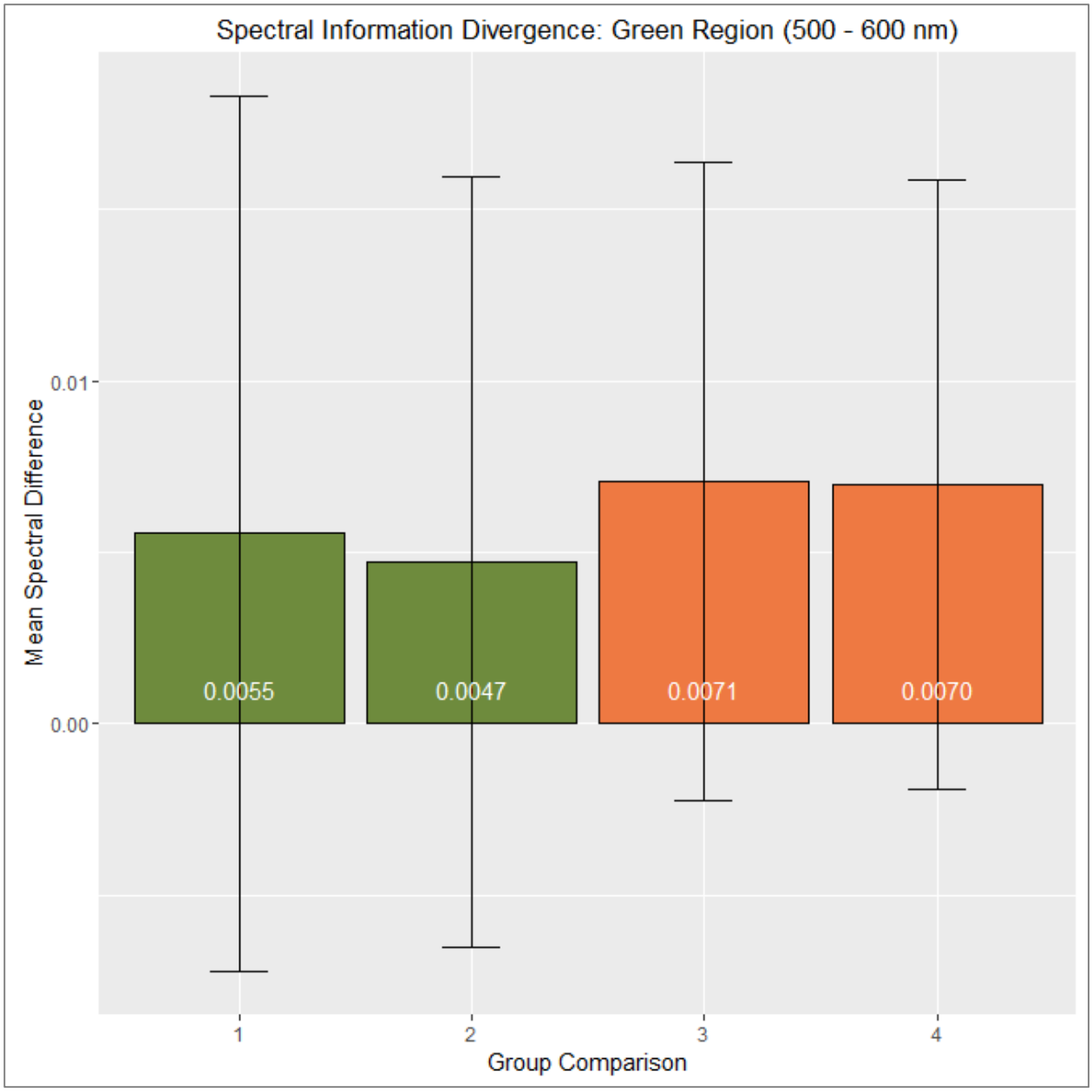

Figure 6.1-9: SID results of green region comparisons between 1) Burial vs. Undisturbed vegetation, Spring, n=137; 2) Disturbed vs. Undisturbed vegetation, Spring, n=154; 3) Burial vs. Undisturbed vegetation, Autumn, n=128; and 4) Disturbed vs. Undisturbed vegetation, Autumn, n=133. Larger values indicate greater spectral difference between vegetation groups used in each comparison. These results demonstrate a greater mean spectral difference in the green region between Autumn samples (3 and 4) than Spring samples (1 and 2). The conventional arbitrary discrete classification threshold for SID is 0.05.

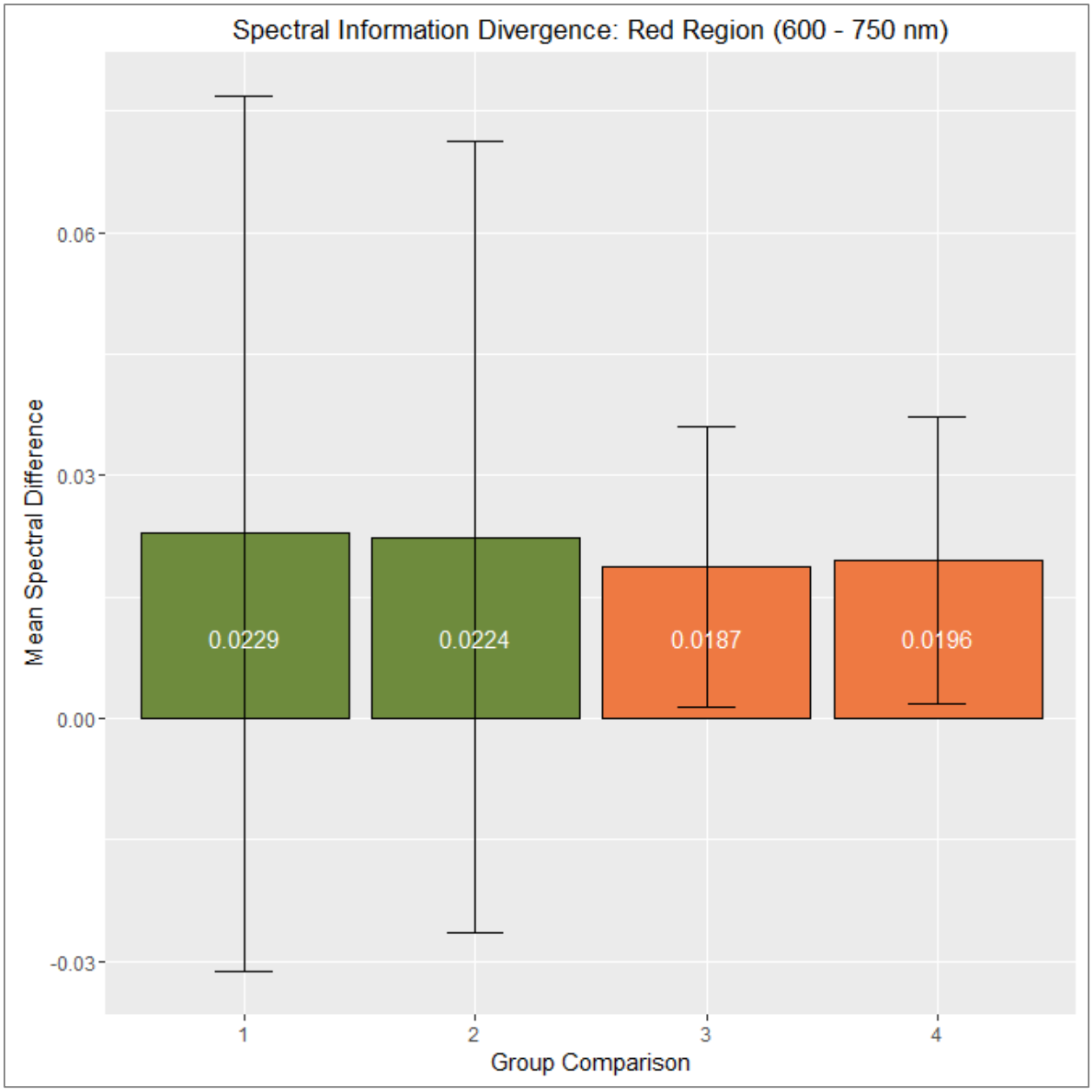

Figure 6.1-10: SID results of red region comparisons between 1) Burial vs. Undisturbed vegetation, Spring, n=137; 2) Disturbed vs. Undisturbed vegetation, Spring, n=154; 3) Burial vs. Undisturbed vegetation, Autumn, n=128; and 4) Disturbed vs. Undisturbed vegetation, Autumn, n=133. Larger values indicate greater spectral difference between vegetation groups used in each comparison. These results demonstrate a greater mean spectral difference in the red region between Spring samples (1 and 2) than Autumn samples (3 and 4). The conventional arbitrary discrete classification threshold for SID is 0.05.

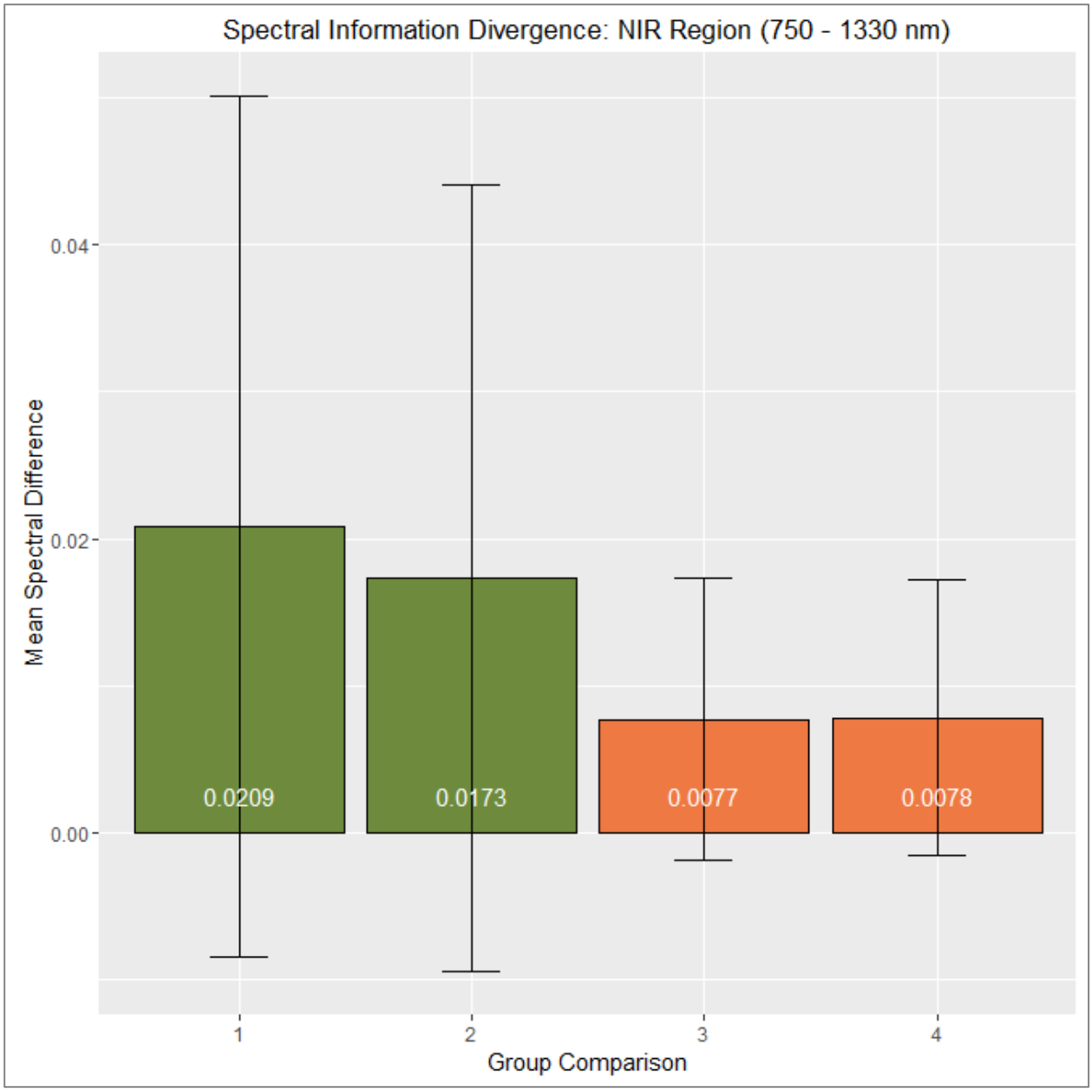

Figure 6.1-11: SID results of near infrared region comparisons between 1) Burial vs. Undisturbed vegetation, Spring, n=137; 2) Disturbed vs. Undisturbed vegetation, Spring, n=154; 3) Burial vs. Undisturbed vegetation, Autumn, n=128; and 4) Disturbed vs. Undisturbed vegetation, Autumn, n=133. Larger values indicate greater spectral difference between vegetation groups used in each comparison. These results demonstrate a greater mean spectral difference in the near infrared region between Spring samples (1 and 2) than Autumn samples (3 and 4). The conventional arbitrary discrete classification threshold for SID is 0.05.

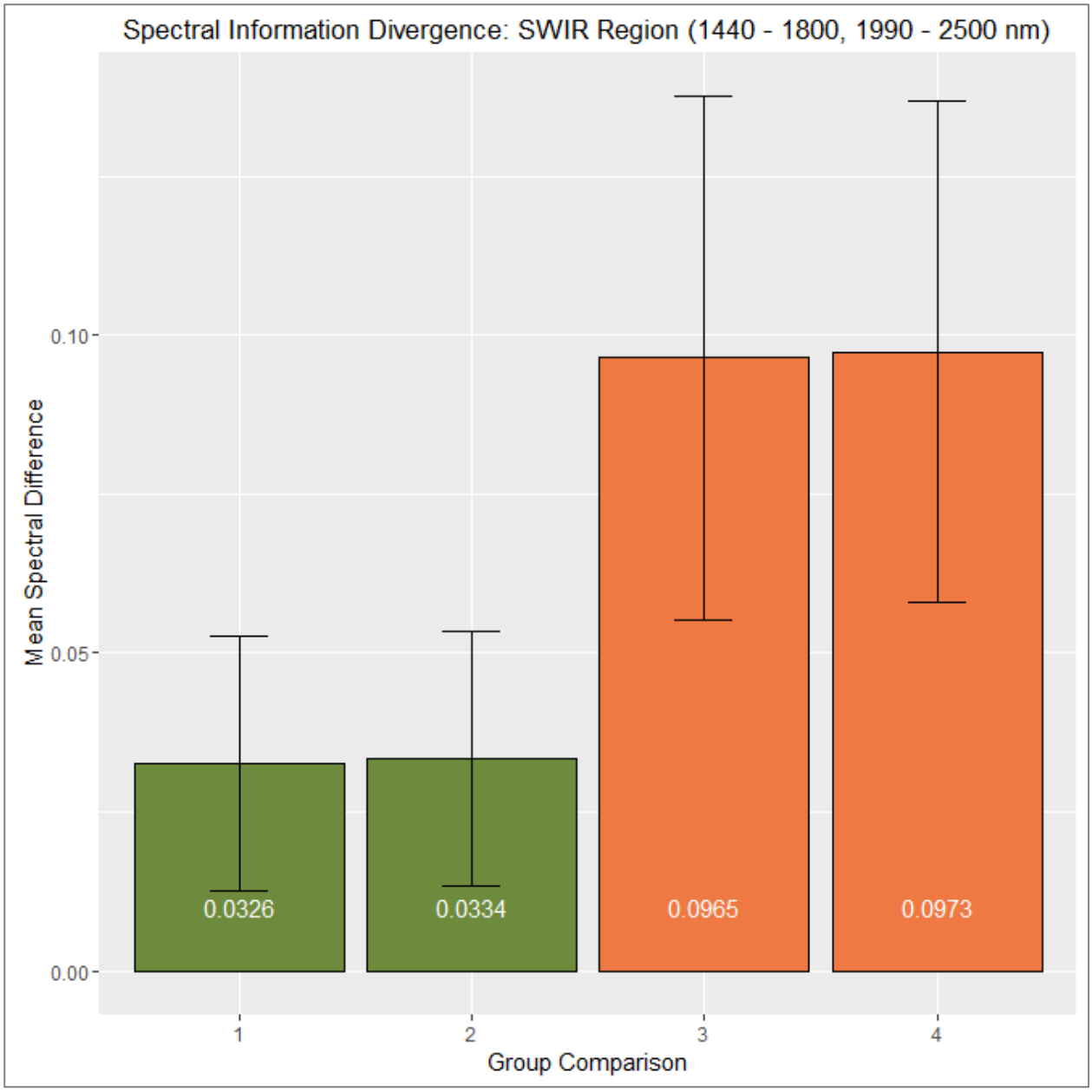

Figure 6.1-12: SID results of shortwave infrared region comparisons between 1) Burial vs. Undisturbed vegetation, Spring, n=137; 2) Disturbed vs. Undisturbed vegetation, Spring, n=154; 3) Burial vs. Undisturbed vegetation, Autumn, n=128; and 4) Disturbed vs. Undisturbed vegetation, Autumn, n=133. Larger values indicate greater spectral difference between vegetation groups used in each comparison. These results demonstrate a greater mean spectral difference in the shortwave infrared region between Autumn samples (3 and 4) than Spring samples (1 and 2). The conventional arbitrary discrete classification threshold for SID is 0.05.

The near infrared region is the least different across all four SAM comparisons (**Figure 6.1-5**), while the red region is the most different for both Spring comparisons (**Figure 6.1-4**) and the shortwave infrared region is the most different for both Autumn comparisons (**Figure 6.1-6**).

SID results for Burial and Undisturbed Spring vegetation spectra include an overall difference of 0.0157 across the full spectrum (**Figure 6.1-7**), with regional differences ranging from 0.0055 in the green region (**Figure 6.1-9**) to 0.0326 in the shortwave infrared region (**Figure 6.1-12**). Results for Disturbed and Undisturbed Spring vegetation spectra include an overall difference of 0.0146 across the full spectrum (**Figure 6.1-7**), with regional differences ranging from 0.0047 in the green region (**Figure 6.1-9**) to 0.0334 in the shortwave infrared region (**Figure 6.1-12**). Results for Burial and Undisturbed Autumn vegetation spectra include an overall difference of 0.0629 across the full spectrum (**Figure 6.1-7**), with regional differences ranging from 0.0071 in the green region (**Figure 6.1-9**) to 0.2512 in the blue region (**Figure 6.1-8**). Results for Disturbed and Undisturbed Autumn vegetation spectra include an overall difference of 0.0635 across the full spectrum (**Figure 6.1-7**), with regional differences ranging from 0.0070 in the green region (**Figure 6.1-9**) to 0.2366 in the blue region (**Figure 6.1-8**). The green region is the least different across all four SID comparisons (**Figure 6.1-9**), while the shortwave infrared region is the most different for both Spring comparisons (**Figure 6.1-12**) and the blue region is the most different for both Autumn comparisons (**Figure 6.1-8**).

When comparing *between* Spring and Autumn results, SAM results demonstrate overall similar separation of groups in vegetation spectra for the full spectrum comparison (**Figure 6.1-1**). Smaller regional SAM comparisons, however, reveal greater separability of Autumn data over Spring data, with the sole exception of the near infrared region that demonstrates greater separability in Spring data over Autumn data (**Figure 6.1-5**). SID comparisons between seasons

confirms the greater separability of Autumn data over Spring data in the full spectrum (**Figure 6.1-7**) and in most regional comparisons, with two exceptions being the red (**Figure 6.1-4**) and near infrared (**Figure 6.1-5**) regions where there is greater separability of Spring data over Autumn data.

When comparing *within* season results, SAM results reveal a small, but consistently greater spectral difference between burial and undisturbed vegetation over generally disturbed and undisturbed vegetation during the Spring season, with the only exception being the blue region (**Figure 6.1-2**). SAM results unanimously agree on a greater spectral difference between generally disturbed and undisturbed vegetation over burial and undisturbed vegetation during the Autumn season for the full spectrum (**Figure 6.1-1**) and for all spectral regions (**Figures 6.1-2 – 6.1-6**). Spring SID comparisons agree with SAM Spring results in that there is a consistently greater spectral difference between burial and undisturbed vegetation; a trend that is observed across the full spectrum (**Figure 6.1-7**) and for all spectral regions (**Figures 6.1-8 – 6.1-12**). SID comparisons within Autumn data reveal greater difference between generally disturbed and undisturbed vegetation over burial and undisturbed vegetation, with two exceptions being the blue (**Figure 6.1-8**) and green (**Figure 6.1-9**) regions of the spectrum.

Differences revealed through *within* seasonal comparisons are small, ranging from 0.0004 – 0.0072 radians for SAM Spring data, 0.0005 – 0.0034 radians for SAM Autumn data, 0.0005 – 0.0036 for SID Spring data, and 0.0001 – 0.0146 for SID Autumn data. The more remarkable trend appears to be separation of vegetation groups *between* seasons. Differences revealed in *between* seasonal comparisons of vegetation groups range from 0.0038 – 0.0484 radians for SAM Burial versus Undisturbed vegetation, 0.0041 – 0.0533 radians for SAM generally Disturbed versus

Undisturbed vegetation, 0.0016 – 0.2389 for SID Burial versus Undisturbed vegetation, and 0.0023 – 0.2253 for SID generally Disturbed versus Undisturbed vegetation.

The results (individual bars, as opposed to *within* or *between* seasonal results comparisons) provide quantitative support for separating spectral samples into discrete classification groups for statistical tests (logistic regression and discriminant function analysis) that require categorical dependent variables. The SAM and SID results support categorical separation as a statistical approach by revealing spectral regions with measurably greater differences (blue, red, and shortwave infrared), and by demonstrating the consistency of those regional spectral differences for vegetation groups and seasons.

6.1.2 Logistic Regression

Logistic regression was used to statistically evaluate the contribution of each wavelength to the separation of vegetation groups. Twelve possible logistic regression models were reduced to two models by following a prescribed training and validation workflow (**Figure 5.2-4**). The twelve possible models included two redundant models and one statistically unviable model that produced only a model constant with no wavelength variables, resulting in nine unique models. Models 2, 5, 6, 7, and 8 correctly classified the 70% training samples at greater than 50%, and were tested using a separate 30% validation sample comprised of new vegetation spectra not used for training the models.

Results derived from the validation process indicate that burial and generally disturbed vegetation spectra can be separated from undisturbed vegetation spectra during Autumn months using validated BLR models 2 and 6, which are both statistically significant ($p<0.001$). Both models include visible and shortwave infrared wavelengths. Overall correct classification

performance of logistic regression models 2 and 6 range from 67.5 – 71.1%, with individual group membership prediction success ranging from 52.9 – 78.3%. BLR models are better at predicting membership of undisturbed vegetation than either burial or generally disturbed vegetation in the validation sample, with a performance difference *within* each model ranging from 18.3 – 25.4 percentage points. Model progression is presented in **Figure 6.1-13**, model performance in **Table 6.1-1** and **Figure 6.1-14,** and models in **Tables 6.1-2** and **6.1-3**.

6.1.3 Discriminant Function Analysis

Twelve possible discriminant function models were reduced to five models by following the same prescribed training and validation workflow used to develop the logistic regression models (**Figure 5.2-4**). The twelve possible models included three redundant models, resulting in nine unique models. All nine models correctly classified the 70% training samples at greater than 50%, and were further tested using a separate 30% validation sample containing new vegetation spectra not used for training the models.

Results derived from the validation process indicate that burial and similar disturbance vegetation spectra can be separated from undisturbed vegetation spectra using any of the five validated DFA models. Four of the models are derived from Autumn data and one from Spring data. All five models are statistically significant ($p<0.001$). All five models include visible wavelengths, and of those models, three also include shortwave infrared wavelengths. Overall correct classification performance of discriminant function models 2, 3, 4, 6, and 9 ranges from 58.5 – 65.8%, with individual group membership prediction success ranging from 52.0 – 73.3%. Four of the five DFA models are better at predicting membership of burial or generally disturbed vegetation than undisturbed vegetation in the validation sample, with performance differences *within* those models ranging from 5.8 – 16.8 percentage points. Model progression is presented in

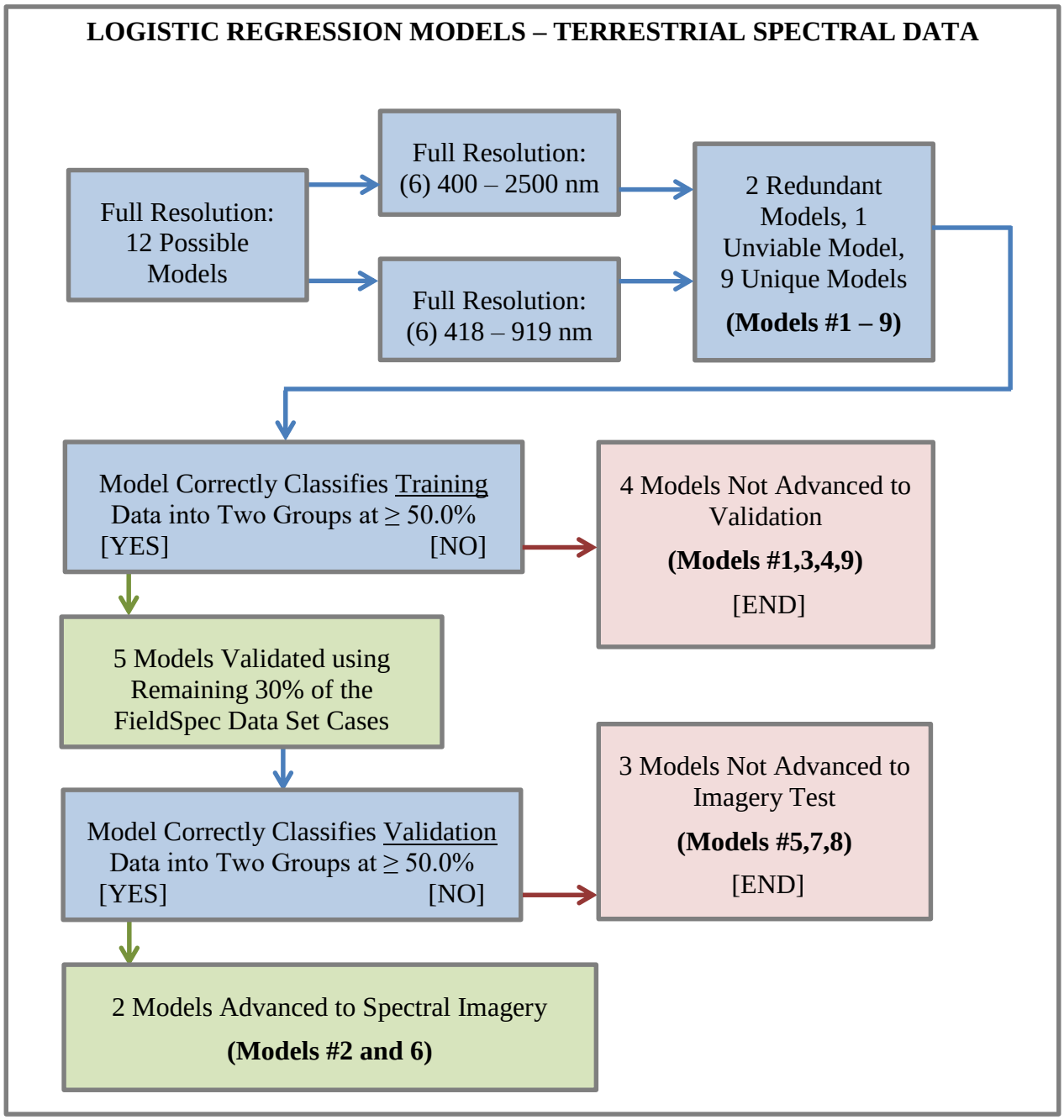

Figure 6.1-13: Logistic regression model workflow results; nine models reduced to two.

Table 6.1-1: BLR model validation performance summary; 30% validation data set; 'Disturbed' refers to combined Burial and Control samples.

BLR Model	Season	Known Group	n=	% Correct	% Overall Correct
2	Autumn	Burials	15	60.0	71.1
		Undisturbed	23	78.3	
6	Autumn	Disturbed	17	52.9	67.5
		Undisturbed	23	78.3	

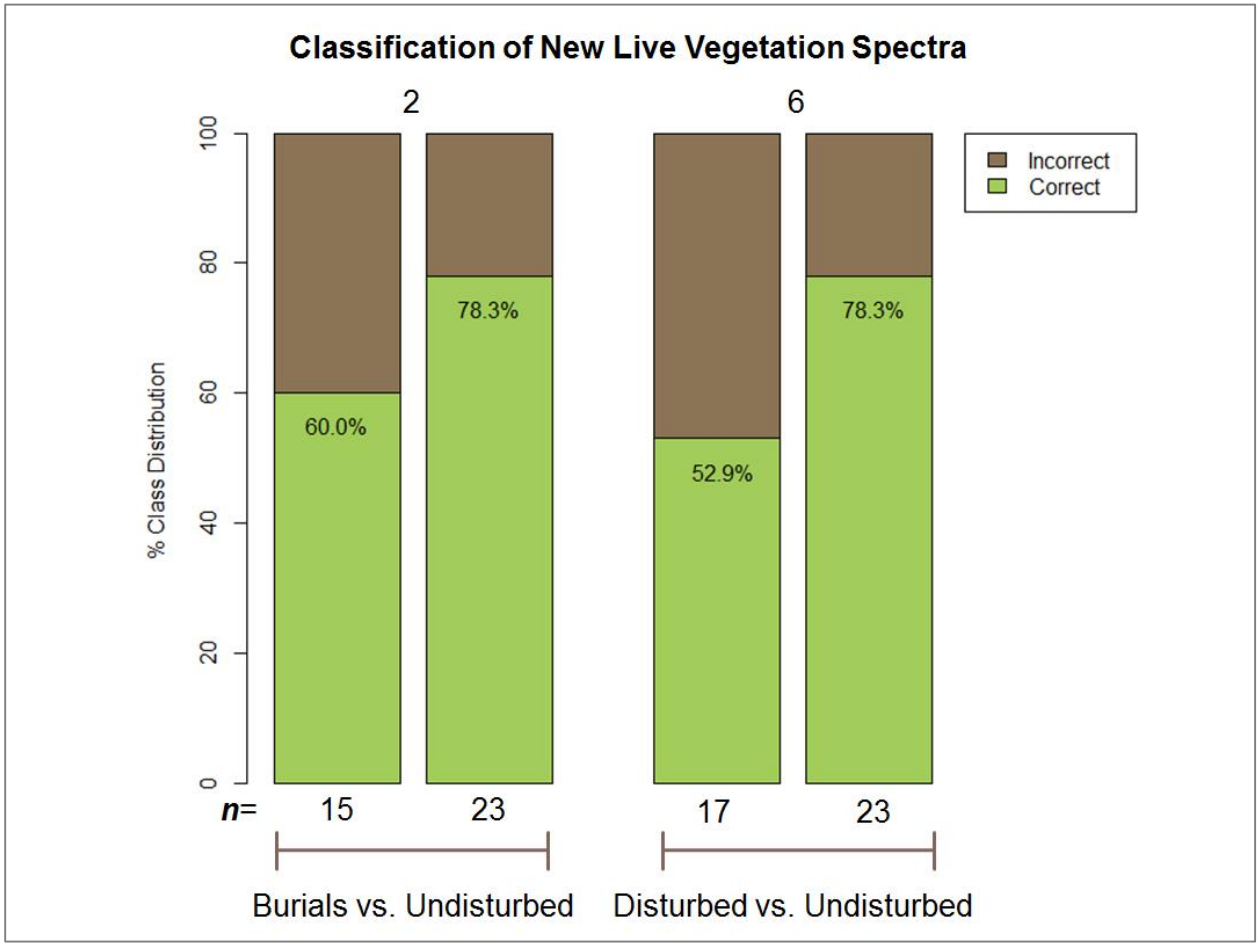

Figure 6.1-14: Graphical representation of BLR model performance presented in Table 6.1-1.

Table 6.1-2: Validated model wavelengths; all models correctly classify both validation data groups at ≥ 50.0%. Detailed BLR classification results presented in **Appendix B, Tables B.1 – B.27**.

BLR Model	**Wavelengths (nm)**
2: Burials/Undisturbed	$\lambda 1$ = 707 $\lambda 2$ = 2423
6: Disturbed/Undisturbed	$\lambda 1$ = 708 $\lambda 2$ = 1993

Table 6.1-3: Validated model coefficients.

BLR Model	**Coefficients**
2: Burials/Undisturbed	Constant = 3.027 $\alpha 1$ = -42.345 $\alpha 2$ = 37.510
6: Disturbed/Undisturbed	Constant = 2.591 $\alpha 1$ = -33.417 $\alpha 2$ = 36.306

Figure 6.1-15, model performance in **Table 6.1-4** and **Figure 6.1-16,** and models in **Tables 6.1-5** and **6.1-6**.

6.1.4 Partial Least Squares Regression

The PLS results highlight individual wavelengths and broad regions along the spectrum that contribute to separation of discrete live vegetation groups. Among first and second factor PLS results are wavelengths with corresponding peak Variable Importance (VIP) values and their surrounding important regions. These results support the presence of variables used in the logistic regression and discriminant function models (**Figures 6.1-17 – 6.1-28**).

First factor PLS results account for variance ranging from 83.4 – 89.0%, and emphasize the importance of the visible and near infrared wavelengths for correctly predicting group membership. All seven statistical models include a visible wavelength that falls within a ±5 nm range of a PLS first factor VIP peak, indicating agreement between the statistical models and PLS variable importance results. Five of the seven statistical models also include at least one shortwave infrared wavelength. None of the first factor PLS results that directly correspond with statistical models suggest shortwave infrared wavelengths are important for predicting group membership.

Second factor PLS results, which account for a smaller amount of variance in the data – but contributing to a cumulative variance percentage point increase ranging from 3.0 – 9.6 – do support the inclusion of shortwave infrared wavelengths. Second factors are also in agreement with all first factors with respect to the inclusion of the visible wavelengths. Second factor variable importance ranges support the inclusion of the majority of shortwave infrared wavelengths in models that include them, with the few exceptions of 2498 nm in DFA Model 2, 2448 and 2480 nm in DFA Model 3, and 2412 nm in DFA Model 6.

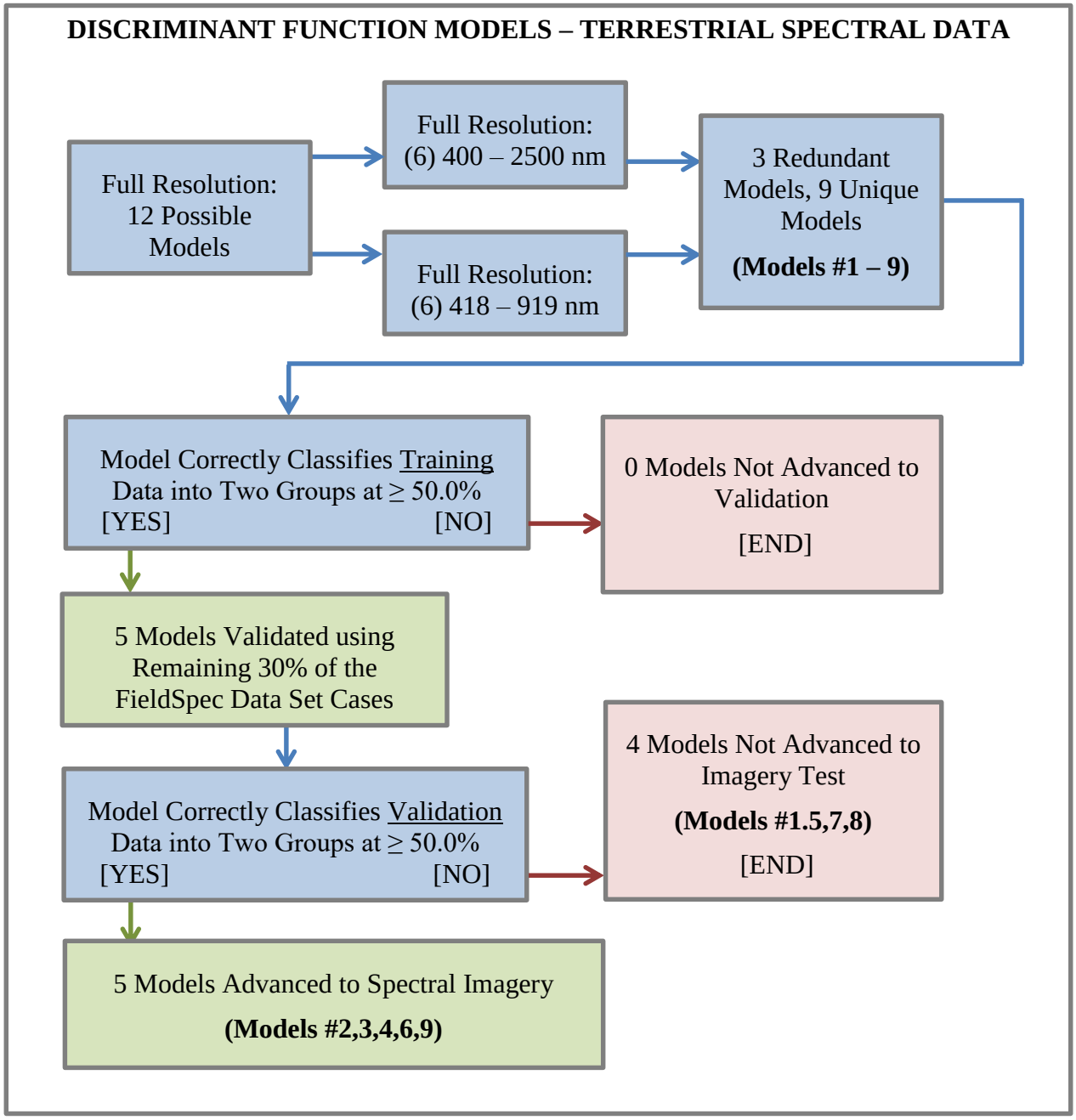

Figure 6.1-15: Discriminant function model workflow results; nine models reduced to five.

Table 6.1-4: DFA model validation performance summary; 30% validation data set. The first model was trained using three groups, but correctly classifies validation data into two groups at ≥ 50.0%; 'Disturbed' refers to combined Burial and Control samples.

DFA Model	Season	Known Group	n=	% Correct	% Overall Correct
2	Autumn	**B**urials	15	73.3	(BCU) 62.5
		Control	2	0.0	(BU) 65.8
		Undisturbed	23	60.9	
3	Spring	Burials	16	68.8	58.5
		Undisturbed	25	52.0	
4	Autumn	Burials	15	66.7	63.2
		Undisturbed	23	60.9	
6	Autumn	Disturbed	17	52.9	62.5
		Undisturbed	23	69.6	
9	Autumn	Disturbed	17	70.6	62.5
		Undisturbed	23	56.5	

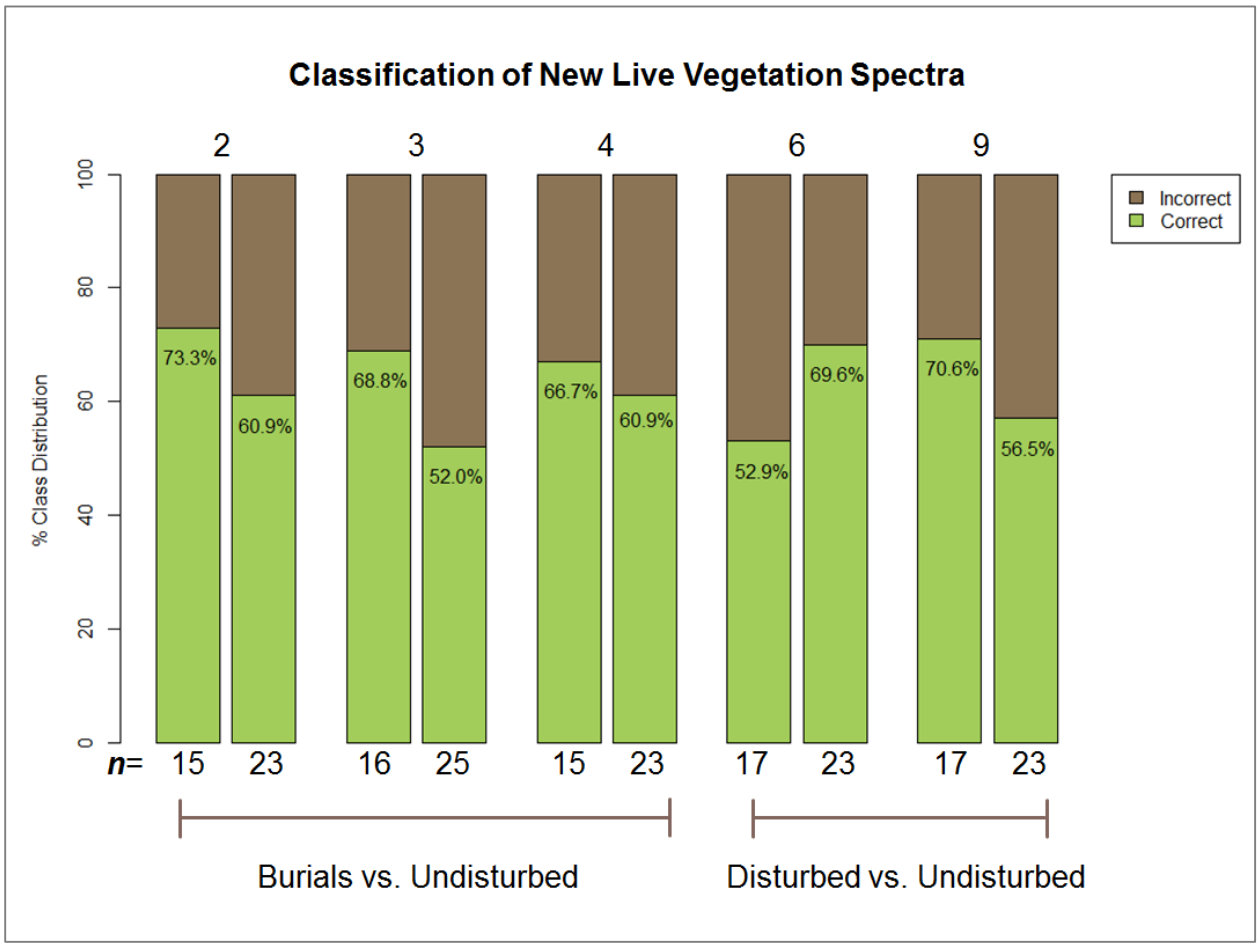

Figure 6.1-16: Graphical representation of DFA model performance presented in **Table 6.1-4**.

Table 6.1-5: Validated model wavelengths; all models correctly classify both validation data groups at ≥ 50.0%. Detailed classification results presented in **Appendix B, Tables B.28 – B.67**.

DFA Model		Wavelengths (nm)		
2: Burials/Control/Undist.		$\lambda 1$ = 708 $\lambda 2$ = 2053 $\lambda 3$ = 2407	$\lambda 4$ = 2445 $\lambda 5$ = 2498	
3:	**Burials/Undist.**	$\lambda 1$ = 761 $\lambda 2$ = 1440 $\lambda 3$ = 2015 $\lambda 4$ = 2291	$\lambda 5$ = 2355 $\lambda 6$ = 2401 $\lambda 7$ = 2405 $\lambda 8$ = 2417	$\lambda 9$ = 2448 $\lambda 10$ = 2459 $\lambda 11$ = 2467 $\lambda 12$ = 2480
4:	**Burials/Undist.**	$\lambda 1$ = 707		
6:	**Disturbed/Undist.**	$\lambda 1$ = 708 $\lambda 2$ = 2006 $\lambda 3$ = 2412		
9:	**Disturbed/Undist.**	$\lambda 1$ = 708		

Table 6.1-6: Validated model coefficients.

DFA Model	Coefficients		
2: Burial	Constant = -2.546	$\alpha 2$ = 41.962	$\alpha 4$ = -26.439
	$\alpha 1$ = 6.821	$\alpha 3$ = -0.652	$\alpha 5$ = 0.651
Control	Constant = -12.925	$\alpha 2$ = 374.836	$\alpha 4$ = 175.919
	$\alpha 1$ = 23.758	$\alpha 3$= -566.458	$\alpha 5$ = 21.366
Undisturbed	Constant = -4.883	$\alpha 2$ = 33.399	$\alpha 4$ = -10.314
	$\alpha 1$ = 29.896	$\alpha 3$ = -24.752	$\alpha 5$ = 3.159
3: Burial	Constant = -6.820	$\alpha 5$ = -573.899	$\alpha 10$ = 64.624
	$\alpha 1$ = 36.497	$\alpha 6$ = -273.600	$\alpha 11$ = -78.656
	$\alpha 2$ = -116.559	$\alpha 7$ = 332.210	$\alpha 12$ = -77.477
	$\alpha 3$ = 214.436	$\alpha 8$ = 27.292	
	$\alpha 4$ = 400.097	$\alpha 9$ = 62.280	
Undisturbed	Constant = -10.577	$\alpha 5$ = 73.052	$\alpha 10$ = 257.155
	$\alpha 1$ = 80.630	$\alpha 6$ = 61.779	$\alpha 11$ = 50.646
	$\alpha 2$ = 306.794	$\alpha 7$ = -160.127	$\alpha 12$ = -5.480
	$\alpha 3$ = -173.959	$\alpha 8$ = -193.261	
	$\alpha 4$ = -441.858	$\alpha 9$ = 214.378	
4: Burial	Constant = -1.866		
	$\alpha 1$ = 19.252		
Undisturbed	Constant = -4.335		
	$\alpha 1$ = 33.926		
6: Disturbed	Constant = -2.142	$\alpha 2$ = 20.546	
	$\alpha 1$ = 11.724	$\alpha 3$ = -1.968	
Undisturbed	Constant = -4.419	$\alpha 2$ = -49.066	
	$\alpha 1$ = 28.427	$\alpha 3$ = 52.454	
9: Disturbed	Constant = -2.004		
	$\alpha 1$ = 19.555		
Undisturbed	Constant = -4.294		
	$\alpha 1$ = 32.412		

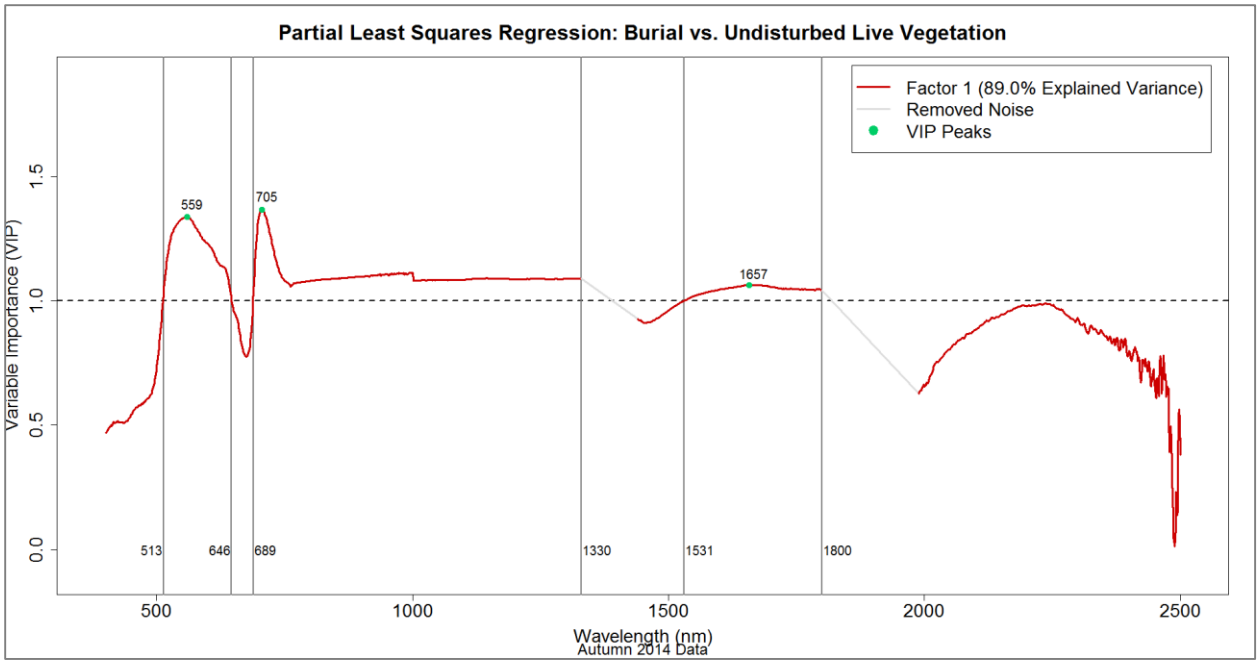

Figure 6.1-17: PLS first factor variable importance (VIP) to group separation; Autumn data (n=128); test for separation of Burial vs. Undisturbed vegetation groups; VIP ≥ 1.0 intercepts as indicated by vertical lines; VIP peaks at 559, 705 and 1657 nm; **Corresponds with BLR Model 2 and DFA Model 2**.

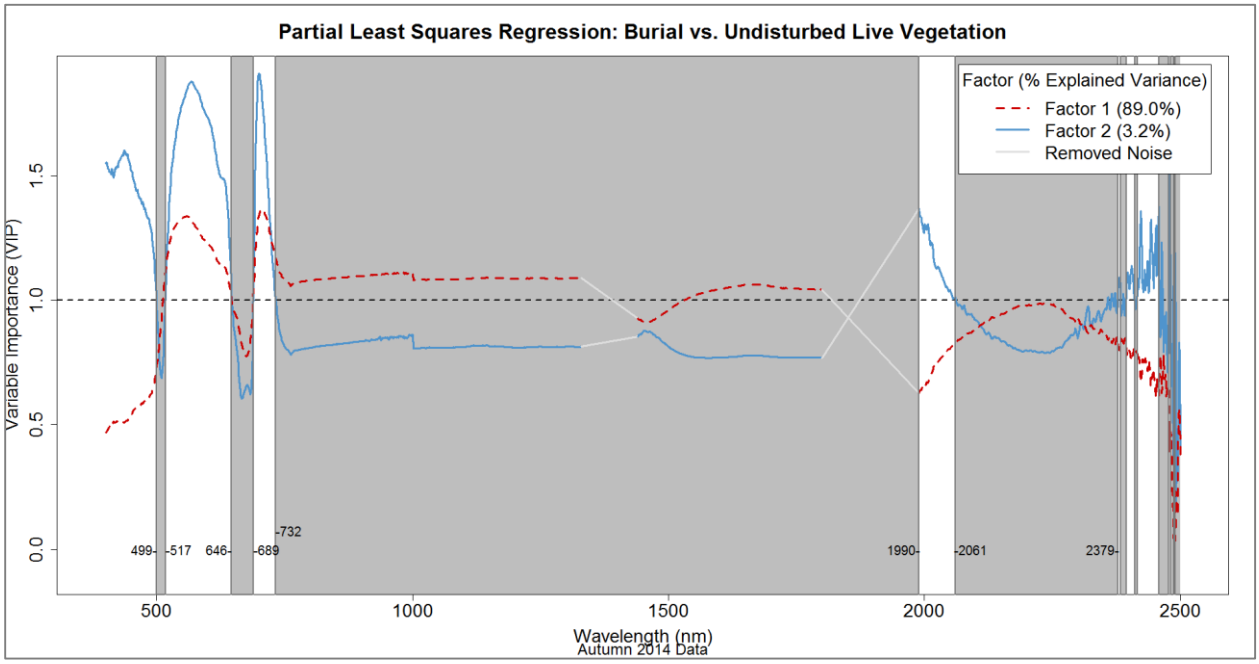

Figure 6.1-18: PLS second factor VIP, Autumn data (n=128); test for separation of Burial vs. Undisturbed vegetation groups, 92.2% cumulative variance of the independent variables explained by the first two latent factors; graphical emphasis on Factor 2 ≥ 1.0 **VIP wavelengths. Factor 1 highlighted in Figure 6.1-17. Corresponds with BLR Model 2 and DFA Model 2**.

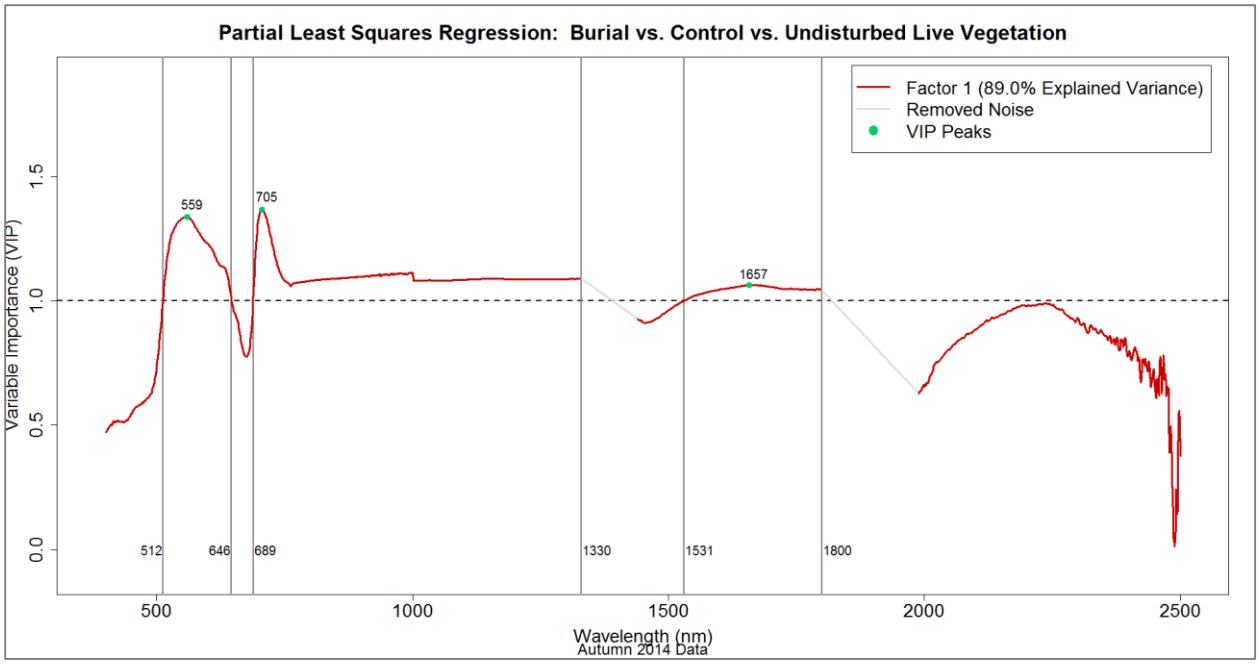

Figure 6.1-19: PLS first factor variable importance (VIP) to group separation; Autumn data (n=133); test for separation of Burial vs. Control vs. Undisturbed vegetation groups; VIP ≥ 1.0 intercepts as indicated by vertical lines; VIP peaks at 559, 705 and 1657 nm; **Corresponds with DFA Model 2**.

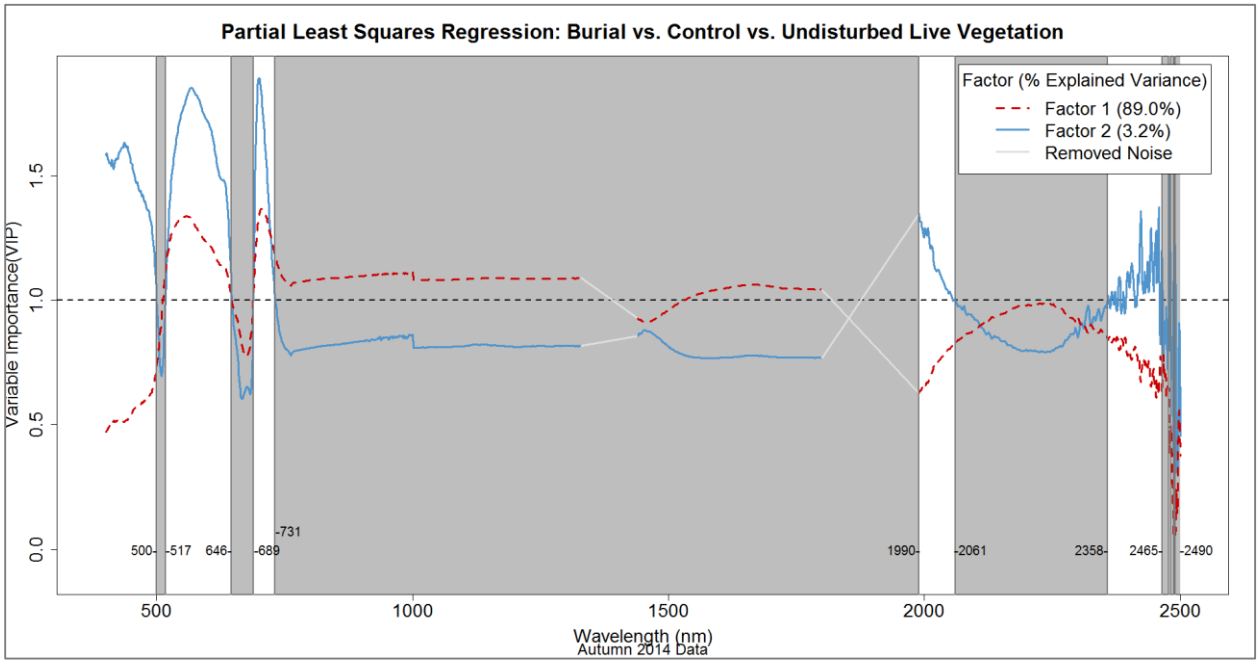

Figure 6.1-20: PLS second factor VIP, Autumn data (n=133); test for separation of Burial vs. Control vs. Undisturbed vegetation groups, 92.2% cumulative variance of the independent variables explained by the first two latent factors; graphical emphasis on Factor 2 ≥ 1.0 VIP wavelengths. Factor 1 highlighted in **Figure 6.1-19**. **Corresponds with DFA Model 2**.

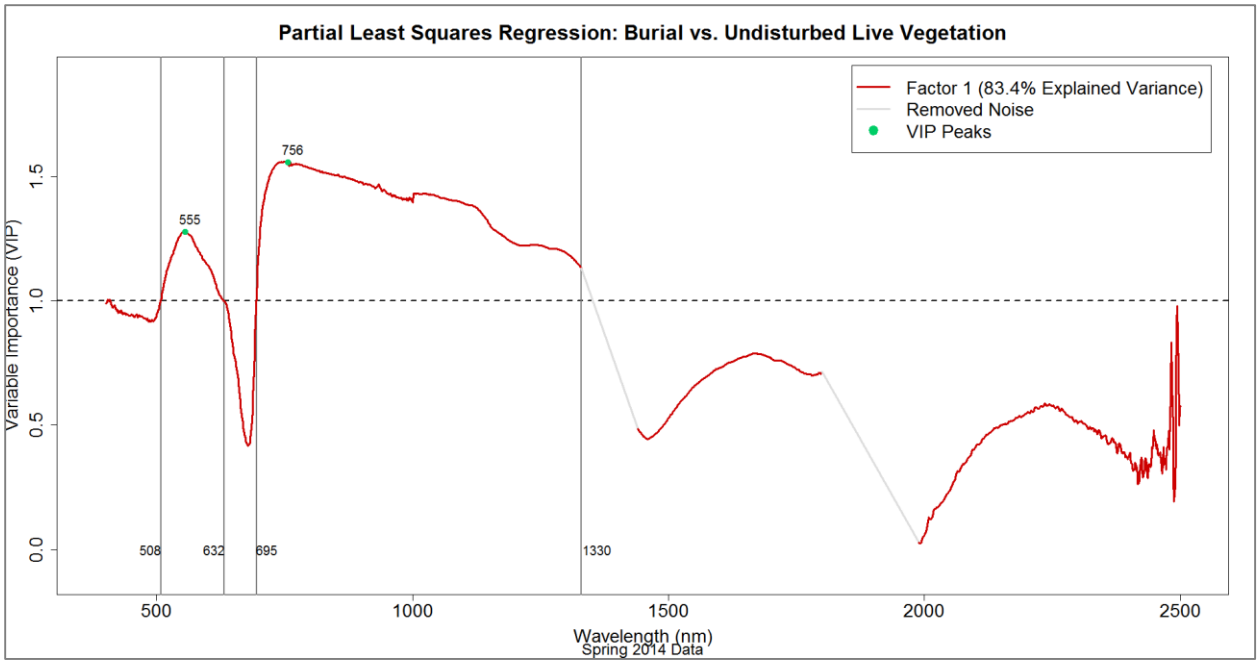

Figure 6.1-21: PLS first factor variable importance (VIP) to group separation, Spring data (n=137); test for separation of Burial vs. Undisturbed vegetation groups; VIP ≥ 1.0 intercepts as indicated by vertical lines; VIP peaks at 555 and 756 nm; **Corresponds with DFA Model 3**.

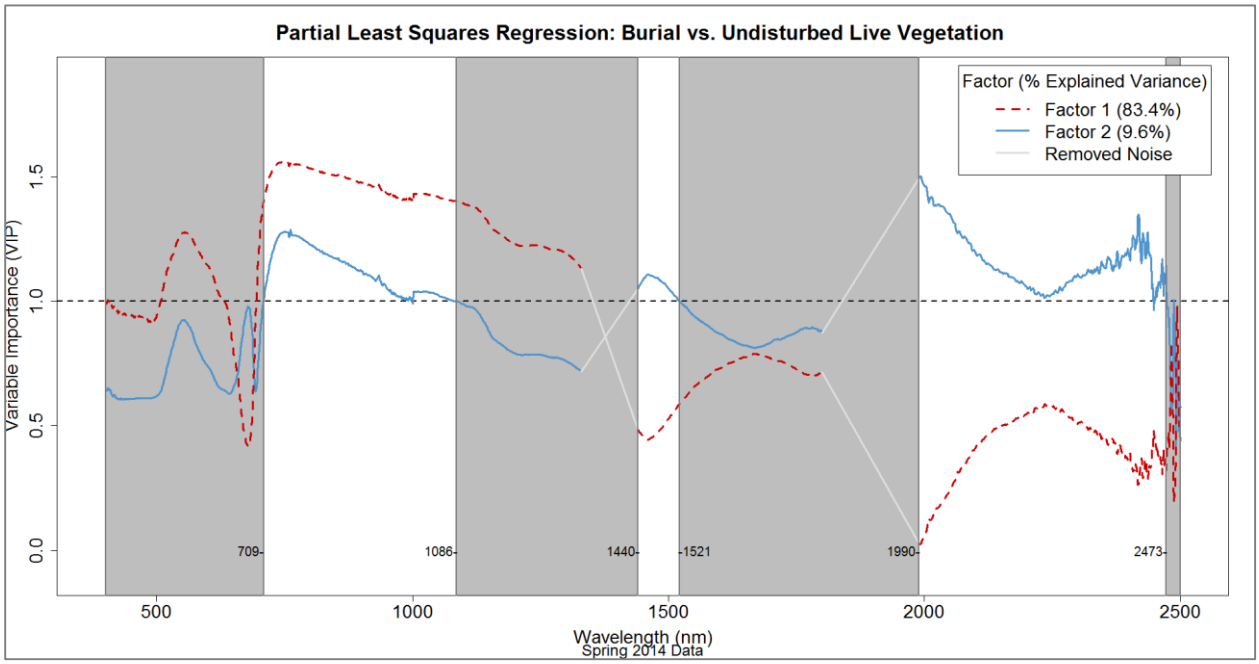

Figure 6.1-22: PLS second factor VIP, Spring data (n=137); test for separation of Burial vs. Undisturbed vegetation groups, 93.0% cumulative variance of the independent variables explained by the first two latent factors; graphical emphasis on Factor 2 ≥ 1.0 VIP wavelengths. Factor 1 highlighted in **Figure 6.1-21. Corresponds with DFA Model 3**.

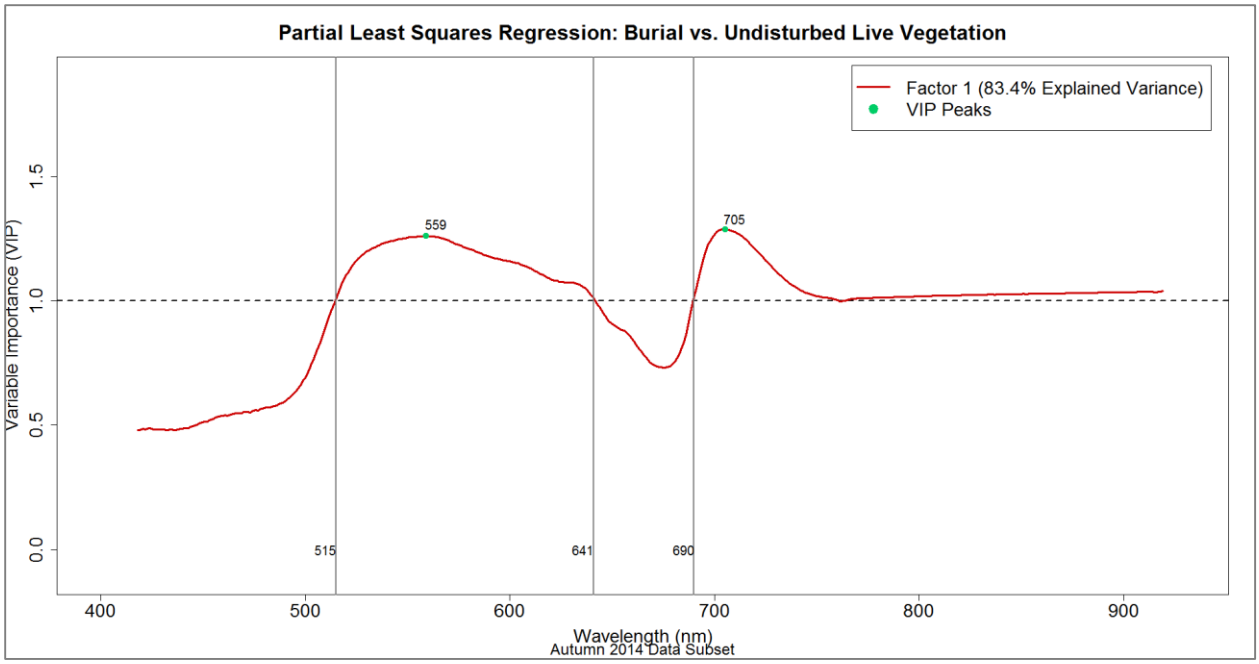

Figure 6.1-23: PLS first factor variable importance (VIP) to group separation, Autumn data (n=128); test for separation of Burial vs. Undisturbed vegetation groups; VIP ≥ 1.0 intercepts as indicated by vertical lines; VIP peaks at 559 and 705 nm; **Corresponds with DFA Model 4**.

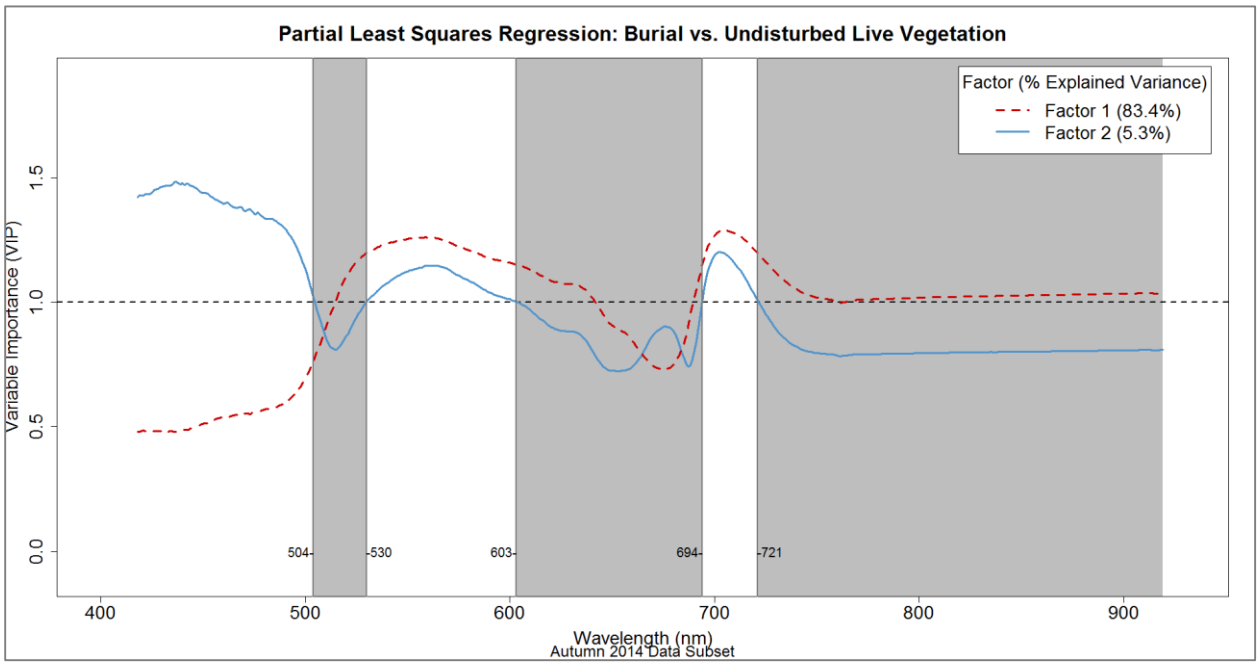

Figure 6.1-24: PLS second factor VIP, Autumn data (n=128); test for separation of Burial vs. Undisturbed vegetation groups, 88.7% cumulative variance of the independent variables explained by the first two latent factors; graphical emphasis on Factor 2 ≥ 1.0 VIP wavelengths. Factor 1 highlighted in **Figure 6.1-23. Corresponds with DFA Model 4**.

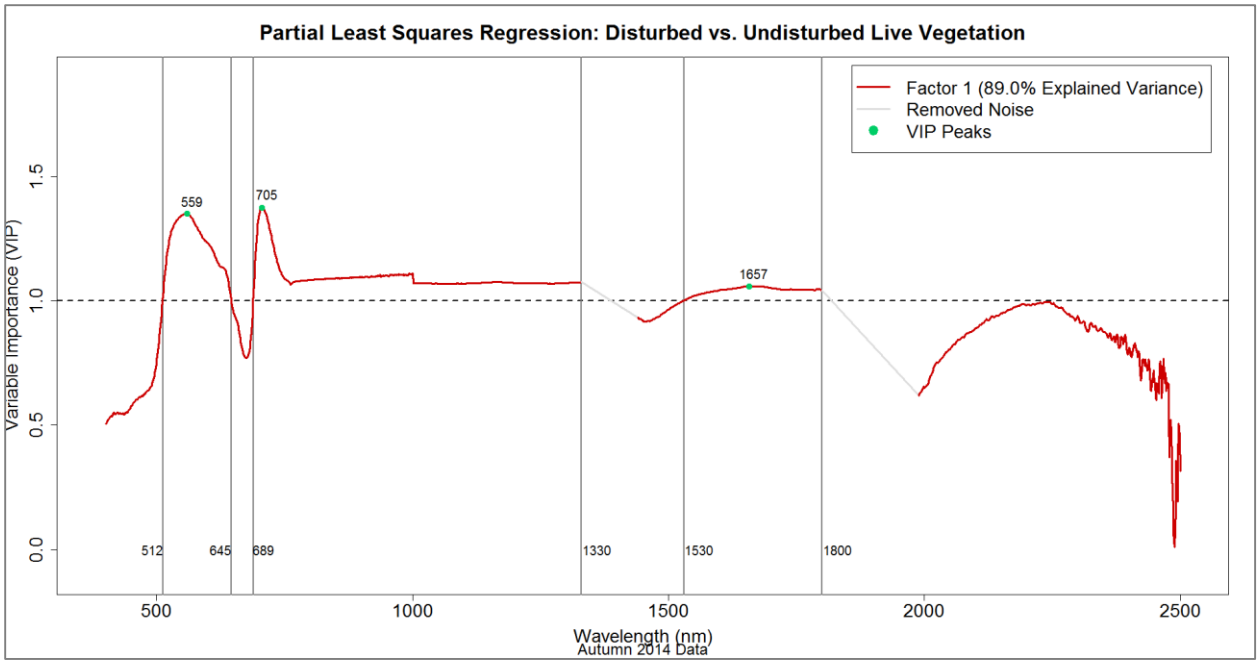

Figure 6.1-25: PLS first factor variable importance (VIP) to group separation, Autumn data (n=133); test for separation of Disturbed vs. Undisturbed vegetation groups; VIP ≥ 1.0 intercepts as indicated by vertical lines; VIP peaks at 559, 705, and 1657 nm; **Corresponds with BLR Model 6 and DFA Model 6**.

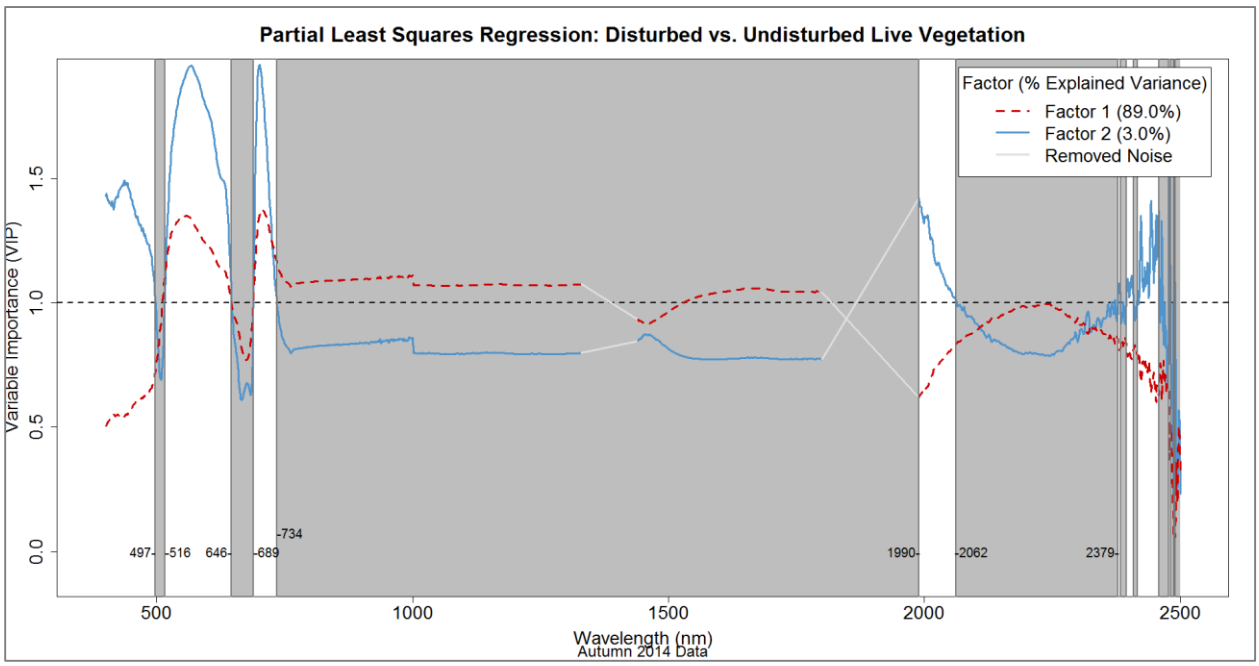

Figure 6.1-26: PLS second factor VIP, Autumn data (n=133); test for separation of Disturbed vs. Undisturbed vegetation groups, 92.0% cumulative variance of the independent variables explained by the first two latent factors; graphical emphasis on Factor 2 ≥ 1.0 VIP wavelengths. Factor 1 highlighted in **Figure 6.1-25. Corresponds with BLR Model 6 and DFA Model 6**.

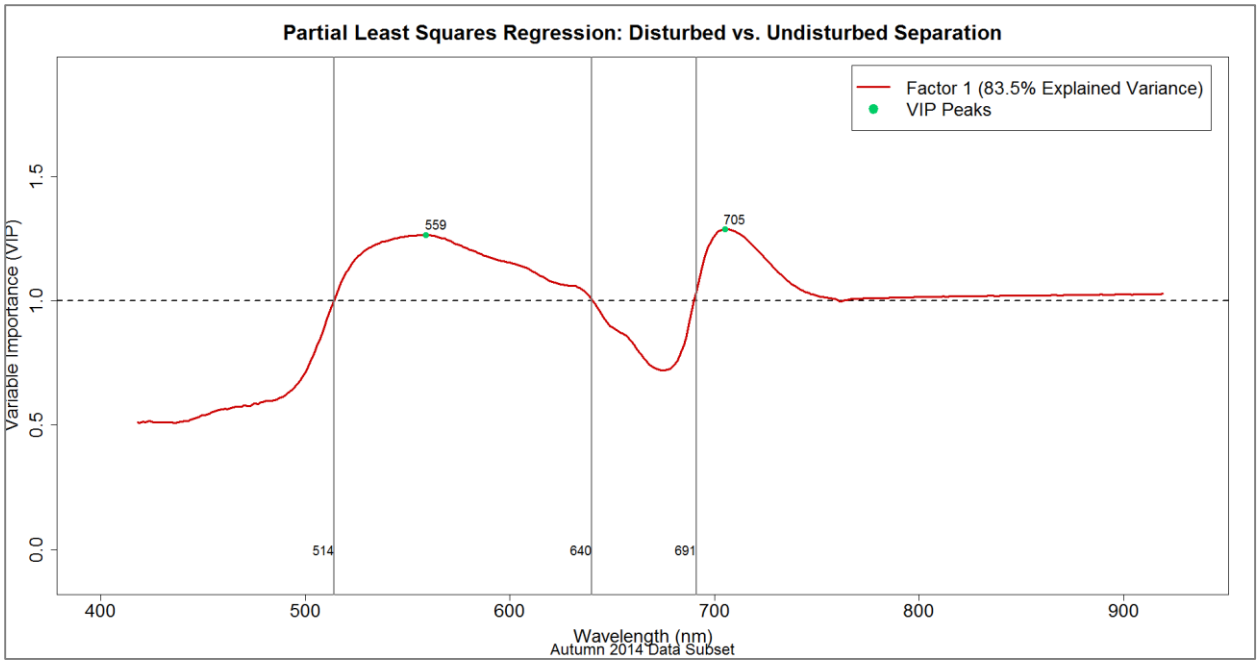

Figure 6.1-27: PLS first factor variable importance (VIP) to group separation, Autumn data (n=133); test for separation of Disturbed vs. Undisturbed vegetation groups; VIP ≥ 1.0 intercepts as indicated by vertical lines; VIP peaks at 559 and 705 nm; **Corresponds with DFA Model 9**.

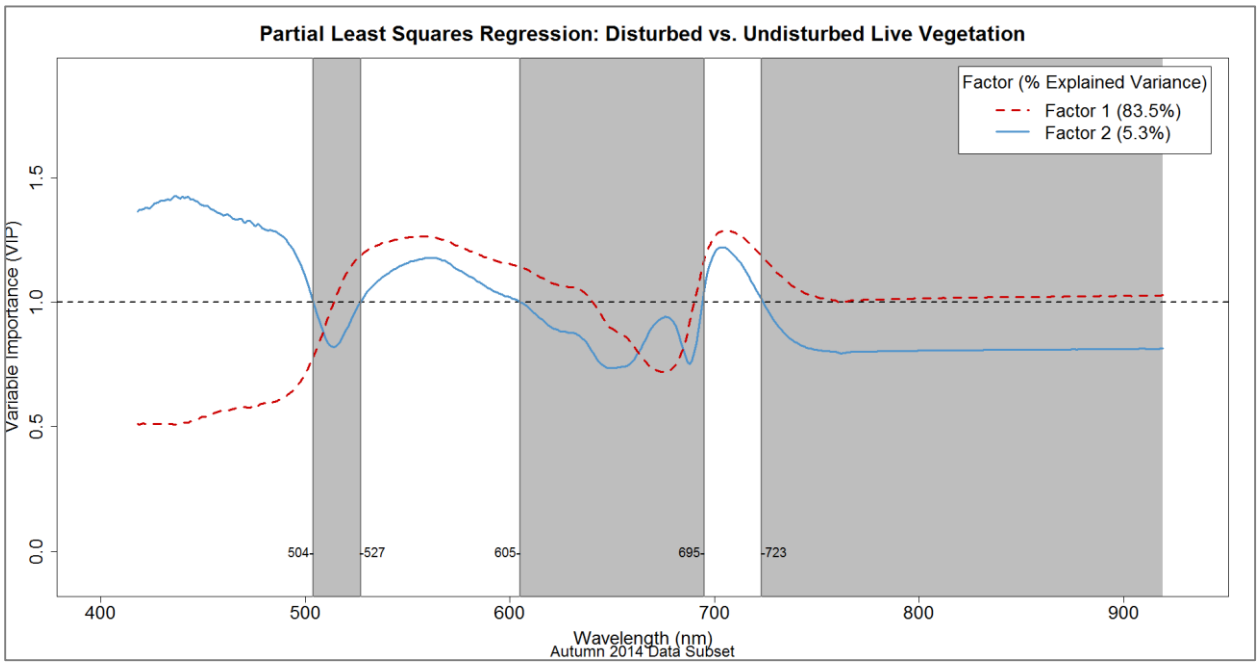

Figure 6.1-28: PLS second factor VIP, Autumn data (n=133); test for separation of Disturbed vs. Undisturbed vegetation groups, 88.8% cumulative variance of the independent variables explained by the first two latent factors; graphical emphasis on Factor 2 ≥ 1.0 VIP wavelengths. Factor 1 highlighted in **Figure 6.1-27. Corresponds with DFA Model 9**.

6.2 Hyperspectral Imagery

6.2.1 Validated Statistical Models

Hyperspectral imagery (HSI) is analyzed to evaluate the potential scalability of terrestrial findings. Applying the two discriminant function models (**Formulas 5.2-1** and **5.2-3**) developed using terrestrial spectral data to the three airborne HSI reflectance spectral collections resulted in unanimous classification for 100% of all study area pixels as either vegetation associated with a burial (**Figure 6.2-1**) or generally disturbed vegetation (**Figure 6.2-2**). Applying the secondary **Formulas 5.2-2** and **5.2-4** to the same reflectance values reveals continuous variation throughout the study area (**Figures 6.2-3 – 6.2-8**), where lesser values (greater negative values) indicate predictions of a burial or general disturbance. The values produced by applying the DFA models range from -2.2 – -0.4. Applying both DFA models to all three HSI collections yields no discernable pattern of disturbance to indicate the study area location is spectrally anomalous from its surroundings. In fact, the results of applying the two DFA models indicate that the study area location is spectrally unremarkable. Moreover, the two DFA model results suggest that the site is visually out-competed by several apparently unrelated anomalies throughout the study area shown as dark blue patches, suggesting vegetation disturbance might be observable at those locations.

6.2.2 Vegetation Indices

Seven common vegetation spectral indices were applied to each of the three HSI collections (**Table 5.3-1**). The normalized difference vegetation index (NDVI), sum green index (SGI), and structure insensitive pigment index (SIPI) used by Leblanc et al. (2014) to isolate unmarked pig burials, are among those tested in this research. Results of these three indices are presented first (**Figures 6.2-9 – 6.2-17**), and grouped by index. Results from the remaining four spectral indices:

Figure 6.2-1: HSI binary classification result from Formula 5.2.1; DFA model 4; 07 May 2015 (same DFA model 3 binary result for all three HSI collections).

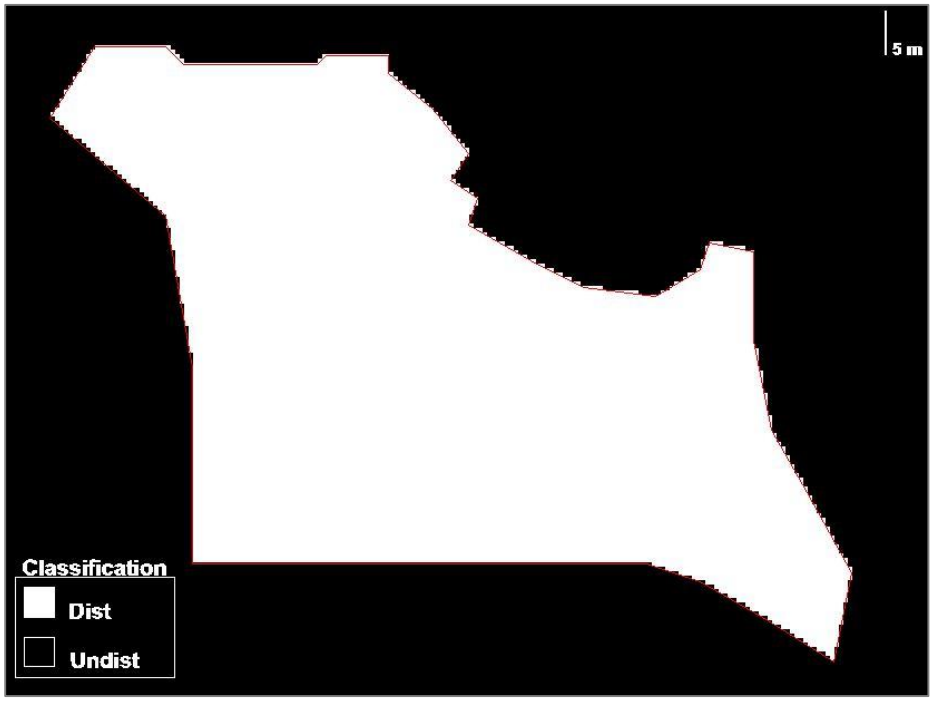

Figure 6.2-2: HSI binary classification result from Formula 5.2.3; DFA model 9; 07 May 2015 (same DFA model 5 binary result for all three HSI collections).

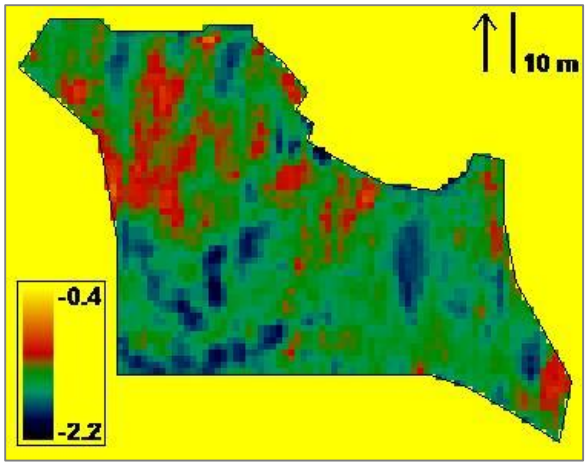

Figure 6.2-3: DFA model 4; 23 March 2015; linear stretch; higher values indicate lower likelihood of a burial.

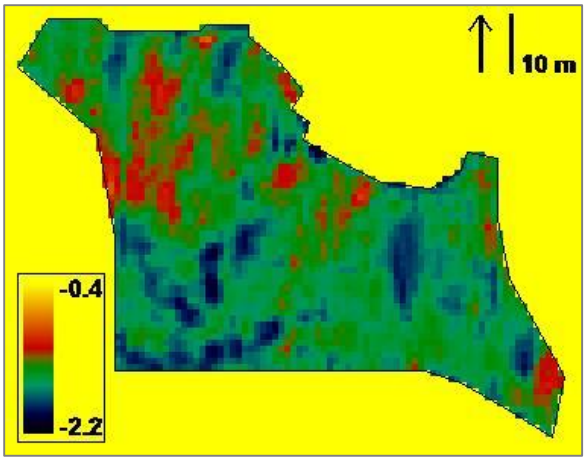

Figure 6.2-4: DFA model 9; 23 March 2015; linear stretch; higher values indicate lower likelihood of disturbance.

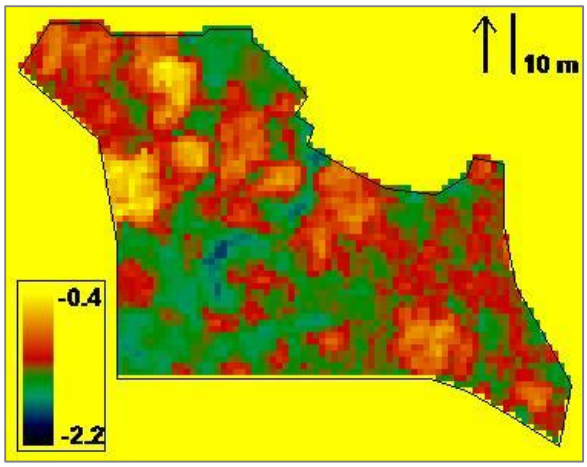

Figure 6.2-5: DFA model 4; 17 April 2015.

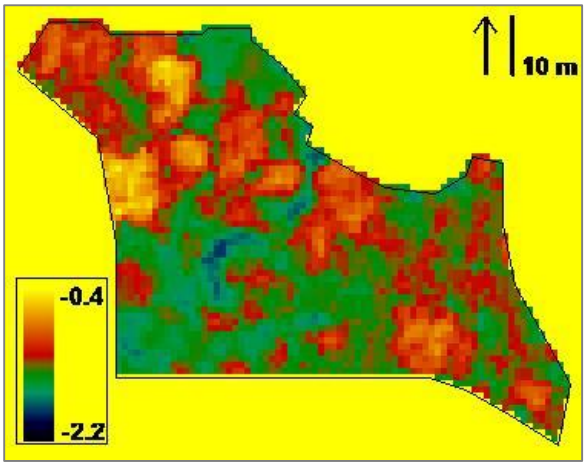

Figure 6.2-6: DFA model 9; 17 April 2015.

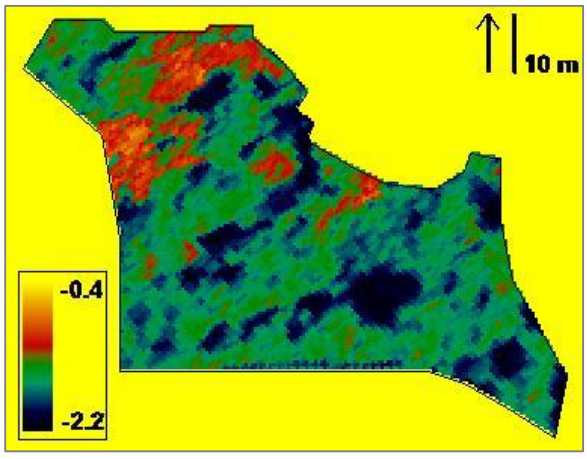

Figure 6.2-7: DFA model 4; 07 May 2015.

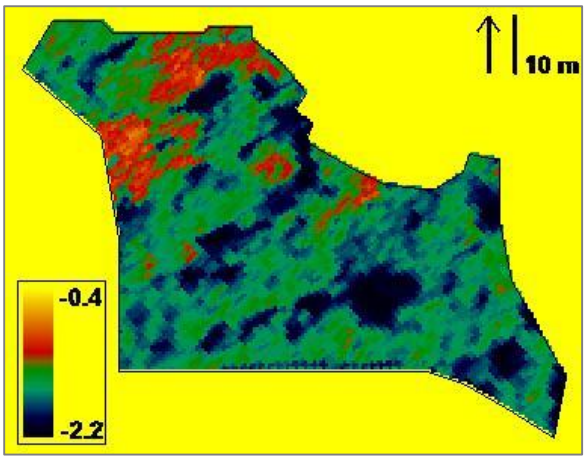

Figure 6.2-8: DFA model 9; 07 May 2015.

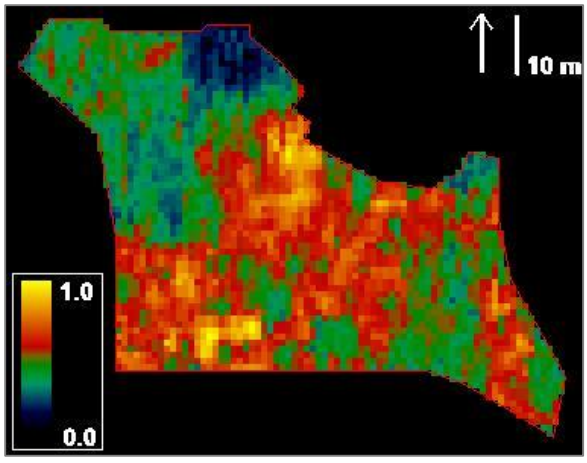

Figure 6.2-9: NDVI; 23 March 2015 ; Gaussian stretch; higher NDVI values indicate increased vegetation health.

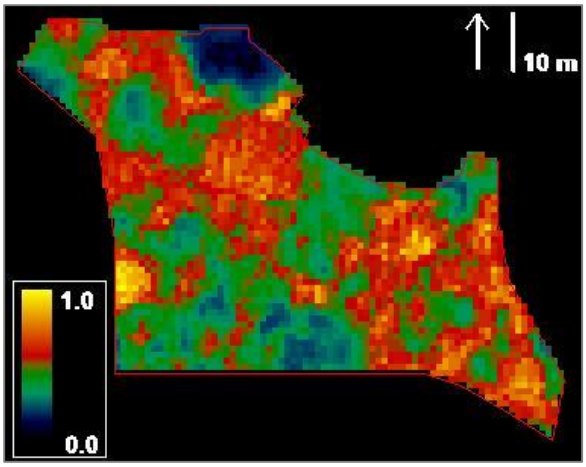

Figure 6.2-10: NDVI; 17 April 2015.

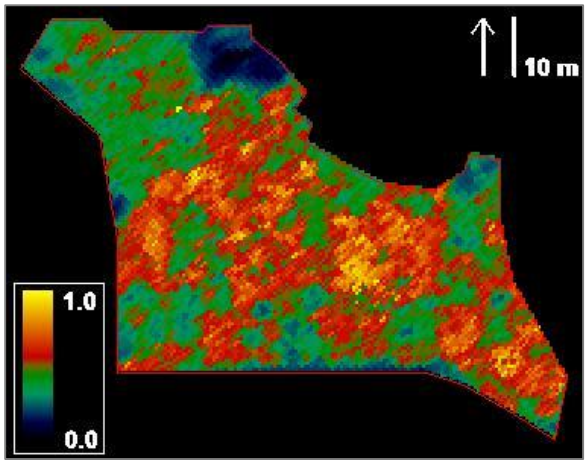

Figure 6.2-11: NDVI; 07 May 2015.

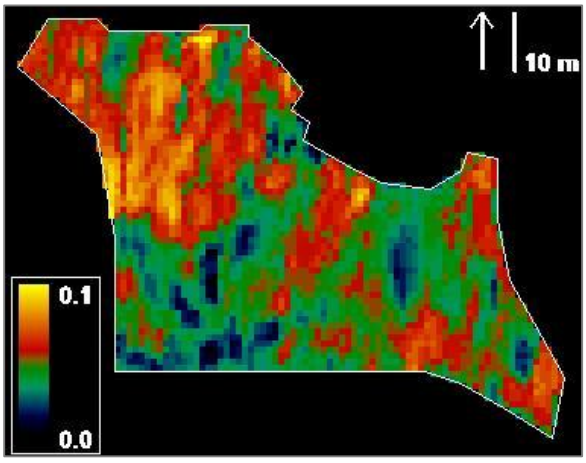

Figure 6.2-12: SGI; 23 March 2015; Gaussian stretch; higher SGI values indicate increased vegetation health.

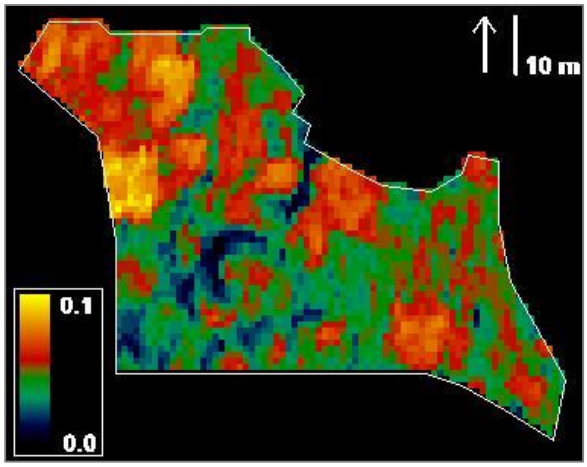

Figure 6.2-13: SGI; 17 April 2015.

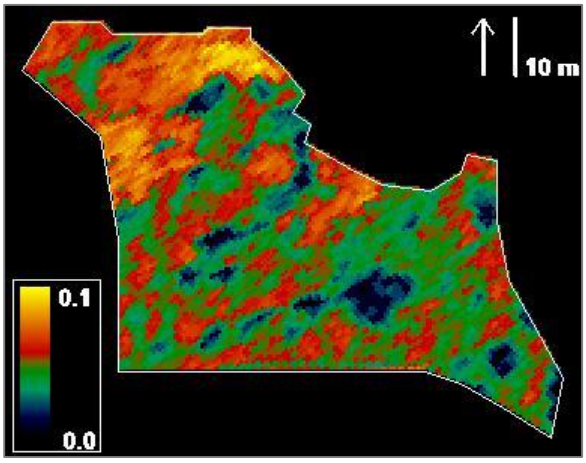

Figure 6.2-14: SGI; 07 May 2015.

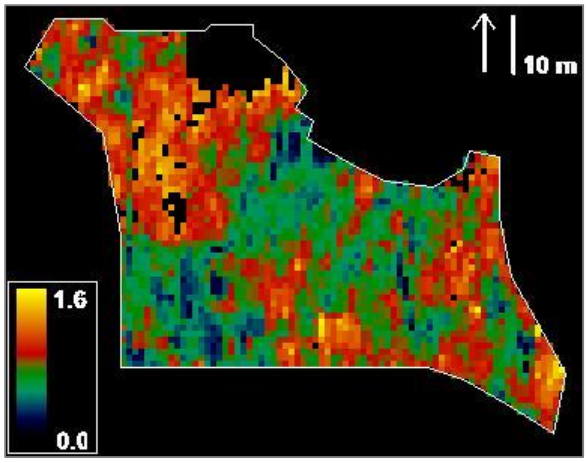

Figure 6.2-15: SIPI; 23 March 2015; Gaussian stretch; higher SIPI values indicate increased vegetation stress.

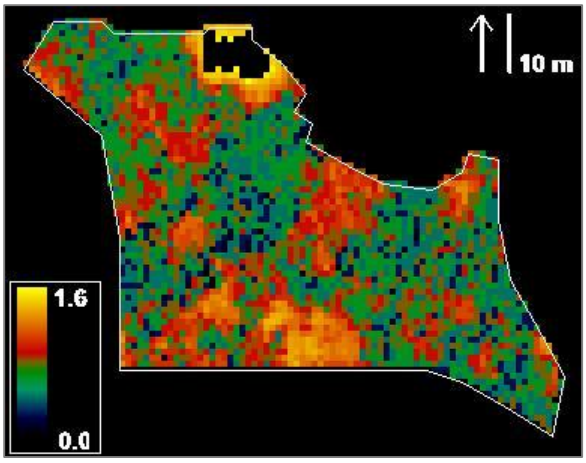

Figure 6.2-16: SIPI; 17 April 2015.

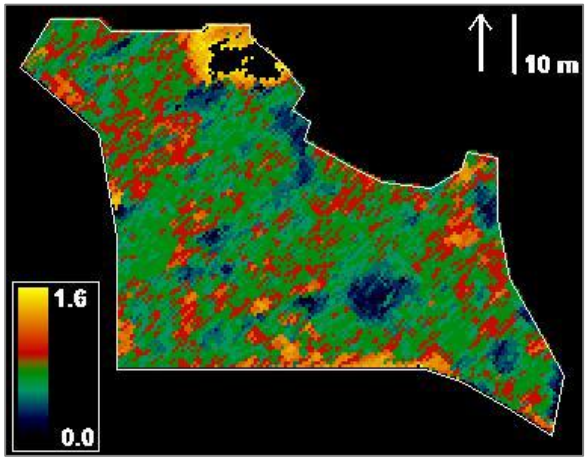

Figure 6.2-17: SIPI; 07 May 2015.

red edge normalized difference vegetation index (RENDVI), modified red edge simple ratio index (MRESRI), modified red edge normalized difference vegetation index (MRENDVI), and red edge position index (REPI), are presented next (**Figures 6.2-18 – 6.2-29**) and are also grouped by index.

NDVI is a measure of healthy green vegetation, where possible values range from 0.0 – 1.0 where higher values indicative of increased vegetation health. The common range for healthy vegetation is 0.2 – 0.8. The NDVI range for the entire study area is 0.07 – 0.78 for the March 2015 HSI collection, 0.16 – 0.93 for the April 2015 HSI collection, and 0.06 – 0.96 for the May 2015 collection (**Figures 6.2-9 – 6.2-11**).

SGI is a measure of vegetation greenness. Possible SGI values range from 0.0 to 0.5, where higher values indicate an increase in vegetation health. The common range for healthy vegetation is 0.1 – 0.25. The SGI range for the entire study area is 0.01 – 0.08 for the March 2015 HSI collection, 0.02 – 0.08 for the April 2015 HSI collection, and 0.00 – 0.07 for the May 2015 collection (**Figures 6.2-12 – 6.2-14**).

SIPI is a measure of canopy vegetation stress. Possible SIPI values range from 0.0 – 2.0, where higher values indicate an increase in canopy stress. The healthy range for green vegetation is 0.8 – 1.8. The SIPI range for the entire study area is 0.00 – 1.59 for the March 2015 HSI collection, 0.00 – 1.63 for the April 2015 HSI collection, and 0.00 – 1.64 for the May 2015 collection (**Figures 6.2-15 – 6.2-17**).

RENDVI is a modification of NDVI, and is also a measure of vegetation health. Possible RENDVI values range from 0.0 – 1.0, where higher values indicate increased vegetation health. The common range for healthy vegetation is 0.2 – 0.9. The RENDVI range for the entire study

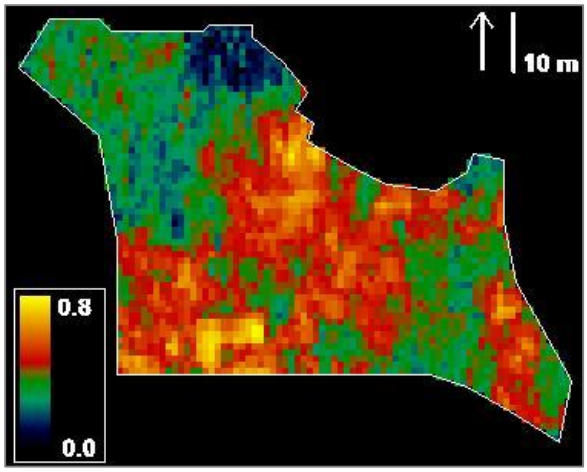

Figure 6.2-18: RENDVI; 23 March 2015; Gaussian stretch; higher values indicate increased vegetation health.

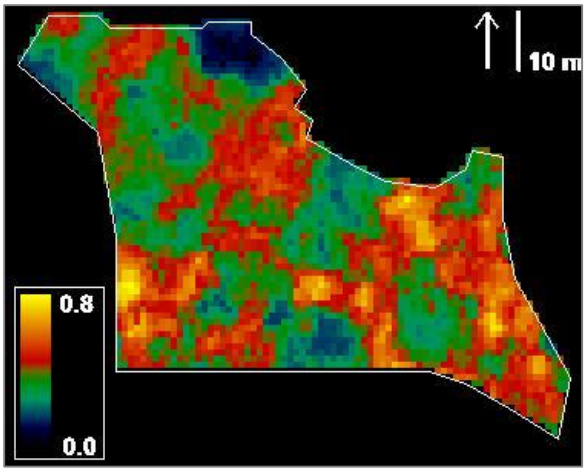

Figure 6.2-19: RENDVI; 17 April 2015.

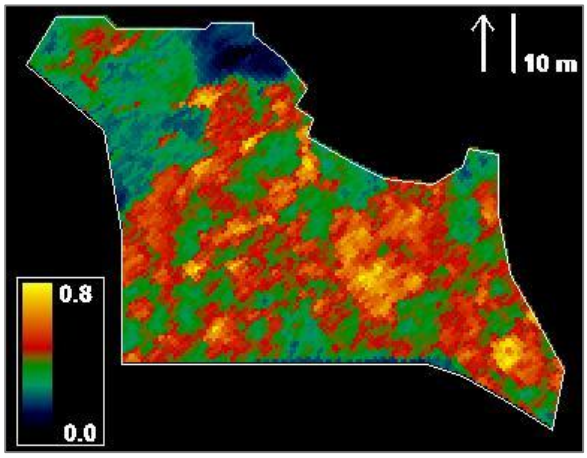

Figure 6.2-20: RENDVI; 07 May 2015.

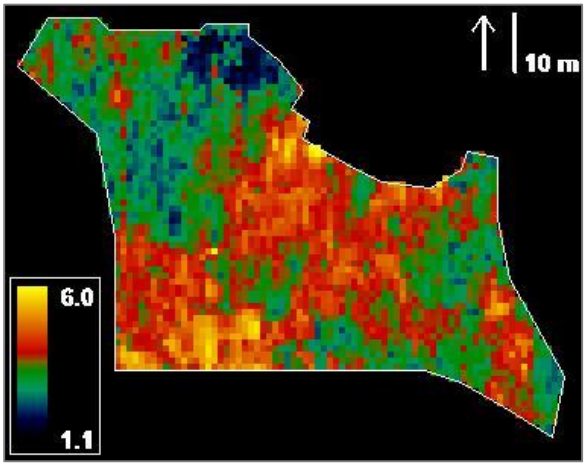

Figure 6.2-21: MRESRI; 23 March 2015; Gaussian stretch; higher values indicate increased vegetation stress.

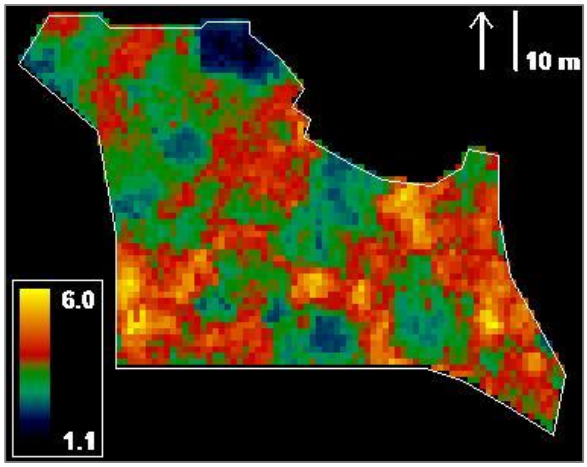

Figure 6.2-22: MRESRI; 17 April 2015.

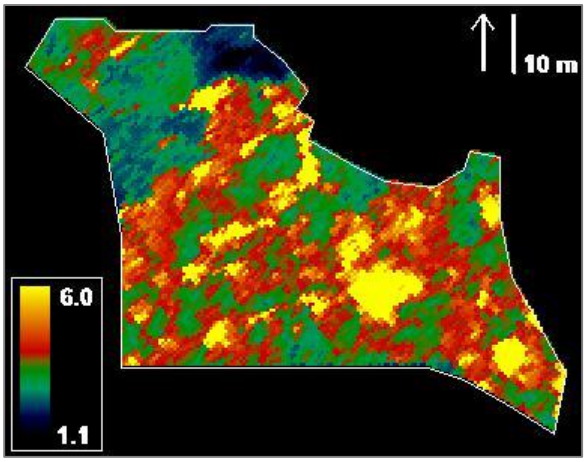

Figure 6.2-23: MRESRI; 07 May 2015.

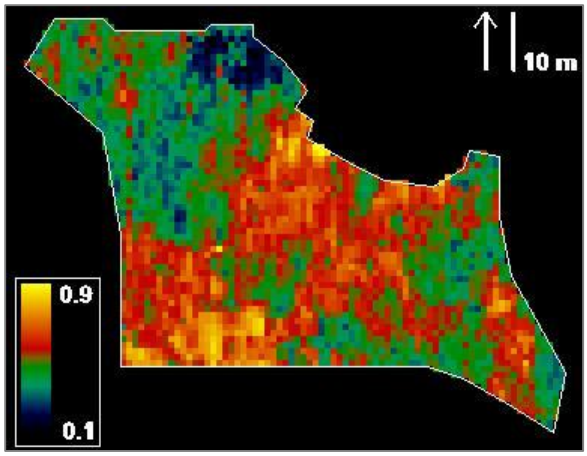

Figure 6.2-24: MRENDVI; 23 March 2015; Gaussian stretch; higher values indicate increased vegetation health.

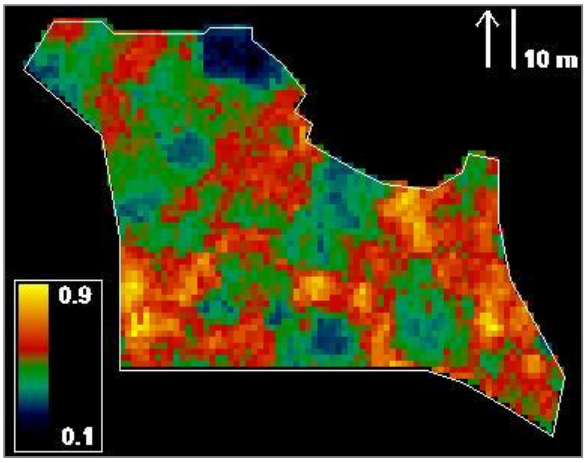

Figure 6.2-25: MRENDVI; 17 April 2015.

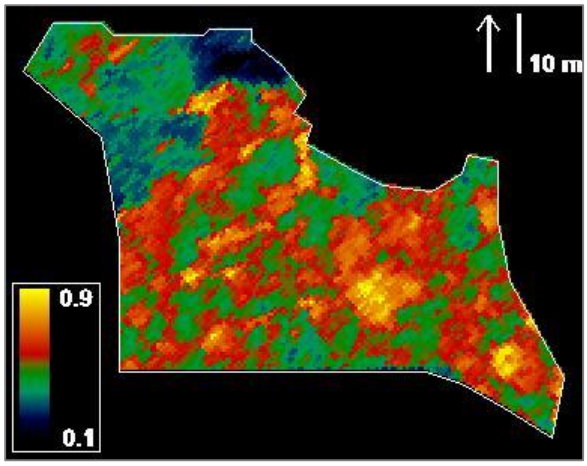

Figure 6.2-26: MRENVDI; 07 May 2015.

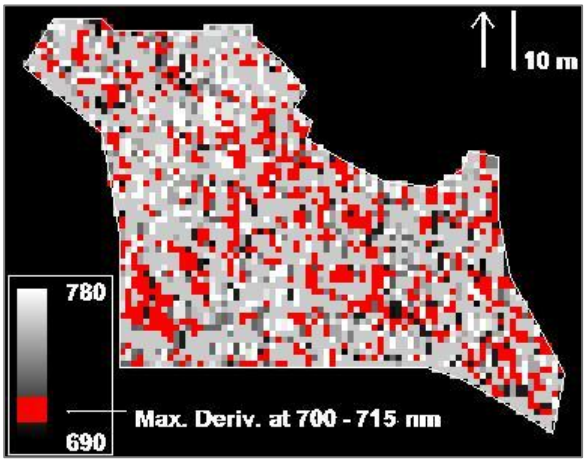

Figure 6.2-27: REPI; 23 March 2015; max slope at ±7 nm of DFA model wavelengths.

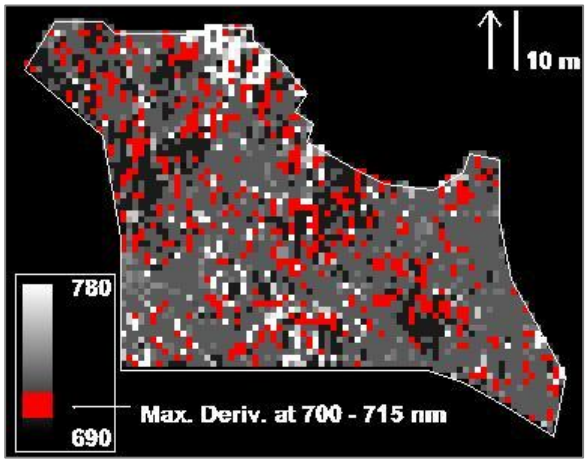

Figure 6.2-28: REPI; 17 April 2015.

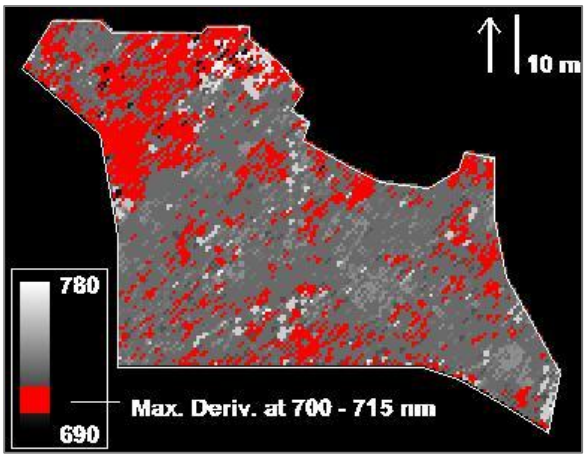

Figure 6.2-29: REPI; 07 May 2015.

area is 0.04 – 0.47 for the March 2015 HSI collection, 0.08 – 0.60 for the April 2015 HSI collection, and 0.03 – 0.75 for the May 2015 collection (**Figures 6.2-18 – 6.2-20**).

MRESRI is a measure of vegetation stress, where higher values indicate increased vegetation stress. Possible MRESRI values range from 0.0 – 30.0. The common range for healthy vegetation is from 2.0 – 8.0. The MRESRI range for the entire study area is 1.14 – 6.01 for the March 2015 HSI collection, 1.27 – 4.92 for the April 2015 HSI collection, and 1.09 – 15.87 for the May 2015 collection (**Figures 6.2-21 – 6.2-23**).

MRENDVI is another modification of NDVI, and is a measure of vegetation health. MRENDVI values range from 0.0 – 1.0, where higher values indicate increased vegetation health. The common range for green vegetation is 0.2 – 0.7. The MRENDVI range for the entire study area is 0.07 – 0.71 for the March 2015 HSI collection, 0.12 – 0.66 for the April 2015 HSI collection, and 0.04 – 0.88 for the May 2015 collection (**Figures 6.2-24 – 6.2-26**).

REPI is an indicator of the wavelength *position* of maximum slope in the red edge (690 – 780 nm) region of the spectrum. REPI values surrounding the variables used in DFA models 4 and 9 (707 and 708 nm) are highlighted in red. There is no apparent spatial clustering of pixels with REPI values from 700 – 715 nm at or near the burial locations within the study area (**Figures 6.2-27 – 6.2-29**).

Applying the seven spectral indices to all three HSI collections yields no discernable spatially clustered pattern of either health or stress to indicate the general burial location is anomalous from its surroundings.

6.3 Multispectral Imagery

6.3.1 Vegetation Index

NDVI is a measure of healthy green vegetation, where values range from 0.0 – 1.0 with higher values indicative of increased vegetation health. The common range for healthy vegetation is 0.2 – 0.8. The normalized difference vegetation index (NDVI) was applied to each of the four MSI collections (**Figures 6.3-1 – 6.3-4**). The NDVI range for the entire study area is 0.0 – 1.0 for all four MSI collections. Applying NDVI to all four MSI collections yields no discernable spatially clustered pattern of vegetation health to indicate the general burial location is spectrally anomalous relative to its surroundings.

6.4 Terrestrial LIDAR

6.4.1 Elevation

Grave surfaces were visualized using terrestrial LIDAR to establish whether the surfaces exhibit mounds, depressions, or no topographic relief. For each image, every pixel contains one elevation value. Elevation data at 5 cm ground sample distance (GSD) are presented in **Figures 6.4-1 – 6.4-4**, one for each of the four collection dates. At 5 cm GSD, all the burial surfaces are not visible because they compete with the overall positive slope of the study area from the northwest to the southeast. Only the grave containing six bodies is distinctive in all post-burial elevation images (**Figures 6.4-3** and **6.4-4**). The Sky-View Factor approach is a measure of sky visibility, and is tolerant of overall uneven terrain, but like absolute elevation data, fails to emphasize the smaller graves as distinctive features, even at 5 cm GSD (**Figures 6.4-5 – 6.4-8**).

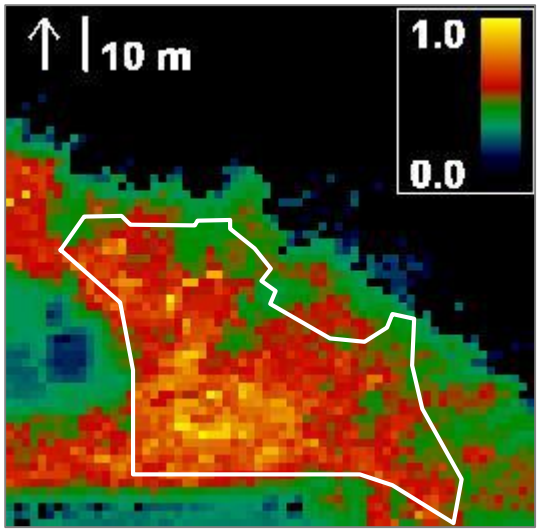

Figure 6.3-1: NDVI; 30 July 2012 (baseline); Gaussian stretch; higher values indicate increased vegetation health.

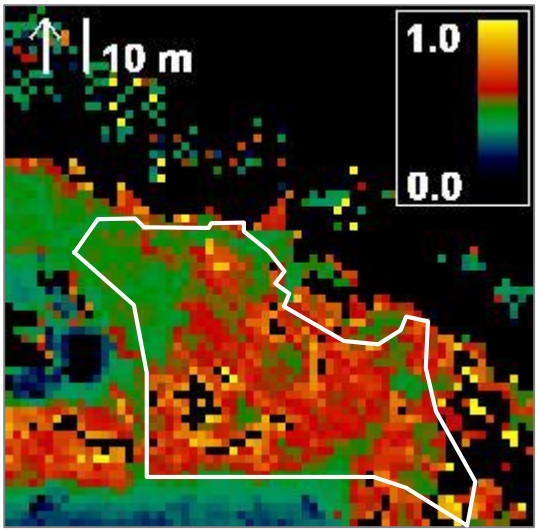

Figure 6.3-2: NDVI; 29 Nov. 2012 (baseline).

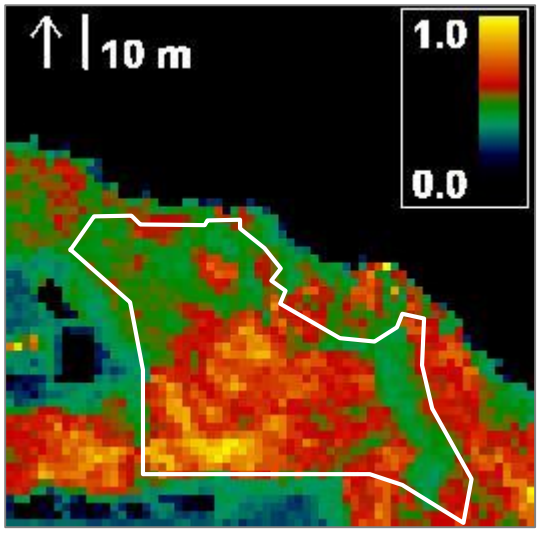

Figure 6.3-3: NDVI; 04 Mar 2013 (post-burial).

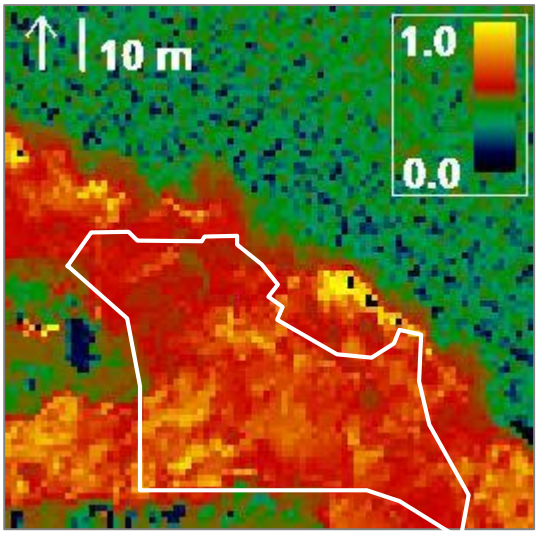

Figure 6.3-4: NDVI; 25 Mar 2015 (post-burial).

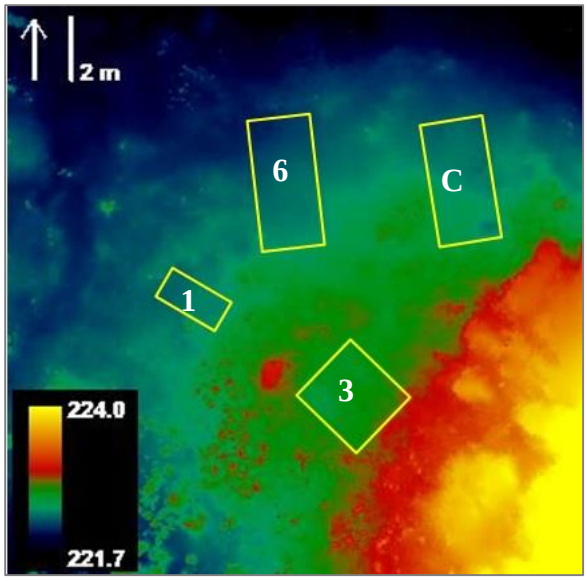

Figure 6.4-1: Elevation measurements of study area on 12 Feb. 2013 (baseline); values indicate actual ground elevation (m); ROI overlays used here for referencing burial locations in **Figures 6.4-2 – 6.4-8**.

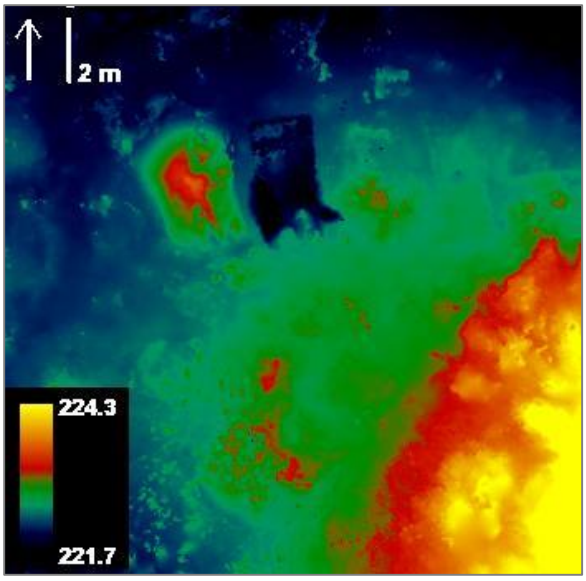

Figure 6.4-2: Elevation measurements of study area on 15 Feb. 2013 (post-burial).

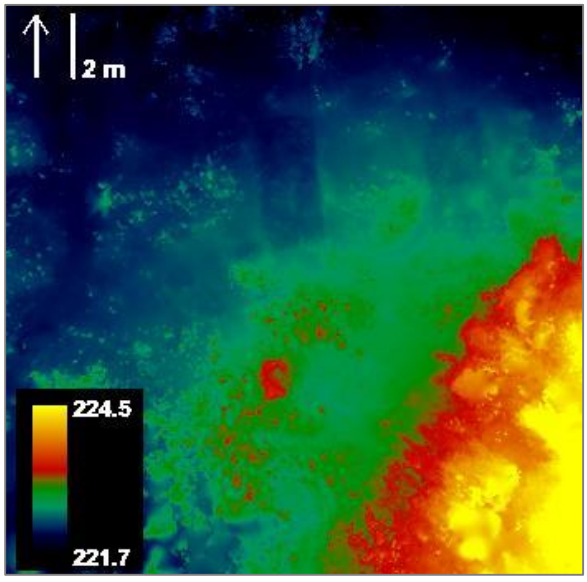

Figure 6.4-3: Elevation measurements of study area on 03 June 2013 (post-burial).

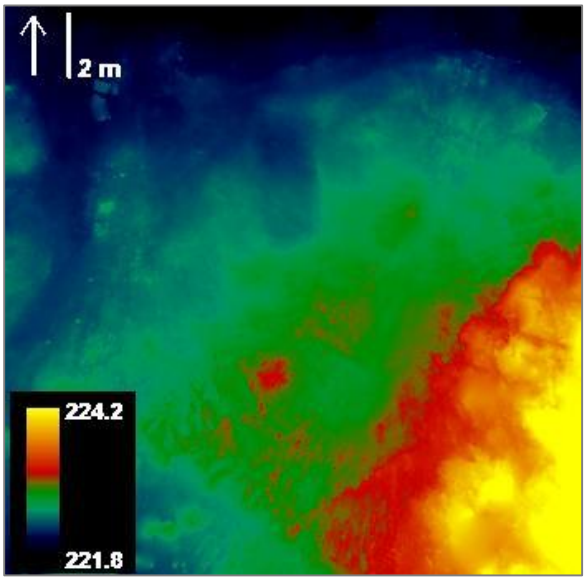

Figure 6.4-4: Elevation measurements of study area on 20 Nov. 2014 (post-burial).

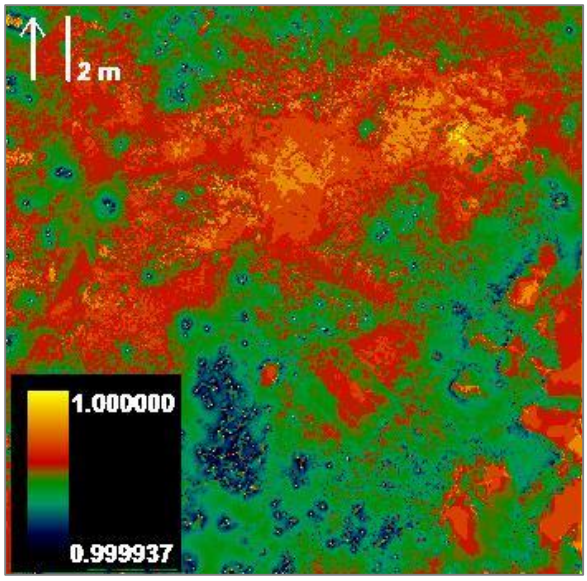

Figure 6.4-5: Sky-View Factor results of study area for 12 Feb. 2013 (baseline) elevation data; Gaussian stretch; higher values indicate higher visibility.

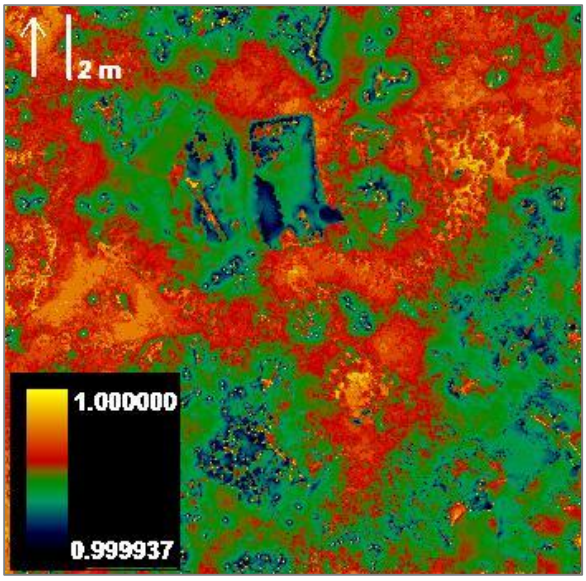

Figure 6.4-6: Sky-View Factor results of study area for 15 Feb. 2013 elevation data.

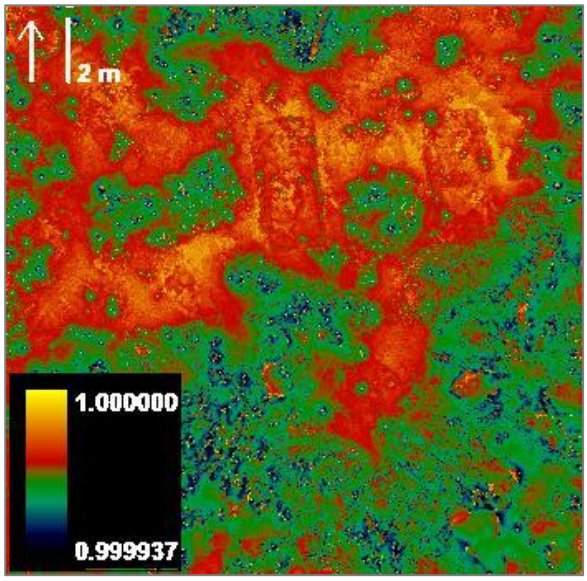

Figure 6.4-7: Sky-View Factor results of study area for 03 June 2013 elevation data.

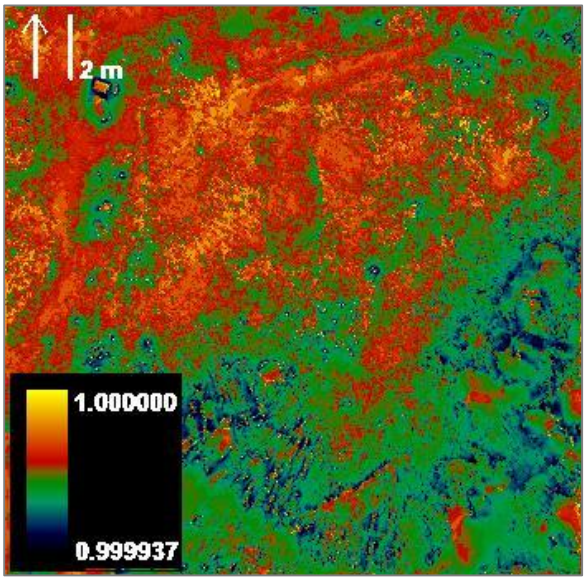

Figure 6.4-8: Sky-View Factor results of study area for 20 Nov. 2014 elevation data.

6.4.2 Elevation Change

Grave surfaces were visualized using terrestrial LIDAR to establish whether the surfaces exhibit elevation gain, elevation loss, or no change. Elevation change is determined by subtracting elevation measurements at an early date from elevation measurements at a later date. Comparisons are made with and without baseline data to simulate both ideal and realistic data scenarios (see **Figure 5.5-4**). The four collections include one pre-burial baseline observation and three post-burial observations. Each of the three post-burial collections is compared to the baseline collection to establish the extent of change over time under the experimental conditions (**Figures 6.4-10 – 6.4-15**). Since a typical forensic investigation will not include a baseline dataset, logical comparisons between all post-burial collections are made and are presented in **Figures 6.4-16 – 6.4-21**. Elevation change images were also run through the Sky-View Factor tool to emphasize differences (**Figures 6.4-22 – 6.4-27**). The original 15 February 2013 elevation image includes the grave containing six bodies, which was not completely backfilled when scans were made. Therefore, results that were derived using the 15 February 2013 elevation change images focus on the graves containing one and three individuals, respectively, and the control unit.

The elevation change data illustrate an important concept to be fully explored in Chapter 7 – that there are probably optimal temporal windows for observing burial surface features, indicating burial footprints emerge and then fade as taphonomic processes act on the grave and its surroundings (**Figures 6.4-10 – 6.4-21**). These windows are seen here only as an immediate elevation gain at the burial surface followed by an elevation loss at the same location. A final, gradual elevation gain is the result of organic debris accumulating in the burial surface depressions.

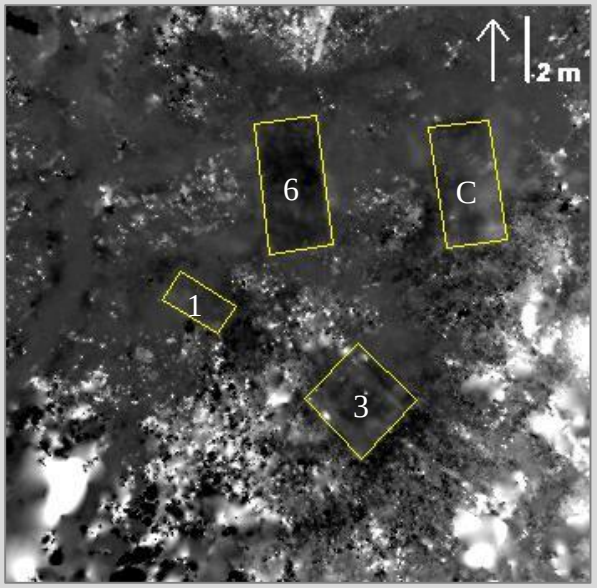

Figure 6.4-9: ROI overlays shown here for referencing burial locations in **Figures 6.4-10 – 6.4-12** and for extracting change data for **Figures 6.4-28 – 6.4-31** (no new data).

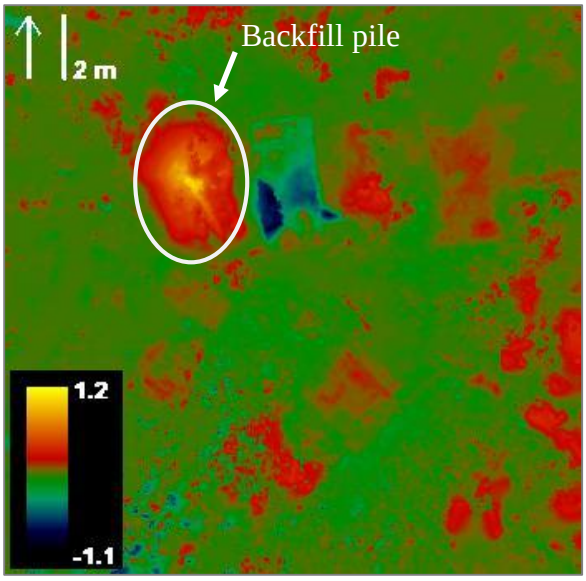

Figure 6.4-10: Elevation changes of study area between 12 Feb. – 15 Feb. 2013; linear stretch; values indicate net elevation change (m).

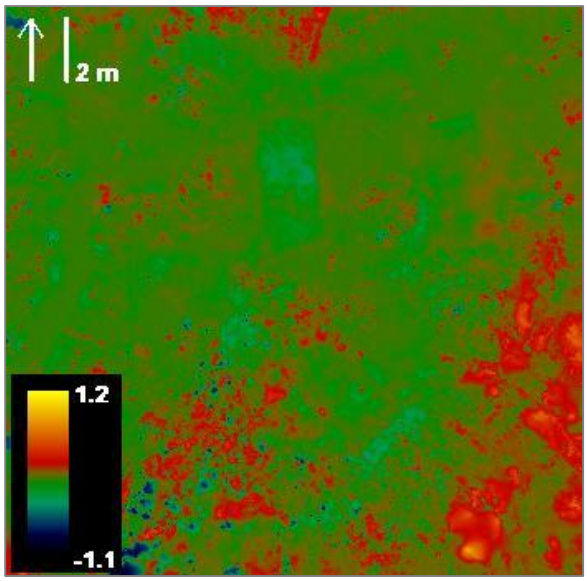

Figure 6.4-11: Net elevation changes of study area between 12 Feb. – 03 June 2013.

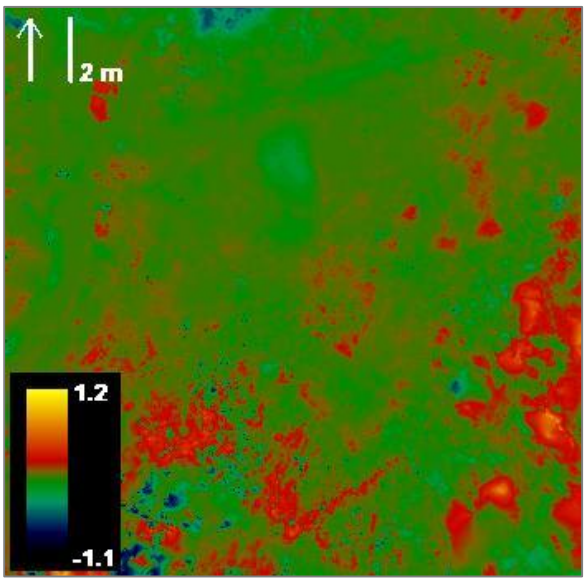

Figure 6.4-12: Net elevation changes of study area between 12 Feb. – 20 Nov. 2014.

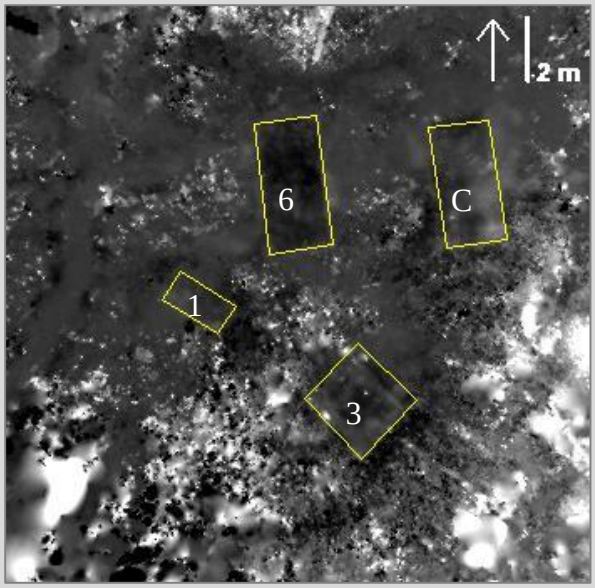

Figure 6.4-9: ROI overlays shown here for referencing burial locations in **Figures 6.4-16 – 6.4-18** and for extracting change data for **Figures 6.4-28 – 6.4-31** (no new data).

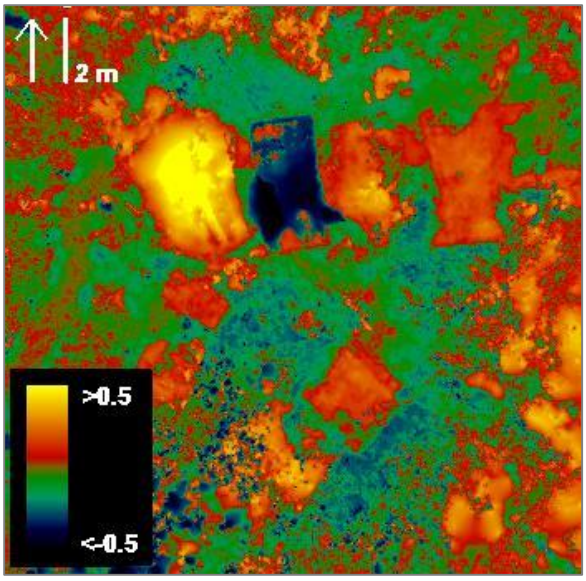

Figure 6.4-13: Elevation changes of study area between 12 Feb. – 15 Feb. 2013; Gaussian stretch; values indicate net elevation change (m).

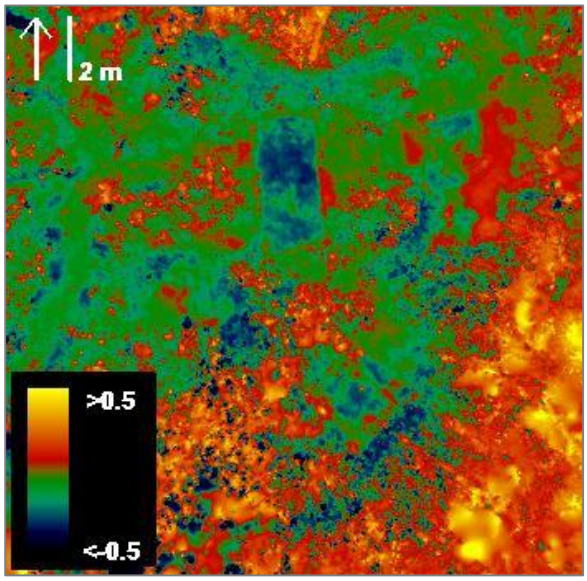

Figure 6.4-14: Elevation changes of study area between 12 Feb. – 03 June 2013.

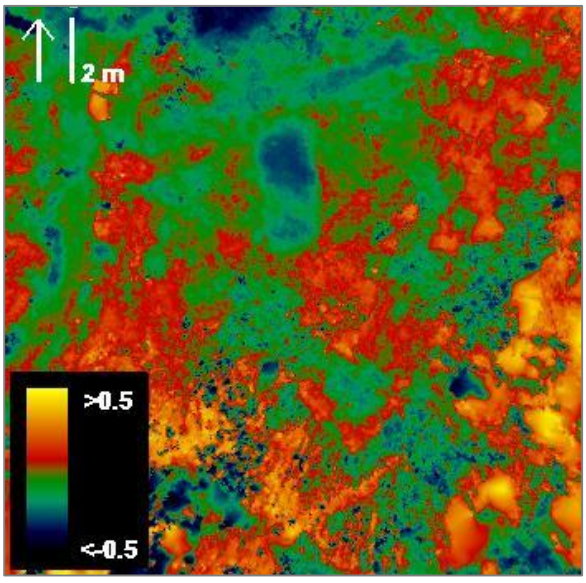

Figure 6.4-15: Elevation changes of study area between 12 Feb. – 20 Nov. 2014.

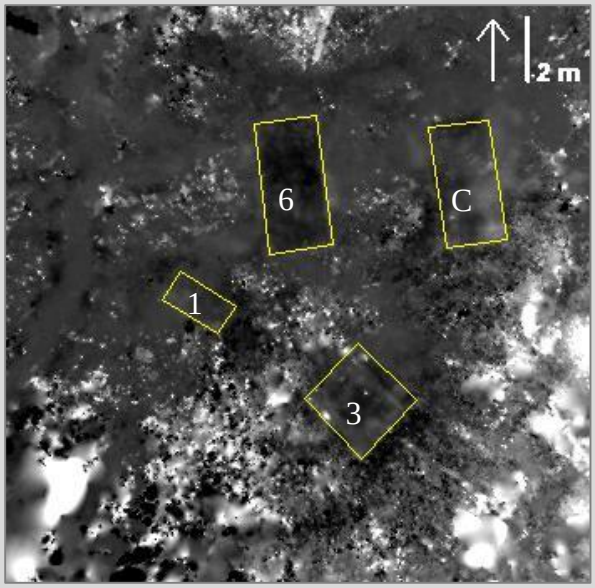

Figure 6.4-9*: ROI overlays shown here for referencing burial locations in **Figures 6.4-13 – 6.4-15** (no new data).

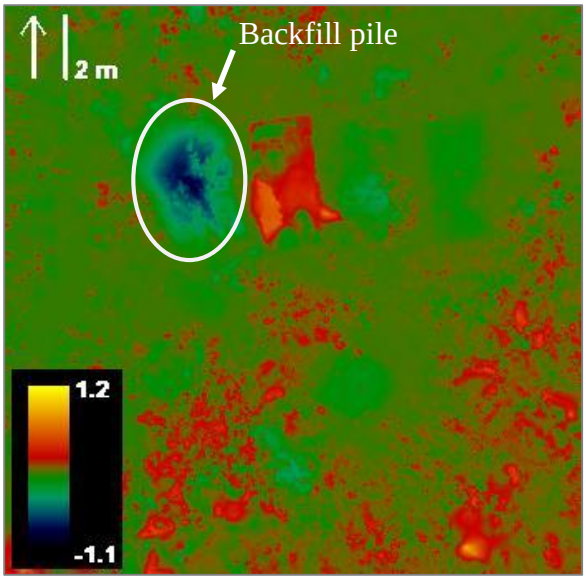

Figure 6.4-16: Elevation changes of study area between 15 Feb. – 03 June 2013; linear stretch; values indicate net elevation change (m).

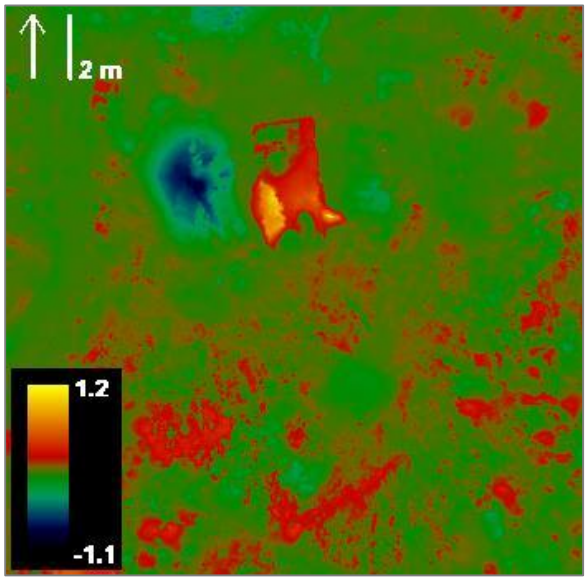

Figure 6.4-17: Elevation changes of study area between 15 Feb. 2013 – 20 Nov. 2014.

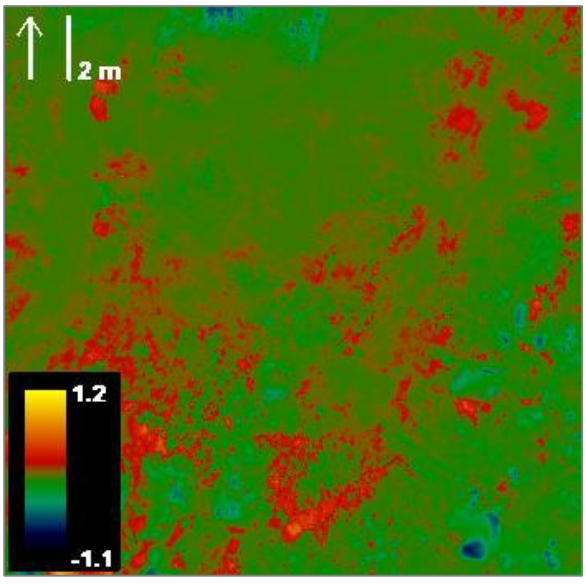

Figure 6.4-18: Elevation changes of study area between 03 June 2013 – 20 Nov. 2014.

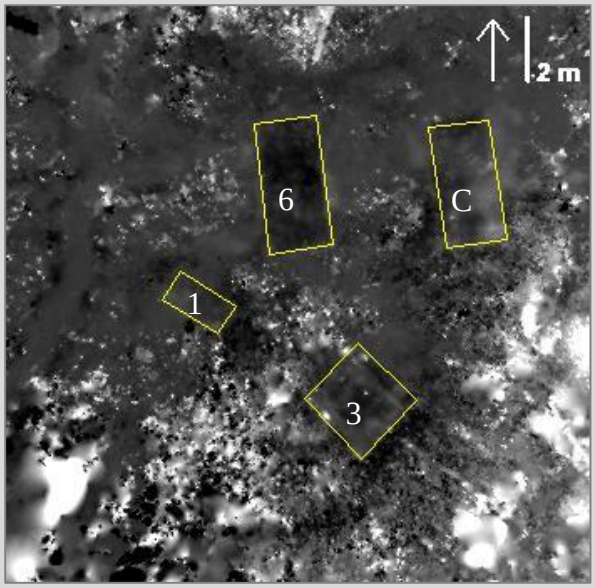

Figure 6.4-9*: ROI overlays shown here for referencing burial locations in **Figures 6.4-13 – 6.4-15** (no new data).

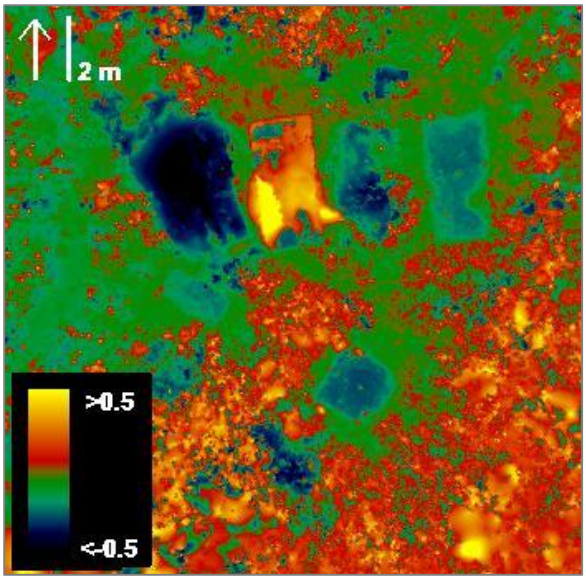

Figure 6.4-19: Elevation changes of study area between 15 Feb. – 03 June 2013; Gaussian stretch; values indicate net elevation change (m).

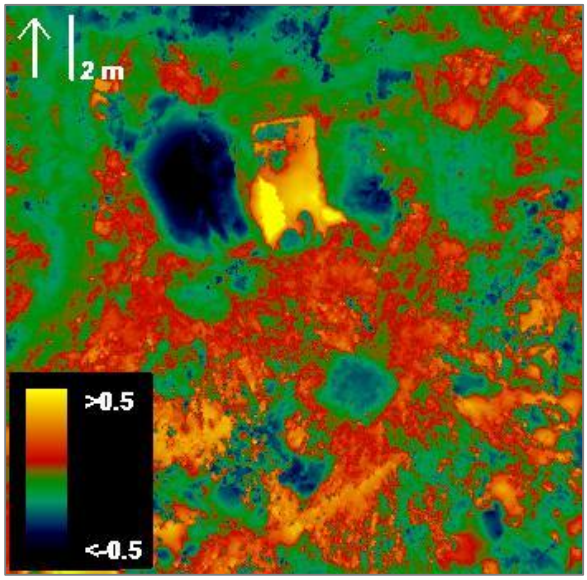

Figure 6.4-20: Elevation changes of study area between 15 Feb. 2013 – 20 Nov. 2014.

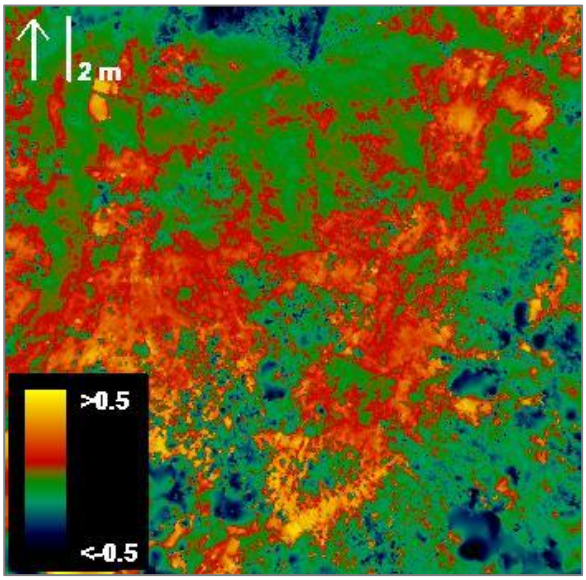

Figure 6.4-21: Elevation changes of study area between 03 June 2013 – 20 Nov. 2014.

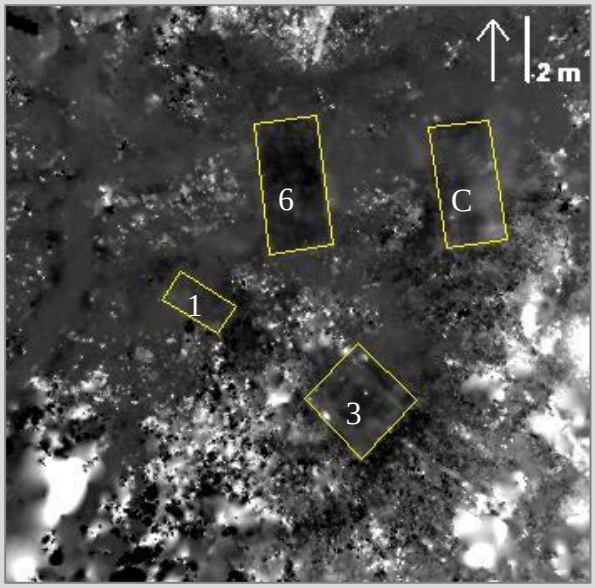

Figure 6.4-9: ROI overlays shown here for referencing burial locations in **Figures 6.4-22 – 6.4-24** and for extracting change data for **Figures 6.4-28 – 6.4-31** (no new data).

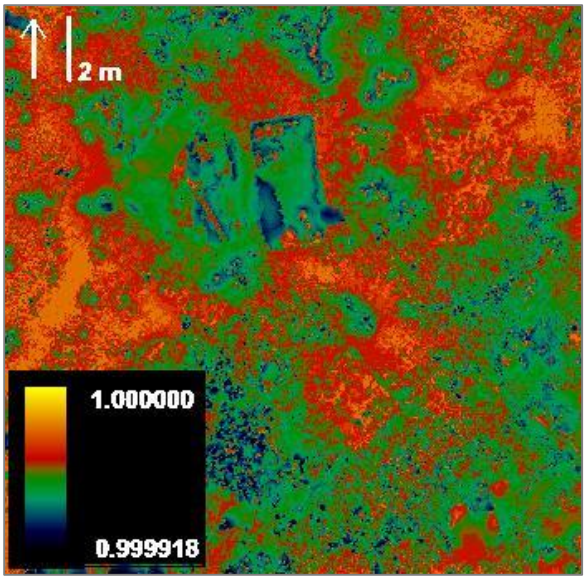

Figure 6.4-22: Sky-View Factor results of study area elevation changes between 12 Feb. – 15 Feb. 2013; Gaussian stretch; <u>higher values indicate higher visibility</u>.

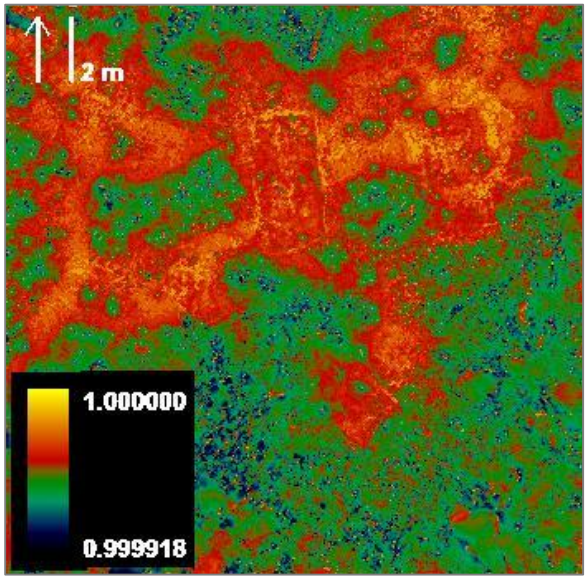

Figure 6.4-23: Sky-View Factor results of study area elevation changes between 12 Feb. – 03 June 2013.

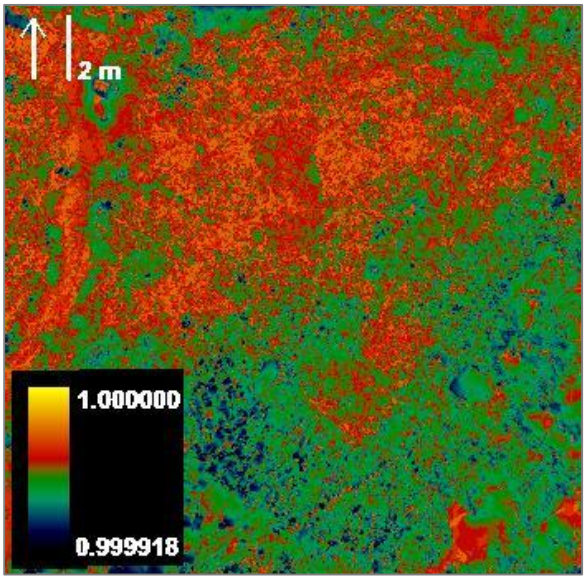

Figure 6.4-24: Sky-View Factor results of study area elevation changes between 12 Feb. – 20 Nov. 2014.

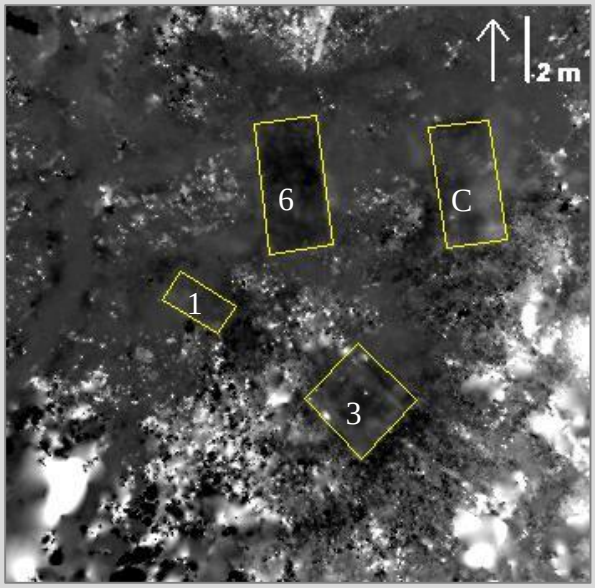

Figure 6.4-9*: ROI overlays shown here for referencing burial locations in **Figures 6.4-25 – 6.4-27** (no new data).

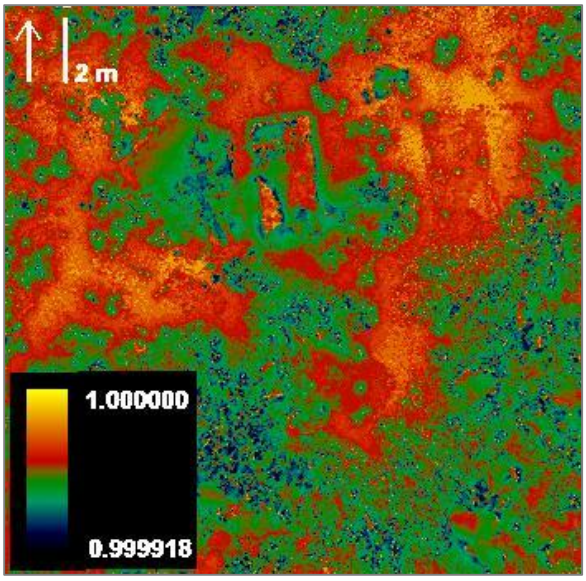

Figure 6.4-25: Sky-View Factor results of study area elevation changes between 15 Feb. – 03 June 2013; Gaussian stretch; higher values indicate higher visibility.

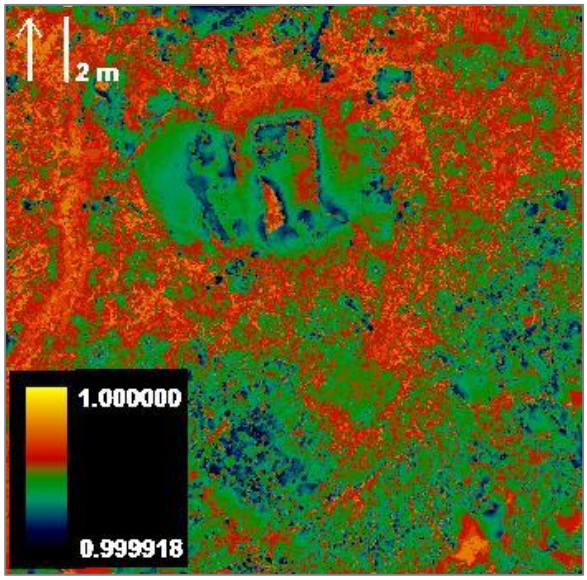

Figure 6.4-26: Sky-View Factor results of study area elevation changes between 15 Feb. 2013 – 20 Nov. 2014.

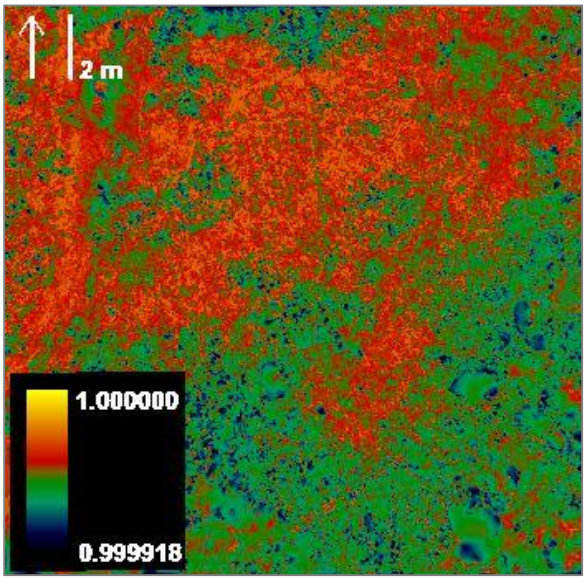

Figure 6.4-27: Sky-View Factor results of study area elevation changes between 03 June 2013 – 20 Nov. 2014.

The elevation change activity measured by terrestrial LIDAR are quantifiable and represent distinctive surface activity relative to the undisturbed surroundings. The surface elevation changes measured for each burial are distinctive to the extent that they can be spatially isolated using the density slice tool in ENVI. Density slices highlight image pixels with values falling within a user-specified range. Density slices were added to each grayscale elevation change image at 2 cm intervals within ranges determined from mean elevation change data presented in **Figures 6.4-28 – 6.4-31**. In this experimental context, grave surface elevation changes are predictable enough that certain elevation changes cluster spatially at precise burial locations, as shown in **Figures 6.4-32 – 6.4-37**. The progression of spatial clustering visibility is presented in (**Table 6.4-1**).

Change comparisons made using baseline elevation measurements, as visually emphasized using density slices **(Figures 6.4-32 – 6.4-37)**, show clustered elevation changes at all grave and control unit surfaces as a net elevation gain concentrated in the 3.0 – 11.0 cm range for all graves and the control unit by 15 February 2013 (one-day post-burial). Clustered surface activity then changes direction to present an elevation loss concentrated in the 4.0 – 12.0 cm range at the grave containing six bodies by 03 June 2013 (four-months post-burial), particularly in the northern portion of the grave that contains all six buried bodies. A similar clustered elevation loss is concentrated in the 0.0 – 8.0 cm range at the grave containing six bodies by 20 November 2014 (21-months post-burial) (**Table 6.4-1**).

The exclusively post-burial comparisons demonstrate a clustered elevation loss concentrated in the 4.0 – 12.0 cm range at the one-grave, three-grave, and control unit surfaces between 15 February – 03 June 2013. The visibility begins to diminish by 03 June 2013, but clustered elevation loss is concentrated in the 1.0 – 9.0 cm range at the three-grave and control unit surfaces between 15 February 2013 – 20 November 2014. Finally, there is no evidence of clustered

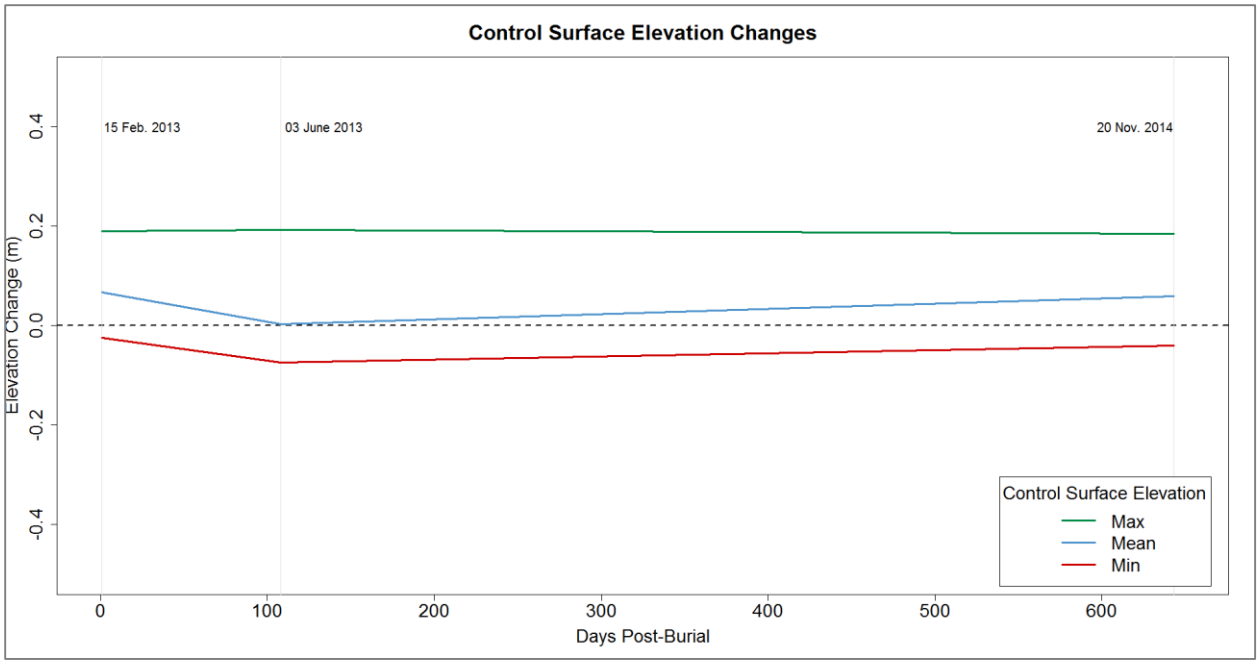

Figure 6.4-28: Control minimum, mean, and maximum surface elevation changes from 12 Feb. 2013 (baseline); data extracted from ROIs depicted in **Figure 6.4-9**.

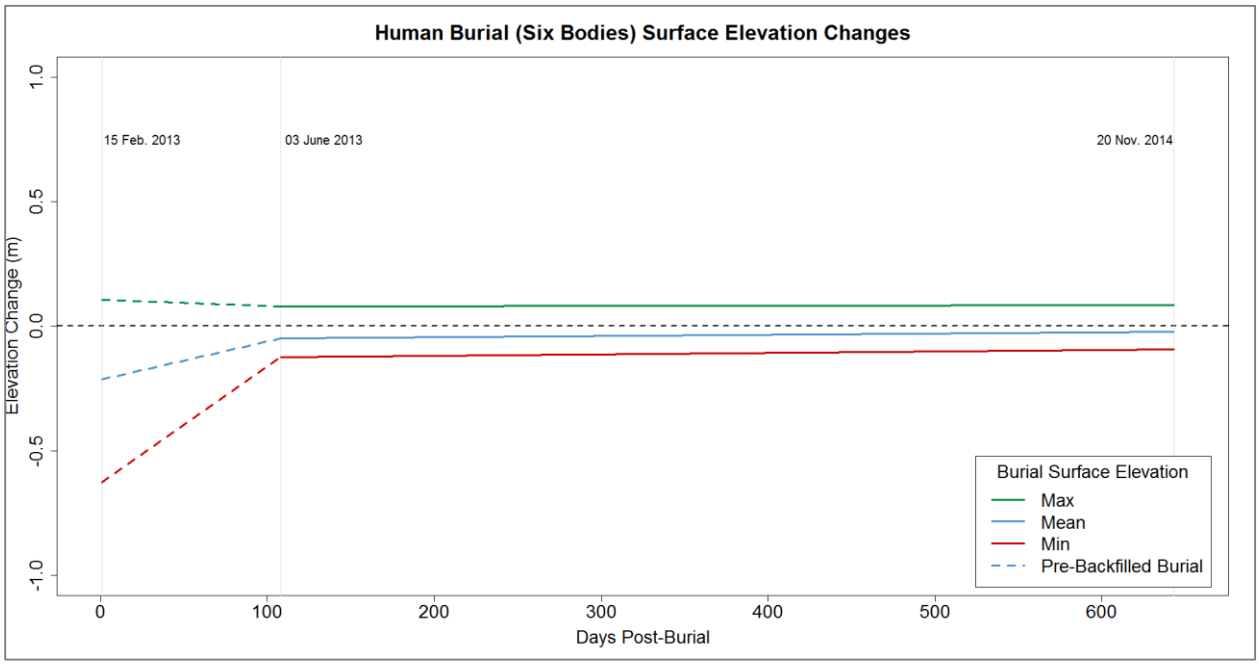

Figure 6.4-29: Six-person grave minimum, mean, and maximum surface elevation changes from 12 Feb. 2013 (baseline); data extracted from ROIs depicted in **Figure 6.4-9**.

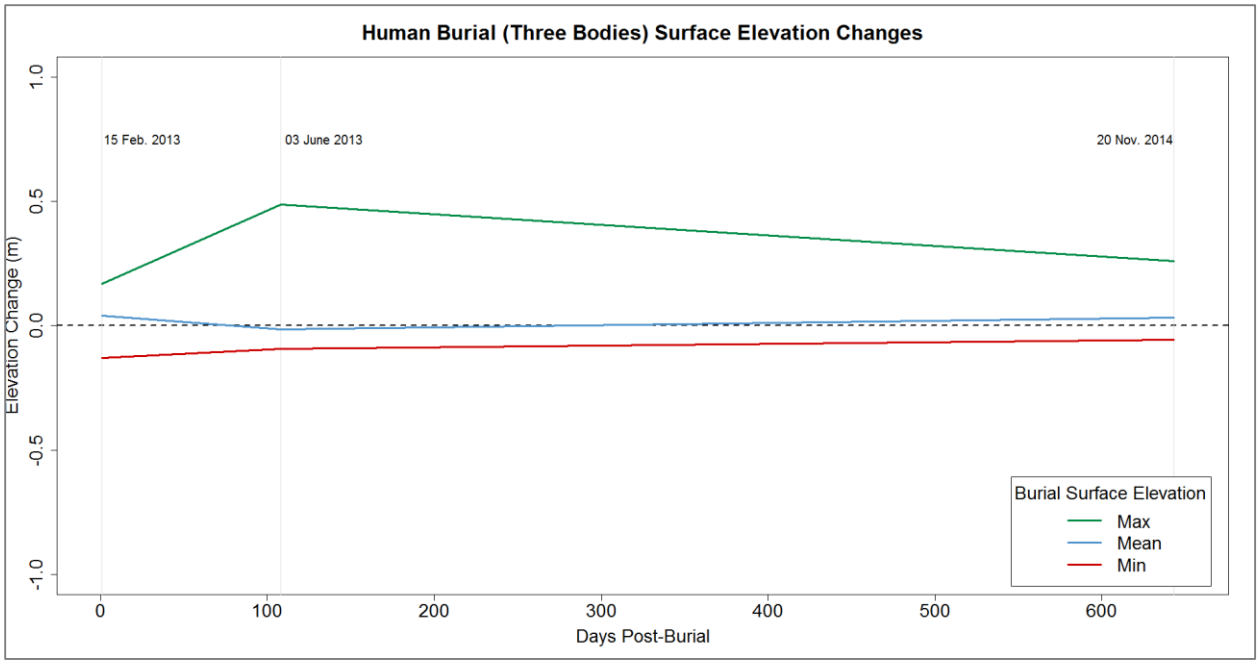

Figure 6.4-30: Three-person grave minimum, mean, and maximum surface elevation changes from 12 Feb. 2013 (baseline); data extracted from ROIs depicted in **Figure 6.4-9**.

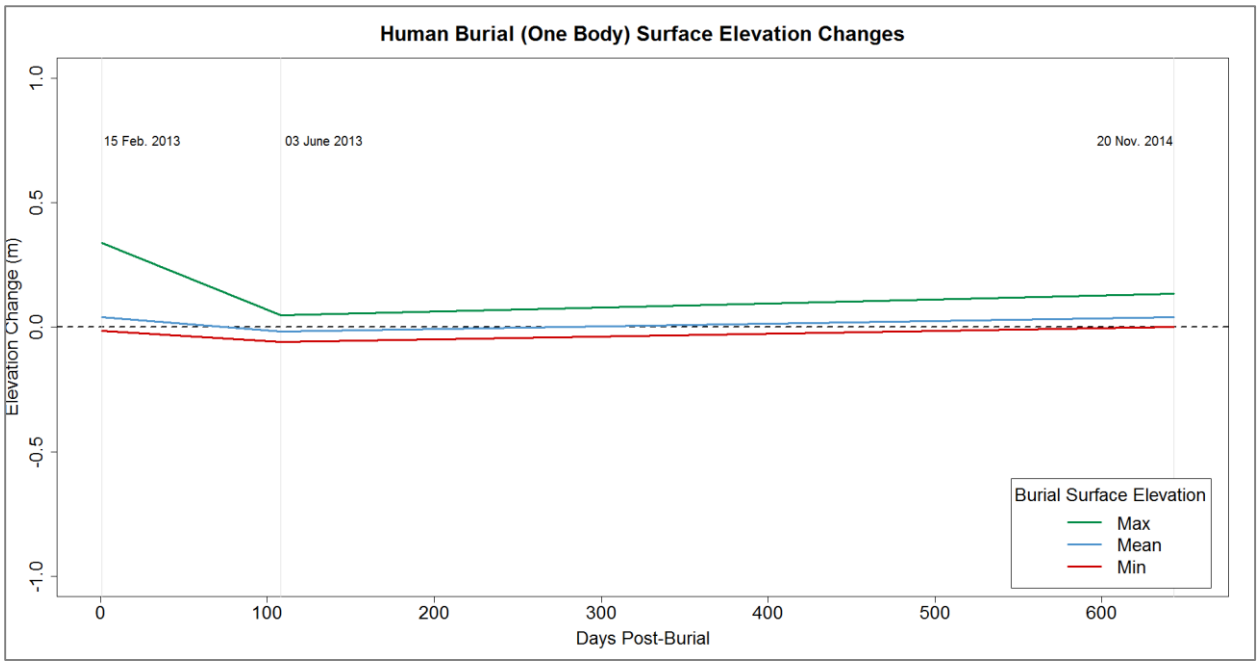

Figure 6.4-31: One-person grave minimum, mean, and maximum surface elevation changes from 12 Feb. 2013 (baseline); data extracted from ROIs depicted in **Figure 6.4-9**.

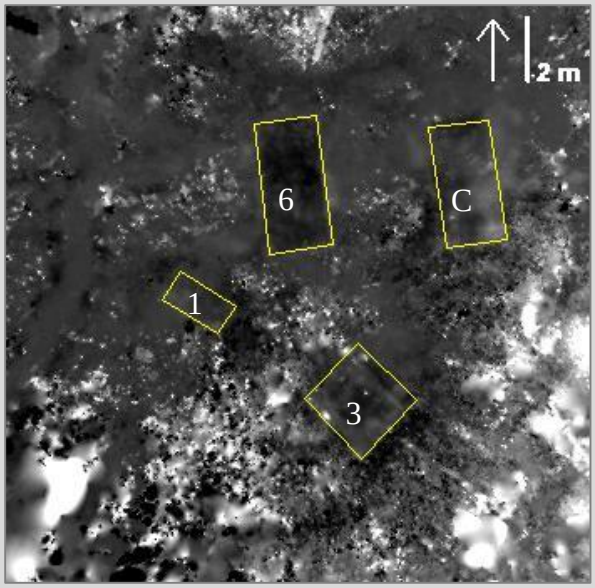

Figure 6.4-9*: ROI overlays shown here for referencing burial locations in **Figures 6.4-32 – 6.4-34** (no new data).

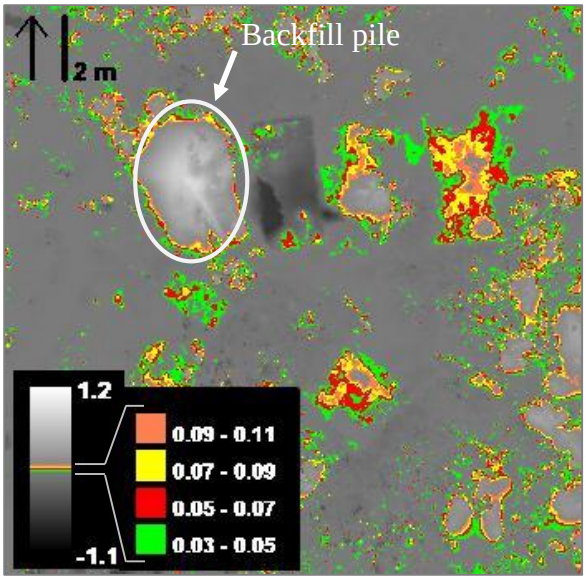

Figure 6.4-32: Elevation changes of study area between 12 Feb. – 15 Feb. 2013; 2 cm density slices added to emphasize elevation change clustering at 0.03 – 0.11 m; values follow means from **Figures 6.4-16 – 6.4-19**.

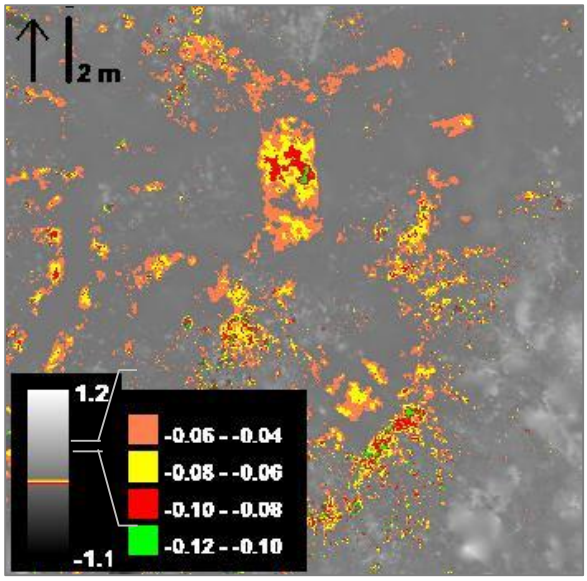

Figure 6.4-33: Elevation changes of study area between 12 Feb. – 03 June 2013; 2 cm density slices added for -0.12 - -0.04 m.

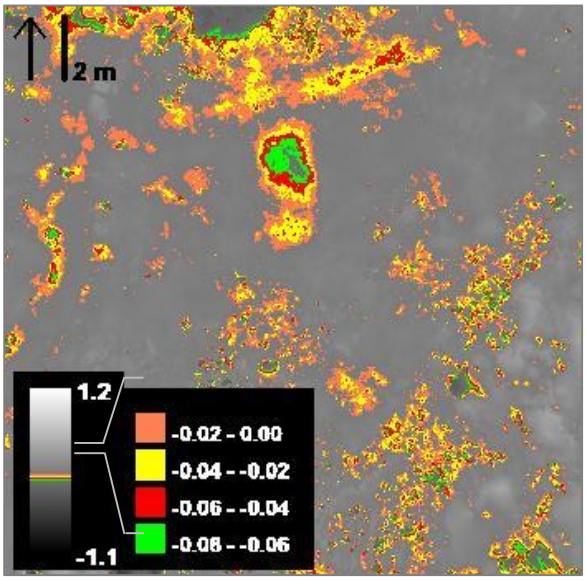

Figure 6.4-34: Elevation changes of study area between 12 Feb. 2013 – 20 Nov. 2014; 2 cm density slices added for -0.08 – 0.00 m.

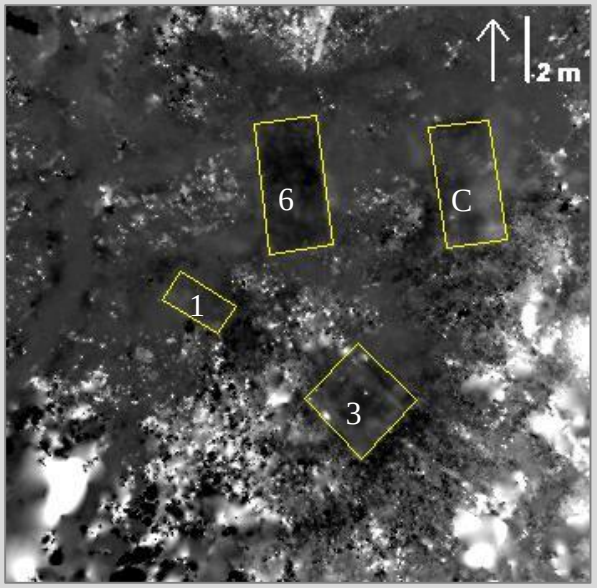

Figure 6.4-9*: ROI overlays shown here for referencing burial locations in **Figures 6.4-35 – 6.4-37** (no new data).

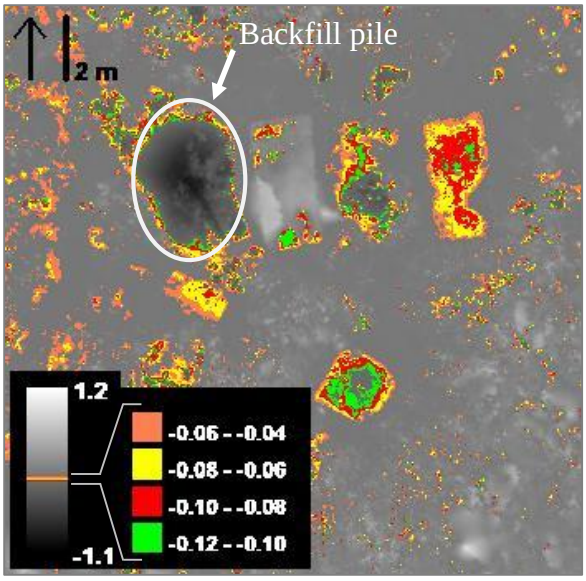

Figure 6.4-35: Elevation changes of study area between 15 Feb. – 03 June 2013; 2 cm density slices added to emphasize elevation change clustering at -0.12 - -0.04 m; values follow means from **Figures E.4 – E.6.**

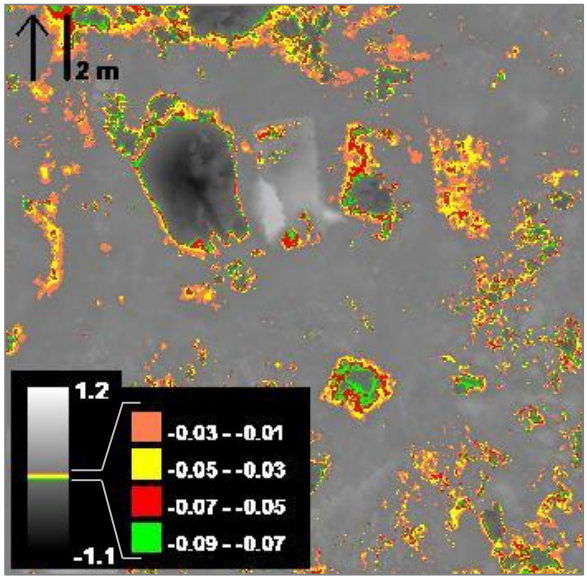

Figure 6.4-36: Elevation changes of study area between 15 Feb. 2013 – 20 Nov. 2014; 2 cm density slices added for -0.09 - -0.01 m.

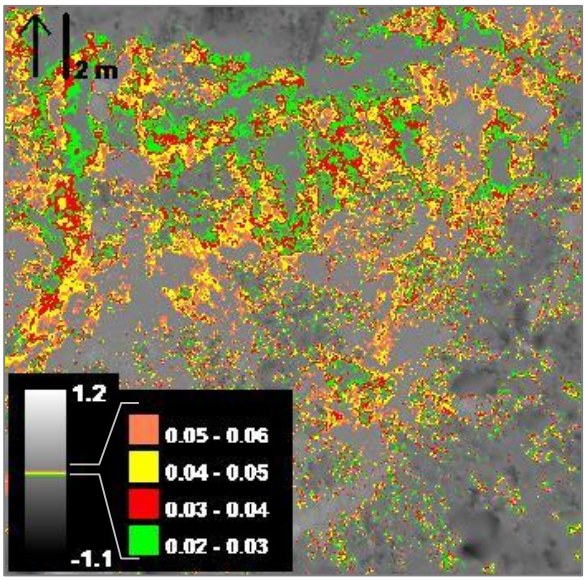

Figure 6.4-37: Elevation changes of study area between 03 June 2013 – 20 Nov. 2014; 2 cm density slices for 0.02 – 0.06 m.

Table 6.4-1: Spatial clustering of net elevation change, as observed for each entire grave surface using density slicing (**Figures 6.4-32 – 6.4-37**); green and red cells indicate visible clustering of elevation gain or loss, respectively, at each grave surface; no highlighting indicates a lack of visible spatial clustering for that location and date combination; "N/A" indicates no data.

	Control	Grave-1	Grave-3	Grave-6
Baseline to 15 Feb. 2013	0.07	0.04	0.04	N/A
Baseline to 03 June 2013	0.00	-0.02	-0.02	-0.05
Baseline to 20 Nov. 2014	0.06	0.04	0.03	-0.02
15 Feb. to 03 June	-0.06	-0.06	-0.06	N/A
15 Feb. to 20 Nov.	-0.01	0.01	-0.00	N/A
03 June to 20 Nov.	0.05	0.06	0.05	0.03

elevation change between 03 June 2013 and 20 November 2014 (**Table 6.4-1**).

The grave containing six bodies was further evaluated using two additional approaches. First, elevation change values were extracted along a 5 cm-wide north-south midline transect depicted in **Figures 6.4-38 – 6.4-43** as elevation change profiles. Second, the entire largest grave surface was divided into the northern portion of the grave directly over the buried bodies and the southern portion which contains no bodies, to separate the overall surface elevation change distributions for each half (**Tables 6.4-2 – 6.4-4**). 15 February collections are included in the elevation profiles to illustrate the extent of change, but are omitted from tables because the collection is dominated by elevation change resulting from uneven and incomplete backfilled soil.

The grave surface activity exhibits an overall ramp-like quality, where the elevation change measurements deviate the most in the northern half of the grave surface. Of the three elevation change profiles that do not include the problematic 15 February collection, two reveal concentrated elevation loss features that are greatest in the northern portion of the grave directly over the buried bodies and another feature in the southern portion of the same grave containing no buried bodies. When compared to baseline elevation, the 03 June 2013 transect (**Figures 6.4-41**) and 20 November 2014 transect (**Figure 6.4-42**) illustrate this trend, while the comparison between 03 June 2013 and 20 November 2014 does not (**Figure 6.4-43**). Elevation loss along the midline transect ranges from 0.6 – 8.6 cm between 12 February and 03 June 2013, with the greatest elevation loss occurring directly over the buried bodies. Similarly, elevation loss along the same transect ranges from 0.5 – 8.3 cm between 12 February 2013 and 20 November 2013, with the greatest elevation loss observed directly over the buried bodies. The difference between the maximum elevation loss along the transect for the northern elevation loss feature and southern elevation loss feature is 1.5 cm for 12 February – 03 June 2013 (**Figure 6.4-41**) and 3.2 cm for 12

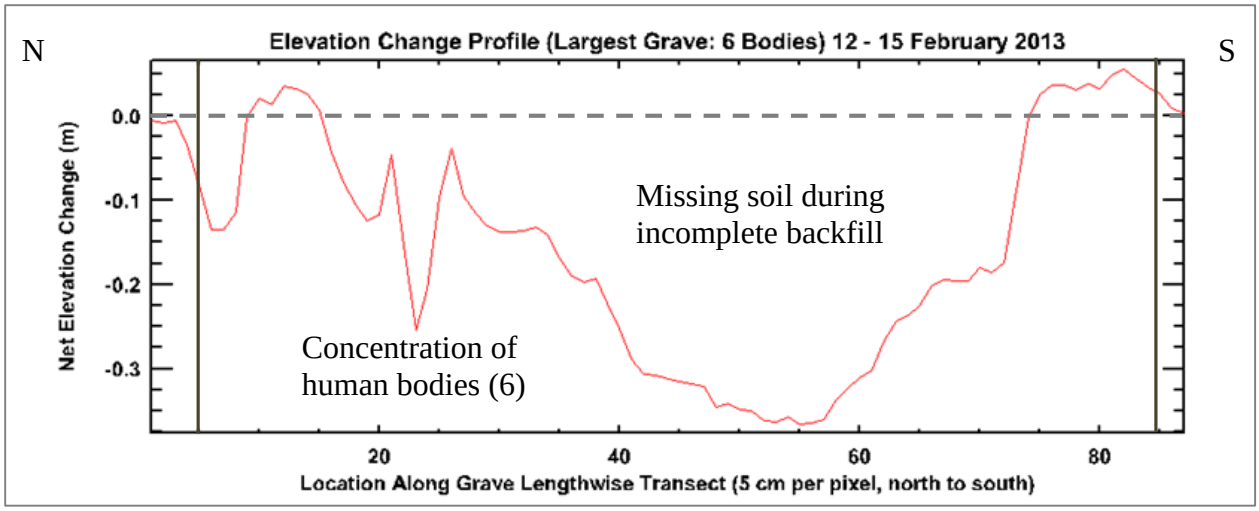

Figure 6.4-38: Net elevation change profile along the north-south midline transect of the largest grave between 12 – 15 February 2013. The dashed horizontal line represents zero net elevation change. Vertical lines represent approximate north/south grave walls. The largest grave was not completely backfilled when the 15 February 2013 collection was made, as observed by the extent of elevation loss between the two dates.

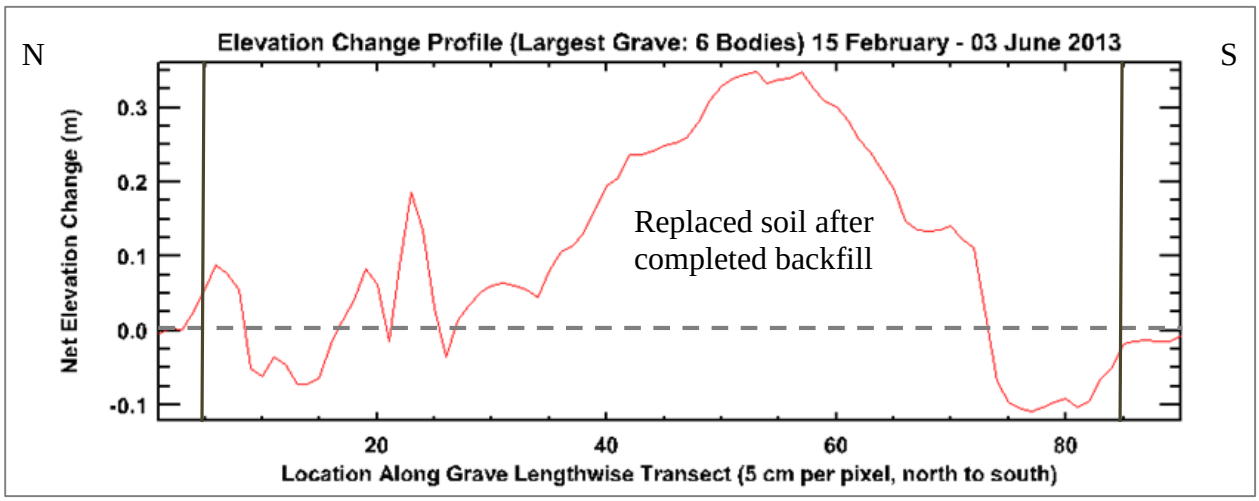

Figure 6.4-39: Net elevation change profile along the north-south midline transect of the largest grave between 115 February – 03 June 2013. The dashed horizontal line represents zero net elevation change. Vertical lines represent approximate north/south grave walls. The largest grave was not completely backfilled when the 15 February 2013 collection was made, as observed by the extent of elevation gain between the two dates.

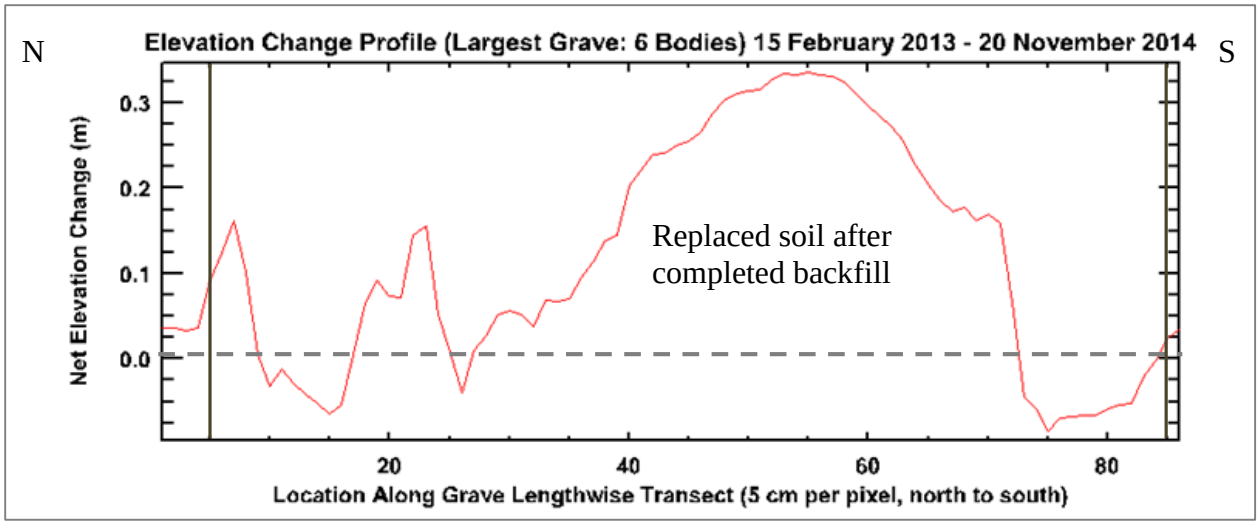

Figure 6.4-40: Net elevation change profile along the north-south midline transect of the largest grave between 15 February 2013 – 20 November 2014. The dashed horizontal line represents zero net elevation change. Vertical lines represent approximate north/south grave walls. The largest grave was not completely backfilled when the 15 February 2013 collection was made, as observed by the extent of elevation gain between the two dates.

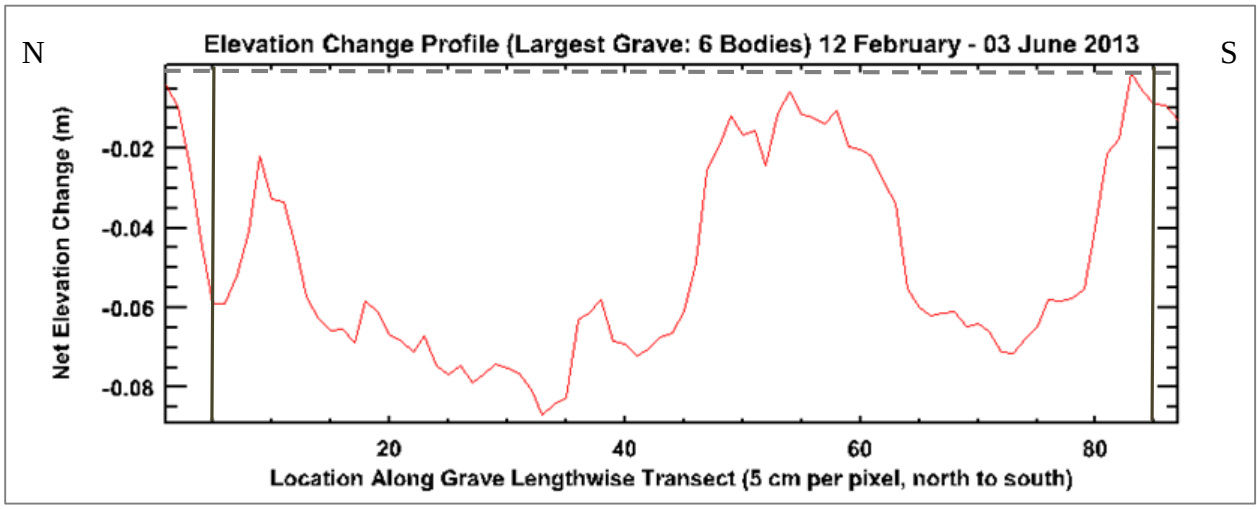

Figure 6.4-41: Net elevation change profile along the north-south midline transect of the largest grave between 12 February – 03 June 2013. The dashed horizontal line represents zero net elevation change. Vertical lines represent approximate north/south grave walls. The greatest elevation change is observed directly over the concentration of buried bodies in the northern half of the grave, followed by elevation loss to a lesser extent directly over the southern half which contains disturbed soil only.

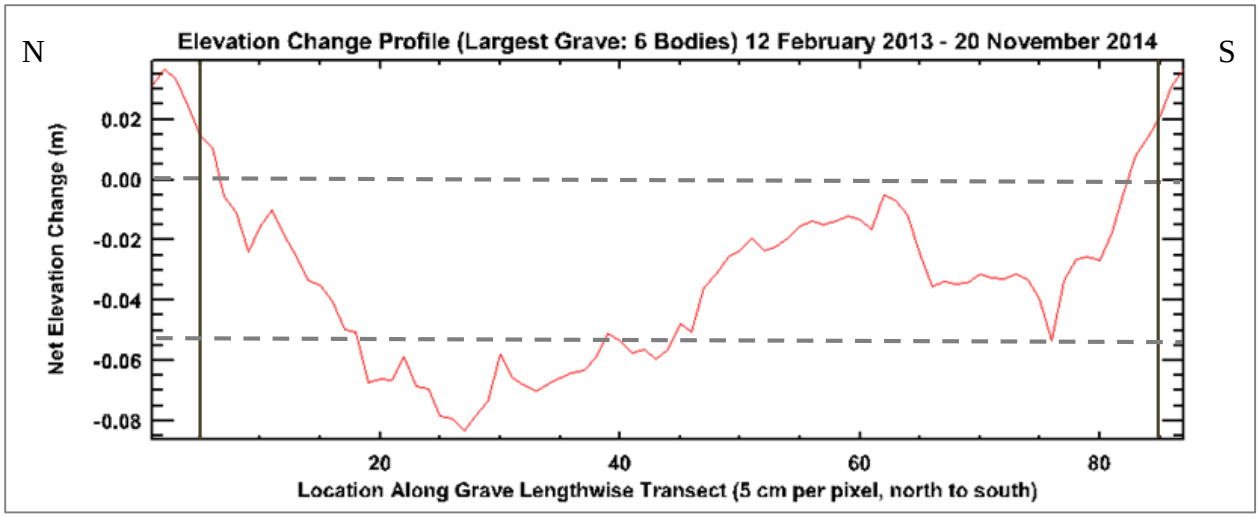

Figure 6.4-42: Net elevation change profile along the north-south midline transect of the largest grave between 12 February 2013 – 20 November 2014. The dashed horizontal line represents zero net elevation change. Vertical lines represent approximate north/south grave walls. The greatest elevation change is observed directly over the concentration of buried bodies in the northern half of the grave (left), followed by elevation loss to a lesser extent directly over the southern half (right) which contains disturbed soil only.

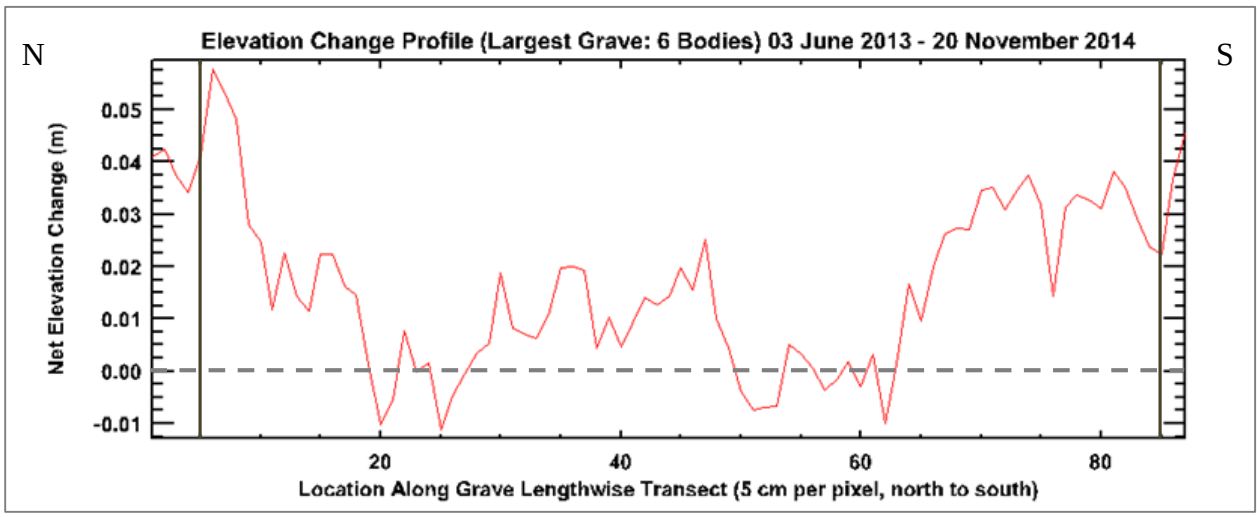

Figure 6.4-43: Net elevation change profile along the north-south midline transect of the largest grave between 03 June 2013 – 20 November 2014. The dashed horizontal line represents zero net elevation change. Vertical lines represent approximate north/south grave walls. Localized elevation change is absent, and replaced with generalized elevation change.

Table 6.4-2: Statistical distributions of net elevation change for the northern and southern halves of the largest grave, generally illustrating the elevation change differences observed directly over a concentration of six buried bodies (North) and directly over disturbed soil (South) between 12 February and 03 June 2013.

12 Feb. – 03 June 2013	Min.	Mean	Max.	St. Dev.
North	-0.118301	-0.056474	0.079102	0.025264
South	-0.125595	-0.042945	0.049438	0.021171

Table 6.4-3: Statistical distributions of net elevation change for the northern and southern halves of the largest grave, generally illustrating the elevation change differences observed directly over a concentration of six buried bodies (North) and directly over disturbed soil (South) between 12 February 2013 and 20 November 2014.

12 Feb. 2013 – 20 Nov. 2014	Min.	Mean	Max.	St. Dev.
North	-0.093796	-0.035028	0.046524	0.032901
South	-0.078506	-0.010140	0.085419	0.023931

Table 6.4-4: Statistical distributions of net elevation change for the northern and southern halves of the largest grave, generally illustrating the elevation change differences observed directly over a concentration of six buried bodies (North) and directly over disturbed soil (South) between 03 June 2013 and 20 November 2014.

03 June 2013 – 20 Nov. 2014	Min.	Mean	Max.	St. Dev.
North	-0.065231	0.021446	0.081558	0.018071
South	-0.058029	0.032805	0.103745	0.016397

February 2013 – 20 November 2014 (**Figure 6.4-42**). No apparent spatial pattern of elevation change is present along the transect between 03 June 2013 and 20 November 2014 (**Figure 6.4-43** and **Table 6.4-4**). These trends are supported by the north-south statistical distributions for the same date comparisons, where the mean elevation change between northern and southern surfaces of the largest grave is 1.35 cm for the 12 February – 03 June 2013 comparison (**Table 6.4-2**), 2.49 cm for the 12 February 2013 – 20 November 2014 comparison (**Table 6.4-3**), and 1.14 cm for the 03 June 2013 – 20 November 2014 comparison (**Table 6.4-3**).

6.5 Airborne LIDAR

6.5.1 Elevation

Airborne LIDAR is analyzed to evaluate the potential scalability of terrestrial findings. For each airborne LIDAR image, every pixel contains one elevation value. Elevation images at 10 cm GSD are presented in **Figures 6.5-1 – 6.5-4,** one for each of the four collection dates, with images showing the full study area extent and insets zoomed to the immediate area surrounding burial locations. None of the airborne LIDAR elevation images reveal distinctive surface anomalies at any of the burial locations.

6.5.2 Elevation Change

Airborne LIDAR elevation change images are derived using the same image subtraction process used for terrestrial LIDAR elevation change images, where one elevation image at an early date is subtracted from another at a later date to produce a net elevation change image. Comparisons are made between all four airborne LIDAR collections and are presented in **Figures 6.5-5 – 6.5-10**. None of the elevation change images reveal distinctive anomalies at any of the burial locations.

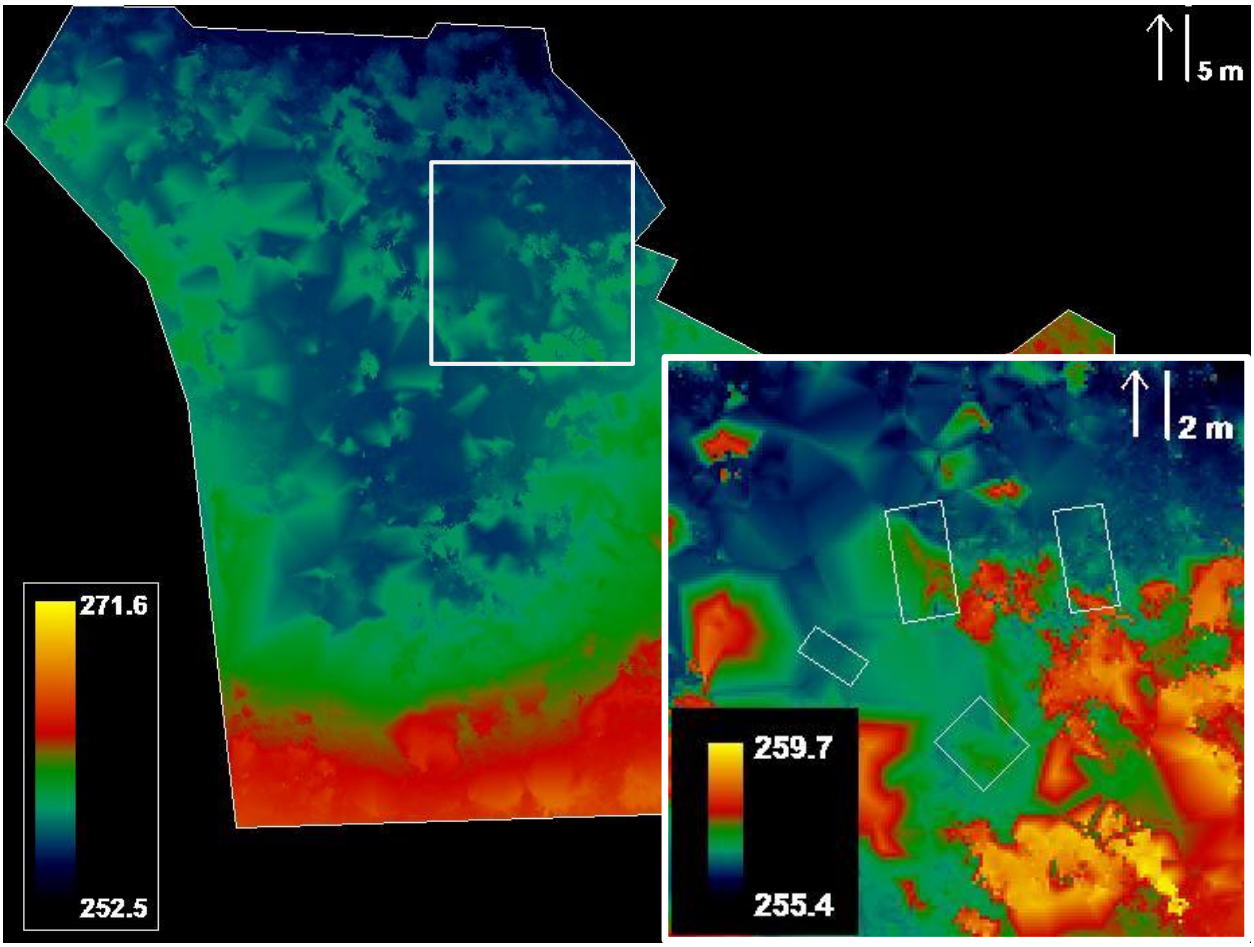

Figure 6.5-1: Elevation measurements of fenced study area (main) with immediate burial area (inset) on 18 September 2014; 10 cm GSD; values indicate ground elevation (m).

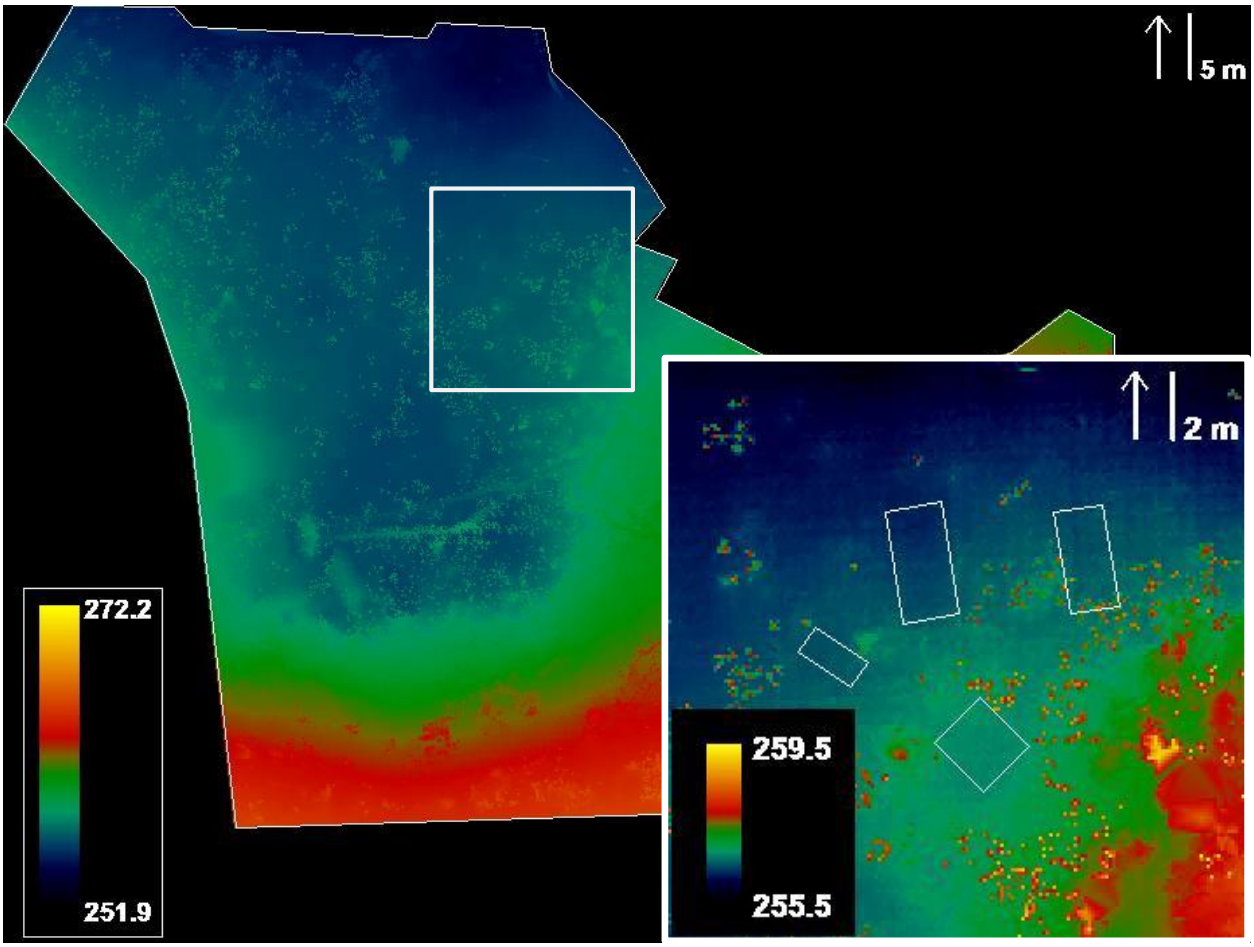

Figure 6.5-2: Elevation measurements of fenced study area (main) with immediate burial area (inset) on 23 March 2015; 10 cm GSD; values indicated ground elevation (m).

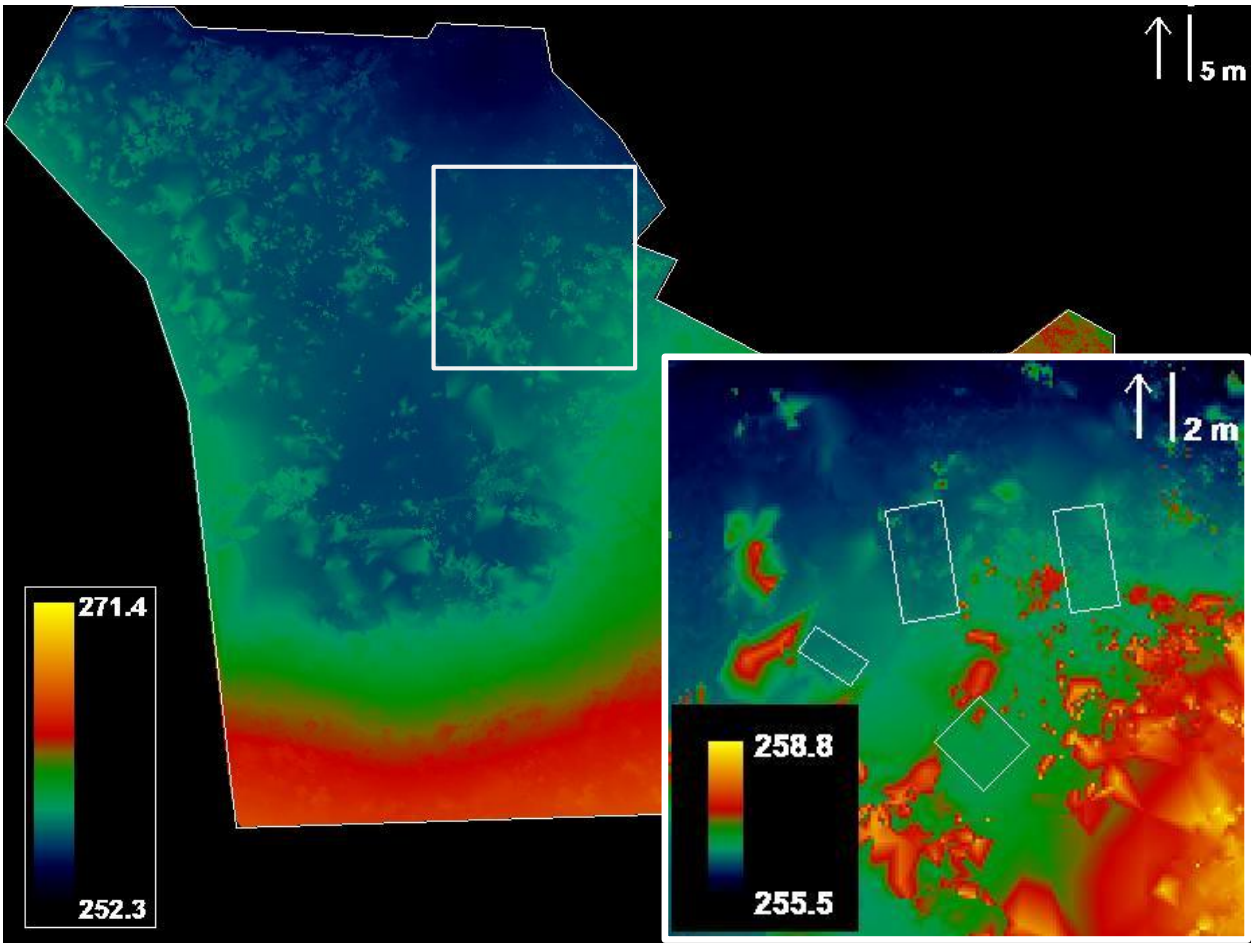

Figure 6.5-3: Elevation measurements of fenced study area (main) with immediate burial area (inset) on 17 April 2015; 10 cm GSD; values indicate ground elevation (m).

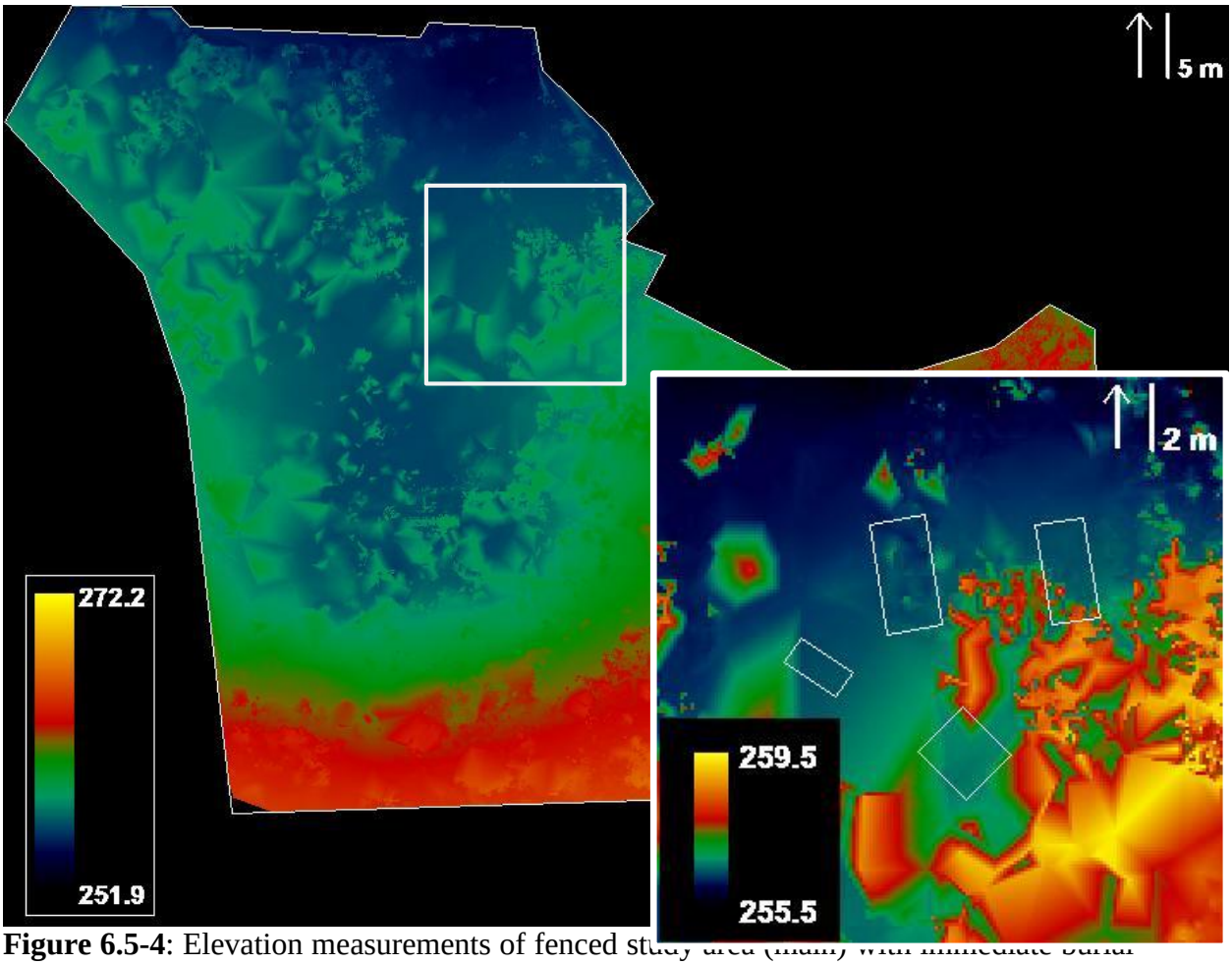

Figure 6.5-4: Elevation measurements of fenced study area (main) with immediate burial area (inset) on 07 May 2015; 10 cm GSD; values indicate ground elevation (m).

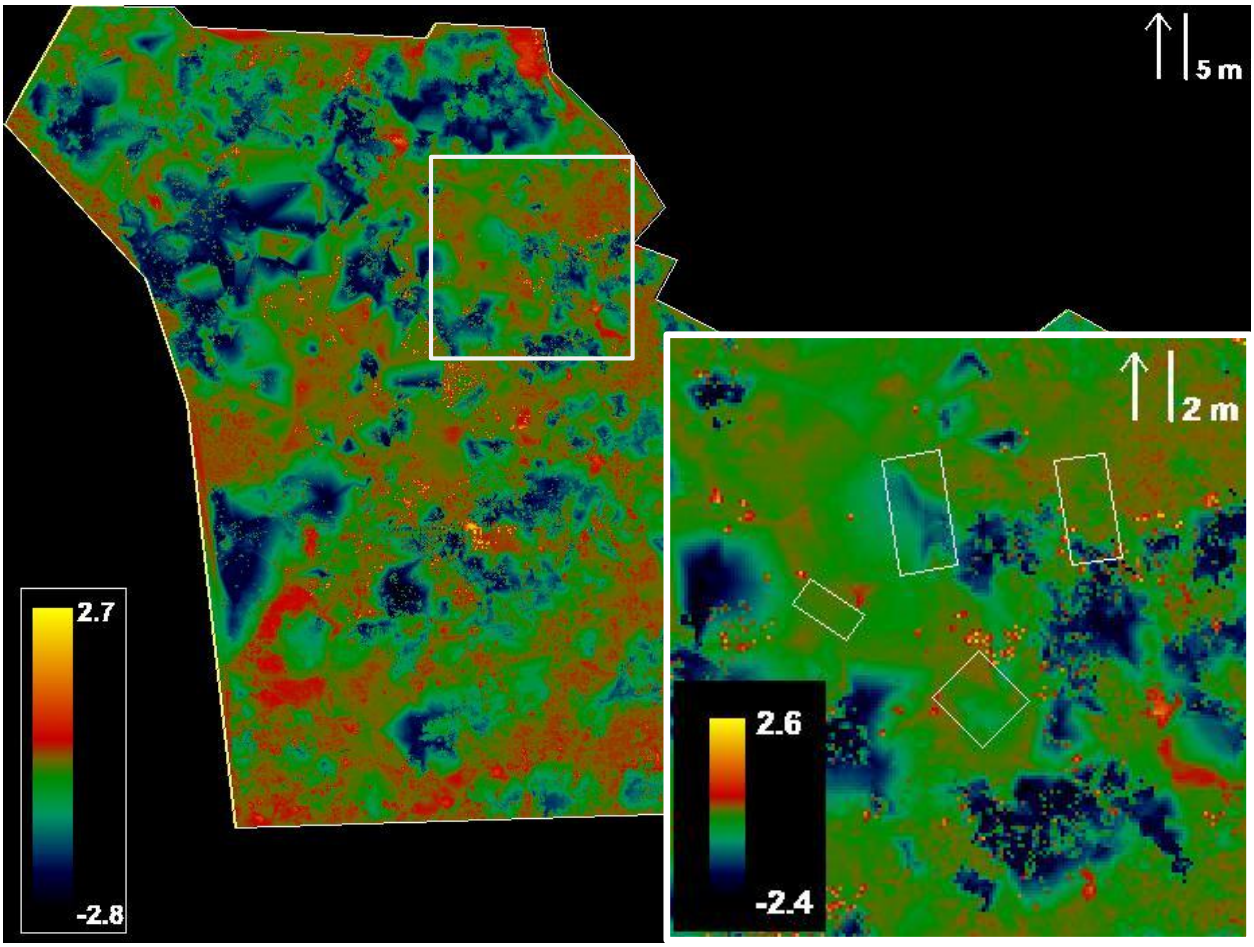

Figure 6.5-5: Elevation changes within fenced study area (main) with immediate burial area (inset) between 18 Sept. 2014 – 23 Mar. 2015; 10 cm GSD; values indicate elevation change (m).

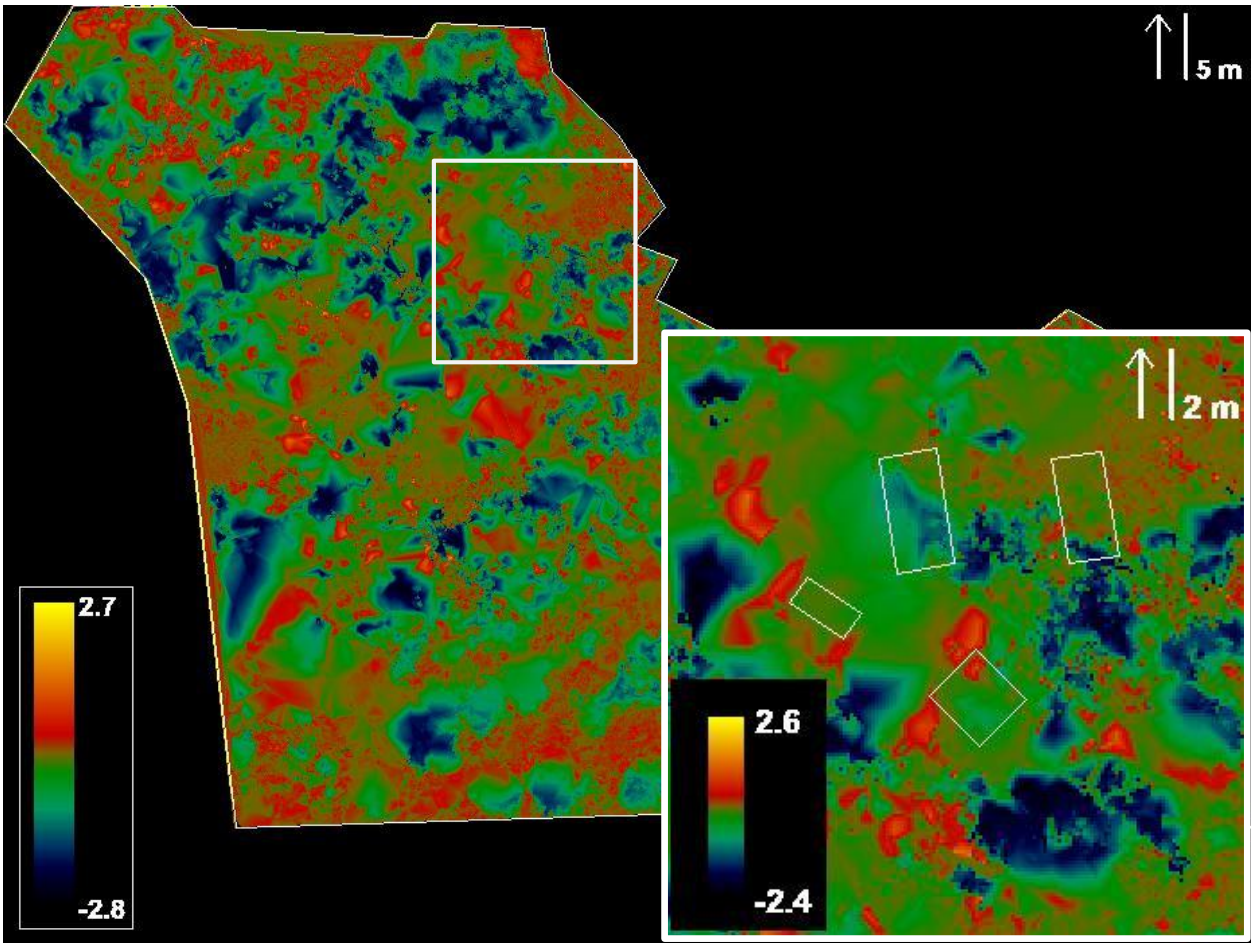

Figure 6.5-6: Elevation changes within fenced study area (main) with immediate burial area (inset) between 18 Sept. 2014 – 17 April 2015; 10 cm GSD; values indicate elevation change (m)

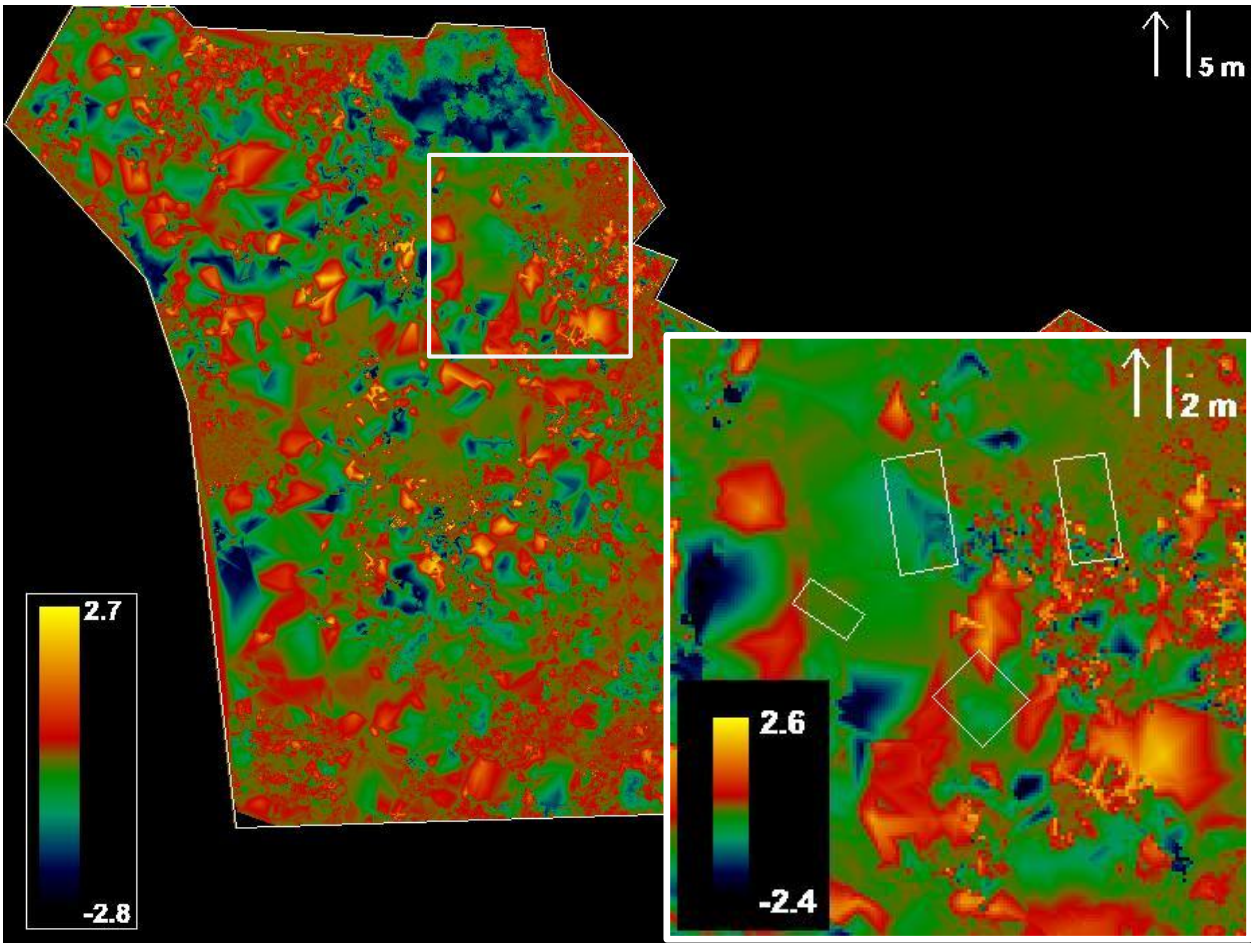

Figure 6.5-7: Elevation changes within fenced study area (main) with immediate burial area (inset) between 18 Sept. 2014 – 07 May 2015; 10 cm GSD; values indicate elevation change (m).

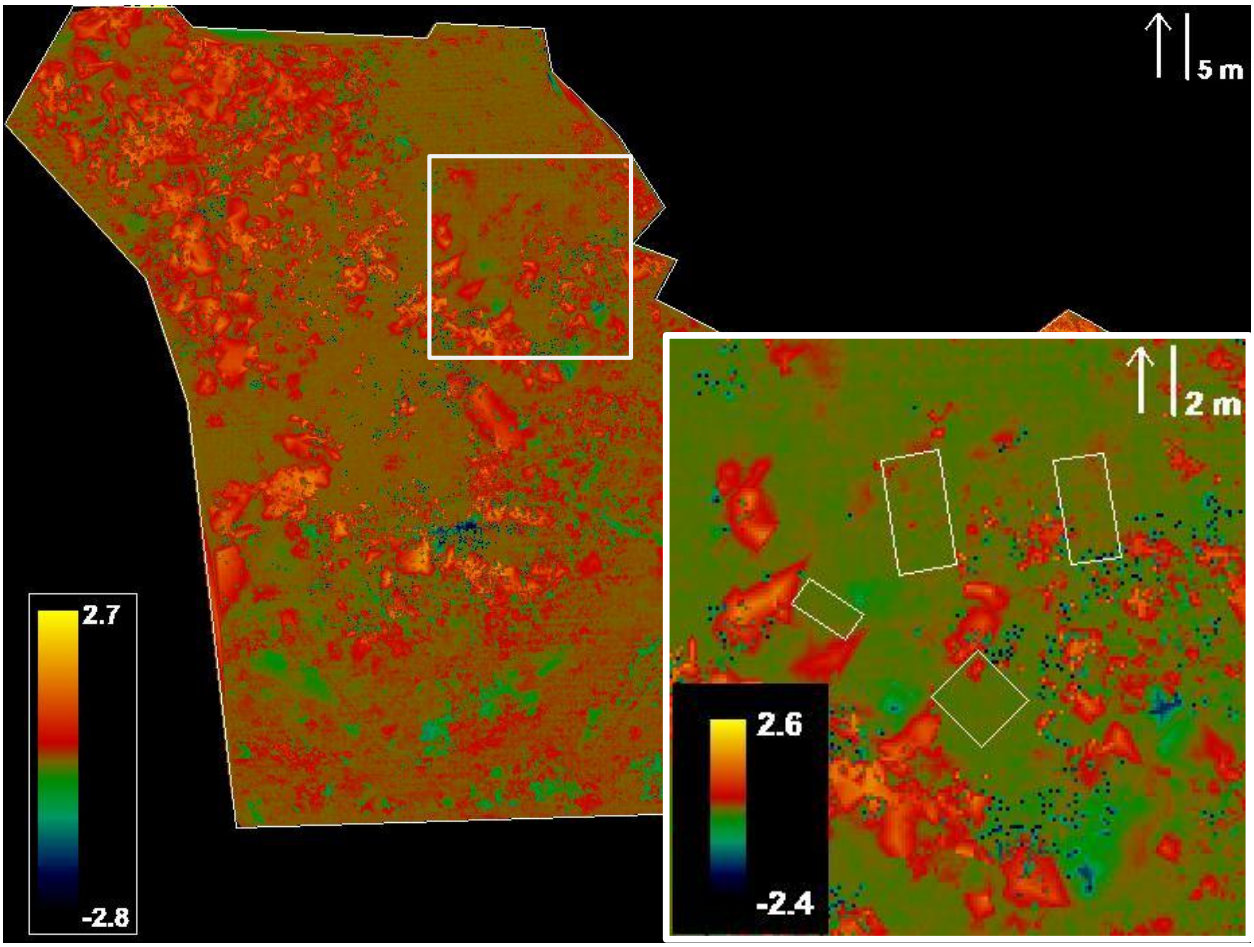

Figure 6.5-8: Elevation changes within fenced study area (main) with immediate burial area (inset) between 23 Mar. – 17 Apr. 2015; 10 cm GSD; values indicate elevation change (m).

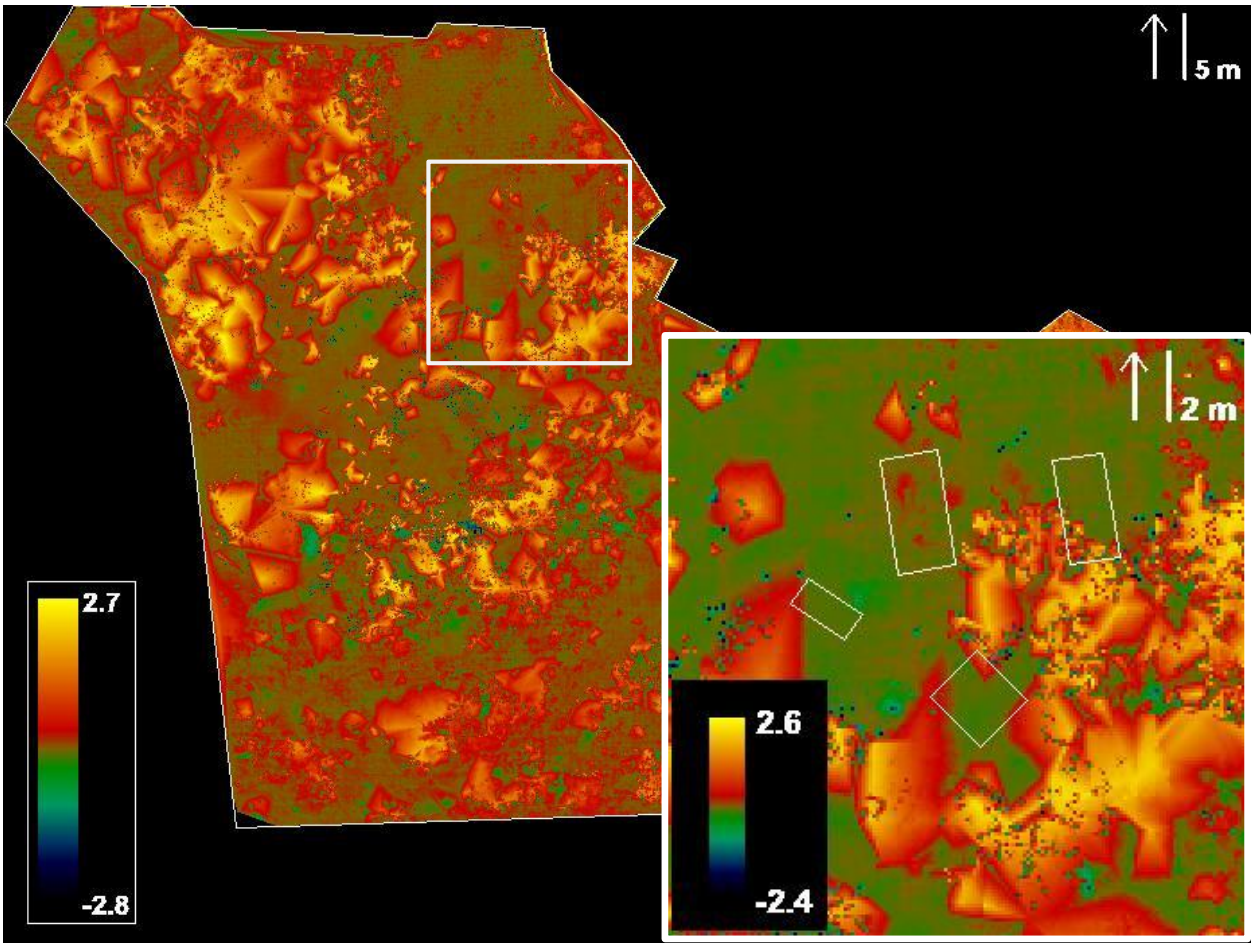

Figure 6.5-9: Elevation changes within fenced study area (main) with immediate burial area (inset) between 23 Mar. – 07 May 2015; 10 cm GSD ; values indicate elevation change (m).

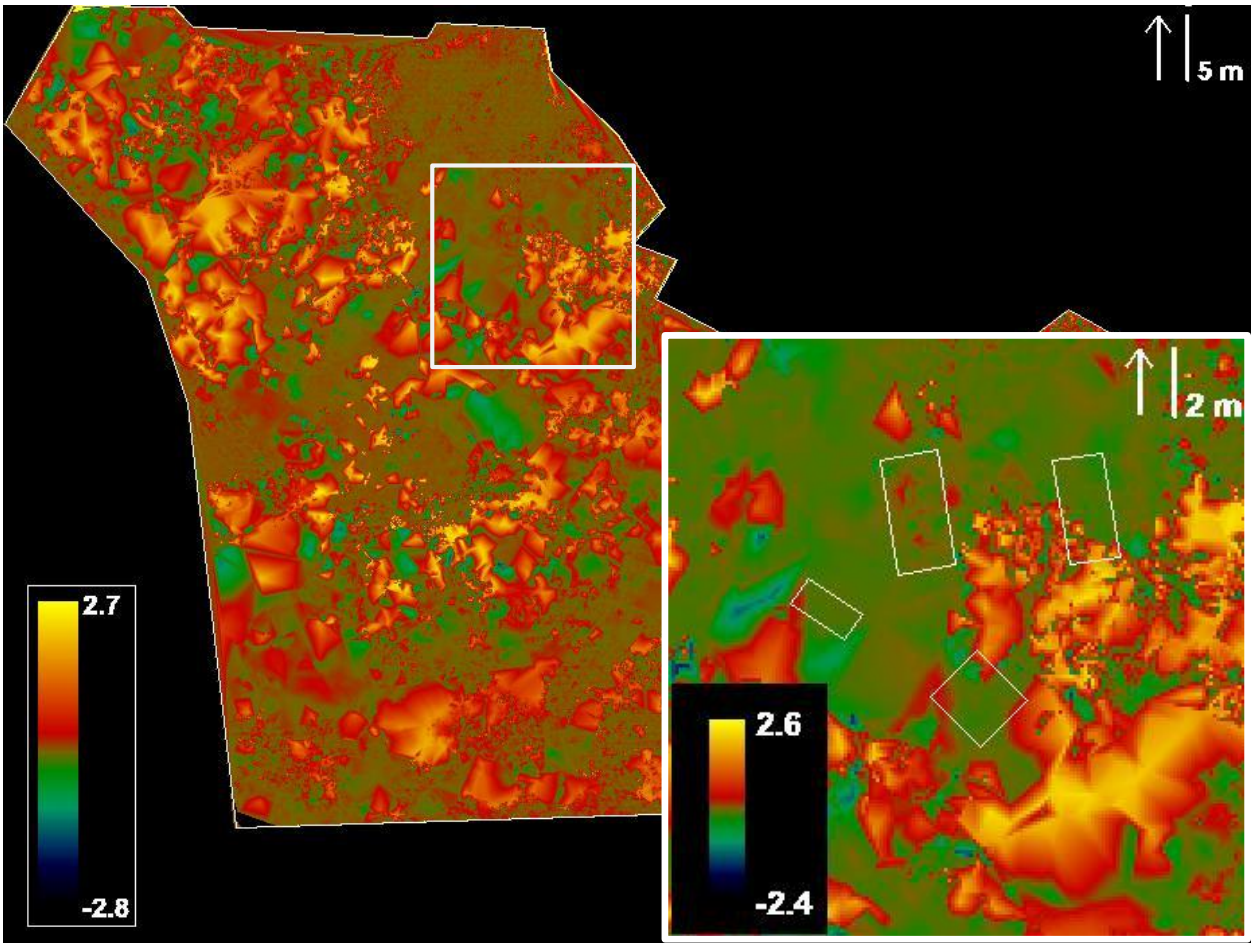

Figure 6.5-10: Elevation changes within fenced study area (main) with immediate burial area (inset) between 17 April – 07 May 2015; 10 cm GSD; values indicate elevation change (m).

CHAPTER 7: DISCUSSION

This chapter discusses the results presented in Chapter 6, focusing on two central notions: 1) human burials chemically influence their environment, and 2) human burials topographically influence their environment. As such, this chapter will discuss the interaction between human burials and their environment using vegetation spectra and surface elevation measurements, and then discuss whether the results support the four hypotheses proposed in Chapter 1.

Hypotheses 1 and 2 presented in Chapter 1 anticipated that human burials, the control unit, and undisturbed ground will show statistically separable vegetation reflectance spectra (Hypothesis 1) and spatially clustered surface elevation changes (Hypothesis 2). Hypotheses 3 and 4 further stated that the reflectance and elevation changes, respectively, would persist throughout the duration of the study. The following chapter is organized by data type, first addressing the spectral findings (Hypotheses 1 and 3), followed by a discussion of the elevation change findings (Hypotheses 2 and 4).

7.1 Vegetation Spectra

Hypotheses 1 and 3 state that vegetation associated with disturbed ground containing human remains (human burials), disturbed ground containing no remains (control unit), and undisturbed ground are statistically separable groups as indicated by differences in reflectance spectra (Hypothesis 1), and that vegetation associated with burials, the control unit, and undisturbed areas exhibit spectral separability for the duration of the study (Hypothesis 3).

Based on the results presented in Chapter 6, these hypotheses are supported. Results show a difference between the undisturbed sample and both of the disturbed sample types (human burials and the control unit) for the duration of the observation period, suggesting that vegetation spectral

differences are influenced by non-specific ground disturbance. The effect of human burials, specifically, on vegetation spectra is undetermined. In terrestrial data, live vegetation spectra associated with human burials or similar disturbance can be reliably separated from undisturbed live vegetation spectra using narrow regions of the spectrum. Moreover, spectral separation was achieved during the entire observation period from March to November 2014, resulting in one model derived from Spring vegetation spectra and six models derived from Autumn vegetation spectra. Model performance appears to vary by wavelength and season, suggesting an optimal spectral range and timeframe for data collection, which are explored in this chapter.

Leaf pigments, but primarily chlorophyll, determine the level of energy absorption in the visible portion of the spectrum, where higher nitrogen concentration results in higher chlorophyll production and increased energy absorption (Knipling 1970). As discussed in Chapter 3, energy that is not absorbed is either transmitted or reflected, and absorption shares an inverse relationship with both reflectance and transmission (which share a positive relationship with each other). These relationships are significant in the application of these findings to human burial detection because as soil and vegetation nitrogen concentrations increase as a result of the body decomposition process, so too does chlorophyll production. As chlorophyll production increases, leaves reflect less solar energy. This trend is observed in the mean reflectance curves of human burial, control unit, and undisturbed vegetation, where vegetation spectra over human burials exhibit the least overall magnitude (indicating increased energy absorption) and undisturbed vegetation spectra exhibit the greatest magnitude (indicating decreased energy absorption).

During the Autumn and Winter months, the sun tracks a relatively low altitude in the southern sky. The tree population at the study area is densest just south of the experimental graves, the combination of which results in an abundance of diffuse sunlight throughout the study area

during that timeframe. Such diffuse lighting conditions present limited opportunities to capture the direct solar illumination of plant leaves required to minimize spectral noise. As a result, the control vegetation spectral sample size is too small to establish whether a difference exists between vegetation associated with human burials versus non-burial disturbance. This shortcoming may be avoided in future work if using an open, unobstructed study area that allows for more direct sunlight. Some predictive models from the current study separate human burial vegetation cases from undisturbed vegetation better than general disturbance cases (grouped human burial and control unit cases) from undisturbed vegetation. While this better separability does not necessarily mean the two types of disturbance vegetation are different, it is worth further investigating with larger sample sizes.

To a forensic anthropologist using a spectrometer to search for a hidden grave, an atypically high or low reflectance spectrum for a particular plant species with a known reflectance curve may represent ground disturbance. However, overall reflectance curves can vary in magnitude even between samples taken from the same leaf surface, depending on the viewing angle of the sensor or rapidly changing light conditions. Moreover, despite the clear ordered trend of mean reflectance curves mentioned above, the distribution of individual reflectance curves tend to overlap between groups. This overlap between groups means that magnitude alone would ultimately fail to reliably predict vegetation disturbance if used in the field as a sole metric for human burial detection. Therefore, in addition to the magnitude of an entire reflectance curve, it is important to consider the greatest contributing individual wavelengths along the spectrum in terms of how, why, and to what degree those important wavelengths can help investigators predict disturbed vegetation.

Red Wavelengths

Narrow red, near infrared, and shortwave infrared wavelengths are included in the seven statistical models developed in this study. The narrow red wavelengths present in the Autumn models (707/708 nm) are consistent with studies that demonstrate – with foci on the contributions of specific wavelengths (as opposed to wide regions) – the positive relationship between nitrogen and chlorophyll concentration (Netto 2005; Yoder and Pettigrew-Crosby 1995), the inverse relationship between nitrogen concentration and reflectance spectra (St.-Jacques and Bellefleur 1991; Thomas and Oerther 1972), and the inverse relationship between chlorophyll concentration and reflectance spectra (Knipling 1970; Sims and Gamon 2002; Yoder and Pettigrew-Crosby 1995). Specifically, St.-Jacques and Bellefleur (1991) identified a nitrogen-correlated wavelength in the red region at 700 nm (r^2=0.70); a wavelength that is positioned on the steep Red Edge vegetation feature only 7-8 nm from the red wavelengths included in the Autumn models, 707 and 708 nm. Additionally, Sims and Gamon (2002) report a chlorophyll-correlated spectral feature located at 705 nm (r^2=0.92), only 2-3 nm from the visible wavelengths included in Autumn models. The relationships between these spectral wavelengths, leaf nitrogen concentration, and leaf chlorophyll concentration are central to the argument that reflectance spectra observed in this study – particularly the 707/708 nm wavelengths – are influenced by an increase in nitrogen that results in an increase in chlorophyll production and a subsequent decrease in reflected energy. As previously illustrated by Mundorff and colleagues (2014), increased nitrogen is likely caused by the human body decomposition process releasing additional nitrogen into the soil. Though, given the lack of evidence to separate the human burial spectra from the control unit spectra, another explanation for the increase may be the mixing of uprooted surface vegetation and soil during the digging activity, where the uprooted vegetation decomposes in the soil, releasing nitrogen for live

plant consumption. Further studies examining the long-term relationship between nitrogen concentration in burial and non-burial disturbed ground may help explain the direction and magnitude of nutrient differences caused by different types of disturbance, and their influence on reflectance spectra.

Near Infrared Wavelengths

The narrow near infrared wavelength included in the Spring model at 761 nm is explained by two phenomena: 1) the Fraunhofer absorption lines and 2) chlorophyll fluorescence. As the sun's energy passes through the atmosphere, that energy interacts with suspended particles at predictable wavelength locations. The Fraunhofer absorption lines are locations of scattered solar energy along the electromagnetic spectrum, expressed as valleys between radiance peaks that are linked to specific elements. There are several thousand mapped Fraunhofer lines depicting absorption features, and among them is a major feature known as the O_2-A band, which represents the atmospheric interaction between O_2 and 760 nm (Fraunhofer 1817). As energy passes through the atmosphere to Earth's surface, a portion of the energy at 760 nm is absorbed by O_2 before it arrives. This energy absorption feature would otherwise be unremarkable in a normalized reflectance spectrum for many other materials, except that the vegetation radiance curve (L_V) contains a slightly shallower O_2-A absorption feature than observed in the white reference radiance curve (L_{WR}) used for calibration. When the white reference radiance curve is used to normalize the vegetation radiance curve ($R = L_V/L_{WR}$), the product is a reflectance curve with a distinctive spike at 760 nm. This spike indicates excess energy, or fluorescence infilling of the O_2-A absorption feature depth (Cogliati et al. 2015; Raychaudhuri 2012). Fluorescence is the emission of radiation at a particular wavelength as a result of incident radiation at shorter wavelengths, and chlorophyll is a known fluorescent biomolecule (Cogliati et al. 2015; Raychaudhuri 2012). Human burial,

control unit, and undisturbed vegetation spectra all exhibit a distinctive reflectance spike at 761 nm, indicating chlorophyll fluorescence in each sample. It appears the amount of fluorescence emission differs between each vegetation group, contributing to group separation, but the contribution is difficult to measure spectrally in the field, and without known chlorophyll concentration. The 761 nm wavelength is but one variable of twelve in the only Spring statistical model, which is the poorest overall performing model. Therefore, future work examining the relationship between disturbed vegetation and chlorophyll concentration may help explain the extent of the contribution that chlorophyll fluorescence makes to, or takes away from, the classification of different types of disturbed vegetation.

Shortwave Infrared Wavelengths

The presence of some narrow shortwave infrared wavelengths in Spring and Autumn models is generally supported by Yoder and Pettigrew-Crosby (1995), who report the relationship between vegetation nitrogen concentration and a series of narrow shortwave infrared wavelengths ranging from 2000 – 2200 nm that are also correlated with, but weaker indicators of, chlorophyll concentration. However, of the 19 shortwave infrared wavelengths included in the seven statistical models produced in this study, only three individual model wavelengths fall within the 2000 – 2200 nm range (2006, 2015, 2053 nm) reported by Yoder and Pettigrew-Crosby (1995). Of the remaining 16 shortwave infrared wavelengths, 14 are situated between 2200 – 2500 nm, which are wavelengths that approach the edge of a window where atmospheric transmission (i.e., the percentage of incident solar energy to pass through the atmosphere) of the Sun's energy is suddenly and drastically reduced. Such windows are the reason wavelengths surrounding 1400 and 1900 nm were removed from the data set before analysis. For this research, the shortwave infrared wavelengths were retained for analysis because, while atmospheric transmission is decreasing at

those wavelengths, it does not approach zero until approximately 2600 nm (Joseph 2005). The effect of reduced atmospheric transmission paired with a decrease in available solar energy in longer wavelengths (Planck's law as a function of temperature at 5772 K), results in the demand for a greater number of lesser contributing wavelengths to adequately classify vegetation groups. However, these physical limitations of the longer wavelength variables may render them unreliable in future work.

In practical terms, subtle differences between disturbed and undisturbed vegetation may be observed in non-experimental contexts using the red, near infrared, and shortwave infrared wavelengths isolated in this study. The validation of these wavelengths using three independent statistical tests indicates that they may perform well in the field, at minimum, as a supplement to other human burial detection methods, such as pedestrian survey, soil probing, or ground-based geophysical technologies. With minimal training, a portable field spectrometer is easily operated in the field and could be used to map spectra along grid points throughout an area of interest to be overlaid with other data types. The limited number of narrow wavelengths used in each statistical model also suggests that instrumentation designed specifically for this application may be worth developing in the future. An instrument sensitive to a few narrow wavelengths would likely be less expensive and more portable than the instrument used in this study, thus making the technology more accessible to a wider range of consumers, such as non-governmental organizations. An application-specific instrument may be configured to generate an instantaneous probability value in the field based on the classification formulas used in this study. Further research fine-tuning our understanding of chlorophyll concentration and chlorophyll fluorescence in a forensic context may eventually facilitate rapid decision making in the field. Such results could be readily interpreted by anyone with intermediate-level training in spectral data collection and analysis.

Timing of Spectral Separability

Six of the seven statistical models were developed using Autumn vegetation spectra, and one was developed using Spring vegetation spectra. All Autumn models perform better than the Spring model in the overall classification of disturbed vegetation spectra. The analytical methods used in this study agree that Autumn spectra are more separable than Spring spectra. No chlorophyll or soil nutrient data were compared to vegetation spectra to confirm the link in the current study. However, the emerging conclusion regarding the performance differences between Spring and Autumn spectra is that spectral divergence occurred sometime between the Spring spectral data collection at 13 months post-burial and the Autumn spectral collection at 20 months post-burial. The difference in separability of vegetation spectra at 13 months (Spring) and 20 months (Autumn) post-burial could be influenced by ongoing human decomposition, plant phenology, plant species population distribution changes throughout the study area, or contributions from two or more of these factors.

While there are no studies on decomposition rates within a mass grave in East Tennessee, decomposition rates of surface remains and individual burials have been studied (Mann et al. 1990). Decomposition timing for buried remains is highly variable, depending on environmental factors, such as temperature and precipitation, to which the current study area was equally exposed at any point in time. It is possible that the buried bodies had not fully decomposed by the time spectral data collection began at 13 months post-burial. Without verifying the decomposition stages of each human burial in this study, the degree and timing of decomposition activity contributing to soil nutrient concentrations remains unknown. This is an important point to make because spectral differences between Spring and Autumn samples may or may not be due to a sudden accumulation of soil nutrients (greater than ambient levels) as a result of annually

reactivated decomposition taking place between the two data collection windows at 13 and 20 months post-burial. It is unclear if decomposition had terminated by 13 months post-burial. However, it is likely that decomposition had at least begun to modify soil nutrient concentrations by this point, based on previous decomposition research on individual burials in east Tennessee (Mann et al. 1990).

Spectral data collection began at approximately 13 months post-burial, so the digging activity had over one full annual cycle to influence surface vegetation in all samples. Moreover, aside from shaded areas, rapid vegetation regrowth was observed at most burial and control surfaces in the two months following interment with minimal difference in the regrowth rate between the disturbance features. Environmental factors known to promote plant growth, such as temperature and precipitation, fluctuate seasonally in east Tennessee. During the terrestrial spectral collection year (2014), temperature and precipitation peaked during the summer months in June and July, respectively (NOAA 2014). While the Autumn spectra were treated to a longer exposure window than the Spring spectra, both samples represent vegetation that had greater than a full year of exposure time to the ground disturbance. What remains to be addressed by this study is whether 1) modified soil nutrients resulting from digging activity or decomposition are consistently influencing plant chlorophyll concentration throughout the year, and there is a delay slightly longer than one year for initial nutrient uptake to occur, or 2) the same modified soil nutrients present a renewed increase in plant chlorophyll concentration each year during certain months that include the Autumn months, but not the Spring months. Therefore, the question at hand is whether seasonal spectral performance differences are driven solely by the timing of soil nutrient availability (i.e., digging activity and decomposition), or also by the timing of nutrient uptake (i.e., seasonality and plant phenology).

The effect of plant phenology, or seasonality, on vegetation reflectance spectra is well documented. The effects of seasonal plant cycles, such as new plant growth, reproduction, senescence, and dormancy, are seen throughout the study area. The onset of each phase is known to be linked to latitude and climate, where mid-latitude climates such as that of East Tennessee are relatively mild, and therefore exhibit less extreme seasonality with wider vegetation growth and reproduction windows (Zhang et al. 2003). However, there is considerable variation for the timing of these phases both within and between species (Polgar and Primack 2011). Moreover, most studies are species-specific or represent low temporal resolution that fail to fully explain whether the Knoxville study area vegetation chlorophyll might be higher in Autumn than in Spring. While studies on plant phenology cannot currently explain the potential for chlorophyll timing at the East Tennessee study area, specifically, it does help explain spectral differences. Image scientists draw on documented plant phases to explain a range of issues, including the effects of phenology on the performance of vegetation indices (Zhang et al. 2003), and monitoring vegetation to track seasonal shifts influenced by global warming (Badeck et al. 2004). Zhang and colleagues (2003) used the Moderate Resolution Imaging Spectroradiometer (MODIS) to demonstrate that vegetation reflectance is sensitive to seasonal change corresponding with the annual growth, maturity, senescence, and dormancy phases that vary based on latitude and climate. In the current study, all sampled leaves were still green during the Autumn collection window (October-November), which may be a qualitative metric, but still a clear indicator of growth and maturity. Pigment differences may have been present between Spring and Autumn (Zhang et al. 2003), but not obvious in the visible wavelengths apparent to the human eye. This point calls back to the earlier discussion on the effect of chlorophyll concentration changes on leaf reflectance, where a subtle increase in chlorophyll results in reduced reflectance. Given that sampling methodology was the same for

Spring and Autumn collection windows, it is clear that plant phenology is at least partially influencing the Autumn-leaning outcome by exhibiting greater differences in reflectance during those months than observed in Spring samples. While it is unexpected that Autumn models would outnumber Spring models, as the abundance of new growth occurs during Spring, perhaps the more advantageous window for forensic investigators to use spectroscopy for unmarked burial detection is during the maturity phase when vegetation has reached a certain level of nutrient stability prior to Autumn senescence.

Seasonal differences that favor the Autumn months in statistical models by a ratio of 6:1 indicate that the Autumn months may be a better window for observing spectral differences between disturbed and undisturbed vegetation. In a clandestine grave scenario, it may be more favorable to prioritize the systematic spectral mapping survey described in the previous section during the Autumn months to maximize differences between disturbed vegetation and vegetation in areas that are not of interest to investigators searching for an unmarked grave. Since spectral differences are subtle and can be difficult to separate under certain circumstances, such as at low instrument resolution or during particular seasonal windows, it may prove important to take advantage of known optimal data collection windows, to exploit those differences when they are expressed in their peak state. Unfortunately, spectral data were not collected continuously for this study, so it is still uncertain whether October and November are the best months to observe those differences. In addition, a closer look at plant physiological activity and its relationship to chlorophyll production and leaf reflectance will help disentangle the effects of the phenology and disturbance.

Spectral differences may also be attributed to changes in population density of opportunistic species at different feature surfaces (i.e., plants that prefer disturbed soil or human

burial soil), as observed in animal experiments (Caccianiga et al. 2012; Callahan 2009; Watson and Forbes 2008). While such population changes may have been present throughout the study area, plant species and their location were not well enough documented to confirm or refute their influence on the spectral results. If such spectral differences were present during the observation period, however, it is possible they were attributable to generic soil disturbance, human decomposition, preference for sunlight, or multiple other uncontrollable factors. This study provides a foundation for future work to explore those questions further.

A lack of observable canopy-level evidence for human burial or similar disturbance signatures in airborne hyperspectral imagery (HSI) is probably due to a combination of factors. The successful application of ground spectra to canopy spectra is dependent on uncontrollable factors, such as canopy structure and solar geometry, favorable atmospheric conditions, and instrument capabilities. The airborne and satellite images were collected under clear atmospheric conditions and were carefully calibrated using a ground target with a known spectral signature, which minimized spectral noise in the data set. Prior to addressing the remaining concerns, the successful application of terrestrial findings first assumes the signature is present in both terrestrial and canopy vegetation. However, this assumption is potentially inaccurate, as the study area canopy is comprised of many large and well established trees that may not be influenced by the human burials or control unit, or have not been exposed to those disturbances for a long enough period of time to be affected by measurable change. If tree canopy remains unaffected by ground disturbance, airborne and satellite imaging will prove unhelpful to investigators searching for unmarked human burials in similar environments. With respect to canopy leaf-off seasons (i.e., months where canopy leaf density is low), a network of bare tree branches extend across the view of the ground surface, contributing to the spectral signature of each image pixel. Moreover, the

overall concentration of live ground vegetation is low during these months, resulting in a low contribution of live vegetation spectra to image pixels. Therefore, canopy leaf-off months tend to be a poor match for testing the statistical models developed using live green vegetation as a training sample, and due to their lack of pigments, dry leaf scatter is likely to provide an inadequate spectral sample for future modeling.

Canopy structure is probably playing a role in poor scalability since the entire canopy and individual leaf surfaces are non-lambertian. A lambertian surface is one that reflects light evenly in all directions, rendering its apparent reflectance value the same regardless of the viewing angle (Lambert 1760; Schott 2007). Canopies are highly textured, and leaves are oriented in many different directions, which affect their apparent brightness from any single overhead viewing position (Lee and Kaufman 1986). By contrast, all terrestrial spectra data were collected under unobstructed solar illumination in the field, and the instrument was in close range of, and aimed near-perpendicular to, each leaf surface to limit variation in data due to sampling methodology. While it is not possible to record data from an aircraft-based platform in the same manner described for terrestrial spectral data, it is possible to estimate the reflectance of a non-lambertian surface as a function of illumination and viewing geometry using a bidirectional reflectance distribution function (BRDF) (Nicodemus et al. 1977). NASA-GSFC has not yet developed a BRDF product for their customers, but it is a possibility for future work. Therefore, it is currently unknown whether or not canopy structure will influence the performance of airborne or satellite imagery for identifying signs of ground disturbance in canopy spectra.

The difference in spectral and spatial resolution between the terrestrial sensor and the airborne and satellite sensors are likely contributors to poor scalability. The 707/708 nm spectral feature is narrow, and due to the airborne Hyperspec spectral resolution of 11.00 nm full width at

half maximum (FWHM) of the 706.12 nm wavelength band (versus 1.4 nm for the ASD FieldSpec 4 instrument) may ultimately escape detection by the airborne Hyperspec sensor. Furthermore, terrestrial instruments allow the operator to collect spectra close to its target, resulting in very high spatial resolution; easily as small as a centimeter, if using a lens and sampling at a distance of a few centimeters. Alternatively, for the current study, the Headwall Hyperspec, passing overhead, produced images with pixels ranging 0.5 – 1.0 m. The same principles hold true for the satellite images, where spatial and spectral resolutions are further decreased due to distance and instrument design. Spatial resolution is relevant to the issue of scalability because in all overhead spectral images, each pixel includes the reflectance value of all the materials located inside each of those areas, resulting in the spectral mixture of several materials. A challenge posed by spectral mixing is that signatures that contribute proportionately less to the spectrally mixed pixel are overwhelmed by the signatures contributing a greater proportion to the pixel, and pixels are not easily unmixed. There is still promise for the future scalability of findings to larger graves, such as those found in Bosnia, spanning tens of meters and containing hundreds of bodies. Additionally, future research may successfully identify smaller burials using high spectral resolution airborne sensors flown at low altitude, perhaps as part of a remotely controlled unmanned aerial system (UAS), to help understand if positional or technological constraints are responsible for poor scalability of terrestrial findings.

Another consideration for the failure to scale may simply be data collection timing. The two terrestrial models advanced to HSI were developed using Autumn vegetation samples, but the HSI were collected during Spring months; a season for poor spectral separability of target groups, as established by the terrestrial spectral findings. As discussed in the previous section, plant phenology has a demonstrated influence on vegetation reflectance (Badeck et al. 2004; Zhang et

al. 2003), and the Spring imagery may not represent peak timing for chlorophyll concentration differences at the canopy level, if they exist. Other factors worth considering in additional research are the differences between species comprising the ground vegetation and canopy, which may have different spectral responses contributing to the classification results. It is also possible that the experimental burials do not influence canopy spectra in measurable quantities, perhaps due to the burials being too small, too recent (or old), or located too far from large rooted trees to cause observable spectral changes at the canopy scale.

These hyperspectral imagery results are applicable only for this experimental context. The same methods and technologies should be tested in other environments and scenarios, including unobstructed environments, and using higher spectral resolution airborne sensors at low altitude. The terrestrial data in the study area environment demonstrate separability of disturbed and undisturbed vegetation spectra and should be used to inform future airborne hyperspectral campaigns that may still hold the potential to assist forensic investigators in the search for unmarked burials in similar environments.

7.2 Topographic Changes

Hypotheses 2 and 4 state that ground surfaces at burials, the control unit, and undisturbed locations exhibit differences as measured by net elevation gain or loss (Hypothesis 2), and that ground surfaces associated with burials, the control unit, and undisturbed locations exhibit differences in elevation change for the duration of the study (Hypothesis 4).

Based on the results presented in Chapter 6, hypothesis 2 is supported and hypothesis 4 *is not* supported. In terrestrial data, elevation activity associated with human burials and similar disturbance without interred bodies (i.e., the control unit) can be visually separated from undisturbed elevation, and is observed as localized elevation change at those locations. The current

findings do not provide evidence that differences in surface elevation changes for human burials and the control unit persist for the duration of the study. Localized elevation change at disturbed surfaces appears to have slowed to a rate that approximates the ambient study area elevation change by the 108 days post-burial collection date. Elevation change direction and magnitude appears to be influenced by the rate of decomposition, suggesting there are optimal collection timeframes for forensic casework that are environmentally dependent. Additionally, the findings reveal that LIDAR may be useful in forensic scenarios that may or may not include baseline elevation data sets.

After a body is buried, loosened soil and buried mass simultaneously occupy the original ground space once filled in with undisturbed, compacted soil (Steadman 2009). The initial post-interment burial surface elevation will depend on the amount of soil replaced during backfilling. If attempts are made to backfill all of the displaced soil, an initial mound will be visible due to loosened soils and the addition of the body mass to the space once occupied only by soil. However, backfilling may cease once the surrounding ground surface is reached, leaving the remaining soil, displaced by the space now occupied by the interred body, on the ground surface off the burial. Over time, the loosened soil gradually settles as a result of gravity and precipitation. As a body decomposes, its mass is redistributed into the soil as nutrients, eventually reducing the concentration of soft tissues. Consequently, grave soil is further redistributed, filling in the areas once occupied by soft body tissue. These volumetric changes cause the surface elevation to increase and/or decrease, depending on the rate of soil compaction and the timing of human decomposition (Mann et al. 1990; Rodriguez and Bass 1985). Rodriguez and Bass (1985) documented the timing of buried human body temperatures in Knoxville, TN, concluding – through the use of temperature as a proxy for decomposition timing – that the most active stages

of the decomposition process begin as early as one week-post burial and can continue for up to ten weeks post-burial, depending on season and climate. Also in East Tennessee, Mann and colleagues reported that timing, for full skeletonization to occur within a burial, could range from "a few months to a year or more" (1990: 107). Similar trends were observed in the current study, at the experimental human burials and control unit, where immediately after the units were backfilled, the loosened soil formed a mound at each surface. This phenomenon is likely due to attempts to backfill as much of the displaced soil as possible, although for the six-person grave it was not possible to backfill all of the removed soil. Within four months post-burial, the mounds settled. The current study reveals the following trends in disturbed ground surface elevation change: 1) between two days *pre*-burial and one day *post*-burial, all disturbance surfaces except the six-person grave, for which there is no one day post-burial elevation data, exhibit a sudden elevation gain, indicating initial ground disturbance. 2) Between 1 day and 108 days post-burial, all disturbance features exhibit elevation loss, indicating soil settling and possible human decomposition. 3) Between 108 days and 643 days post-burial, no additional localized change was apparent at any of the human burial or control unit surfaces. This outcome may indicate that, by 108 days post-burial, localized soil settling and human decomposition have slowed, or potentially stopped.

The net elevation changes observable at the burial surfaces are the result of a combination of factors that are most active in the weeks and months immediately following burial, including soil settling and body decomposition. The result is a localized net elevation loss at the burial surface that is not observed at undisturbed locations. Elevation changes that are observed at undisturbed locations are smaller, amorphic (i.e., not elongated features), and not clustered in the same spatial density as seen at the disturbance locations. The localized changes in elevation extend to the linear edges of each disturbance feature, clearly illustrating the precise location of each

human burial and the control unit. Given the agreement between the observed elevation changes and the likely timing of decomposition (Rodriguez and Bass 1985; Mann et al. 1990), as well as observations of common (though not universal) burial surface activity (Owsley 2001; Steadman 2009), the elevation changes observed in this study confirm that burials and disturbance without interred remains possess a degree of generally predictable elevation activity, such as immediate elevation gain followed by gradual elevation loss, then stagnation.

Variation in elevation change is observed at disturbance feature surfaces, where the greatest elevation changes, whether gain or loss, is generally observed near the center of each feature and the least elevation change near the edges. The concentration of greatest elevation change at the approximate centers of each feature is likely due to the distribution of disturbed soil during backfill, where the peak of each surface mound is located near the center. This trend is observed in elevation gain and elevation loss images of all disturbance features, including the control unit, so it is likely that the vertical dimension of displaced soil volume is a factor in the magnitude of elevation loss as the soil settles. The volume and distribution of backfilled soil for each human grave and the control unit was not controlled as part of the interment process. However, elevation gain measurements between baseline and one day post-burial reveal that the volume and spatial distribution of soils for each feature were not equal at each surface, nor were they proportionate for each feature's volumetric dimensions.

It is unknown how much elevation loss is attributable to soil settling and decomposition, respectively. Since the six-person grave and the control unit were not observed equally throughout the study period, there is not enough evidence to support differences between human burial and similar disturbance elevation changes. However, the six-person grave exhibits a unique trend, where elevation loss is greatest in the northernmost-center portion of the grave surface where the

buried bodies are concentrated. This gradual increase in elevation loss from the south to the north presents no clear boundary between the area containing the human bodies (north) and the area that contains no bodies (south). Since the southern portion of the grave is not isolated, which means there is no separation of experimental treatment and control, the grave surface was arbitrarily separated into two halves – the northern half containing all six bodies, and the southern half containing none – to establish approximate differences in elevation change between the northern and southern portions of the six-person grave. The statistical distributions of the northern and southern grave surfaces are consistent with the trends illustrated in elevation change profiles, where a greater elevation loss is observed at the surface directly over the concentration of six bodies. The more important finding, however, is that southern elevation loss – observed along the transect and the statistical distribution of the entire southern half – falls within the extremes of elevation change observed at the actual experimental control, but is several centimeters off from the mean. This finding demonstrates that, while the northern portion of the largest grave was likely influenced by human body decomposition over and above the effects of soil settling alone, as seen in the differences between the northern and southern halves, the southern half is not an adequate analytical substitute for the actual control unit. These findings hint at differences between human burial and control elevation changes, but the extent of these changes should be explored in future research.

The temporal resolution of data collection does not support definitive conclusions about the individual contributions of soil settling and decomposition to surface elevation loss. The northernmost elevation loss at the location of the six bodies is observable as early as 108 days post-burial (the first post-burial collection to record elevation data at this burial surface), the same date the southern elevation loss is first observed. The overall elevation loss continues to be visible

as a surface depression at 643 days post-burial, but not as additional elevation change, so it is unclear if the timing of soil settling and human decomposition differ. The difference in elevation loss between the northern and southern halves of the largest burial at two post-burial dates suggest that the *rates* of change for a human burial and similar disturbed soil may differ at certain times post-burial. However, two comparisons are insufficient to meaningfully describe those rates of change. Future research that controls the interment process and monitors subsurface decomposition activity will help shed light on the extent and timing of soil settling and decomposition and the influence of these factors on the expression of surface elevation change. Future research that includes more complete data, such as equal and more frequent observations of burial disturbance and disturbance without interred remains, will help establish if differences exist. Until direct comparisons between human burials and similar disturbance can establish a usable elevation change pattern, forensic investigators will need to rely on separating disturbed ground from undisturbed ground, which – depending on recent land use – will still help isolate areas of interest for follow up investigation.

The size of each disturbance feature appears to have little influence on the magnitude of surface elevation change. As mentioned, the six-person grave surface elevation was not measured at one day post-burial, and it was not possible to backfill all of its removed soil, which likely contributes to the formation of the surface depression. However, there is complete data for the remaining two human graves and the control unit which demonstrate that, during each comparison of elevation gain and elevation loss, the one-person and three-person graves exhibited approximately the same elevation change. While containing no interred human remains, but being twice the size in volume of the three-person grave, the control unit exhibited almost twice the elevation gain immediately post-burial and the same elevation loss 108 days post-burial as both

the one-person and three-person graves. If it were the case that the vertical dimension of displaced soil volume is the sole factor in the magnitude of elevation loss as the soil settles, then the control would be expected to exhibit greater elevation loss than either of the smaller human graves. This finding resulting from the one-person and three-person comparison suggests that the magnitude of elevation change may not be dependent on grave size. However, if the effects of soil settling and decomposition to elevation change can be sufficiently disentangled by future research that seeks to document those factors, differences between human grave and non-grave disturbance may become more evident.

The trends in elevation change are significant in the application of LIDAR findings to human burial detection because surface elevation increases or decreases can be simultaneously compared to ambient elevation changes of the surrounding area, which will generally occur to a lesser degree than at the disturbance locations. This trend is observed at the human burials, control unit, and undisturbed ground surfaces, where human burial and control unit surfaces exhibit spatially clustered elevation change in the 108 days following interment, while the surrounding undisturbed surfaces, for the most part, do not.

The precise timing of peak elevation change differences between disturbance surfaces and undisturbed areas are still unknown, as data collection was infrequent and irregularly spaced. For example, in the current study, 107 days passed between the first and second post-burial data collections, and 535 days passed between the second and third post-burial data collections. Either of these two windows may have contained the maximum elevation change, as compared to the surrounding undisturbed ground surfaces. Multiple data collections made between 1 and 108 days following interment may reveal localized elevation changes at the burials' surfaces, even when a mound or surface depression was nonexistent or not evident to an observer. Future research may

narrow the optimal windows for capturing maximum elevation gain and elevation loss. Until elevation change phenomena are better understood in different environmental and contextual conditions, including graves containing more bodies that may decompose more slowly, it is currently advisable to collect data early and often until localized elevation change becomes evident.

These results offer promise for forensic scenarios where a rapid response to an unmarked burial is possible. However, because the temporal resolution of data collection was low, the elevation activity expiration date of 108 days post-burial should be treated as an approximation, but especially so in conditions that drastically differ from the experimental study (e.g., soils, climate, season, grave size, grave depth, size of individuals). Such variables may affect the rate of soil settling, the human body decomposition rate and, subsequently, the expression of surface elevation change. While the exact ranges of elevation change will likely vary based on time-since-burial and environment, to the investigator, the disturbance features will likely appear localized because the subsurface processes are mostly independent of the uniform extrinsic processes that influence the entire study area.

This study demonstrates that surface mounds or depressions (as opposed to elevation gain or loss) are unreliable topographic features for identifying unmarked burial surfaces due to the extent of topographic variation within the study area that helps disguise the disturbance features. Previous research has attempted to identify burial surfaces by measuring elevation data in an area of interest at a single point in time (Weitman 2012), which has failed to demonstrate the existence of topographic anomalies. The findings of the current study illustrate the problematic nature of collecting only one data set, as single collections can fail to normalize generalized change to highlight localized change. Naturally occurring mounds and depressions are common in different

landscapes, and can easily be mistaken for human burials during an investigation, or overlooked as natural landscape variation. All disturbance features (excluding the largest human burial, which was not included in the first post-burial scan) exhibited a surface mound immediately following interment, but only the largest human burial formed a surface depression, and was discussed previously. The depressed surface renders that burial visible as an elevation loss in comparisons with pre-burial data until leaf litter accumulates within the depression, effectively bringing the surface up to the surrounding elevation. This finding, and the lack of surface depressions at any other disturbance location, confirms that there is a measure of variability to the elevation activity based on poorly understood factors. It may not be possible to visualize burial surfaces with just one data set, no matter when a collection takes place, which is consistent with Weitman's (2012) conclusion following a single LIDAR survey performed in a Georgia cemetery, where she found burial surface elevations were too similar to that of their surroundings to adequately isolate the individual burial locations. The current study also confirms the accounts of forensic anthropologists who have reported that a lack of consistent topographic evidence adds to the difficulty of locating unmarked human burials (Davenport and Harrison 2011; Steadman 2009), which upholds the current elevation change approach as the most viable topographic method for identifying disturbed surfaces.

Elevation change differences between disturbed and undisturbed ground surfaces have clear application in non-experimental contexts. The spatial clustering of elevation change indicates this method may perform well in the field as an addition to other burial detection methods, such as pedestrian survey, soil probing, or ground-based geophysical technologies. In addition, findings from this study indicate that an approach combining spectral and LIDAR data may significantly improve overall results, particularly where vegetation and topographic anomalies spatially agree.

Point cloud data require a more involved data management workflow than spectra to produce a result, and the window of opportunity appears to be relatively narrow at this study area location for graves of this size. However, localized elevation change in a landscape – particularly if it follows the disturbance trend previously outlined – is an especially strong sign of disturbance. While it seems that vegetation spectra may be the more viable long-term indicator of disturbance, less predictable factors, such as soil nutrient variation, are known to influence chlorophyll production, as discussed previously. On the other hand, fewer phenomena help explain localized elevation change, suggesting that observed elevation change that is consistent with the directional trends presented in this study may indicate ground disturbance, thus presenting a strong argument for follow up investigation.

With training, a tripod-mounted laser scanner is easily operated in the field and can be used to measure ground surface throughout an area of interest to be combined with other data types. The recent development of multispectral LIDAR scanning technology holds promise for the future development of sensors that can accomplish 3D spectral data collection. Such a technology will potentially reduce the time and monetary investments into forensic investigations and would make the technology more accessible to a wider range of consumers.

The patterns established in terrestrial LIDAR data are not observed in the airborne LIDAR data for three possible reasons. The first and most certain reason is that, for some collections, no pulses were returned at the ground surface. For the April and May 2015 aerial collections, very few – and in some cases, zero – ground points were recorded at the burial surfaces due to the density of tree canopy that obscures the study area. The exception was the March collection, which included very high point density and evenly distributed ground points at all burial and control surfaces. The September 2014 collection resulted in a relatively even ground point distribution,

but the density was lower than the March 2015 data set, likely because canopy leaf density in September is not at peak levels, but not as low as in March, leaving fewer gaps between canopy. Low ground point density limits the spatial resolution of image products produced using point cloud data because there are fewer samples across the landscape with which to populate image pixels. Moreover, comparisons between two collections are computationally limited to the lowest spatial resolution image in any pair comparison, as two images of different spatial dimensions cannot be directly compared; the higher resolution data must be down-sampled to match the lower resolution data. For collections where no points populate the ground surface at a disturbance feature surface, data gaps are interpolated based on surrounding point data, rendering illogical comparisons between measured data and approximated data. The most straightforward way to overcome this issue in canopied environments is to acquire airborne LIDAR collections exclusively during leaf-off months, which – depending on the environment – still presents a periodic collection window recurring annually.

Second, the elapsed time since burial may contribute to why burial surfaces are not visualized with airborne LIDAR data. The terrestrial LIDAR data establish that elevation changes decrease with time and that elevation change activity no longer clustered at disturbance surfaces by 108 days post-burial. Given the airborne LIDAR collections were made approximately two years post-burial suggests that all activity had subsided. Third, due to sensor motion and distance from the ground surface targets, the cumulative geopositional error (i.e., error attributed to the scanner, navigation unit, and flight turbulence) may have exceeded the magnitude of elevation change at the disturbance features. However, with the issue of low density – or zero – points reaching the ground surface, the second and third reasons are theoretical and cannot be confirmed.

Like the airborne hyperspectral and satellite multispectral imagery results, the airborne LIDAR data findings are applicable only for this experimental context. These same methods and technologies should be tested in other environments and scenarios, including data from unobstructed landscapes collected at low altitude to generate high density ground point clouds, particularly in the few months immediately following interment. The terrestrial data demonstrate remarkable visual separability of disturbed and undisturbed elevation change and should be used to inform future airborne LIDAR campaigns that may still hold the potential to assist forensic investigators in the search for unmarked burials.

7.3 Remote Sensing as a Tool for Unmarked Burial Detection

At present, remote sensing does not offer stand-alone human burial detection capability, but it is a promising supplement to existing grave detection methods. The direction, magnitude, and timing of peak disturbance signatures – both spectral and topographic – are not fully understood, which temporally limits the application of these remote sensing signatures. However, the agreement of findings derived from these two very different remote sensing data types demonstrates the potential effectiveness of a multi-modal, (i.e., "data fusion,") data collection strategy for assisting with the detection of small or subtle features, such as a human grave. With the current data set, any similarity or difference between human burials and the control unit are speculative, due to data gaps discussed previously, and will require additional testing to establish whether quantifiable differences between the different types of disturbance exist and whether they can be used to isolate human burials. Though, the ability to identify disturbance, whatever the cause, is still an important advancement for the forensic community to help prioritize areas of interest for follow-up field investigation, particularly when the search area is defined by reliable information, but the size of the area is too large for traditional methods.

7.4 Limitations

Describing the study limitations will hopefully assist future researchers in their design ofsimilar experimental research in forensic remote sensing.

Line-of-Sight Limiting Tree Canopy

The experimental human burials and the control unit are located in a study area covered by dense tree canopy, which means their surfaces are unobservable using passive sensors like airborne imaging spectrometers. The canopy also limits the amount of ground points that active sensors can generate. The canopy leaf density is reduced during the winter months after the leaves have fallen, which means greater ground visibility. The winter season, however, minimizes the amount of live vegetation on the ground or at the canopy level to apply the ground-based spectral findings developed using live vegetation. The lack of direct burial visibility means that the terrestrial data findings cannot be validated in remote imagery until experimental research is performed in an open environment. Terrestrial findings should be applied to remote imagery containing unobstructed targets, as remote sensing may still be capable of isolating burial signatures in more open environments.

The Timing of Peak Signature Disparities

The results of this research indicate that differences exist between signatures of the experimental disturbance groups and undisturbed samples. Unfortunately, the previously mentioned data gaps prevented a full analysis, resulting in a poor understanding of the timing of vegetation spectra and topographic signatures. The portable spectroradiometer was not available until 13-months post-burial, so vegetation spectra during the first year are undocumented. As a result, the emergence, peak disparity, and re-convergence of disturbed and undisturbed vegetation

spectra and surface elevation changes are unknown. It is also uncertain if signatures fluctuate throughout the year due to seasonal cycles, or if signatures consistently diminish up to a final convergence point with undisturbed samples. It would prove most valuable to understand the timing for each of the signatures by performing a multi-year study that follows a more evenly distributed and more frequent data collection strategy.

Unequal Human Burial and Control Unit Samples Sizes

Spectral classification results reveal that human burial and control unit vegetation spectra may not be reliably separable from each other. Previous research demonstrates that nutrient uptake is affected by human decomposition (Mundorff et al. 2014) and non-burial nutrient-modified disturbance (Commisso and Nelson 2008; Commisso and Nelson 2010; Vitousek 1982), but the magnitude and directional effects of nitrogen concentration and their source on different types of disturbed vegetation spectra have not been adequately studied. Unfortunately, all studies – including previous research and the current study – fail to make direct comparisons of signatures between human burials and non-burial disturbance. All Autumn models developed during this research, whether they were developed using only human burial vegetation spectra or all disturbance vegetation spectra, include the same 707 or 708 nm wavelength feature. The consistent presence of that spectral feature between all Autumn models may be explained by the fact that the human burial spectral sample is disproportionately larger than that of the control unit vegetation spectral sample due to a lack of direct sunlight at the control unit. A similar data issue exists in the LIDAR data, where the largest human burial was not completely backfilled in time for the first post-burial scan, resulting in a considerable data gap. Unequal sample sizes limited opportunities to draw defensible conclusions on the uniqueness of a human burial signature.

CHAPTER 8: CONCLUSION

The purpose of this study was to establish if spectral and topographic signatures are unique to human graves for the development of a human burial detection methodology. This study contributes valuable information to the fields of anthropology and remote sensing by establishing signatures of human graves and a control unit. Further, the results highlight eight broad findings regarding human grave signatures:

1. Differences exist in narrow red, near infrared, and shortwave infrared reflectance spectra between disturbed vegetation and undisturbed vegetation, such that they can be used to separate vegetation into discrete groups at a rate greater than random chance. The differences are likely due to digging activity. Digging activity may modify soil nutrient concentrations, thereby influencing the chlorophyll concentration in leaves. Changes in chlorophyll concentration results in predictable changes in reflected solar energy, which may be used as an indicator of ground disturbance.
2. With respect to these differences, wavelengths in the red spectral region perform better than longer wavelengths in the near infrared and shortwave infrared regions at separating disturbed and undisturbed vegetation. Better separability in the red spectral region is likely due to the greater availability of incident solar energy that can be reflected at those wavelengths, thus increasing the signal strength, as dictated by established Planck curve characteristics and atmospheric transmission windows.
3. Spectra sampled in Autumn months perform better at separating disturbed and undisturbed vegetation than spectra sampled in Spring months. Seasonally specific separability may be due to a phenologically driven leaf pigment response during the Autumn months. In Autumn, live plants are approaching an annual dormancy phase when chlorophyll

concentration differs due to seasonal changes soil nutrient uptake, which influence the amount of reflected solar energy that can be measured spectrally.

4. The terrestrial spectral wavelengths fail to differentiate between disturbed and undisturbed vegetation when applied to airborne hyperspectral imagery (HSI) and satellite multispectral imagery (MSI). The failure of terrestrial spectra to scale well to airborne or satellite imagery is likely due to more than one factor. Differences between ground and canopy vegetation influence the reflectance spectral response likely due to species-correlated pigment concentration levels and sensor viewing geometry that contributes to greater data variability. Models trained with terrestrial vegetation spectra sampled at nadir (perpendicular to the leaf surface) may generate false positives or false negatives in canopy vegetation that cannot be sampled with the same consistent viewing geometry. Additionally, airborne and satellite imagery possess reduced spectral and spatial resolutions compared to terrestrial spectra collected *in situ*, where remote instruments are probably not sensitive enough to separate disturbance from non-disturbance spectra without diluting the signal, suggesting those instruments may not be useful for human grave detection. Finally, it is possible that a canopy disturbance signature does not exist due to the human burials and the control unit being too old, too recent, or not significant enough to influence canopy level spectra, suggesting airborne and satellite instruments are not useful for detecting small-scale disturbance under tree canopy.
5. Differences exist in the elevation change measurements between disturbed and undisturbed ground surfaces, such that ground disturbance can be separated visually as distinct, spatially clustered topographic anomalies. Identifiable topographic anomalies are

likely due to initial digging activity and the subsequent redistribution of soil and buried mass, revealing elevation loss.

6. Net elevation change measurements perform better at differentiating between disturbed and undisturbed ground surfaces than absolute elevation measurements (i.e., mounds, depressions) because elevation change comparisons effectively normalize the naturally occurring topographic variation that exists throughout the study area and helps disguise the disturbance features.
7. Elevation change activity does not persist indefinitely as localized elevation change at human burial and similar disturbance locations. Evidence of elevation changes, such as elevation loss, dissipates over time and is likely due to the slowing of soil settling and human decomposition activity over time. Any possible ongoing elevation change not observed in this research may be the result of accumulated ground surface debris, such as dry leaves, that obstruct the laser pulse.
8. Localized elevation change activity is not visible at disturbance locations in elevation change data derived from airborne LIDAR. Airborne LIDAR's inability to detect elevation change is due to intrinsic and extrinsic factors. The dense tree canopy resulted in significant data gaps at the burial surfaces that prevented meaningful data analysis. Logistically, the airborne surveys did not begin until approximately two years post-burial, at which point terrestrial LIDAR analysis indicates a decline in surface elevation activity.

This study presents the likely drivers of disturbance signatures, as observed by two remote sensing technologies. The results indicate that disturbance signatures can be separated spectrally and topographically. A disturbance signature is characterized by diminished reflectance values located at 707/708 nm, 761 nm, and a series of shortwave infrared wavelengths. The disturbance

spectral signature, as captured at nearly every model wavelength during Autumn months, is likely expressed as an increase in chlorophyll concentration, which increases solar energy absorption (and decreases solar energy reflection). The disturbance signature is also likely expressed as a difference in the magnitude of chlorophyll fluorescence infilling at 761 nm during the Spring months. Disturbance signatures are further characterized by localized net elevation changes at the human burial and control unit surfaces. These surface changes follow a general pattern of elevation gain immediately after burial, then an elevation loss during the next few months, the timing of which appears to correspond with the documented timeline of decomposition processes in East Tennessee. Elevation loss is then followed by stagnation of further elevation change. These signatures, with refinement of detection methods through additional research, are potentially measurable in non-experimental settings.

The findings of this study have immediate application to humanitarian and evidence-based efforts in locating unmarked human burials. As discussed in Chapter 2, international humanitarian law (IHL) dictates that families of missing persons have a right to know the fate of their missing relatives. Similarly, IHL establishes that parties of conflict have a responsibility to account for the dead. The findings of this study establish two previously undocumented ground disturbance signatures that, in combination with each other or with existing methods for burial detection, can help prioritize areas that are under active investigation. The documented signatures discovered in the current study are not necessarily indicative of human burials; rather, they are signatures consistent with ground disturbance and present an evidence-based probative tool for detection. The ability to remotely investigate a large swath of land to identify ground disturbance signatures will improve the efficiency of human burial detection by isolating potential disturbance for additional targeted ground-based investigation.

The humanitarian and evidence-based implications of an improved rate of human grave detection are significant. Some families wish to know the truth about past events, the fate of their missing loved ones, and desire the return of the physical remains of the dead. Recovering a body once declared disappeared serves an important role in providing evidence for those needs and desires. For example, recovering the mortal remains of disappeared Nepalese men allows their widows who must otherwise reside – often with significant resentment and abuse – with her husband's family, to remarry (Robins 2011). Locating hidden graves and the subsequent recovery of human remains allows families to carry out funerary rituals otherwise prohibited without the physical remains of the missing. In Zimbabwe, the performance of funerary rituals is necessary for families to cope with loss, where ambiguity of a disappearance disrupts the grieving process. Location of hidden graves and subsequent recovery of human remains allows the process to move forward (Eppel 2014). A similar desire for the physical remains is expressed by families of US military service personnel who have gone missing during wartime. Fulfilling the needs of these families is perpetually hindered by the difficulties of locating unmarked human burials, which is precisely the information gap this research has attempted to address.

Some unmarked burials are already identifiable using existing detection methods. In such cases, remote sensing may assist those methods, adding valuable data to the mosaic, thus reducing the ground time required by a search team. Remote sensing has the advantage of covering more land than terrestrial methods, and remote sensing does not require positioning a sensor directly above a grave (e.g., active sensors), which again translates to less time a recovery team needs to be on the ground and, sometimes, in harm's way. Additionally, remote sensing has the added utility of monitoring known but inaccessible graves during ongoing conflict. Monitoring grave sites can provide evidence needed for the international community to apply political pressure to offending

governments (Willum 2000; Marx and Goward 2013) or to document attempts to hide evidence, such as the case in Bosnia, where perpetrators relocated bodies buried in mass graves to secondary and tertiary grave sites (ICMP 2004; Skinner et al. 2001)

The current study represents an improvement on previous forensic remote sensing studies that attempted to use spectroscopy to visualize non-human burials from airborne platforms (Kalacska and Bell 2006; Kalacska et al. 2009; LeBlanc et al. 2014). Separation in those cases is attributable to exposed burial soils, and no attempts were made to establish burial signatures for later use as a reference sample during non-experimental unmarked burial detection. The current study is the first to compare spectra between burial and undisturbed vegetation to help separate human burials lacking exposed surface soils. Adding to the science of forensic remote sensing, the current research represents the first ever burial surface elevation change study using LIDAR point cloud data. Using terrestrial remote sensing technologies, this dissertation establishes spectral and topographic burial signatures to be referenced in non-experimental circumstances. These new signatures can be used as a supplement to existing burial detection methods, and further studies may eventually lead to stand-alone remote sensing burial detection methods.

From a practical standpoint, human burial detection will likely remain multi-disciplinary and multi-modal for the foreseeable future. As future studies such as this one continue to bring together fragments of information about disturbance signatures, we will better understand what makes different types of disturbance uniquely identifiable, and ultimately, detectable. The findings of this work will be most useful as a methodological supplement to improve upon existing methods, or as a component of a predictive modeling approach to locating human burials. These findings are also foundational building blocks with which additional research can develop and refine remote detection methods. This research establishes that anomalies are visible in terrestrial

spectral and topographic data, and investigators are encouraged to begin integrating those technologies into their existing field survey protocol, when possible.

Summary

This is the first study to specifically compare live vegetation spectra from human burial disturbance, non-burial disturbance, and undisturbed ground. It is also the first to use LIDAR as a tool for measuring human burial surface elevation changes over time. At present, the findings of terrestrial data analyses are enough to strongly support non-experimental field testing and additional experimental research into remote sensing as a forensic tool. Current burial detection methods can be augmented with these findings to help forensic investigators make more informed decisions about locating buried human remains. Fine tuning these methods, and establishing additional signatures indicative of buried human remains to facilitate their location will reduce costly and time-consuming fieldwork, further limiting investigators exposure to safety hazards on the ground. From an accounting perspective, the results of this study suggest that terrestrial spectroscopy and LIDAR may be useful technologies for identifying disturbed vegetation spectra and surface elevation changes, respectively. Given the rapid collection of remote sensing data, it may be worthwhile to integrate these technologies into existing burial detection protocol.

8.1 Future Directions

This study is a preliminary investigation of the relationship between human burials and their immediate environment, but inevitably, additional questions have emerged from the findings. More research is needed to understand the relationship between human burials, grave soils, regrowth of vegetation over human remains, the distribution of buried decomposing mass, the

timing of signature expressions, differences between grave sizes and number of interred individuals, and differences between human burials and non-burial disturbance.

Future research will benefit most from an unobstructed experimental setting that is conducive to simultaneous passive and active remote sensing. Passive sensor line-of-sight is severely restricted by the tree canopy during leaf-on months, and is a poor spectral match for leaf-off months when the ground surface is unobstructed, due to the low volume of live vegetation. In leaf-on conditions, LIDAR performs better than HSI due to its ability to provide an energy source that passes through gaps in tree canopy. It is perhaps the case that airborne remote sensing is poorly matched for burial detection in densely canopied environments. However, the terrestrial findings of the current study provide an adequate foundation for future research in unobstructed environments using ground-based and airborne sensing platforms.

Given the time-sensitive nature of human decomposition, particularly in warmer climates, future studies will benefit from a more frequent and evenly spaced data collection schedule to monitor the timing of potentially optimal windows for exploiting spectral or topographic signatures associated with human burials. This study presents snapshots of the longer timeline of burial signature expressions and it is not yet clear if signatures between groups were captured at their peak disparity or if peak disparity has yet to occur. Additional data collections not acquired in this study, such as recording a botanical inventory map, measuring gaseous emissions, or monitoring sub-surface temperature will help pinpoint decomposition stages, which may help determine which temporal windows are useful for applying remote sensing technologies.

Five of the seven statistical models developed to separate disturbed and undisturbed vegetation spectra include at least one shortwave infrared wavelength. Many of those individual wavelengths are potentially poor classifiers in reality, due to Planck curve characteristics and

reduced atmospheric transmission at longer wavelengths. However, several of those shortwave infrared wavelengths – namely, those in the 1440 – 2200 nm range – would be mostly unaffected by these two phenomena and are potentially valid and useful contributors to vegetation classification for this application. This research could not verify the performance of shortwave infrared wavelengths using airborne HSI because the imaging spectrometer range was limited to 400 – 1000 nm. Therefore, given the findings of this study, it is worth evaluating the contribution of shortwave infrared wavelengths as disturbed vegetation classifiers in future research.

Finally, this research took advantage of several frequentist statistical methods for spectral classification and visualization methods for establishing topographic patterns. As more data are collected to support predictive modeling, and as signatures are better understood as functions of time and circumstance, a Bayesian statistical approach will help more fully model the geophysical and contextual variables that indicate human burial presence. Additional data variables, such as soil nitrogen concentration, leaf chlorophyll concentration, or plant species density and location will help establish the drivers of vegetation spectral differences between samples. Similarly, subsurface data indicative of active decomposition, such as temperature and gaseous emissions, will help determine whether elevation change is primarily driven by soil settling or the redistribution of decomposing mass.

REFERENCES

Abrahams F, Peress G, Stover E. A Village Destroyed: May 14, 1999, War Crimes in Kosovo. Berkeley: University of California Press, 2002.

Addison T and Bruck T. Making Peace Work: The Challenges of Social and Economic Reconstruction. Palgrave Macmillan, 2008.

African Charter on the Rights and Welfare of the Child, Resolution 197 (XVI). Monrovia, 1990.

Aldana R. A Victim-Centered Reflection on Truth Commissions and Prosecutions as a Response to Mass Atrocities. Journal of Human Rights. 2006 5(1):107-126.

Altaweel M. The Use of ASTER Satellite Imagery in Archaeological Contexts. Archaeological Prospection 2005 12:151-166.

Anderson B, Meyer J, Carter DO. Dynamics of Ninhydrin-Reactive Nitrogen and pH in Gravesoil During the Extended Postmortem Interval. Journal of Forensic Sciences. 58(5):1348-1352.

Antkowiak TM. An Emerging Mandate for International Courts: Victim-Centered Remedies and Restorative Justice. Stanford Journal of International Law. 2011 47:279-332.

Areh I, Umek P. Personal characteristics and validity of eyewitness testimony. In: Gorazd M, Pagon M, Dobovsek B, editors. Policing in Central and Eastern Europe: Dilemmas of Contemporary Criminal Justice. Ljubljana: University of Maribor, 2004:1-5.

Armatta J. Twilight of Impunity: The War Crimes Tribunal of Slobodan Milošević. Duke University Press, 2010.

Aronson JD. The Strengths and Limitations of South Africa's Search for Apartheid-Era Missing Persons. *The International Journal of Transitional Justice*. 2012. 5(2):262-281.

Artz JA, Bristow ELD, Whittaker WE. Mapping Precontact Burial Mounds in Sixteen Minnesota Counties using Light Detection and Ranging (LIDAR). The Office of the Iowa State Archaeologist and the University of Iowa, 2013.

Badeck F-W, Bondeau A, Bottcher K, Doktor D, Lucht W, Schaber J, Sitch S. Responses of Spring Phenology to Climate Change. *New Phytologist*. 2004. 162(2):295-309.

Barone PM, Swanger KJ, Stanley-Price N, Thursfield A. Finding Graves in a Cemetery: Preliminary Forensic GPR Investigations in the Non-Catholic Cemetery in Rome (Italy). Measurement 2015 80:53-57.

Benninger LA, Carter DO, Forbes SL. The Biochemical Alteration of Soil Beneath a Decomposing Carcass. Forensic Science International. 2008 180:70-75.

Besl PJ, McKay ND. A Method for Registration of 3-D Shapes. IEEE Transactions on Pattern Analysis and Machine Intelligence. 14(2):239-256.

Bevan BW. The Search for Graves. Geophysics 1991 56(9):1310-1319.

Bewley RH, Crutchley SP, Shell CA. New light on an ancient landscape: LIDAR Survey in the Stonehenge World Heritage Site. Antiquity 2005 75:636-647.

Bladon P, Moffat I, Guilfoyle D, Beal A, Milani J. Mapping Anthropogenic Fill with GPR for Unmarked Grave Detection: A Case Study from a Possible Location of Mokare's Grave, Albany, Western Australia. Exploration Geophysics 2011 42:249-257.

Blankenship RE. Molecular Mechanisms of Photosynthesis. John Wiley & Sons, 2014.

Bock JH, Norris DO. Forensic Botany: An Under-Utilized Resource. Journal of Forensic Sciences. 1997 42(3):364-367.

Boggs JL, Tsegaye TD, Coleman TL, Reddy KC, Fahsi A. Relationship Between Hyperspectral Reflectance, Soil Nitrate-Nitrogen, Cotton Leaf Chlorophyll, and Cotton Yield: A Step Toward Precision Agriculture. Journal of Sustainable Agriculture. 2003 22(3):5-16.

Bomberger K. Maintain Public and Political Focus on the Effort to Find Those Who are Still Missing [Interview]. 21 March 2015. [http://www.icmp.int/uncategorized/one-director-of-the-missing-persons-institute-of-bosnia-and-herzegovina-issufficient/]

Boss P. Ambiguous Loss: Learning to Live with Unresolved Grief. Cambridge: Harvard University Press, 1999.

Boyd RM. Buried Body Cases. FBI Law Enforcement Bull. 1979 48(2):1-7.

Buck SC. Searching for Burials using Geophysical Technology: Field Tests with Ground Penetrating Radar, Magnetometry and Electrical Resistivity. Journal of Forensic Sciences 2003 48(1):1-7.

Büyüksaraça A, Yalçınerb CC, Ekincia YL, Demircia A, Yücelc MA. Geophysical Investigations at Agadere Cemetery, Gallipoli Peninsular, NW Turkey. Australian Journal of Forensic Sciences. 2013 1-13.

Brinkerhoff DW. Rebuilding Governance in Failed States and Post-Conflict Societies: Core Concepts and Cross-Cutting Themes. Public Administration and Development. 2005 25:3-14.

Caccianiga M, Bottacin S, Cattaneo C. Vegetation Dynamics as a Tool for Detecting Clandestine Graves. Journal of Forensic Sciences. 2012 57(4):983-988.

Callahan CA. Vegetation Colonization of Experimental Grave Sites in Central Texas [thesis]. San Marcos, TX: Texas State University, 2009.

Card BL, Baker IL. GRID: A Methodology Integrating Witness Testimony and Satellite Imagery Analysis for Documenting Alleged Mass Atrocities. Genocide Studies and Prevention: An International Journal. 2014 8(3):1-15.

Carson WP, Barrett GW. Succession in Old-Field Plant Communities: Effects of Contrasting Types of Nutrient Enrichment. Ecology. 69(4):984-994.

Carter DO, Tibbett M. Taphonomic Mycota: Fungi with Forensic Potential. Journal of Forensic Sciences. 2003 48(1):1-4.

Carter DO, Yellowlees D, Tibbett M. Cadaver Decomposition in Terrestrial Ecosystems. Naturwissenschaften. 2007 94:12-24.

Chase AF, Chase DZ, Weishampel JF, Drake JB, Shrestha RL, Slatton KC, Awe JJ, Carter WE. Airborne LiDAR, Archaeology, and the Ancient Maya Landscape at Caracol, Belize. Journal of Archaeological Science 2011 38(2):387-398.

Cheetham P. Forensic geophysical survey. In: Hunter J, Cox M, editors. Forensic Archaeology; Advances in Theory and Practice. Boca Raton: CRC Press, 2005:62-95.

Cheetham PN, Hanson I. Excavation and Recovery in Forensic Archaeological Investigations. In: Blau S, Ubelaker DH, editors. Handbook of Forensic Anthropology and Archaeology. Walnut Creek: Left Coast Press, 2009.

Christensen AM, Passalacqua NV, Bartelink EJ. Forensic Anthropology: Current Methods and Practice. Academic Press, 2014.

Christensen AM, Lowe WM, Reinecke GW. The Forensic Bulldozer as a Clandestine Grave Search Tool. Forensic Science Communications. 2009 11(4).

Cogliati S, Rossini M, Julitta T, Meroni M, Schickling A, Burkart A, Pinto F, Rascher U, Colombo R. Continuous and Long-Term Measurements of Reflectance and Sun-Induced Chlorophyll Fluorescence by using Novel Automated Field Spectroscopy Systems. *Remote Sensing of Environment*. 2015. 1-12.

Cole B, McMorrow J, Evans M. Spectral Monitoring of Moorland Plant Phenology to Identify a Temporal Window for Hyperspectral Remote Sensing of Peatland. ISPRS Journal of Photogrammetry and Remote Sensing. 2014. 90:49-58.

Collier P. Policy for Post-conflict Societies: Reducing the Risks of Renewed Conflict. Proceedings of the Economics of Political Violence Conference, Princeton, NJ 2000.

Comer DC, Harrower MJ (Eds.). Mapping Archaeological Landscapes from Space. New York: Springer, 2013)

Commisso R, Nelson D. Correlation between modern plant delta N-15 values and activity areas of Medieval Norse farms. Journal of Archaeological Science. 2008 35(2):492-504.

Commisso RG, Nelson DE. Stable Nitrogen Isotopic Examination of Norse Sites in the Western Settlement of Greenland. Journal of Archaeological Science. 2010 37(6):1233-1240.

Congram D. Spatial Analysis and Predictive Modeling of Unmarked Burials from Rearguard Repression of the Spanish Civil War [dissertation]. Burnaby (CAN): Simon Fraser University, 2010.

Congram D. A Clandestine Burial in Costa Rica: Prospection and Excavation. Journal of Forensic Sciences. 2008 53(4):793-796.

Connor MA. The Archaeology of Contemporary Mass Graves. The Society for American Archaeology, SAA Bulletin. 1996 14(4).

Convention (IV) Relative to the Protection of Civilian Persons in Time of War, Article 26. Geneva, 1949.

Cook BD, Corp LA, Nelson RF, Middleton EM, Morton DC, McCorkel JT, Masek JG, Ranson KJ, Ly V, Montesano PM. NASA Goddard's LIDAR, Hyperspectral, and Thermal (G-LiHT) Airborne Imager. Remote Sensing. 2013 5:4045-4066.

Corns A, Shaw R. High Resolution 3-Dimensional Documentation of Archaeological Monuments and Landscapes using Airborne LiDAR. Journal of Cultural Heritage 2009 108:e72-e77.

Corte Constitucional de Colombia. Ley 975 de 2005.

Corte Constitucional de Colombia. Constitucional Claim Decision C-370 de 2006.

Cox M, Flavel A, Hanson I. The Scientific Investigation of Mass Graves: Towards Protocols and Standard Operating Procedures. Cambridge University Press, 2008.

Crettol M, La Rosa AM. The Missing and Transitional Justice: The Right to Know and the Fight Against Impunity. International Review of the Red Cross. 2006 88(862):355-362.

Crossland Z. Of Clues and Signs: The Dead Body and Its Evidential Traces. American Anthropologist. 2009 111(1):69-80.

Curran P, Windham W, Gholz H. Exploring the Relationship Between Reflectance Red Edge and Chlorophyll Concentration in Slash Pine Leaves. Tree Physiology. 1995 15:203-206.

Dalan RA, De Vore SL, Clay RB. Geophysical Identification of Unmarked Historic Graves. Geoarchaeology. 2010 25(5): 572-601.

Danner M. The Truth of El Mozote. The New Yorker. December 1993.

Dautartas A, Jantz L, Vidoli G, Steadman DW. A Multidisciplinary Validation Study of Non-Human Animal Models for Decomposition Research: A Time Series Approach. Proceedings of the Academy of Forensic Sciences, 67th Annual Scientific Meeting, Orlando, FL 2015:106.

Dautartas A, Steadman DW, Mundorff AZ, Jantz L, Vidoli G. A Comparison of Seasonal Decomposition Patterns Between Human and Non-Human Models. Proceedings of the American Academy of Forensic Sciences, 68th Annual Scientific Meeting, Las Vegas, NV. 2016:180.

Davenport A, Harrison K. Swinging the Blue Lamp: The Forensic Archaeology of Contemporary Child and Animal Burial in the UK. Mortality. 2011 16(2):176-190.

De Leon J. The Land of Open Graves: Living and Dying on the Migrant Trail. University of California Press, 2015.

des Forges A. Leave None to Tell the Story: Genocide in Rwanda. New York: Human Rights Watch, 1999.

Doretti M, Burrell J. Gray Spaces and Endless Negotiations: Forensic Anthropology and Human Rights. In: Fox RG, Field LW, editors. Anthropology Put to Work. New York: Berg, 2007.

Doretti M, Fondebrider L. Science and Human Rights: Truth, Justice, Reparation, and Reconciliation, a Long Way in Third World Countries. In: Buchli V, Lucas G, editors. Archaeologies of the Contemporary Past. New York: Routledge, 2002.

(DPAA). The Defense POW/MIA Accounting Agency. Personnel Unaccounted From Past Conflicts. http://www.dpaa.mil/OurMissing/PastConflicts.aspx

Du H, Chang C, Ren H, D'Amico FM, JO Jensen J. New Hyperspectral Discrimination Measure for Spectral Characterization. Optical Engineering, 2004 43(8): 1777-1786.

(EAAF) The Argentine Forensic Anthropology Team. Biannual Report, 1994 – 1995.

(EAAF) The Argentine Forensic Anthropology Team. EAAF Objectives. http://eaaf.typepad.com/about_us/

Eppel S. Bones in the Forest in Matabeleland, Zimbabwe: Exhumations as a Tool for Transformation. The International Journal of Transitional Justice. 2014 8(3):404-425.

Eppel S. Healing the Dead: Exhumation and Reburial as a Route to Truth Telling and Reclaiming the Past in Rural Zimbabwe. In: Borer RA, editor. Telling the Truths: Truth Telling and Peace Building in Post-Conflict Societies. Notre Dame: Univ. of Notre Dame Press, 2006.

Evans DH. Airborne Laser Scanning as a Method for Exploring Long-Term Socio-Ecological Dynamics in Cambodia. Journal of Archaeological Science. 2016 74:164-175.

Evans DH, Fletcher RJ, Pottier C, Chevance JB, Soutif D, Tan BS, Im S, Ea D, Tin T, Kim S, Cromarty C, De Greef S, Hanus K, Bâty P, Kuszinger R, Shimoda I, Boornazian G. Uncovering Archaeological Landscapes at Angkor using LIDAR. Proceedings of the National Academy of Sciences. 2013 110(31):12595-12600.

Federal Bureau of Investigation. NCIC Missing Person and Unidentified Person Statistics, 2013.

Fife DN, Nambiar EKS. Effect of Nitrogen on Growth and Water Relations of Radiata Pine Families. Plant and Soil. 1995. 168-169:279-285.

Fondebrider L. The Application of Forensic Anthropology to the Investigation of Cases of Political Violence: Perspectives from South America. In: Blau S, Ubelaker DH, editors. Handbook of Forensic Anthropology and Archaeology. Walnut Creek: Left Coast Press, 2009.

Francaviglia RV. The Cemetery as an Evolving Cultural Landscape. Annals of the Association of American Geographers. 1971 61(3):501-509.

France DL, Griffin TJ, Swanburg JG, Lindemann JW, Davenport GC, Trammel V, Armbrust CT, Kondratieff B, Nelson A, Castellano K, Hopkins D. A Multidisciplinary Approach to the Detection of Clandestine Graves. Journal of Forensic Sciences. 1992 37(6):1445-1458.

Franklin SE. Remote Sensing for Sustainable Forestry Management. Boca Raton: CRC Press, 2001.

Fraunhofer J. Brechungs-undFarbenzerstreuungs-Vermögens verschiedener Glasarten, in Bezug auf die Vervollkommnung achromatischer Fernröhre. Die Akademie, 1817.

Gaffney C, Harris C, Pope-Carter F, Bonsall J, Fry R, Parkyn A. Still Searching for Graves: An Analytical Strategy for Interpreting Geophysical Data used in the Search for "Unmarked" Graves. Near Surface Geophysics. 2015 13(6):557-569.

Gagnon Jr., VP. Ethnic Nationalism and International Conflict: The Case of Serbia. International Security. 19(3):130-166.

García-Godos J, Lid KAO. Transitional Justice and Victims' Rights before the End of a Conflict: The Unusual Case of Colombia. *Journal of Latin American Studies* 42(2010):487-516.

Gassiot EG, Steadman DW. The Political, Social and Scientific Contexts of Archaeological Investigations of Mass Graves in Spain. Archaeologies. 2008 4(3):429-444.

Gates D, Keegan HJ, Schleter JC, Weidner VR. Spectral Properties of Plants. Applied Optics. 1965 4(1):11-20.

Gausman HW. Reflectance of Leaf Components. Remote Sensing of Environment. 1977. 6:1-9.

Geladi P, Kowalski B. Partial Least Squares Regression: A Tutorial. Analytica Chimica Acta 1986 185:1-17.

Gibson P. Introductory Remote Sensing Principles and Concepts. New York: Routledge, 2013.

Goetz AFH, Vane G, Solomon JE, Rock BN. Imaging Spectroscopy for Earth Remote Sensing. Science. 1985 228(4704):1147-1153.

Gonzalez E, Varney H. Truth-Seeking: Elements of Creating an Effective Truth Commission. Amnesty Commission of the Ministry of Justice of Brazil, 2013.

Goossens R, Wulf AD, Bourgeois J, Gheyle W, Willems T. Satellite Imagery and Archaeology: The Example of CORONA in the Altai Mountains. *Journal of Archaeological Science.* 33:745-755.

Gross JT. Neighbors: The Destruction of the Jewish Community in Jedwabne, Poland. Princeton, NJ: Princeton University Press, 2001.

Gulick K. Protection of Family Life. Studies in Transnational Legal Policy. 2010 41:291-336.

Gumerman GJ, Lyons TR. Archaeological Methodology and Remote Sensing. *Science*. 1971. 172(3979):126-132.

Gupta RP. Remote Sensing Geology. 2nd ed. New York: Springer, 2003.

Haglund WD, Connor M, Scott DD. The Archaeology of Contemporary Mass Graves. Historical Archaeology. 2001 35(1):57-69.

Haglund WD, Sorg MH. Forensic Taphonomy: The Post-Mortem Fate of Human Remains. Boca Raton: CRC Press, 1997.

Hansen, JD, Pringle JK, Goodwin J. GPR and Bulk Ground Resistivity Surveys in Burial Yards: Locating Unmarked Burials in Contrasting Soil Types. Forensic Science International. 2014;237:e14-e29.

Hanson I, Personal Communication, Nov 2012.

Harris EC. Principles of Archaeological Stratigraphy. New York:Elsevier, 2014.

Harrison M, Donnelly LJ. Locating Concealed Homicide Victims: Developing the Role of Geoforensics. In: Ritz K, Dawson L, Miller D, editors. Criminal and Environmental Soil Forensics. New York: Springer, 2009.

Henckaerts J. Study on Customary International Humanitarian Law: A Contribution to the Understanding and Respect for the Rule of Law in Armed Conflict. Customary Law. 2005 87(857):175-212.

Henckaerts J, Doswald-Beck L, Alvermann C. Customary International Humanitarian Law. Cambridge University Press, 2005.

Holliday VT. Soils in Archaeological Research. Oxford, UK: Oxford University Press, 2004.

Hopkins DW, Wiltshire PEJ, Turner BD. Microbial Characteristics of Soils from Graves: An Investigation at the Interface of Soil Microbiology and Forensic Science. Applied Soil Ecology. 2000 14:283-288.

Hoskuldsson A. PLS Regression Methods. Journal of Chemometrics. 1988 2:211-228.

Human Rights Center. Beyond Reasonable Doubt: Using Scientific Evidence to Advance Prosecutions at the International Criminal Court. Berkeley School of Law, 2012.

Human Rights Watch. Justice Compromised: The Legacy of Rwanda's Community-based Gacaca Courts. New York, 2011.

Hunter J, Simpson B. Preparing the Ground: Archaeology in a War Zone. In: Ferllini R, editor. Forensic Archaeology and Human Rights Violations. Springfield: Thomas, 2007.

Hunter J, Roberts C, Martin A. Studies in Crime: An Introductin to Forensic Archaeology. Routledge: London, 1996.

Ignatiew RJ. Jedwabne Tragedy: Final Findings of Poland's Institute for National Memory. *Info Poland*. July 2002.

International Commission on Missing Persons. Mandate. http://www.icmp.int/about-us/mandate/

International Commission on Missing Persons. Where We Work: Europe. http://www.icmp.int/where-we-work/europe/

International Commission on Missing Persons. Maintain Public and Political Focus on the Effort to Find Those Who Are Still Missing, 2015.

International Commission on Missing Persons. Colombia's Response to Enforced Disappearances: Overview and Recommendations. Sarajevo: ICMP, 2008.

International Commission on Missing Persons. Batajnica Summary Report: Forensic Monitoring Activites. Sarajevo: ICMP, 2004.

International Convention for the Protection of All Persons from Enforced Disappearance, Resolution 61/177. The United Nations, 2006.

International Criminal Tribunal for the Former Yugoslavia. Decision on Motion for Judgement of Acquittal, Prosecutor vs. Slobodon Milošević. 16 June 2004.

International Criminal Tribunal for the Former Yugoslavia. Milošević Trial Transcripts. 14 February 2002.

Jackson LE, Strauss RB, Firestone MK, and Bartolome JW. Plant and Soil Nitrogen Dynamics in California Annual Grassland. Plant and Soil. 1988 110:9-17.

Jessee E, Skinner M. A Typology of Mass Grave and Mass Grave-Related Site. Forensic Science International. 2005 152(1):55-59.

Jervis JR, Pringle JK. A Study of the Effect of Seasonal Climatic Factors on the Electrical Resistivity Response of Three Experimental Graves. Journal of Applied Geophysics. 2014 108:53-60.

Johnson JK, Haley BS. Sensor and Data Fusion Technologies in Archaeology. In: Proceedings of the ISPRS WG VII/5 Workshop; 2011 Nov 18-19; Cologne.

Joseph G. Fundamentals of Remote Sensing, 2nd Ed. Hyderabad: Universities Press, 2005.

Juhl K, Olsen OE. Societal Safety, Archaeology and the Investigation of Contemporary Mass Graves. Journal of Genocide Research. 2006 8(4):411-435.

Kalacska M, Bell LS. Remote Sensing as a Tool for the Detection of Clandestine Mass Graves. Canadian Society of Forensic Science Journal. 2006 39(1):1-13.

Kalacska ME, Bell LS, Sanchez-Azofeifa GA, Caelli T. The Application of Remote Sensing for Detecting Mass Burials: An Experimental Animal Case Study from Costa Rica. Journal of Forensic Sciences. 2009 54(1):159-166.

Kaye D. Justice Beyond the Hague: Supporting the Prosecution of International Crimes in National Courts. Council on Foreign Relations, Council Special Report, No. 61, June 2011.

Keene J. Bodily Matters Above and Below Ground: The Treatment of American Remains from the Korean War. The Public Historian. 2010 32(1):59-78.

Killam EW. The Detection of Human Remains, 2nd Ed. Charles C. Thomas: Springfield, 2004.

Kirschner RH, Hannibal KE. The Application of the Forensic Sciences to Human Rights Investigations. Medicine and Law. 1994 13(5/6):451-460.

Klinkner M. Forensic Science for Cambodian Justice. The International Journal of Transitional Justice. 2008 2:227-243.

Knipling EB. Physical and Physiological Basis for the Reflectance of Visible and Near-Infrared Radiation from Vegetation. *Remote Sensing of Environment.* 1970. 1:155-159.

Kokalj Z, Zaksek K, Ostir K. Application of Sky-View Factor for the Visualization of Historic Landscape Features in LIDAR-Derived Relief Models. Antiquity. 2011 327(85):263-273.

Komar D. Patterns of Mortuary Practice Associated with Genocide Implications for Archaeological Research. Current Anthropology. 2008 49(1):123-133.

Kovras I. Unearthing the Truth: The Politics of Exhumations in Cyprus and Spain. *History and Anthropology*. 2008. 19(4):371-390.

Kruse FA, Lefkoff AB, Boardman JB, Heidebrecht KB, Shapiro AT, Barloon PJ, Goetz AFH. The Spectral Image Processing System (SIPS) – Interactive Visualization and Analysis of Imaging Spectrometer Data. Remote Sensing of Environment. 1993 44:145 – 163.

Kvamme K, Ernenwein E, Harburial M, Sever T, Harmon D, Limp F. New Approaches to the Use and Integration of Multi-Sensor Remote Sensing for Historic Resource Identification and Evaluation. University of Arkansas, Center for Advanced Spatial Technologies. 2006.

Lambert JH, DiLaura DL. Photometry, or, on the Measure and Gradations of Light, Colors, and Shade: Translation from the Latin of Photometria, sive, de mensura et gradibus luminis, colorum et umbrae. Illuminating Engineering Society of North America, 2001.

Larson DO, Vass AA, Wise M. Advanced Scientific Methods and Procedures in the Forensic Investigation of Clandestine Graves. Journal of Contemporary Justice. 2011 27(2):149-182.

Lasaponara R, Coluzzi R, Gizzi FT, Masini N. On the LiDAR contribution for the archaeological and geomorphological study of a deserted medieval village in Southern Italy. Journal of Geophysics and Engineering. 2010 7:155-163.

Lasaponara R, Masini N. Satellite Remote Sensing in Archaeology: Past, Present, and Future Perspectives. Journal of Archaeological Science. 2011 38:1995-2002.

Lasseter AE, Jacobi KP, Farley R, Hensel L. Cadaver Dog and Handler Team Capabilities in the Recovery of Buried Human Remains in the Southeastern United States. Journal of Forensic Sciences. 2003 48(3):617-621.

LeBlanc G, Kalacksa M, Soffer R. Detection of Single Burials by Airborne Hyperspectral Imaging. Forensic Science International. 2014;245:17-23.

Lee TY, Kaufman YJ. Non-Lambertian Effects on Remote Sensing of Surface Reflectance and Vegetation Index. Geoscience and Remote Sensing, IEEE Transactions. 1986 GE-24(5):699-708.

Lloyd M. Exhuming a Painful Past: Anthropologists Dig up Guatemalan Massacre Sites as Victims' Families Watch. The Chronicle of Higher Education. 2002 48(29):42-43.

Lundy P, McGovern M. Whose Justice? Rethinking Transitional Justice from the Bottom Up. Journal of Law and Society. 2008 35(2): 265-292.

Maitra S, Yan J. Principal Component Analysis and Partial Least Squares: Two Dimension Reduction Techniques for Regression. Casualty Actuarial Society, Discussion Paper Program. 2008 79-90.

Mamdani M. When Victims Become Killers. Princeton: Princeton University Press, 2002.

Mann RW, Bass WM, Meadows L. Time Since Death and Decomposition of the Human Body: Variables and Observations in Case and Experimental Field Studies. Journal of Forensic Sciences. 1990 103-111.

Martin Molina C, Pringle JK, Saumett M, Hernandez O. Preliminary Results of Sequential Monitoring of Simulated Clandestine Graves in Colombia, South America, Using Ground Penetrating Radar and Botany. Forensic Science International. 2015 248:61-70.

Masini N, Lasaponara R, Orefici G. Addressing the Challenge of Detecting Archaeological Adobe Structures in Southern Peru Using QuickBird Imagery. Journal of Cultural Heritage. 2009 10S:e3-39.

Menard S. Applied Logistic Regression Analysis. Thousand Oaks: Sage, 2002.

Mendeloff D. Truth-Seeking, Truth-seeking, and Post-Conflict Peacebuilding: Curb the Enthusiasm? International Studies Review 2004 6:355-380.

Miller WF, Walls MD, Blakeman C. Applications of Remote Sensing in Archaeological Site Identification. NASA. 1974. 1-24.

Mundorff AZ, Figueroa-Soto C, Commisso R. Assessing the Usefulness of Plant $\delta^{15}N$ as a New Forensic Tool to Identify Clandestine Burials. In: Proceedings of the American Academy of Forensic Sciences Annual Meeting; 2014 Feb 17-22; Seattle.

NASA The National Aeronautical and Space Administration. Earth Observatory: Remote Sensing Accomplishments
http://earthobservatory.nasa.gov/Features/RemoteSensing/remote_09.php

NASA. A History of NASA Remote Sensing Contributions to Archaeology. *Journal of Archaeological Science*. 2011. 38:2003-2009.

Netto AT, Campostrini E, Goncalves de Oliveira J, Bressan-Smith RE. Photosynthetic Pigments, Nitrogen, Chlorophyll a Flourescence and SPAD-502 Readings in Coffee Leaves. Scientia Horticulturae. 2005 104:199-209.

Nero C, Aning AA, Danour SK, Noye RM. Delineation of Graves Using Electrical Resistivity Tomography. Journal of Applied Geophysics. 2016 126:138-147.

Nicodemus FE, Richmond JC, Hsia JJ. Geometrical Considerations and Nomenclature for Reflectance. Institute for Basic Standards, National Bureau of Standards. Washington, DC, 1977.

Norton EA. The Application of In Situ Reflectance Spectroscopy for the Detection of Mass Graves [thesis]. Cranfield (UK): Cranfield University, 2010.

Nwogu NV. When and Why it Started: Deconstructing Victim-Centered Truth Commissions in the Context of Ethnicity-Based Conflict. International Journal of Transitional Justice. 2010 4(2): 275-289.

Olsen TD, Payne LA, Reiter AG, Wiebelhaus-Brahm E. When Truth Commissions Improve Human Rights. International Journal of Transitional Justice. 2010. 4:457-476.

Owsley DW. Why the Forensic Anthropologist Needs the Archaeologist. Historical Archaeology. 2001 35(1):35-38.

Owsley DW. Techniques for Locating Burials, with Emphasis on the Probe. Journal of Forensic Sciences. 1995 40:735-740.

Parcak S (Ed.). Satellite Remote Sensing for Archaeology. New York: Routledge, 2009.

Pearlman AR. Digging for Truth, Justice, or the Humanitarian Way: Priorities in Post-Genocide Transitional Justice and Exhumations of Mass Graves. US Department of Defense, Arlington, 2008.

Penuelas J, Baret F, Filella I. Semi-Empirical Indices to Assess Carotenoids/Chlorophyll-a Ratio from Leaf Spectral Reflectance. Photosynthetica. 1995 31:221-230.

Petrig A. The War Dead and their Gravesites. International Review of the Red Cross. 2009 91(874):341-369.

Physicians for Human Rights. Satellite Images of Mass Grave Site. http://physiciansforhumanrights.org/issues/mass-atrocities/afghanistan-war-crime/satellite-images.html, 2009.

Physicians for Human Rights. Forensic Monitoring Project Report: Bijelo Polje Exhumations. State Commission Report. Boston, 1998.

Polgar CA, Primack RB. Leaf-out Phenology of Temperate Woody Plants: from Trees to Ecosystems. New Phytologist. 2011 926-941.

Pollack MSCE. Intentions of Burial: Mourning, Politics, and Memorials Following the Massacre at Srebrenica. Death Studies. 2003 27(2):125-142.

Pringle JK, Jervis J, Cassella JP, Cassidy NJ. Time-Lapse Geophysical Investigations Over a Simulated Urban Clandestine Grave. Journal of Forensic Sciences. 2008 53(6):1405-1416.

Protocol Additional to the Geneva Conventions of 12 August 1949, and Relating to the Protection of Victims of International Armed Conflict (Protocol I), 1977.

Prunier G. The Rwanda Crisis: History of a Genocide. New York: Columbia University Press, 1995.

Pu R, Gong P. Hyperspectral Remote Sensing of Vegetation Bioparameters. In: Weng Q, editor. Advances in Environmental Remote Sensing: Sensors, Algorithms, and Applications. Boca Raton: CRC Press, 2011.

Quinn GP, Keough MJ. Experimental Design and Data Analysis for Biologists. Cambridge University Press, 2002.

R Core Team. R: A Language and Environment for Statistical Computing. R Foundation for Statistical Computing. Vienna, Austria. [https://www.R-project.org/] 2015.

Raychaudhuri B. Remote Sensing of Solar-Induced Chlorophyll Fluorescence at Atmospheric Oxygen Absorption Band Around 760 nm and Simulation of that Absorption in Laboratory. *IEEE Transactions on Geoscience and Remote Sensing*. 50(10):3908-3914.

Riley MA. Automated Detection of Prehistoric Conical Burial Mounds from LIDAR Bare-Earth Digital Elevation Models [thesis]. Maryville: Northwest Missouri State University, 2009.

Robins S. Towards a Victim-centered Transitional Justice: Understanding the Needs of Families of the Disappeared in Postconflict Nepal. The International Journal of Transitional Justice. 2011 5:75-98.

Rodriguez WC, Bass WM. Decomposition of Buried Bodies and Methods that May Aid in Their Location. Journal of Forensic Sciences. 35(1):103-111.

Rosenblatt A. Digging for the Disappeared: Forensic Science after Atrocity. Stanford University Press, 2015.

Rouse J, Haas R, Schell J, Deering D. Monitoring Vegetation Systems in the Great Plains with ERTS. In: Proceedings of the Third ERTS Symposium; 1973 Dec 10-14; Washington, DC.

Rowlands A, Sarris A. Detection of Exposed and Subsurface Archaeological Remains using Multi-sensor Remote Sensing.

Rugg J. Defining the Place of Burial: What Makes a Cemetery a Cemetery? Mortality 2000 b5(3):259-275.

Salsarola D, Poppa P, Amadasi A, Mazzarelli D, Gibelli D, Zanotti E, Porta D, Cattaneo C. The Utility of Ground-Penetrating Radar and Its Time-Dependence in the Discovery of Clandestine Burials. Forensic Science International. 2015 253:119-124.

Sanchez G. plsdepot:Partial Least Squares (PLS) Data Analysis Methods. R Package Version 0.1.17. [http://CRAN.R-project.org/package=plsdepot] 2012.

Sanford V. Excavations of the Heart: Reflections on Truth, Memory, and Structures of Understanding. In: Sanford V and A Angel-Ajani (eds.) Engaged Observer: Anthropology, Advocacy, and Activism. New Brunswick: Rutgers University Press, 2006.

Sanford V. Buried Secrets: Truth and Human Rights in Guatemala. Palgrave Macmillan, 2003.

The Satellite Sentinel Project. Cover-Up: New Evidence of Three Mass Graves in South Kordofan. http://hhi.harvard.edu/publications/cover-new-evidence-three-mass-graves-south-kordofan, 2011.

Saturno W, Sever TL, Irwin DE, Howell BF, Garrison TG. Putting Us on the Map: Remote Sensing Investigation of the Ancient Maya Landscape. In: Wiseman J, El-Baz F, editors. Remote Sensing in Archaeology. New York: Springer, 2007.

Scagel CF, Guihong B, Fuchigami LH, Regan RP. Seasonal Variation in Growth, Nitrogen Uptake and Allocation by Container-Grown Evergreen and Deciduous Rhododendron Cultivars. HortScience 2007 42(6):1440-1449.

Schaepman-Strub G, Painter T, Huber S, Dangel S, Schaepman ME, Martonchik J, Berendse F. About the Importance of the Definition of Reflectance Quantities – Results of Case Studies. Proceedings of the XXXV ISPRS Congress, 2004.

Schmitt S. Mass Graves and the Collection of Forensic Evidence: Genocide, War Crimes, and Crimes against Humanity. In: Haglund WD, Sorg MH, editors. Advances in Forensic Taphonomy: Method, Theory, and Archaeological Perspectives. Boca Raton: CRC Press, 2001.

Schott JR. Remote Sensing: The Image Chain Approach. Oxford, UK: Oxford University Press, 2007.

Schultz JJ. The Application of Ground-Penetrating Radar for Forensic Grave Detection. In: Dirkmaat DC, editor. A Companion to Forensic Anthropology. Malden: Wiley-Blackwell, 2012.

Schultz JJ, Dupras TL. The Contribution of Forensic Archaeology to Homicide Investigations. Homicide Studies. 2008 12(4):399-413.

Schultz JJ, Martin MM. Controlled GPR Grave Research: Comparison of Reflection Profiles between 500 – 250MHz. Forensic Science International. 2011 209(1-3):64-69.

Schwarz J, Staenz K. Adaptive Threshold for Spectral Matching of Hyperspectral Data. Canadian Journal of Remote Sensing. 2001 27(3):216-224.

Scollar I, Tabbagh A, Hesse A, Herzog I. Archaeological Prospecting and Remote Sensing. 2nd Ed. Cambridge University Press, 2009.

Scott J, Hunter JR. Environmental Influences on Resistivity Mapping for the Location of Clandestine Graves. The Geological Society. 2004 232:33-38.

Schotsmans EM, Denton J, Dekeirsschieter J, Ivaneanu T, Leentjes S, Janaway RC, Wilson AS. Effects of Hydrated Lime and Quicklime on the Decay of Buried Human Remains using Pig Cadavers as Human Body Analogues. Forensic Science International. 2012 217:50-59.

Schotsman EMJ, Van de Voorde W, De Winne J, Wilson AS. The Impact of Shallow Burial on Differential Decomposition to the Body: A Temperate Case Study. Forensic Science International.2011 206:e43-e48.

Schürch P, Densmore AL, Rosser NJ, Lim M, McArdell BW. Detection of Surface Change in Complex Topography using Terrestrial Laser Scanning: Application to the Illgraben Debris-Flow Channel. Earth Surface Processes and Landforms. 36(14):1847-1859.

Shan J, Sampath A. Urban Terrain and Building Extraction from Airborne LIDAR Data. In: Weng Q, Quatttrochi DA, editors. Urban Remote Sensing. Boca Raton: CRC Press, 2006.

Shaw R. Memory Frictions: Localizing the Truth and Reconciliation Commission in Sierra Leone. The International Journal of Transitional Justice. 2007 1:183-207.

Skaar E. Reconciliation in a Transitional Justice Perspective. *Transitional Justice Review.* 2012. 1:54-103.

Skinner M. Planning the Archaeological Recovery of Evidence from Recent Mass Graves. Forensic Science International. 1987 34(4):267-287.

Skinner M, Alemijevic D, Djuric-Srejic M. Guidelines for International Forensic Bio-archaeology Monitors of Mass Grave Exhumations. Forensic Science International. 2003 134:81-92.

Skinner M, York HP, Connor MA. Post-burial disturbance of burials in Bosnia and Herzegovina. In: Haglund WD, Sorg MH, editors. Advances in Forensic Taphonomy: Method, Theory and Archaeological Perspectives. Boca Raton: CRC Press, 2001.

Sims D, Gamon J. Relationships Between Leaf Pigment Content and Spectral Reflectance Across a Wide Range of Species, Leaf Structures, and Developmental Stages. Remote Sensing of Environment. 2002 81:337-354.

Smalley GW. Seasonal Variation in the Nutrient Composition of Yellow-Poplar Leaves. Sewanee, TN: US Forest Service – USDA, 1971.

Snirer E. Hyperspectral Remote Sensing of Individual Gravesites – Exploring the Effects of Cadaver Decomposition on Vegetation and Soil Spectra [thesis]. Montreal (CAN): McGill University, 2013.

Sobotkova A, Ross SA. High-Resolution, Multi-Spectral Satellite Imagery and Extensive Archaeological Prospection: Case Studies from Apulia, Italy and Kazanluk, Bulgaria. In: Campano S, Forte M, Liuzza C (Eds.) Space, Time, Place: Third International Conference on Remote Sensing in Archaeology. 2010. 2118:25-28.

St.-Jacques C. Bellefleur P. Determining Leaf Nitrogen Concentration of Broadleaf Tree Seedlings by Reflectance Measurements. Tree Physiology. 1991. 8:391-398.

Staub E. Reconciliation after Genocide, Mass Killing, or Intractable Conflict: Understanding the Roots of Violence, Psychological Recovery, and Steps toward a General Theory. Political Psychology. 2006 27(6):867-894.

Staub E, Pearlman LA. Healing, Reconciliation and Forgiving after Genocide and other Collective Violence. In: Helmick SJ, Petersen RL, editors. Forgiveness and Reconciliation: Religion, Public Policy and Conflict Transformation. Randor, PA: Templeton Foundation Press, 2001.

Steadman DW, Dautartas A, Mundorff AZ, Vidoli G, Jantz L. Differential Raccoon Scavenging Among Pig, Rabbit and Human Subjects. Proceedings of the American Academy of Forensic Sciences, 68th Annual Scientific Meeting, Las Vegas, NV. 2016:192.

Steadman DW. Hard Evidence: Case Studies in Forensic Anthropology, 2nd Ed. Prentice Hall: NJ, 2009.

Steele C. Archaeology and the Forensic Investigation of Recent Mass Graves: Ethical Issues for a New Practice of Archaeology. Archaeologies: Journal of the World Archaeological Congress. 2008 4(3):414-428.

Stover E. The Witnesses: War Crimes and the Promise of Justice in the Hague. University of Pennsylvania Press, 2011.

Stover E. In the Shadow of Nuremburg: Pursuing War Criminals in the Former Yugoslavia and Rwanda. Medicine and Global Survival. 1995 2(3):140-146.

Stover E, Haglund WD, Samuels M. Exhumation of Mass Graves in Iraq: Considerations for Forensic Investigations, Humanitarian Needs, and the Demands of Justice. Journal of the American Medical Association. 2003 290(5):663-666.

Stover E, Shigekane R. The Missing in the Aftermath of War: When Do the Needs of Victims' Famillies and International War Crimes Tribunals Clash? International Committee of the Red Cross. 2002 84(848):845-866.

Stuesse A. Si Hubo Genocido: Anthropologists and the Genocide Trial of Guatemela's Ríos Montt. American Anthropologist. 2013. 115(4):658-666.

Thenkabail, PS, Lyon JG, Huete A. Hyperspectral Remote Sensing of Vegetation. Boca Raton: CRC Press, 2011.

Thomas JR, Oerther GF. Estimating Nitrogen Content of Sweet Pepper Leaves by Reflectance Measurements. Agronomy Journal. 1972. 64:11-13.

Thoms ONT, Ron J, Paris R. State-Level Effects of Transitional Justice: What Do We Know? The International Journal of Transitional Justice. 2010 4:329-354.

Trotter A. Witness Intimidation in International Trials: Balancing the Need for Protection Against the Rights of the Accused. George Washington International Law Review. 2012 44:521-537.

Tsay ML, Gjerstad DH, Glover R. Tree Leaf Reflectance: A Promising Technique to Rapidly Determine Nitrogen and Chlorophyll Concentration. Canadian Journal of Forest Research. 1982. 12(4):788-792.

Tuller H, Hofmeister U, Daley S. Spatial Analysis of Mass Burial Mapping Data to Assist in the Reassociation of Disarticulated and Commingled Human Remains. In: Adams B, Byrd J, editors. Recovery, Analysis, and Identification of Commingled Human Remains. Totowa: Humana Press, 2008.

Ubelaker DH. Human Skeletal Remains: Excavation, Analysis, Interpretation, 3rd Ed. Washington, DC: Taraxacum, 1999.

United Nations Manual on the Effective Prevention and Investigation of Extra-Legal, Arbitrary, and Summary Executions, E/ST/CSDHA/.12. The United Nations, 1991.

van der Meer FD, de Jong. Imaging Spectrometry: Basic Principles and Prospective Applications. New York: Springer, 2011.

Vass A, Thompson CV, Wise M. New Forensics Tool: Development of an Advanced Sensor for Detecting Clandestine Graves. NIJ Final Report, 2010

Vaughan RA. Remote Sensing Applications in Meteorology and Climatology. New York: Springer, 2012.

Veale A, Stavrou A. Former Lord's Resistance Army Child Soldier Abductees: Explorations of Identity in Reintegration and Reconciliation. Peace and Conflict: Journal of Peace Psychology. 2007 13(3):273-292.

Verbitsky H. The Flight: Confessions of an Argentine Dirty Warrior. The New Press, 1996.

Vitousek P. Nutrient Cycling and Nutrient Use Efficiency. American Naturalist. 1982 553-572.

Wack R, Wimmer A. Digital Terrain Models from Airborne Laser Scanner Data: A Grid Based Approach. ISPRS Commission II I Symposium, 9 – 13 September 2002, Austria.

Wagner S. The Social Complexities of Commingled Remains. In: Adams B and J Byrd (eds.) Commingled Human Remains: Methods in Recovery, Analysis, and Identification. Academic Press, 2014.

Wagner S. To Know Where He Lies: DNA Technology and the Search for Srebrenica's Missing. Berkeley: University of California Press, 2008.

Wald PM. Dealing with Witnesses in War Crime Trials: Lessons from the Yugoslav Tribunal. Yale Human Rights and Development Law Journal. 2002 5:217-239.

Walter BF. Does Conflict Beget Conflict? Explaining Recurring Civil War. Journal of Peace Research. 2004 41(3):371-388.

Watson CJ, Forbes SL. An Investigation of the Vegetation Associated with Grave Sites in Southern Ontario. Journal of the Canadian Society of Forensic Science. 2008 41(4):199-207.

Weinstein H. Where There is No Body: Trauma and Bereavement in Communities Coping with the Aftermath of Mass Violence. The ICRC Workshop on Support for Families of People Unaccounted for. Geneva, Switzerland, 10-11 June 2002.

Weitman SL. Using Archaeological Methods in Cemetery Surveys with Emphasis on the Application of LIDAR [thesis], Statesboro, GA: Georgia Southern University, 2012.

Weng Q. Scale Issues in Remote Sensing. John Wiley & Sons, 2014.

White DA. Transportation, Integration, Facilitation: Prehistoric Trail Networks of the Western Papagueria [dissertation]. Boulder, CO: The University of Colorado, 2007.

White DA. AVIRIS and Archaeology in Southern Arizona. AVIRIS Proceedings. NASA, 2003.

Wickham H. ggplot2: Elegant Graphics for Data Analysis. Springer-Verlag New York, 2009.

Williams ED, Crews JD. From Dust to Dust: Ethical and Practical Issues Involved in the Location, Exhumation, and Identification of Bodies from Mass Graves. Croatian Medical Journal. 2003 44(3):251-258.

Willum B. Eyes in the Sky: In Service of Humanity? Imaging Notes, October 2000.

Wiseman JR, F El-Baz F (Eds.). Remote Sensing in Archaeology. New York: Springer, 2007.

Witmer FDW. Remote Sensing of Violent Conflict: Eyes from Above. International Journal of Remote Sensing. 2015 36(9):2326-2352.

Woolley JT. Reflectance and Transmittance of Light by Leaves. Plant Physiology. 1971. 47:656-662.

Wright R. Where Are the Bodies? In the Ground. The Public Historian. 2010 32(1):96-107.

Yoder BJ, Pettigrew-Crosby RE. Predicting Nitrogen and Chlorophyll Content and Concentrations from Reflectance Spectra (400 – 2500 nm) at Leaf and Canopy Scales. Remote Sensing of Environment. 1995 53(3):199-211.

Young JE. The Texture of Memory: Holocaust Memorials and Meaning. Yale University Press: Princeton, 1993.

Zaksek K, Ostir K, Kokalj Z. Sky-View Factor as a Relief Visualization Technique. Remote Sensing. 2011 3: 398-415.

Zeibak R, Filin S. Change Detection via Terrestiral Laser Scanning. IASPRS. 2007 36(3):430-435.

Zhang X, Friedl MA, Schaaf CB, Strahler AH, Hodges JCF, Gao F, Reed B, Huete A. Monitoring Vegetation Phenology using MODIS. *Remote Sensing of Environment*. 2003. 471-475.

APPENDICES

Appendix A: Spectral Comparisons per Individual Burial/Control

Spectral Angle Mapper (SAM)

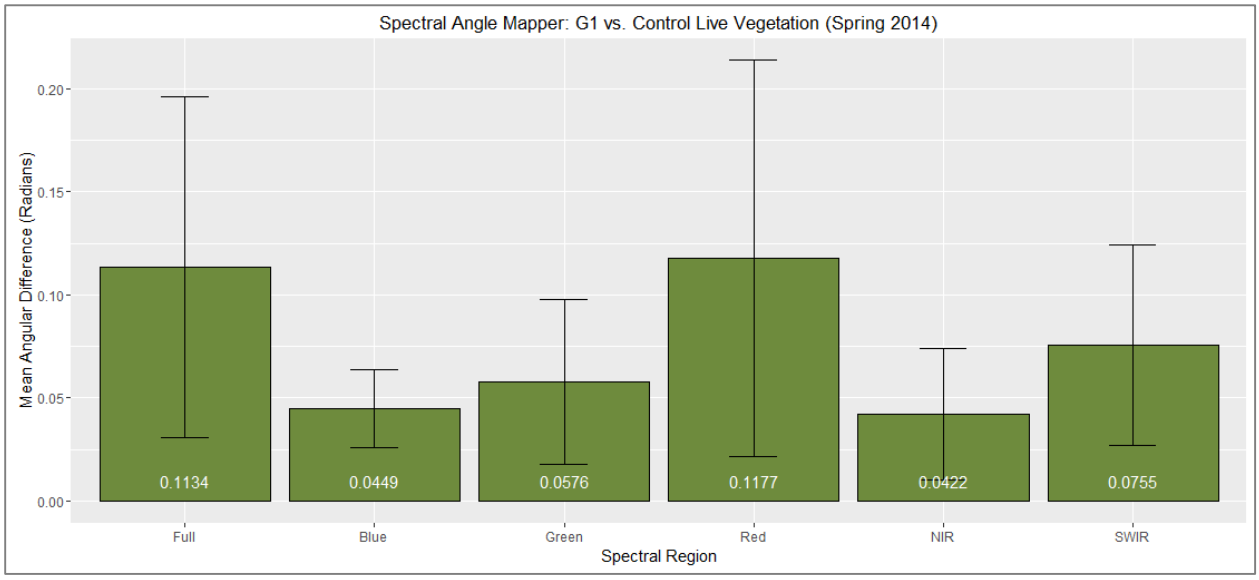

Figure A.1: Spectral Angle Mapper (SAM) results; Spring FieldSpec samples; all individual G1 spectra (n=16) vs. Control spectral mean (derived from n=17) mean; comparisons of full spectrum and regions (left to right).

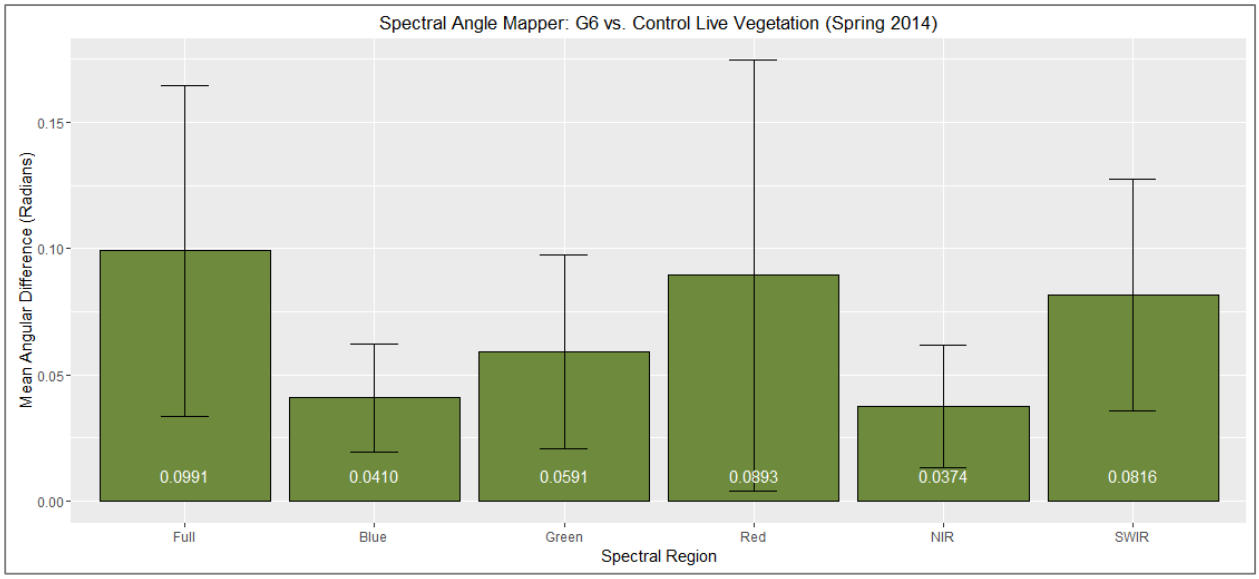

Figure A.2: Spectral Angle Mapper (SAM) results; Spring FieldSpec samples; all individual G6 spectra (n=36) vs. Control spectral mean (derived from n=17); comparisons of full spectrum and regions (left to right).

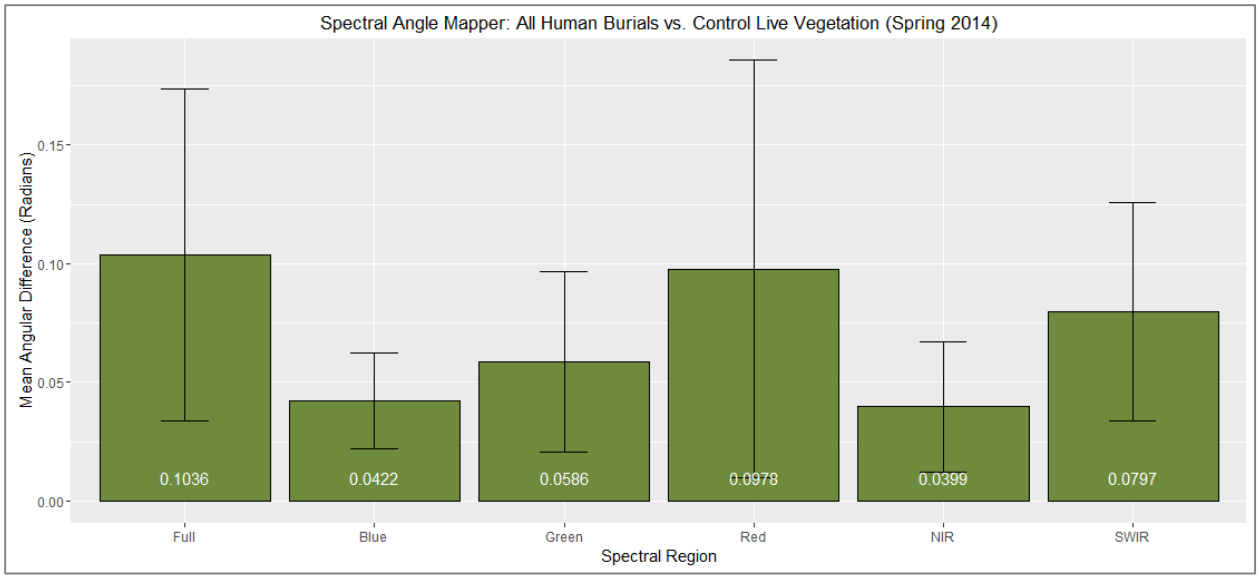

Figure A.3: Spectral Angle Mapper (SAM) results; Spring FieldSpec samples; all individual human Burial spectra (n=53) vs. Control spectral mean (derived from n=17); comparisons of full spectrum and regions (left to right).

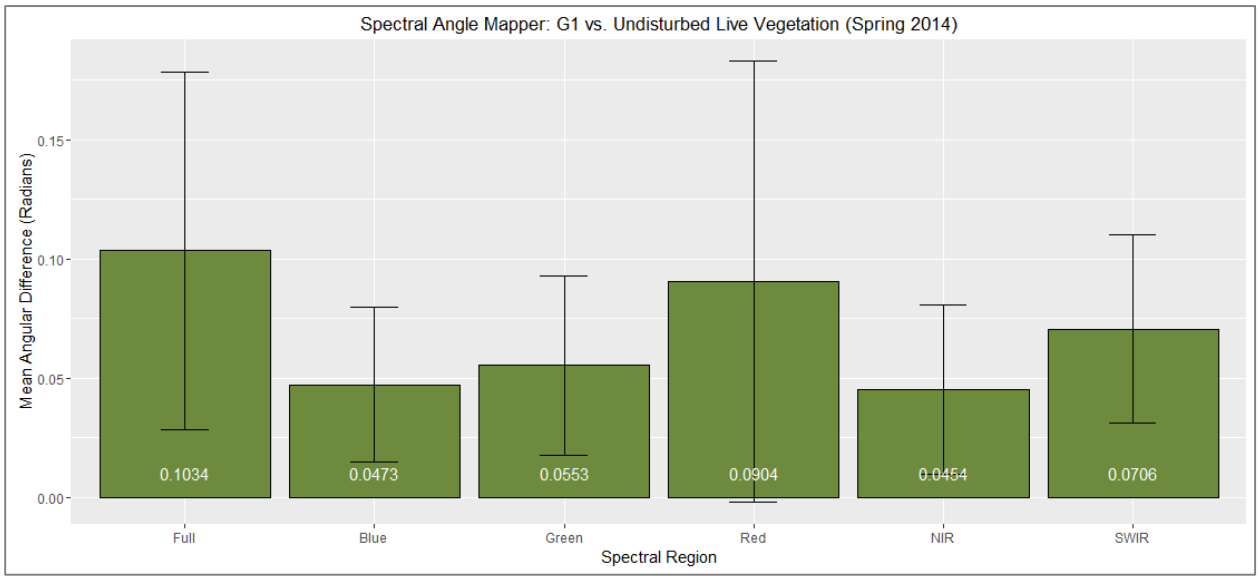

Figure A.4: Spectral Angle Mapper (SAM) results; Spring FieldSpec samples; all individual G1 spectra (n=16) vs. Undisturbed spectral mean (derived from n=84); comparisons of full spectrum and regions (left to right).

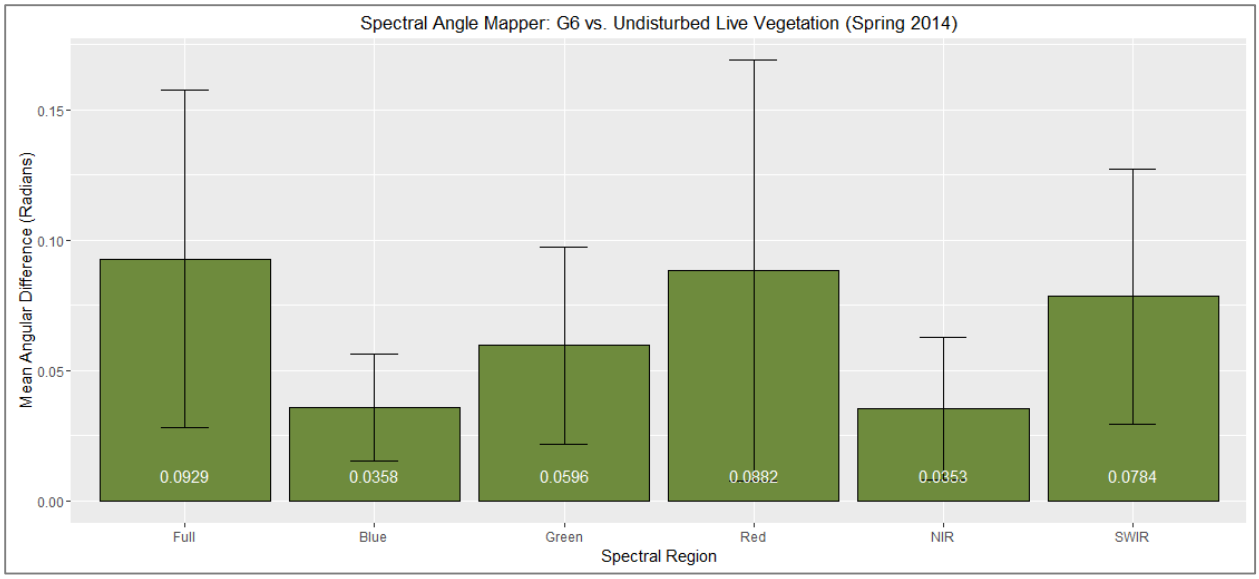

Figure A.5: Spectral Angle Mapper (SAM) results; Spring FieldSpec samples; all individual G6 spectra (n=36) vs. Undisturbed spectral mean (derived from n=84); comparisons of full spectrum and regions (left to right).

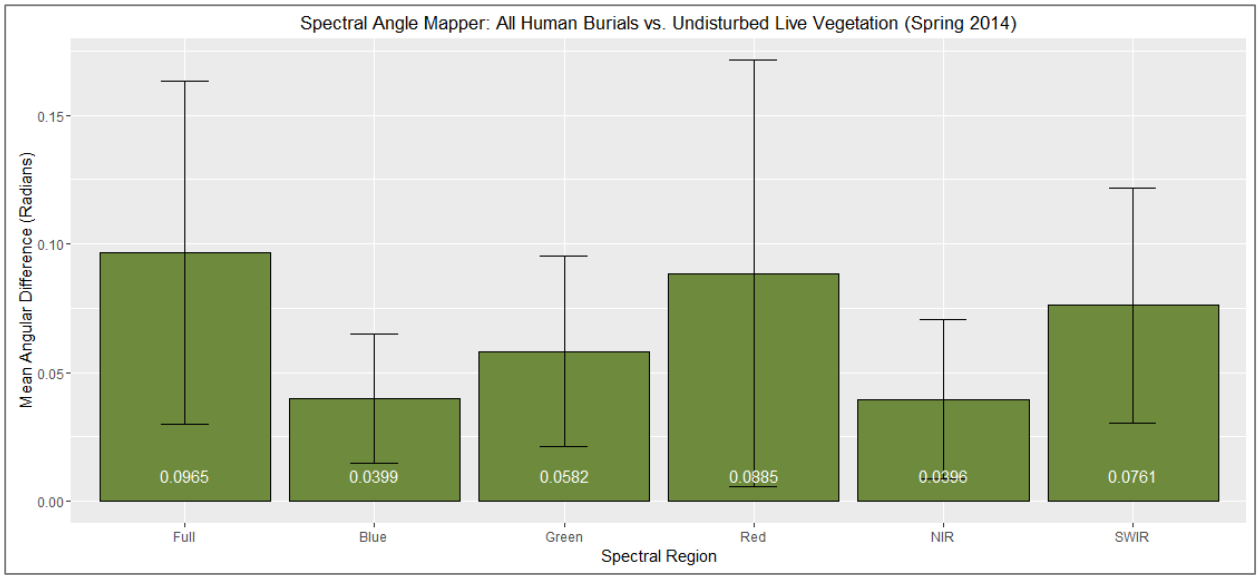

Figure A.6: Spectral Angle Mapper (SAM) results; Spring FieldSpec samples; all individual human Burial spectra (n=53) vs. Undisturbed spectral mean (derived from n=84); comparisons of full spectrum and regions (left to right).

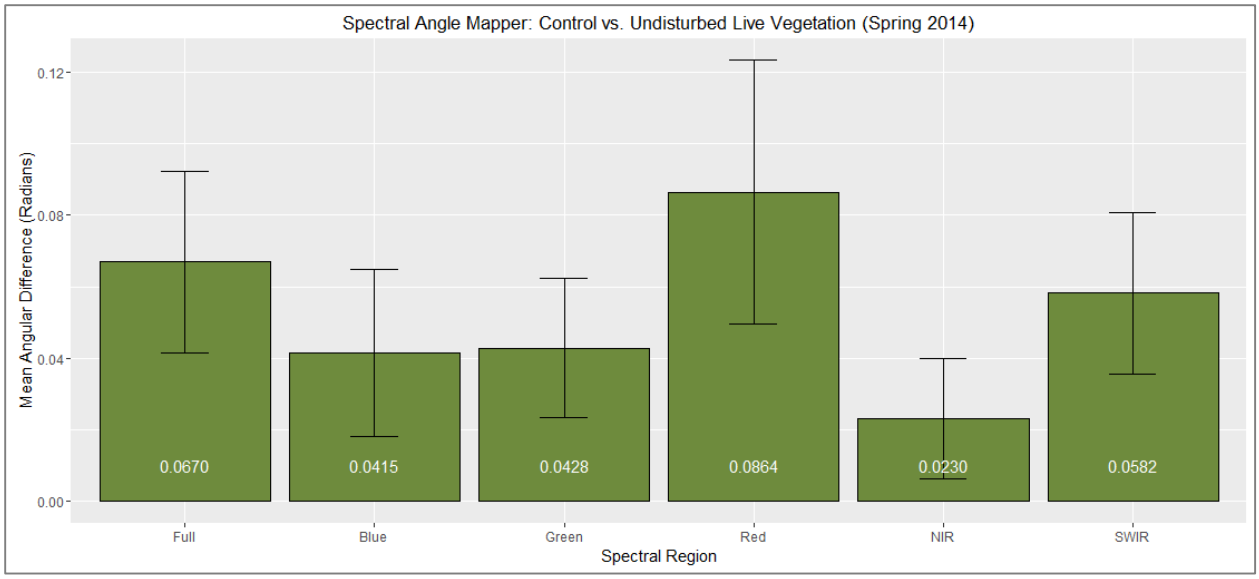

Figure A.7: Spectral Angle Mapper (SAM) results; Spring FieldSpec samples; all individual Control spectra (n=17) vs. Undisturbed spectral mean (derived from n=84); comparisons of full spectrum and regions (left to right).

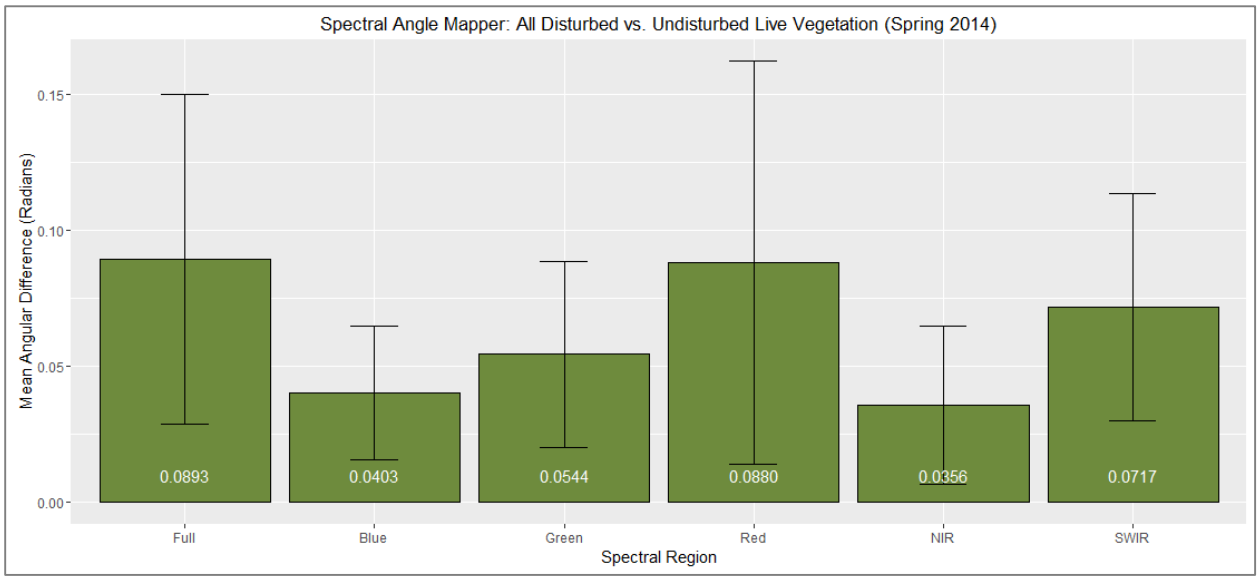

Figure A.8: Spectral Angle Mapper (SAM) results; Spring FieldSpec samples; all individual human burial and control ('Disturbed') spectra (n=70) vs. Undisturbed spectral mean (derived from n=84); comparisons of full spectrum and regions (left to right).

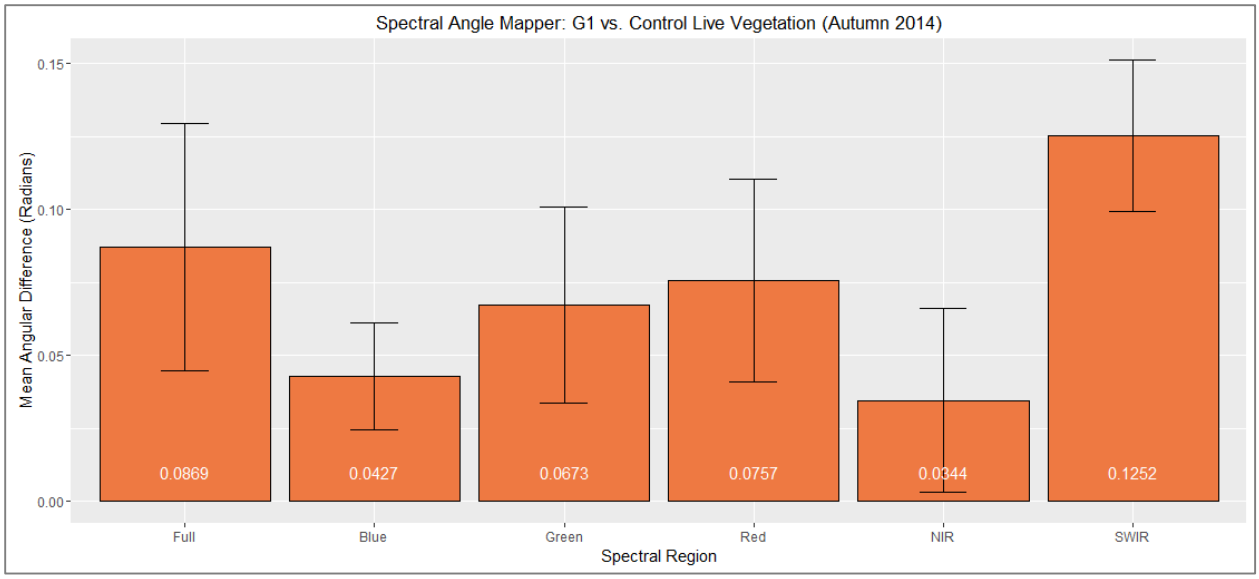

Figure A.9: Spectral Angle Mapper (SAM) results; Autumn FieldSpec samples; all individual G1 spectra (n=11) vs. Control spectral mean (derived from n=5) mean; comparisons of full spectrum and regions (left to right).

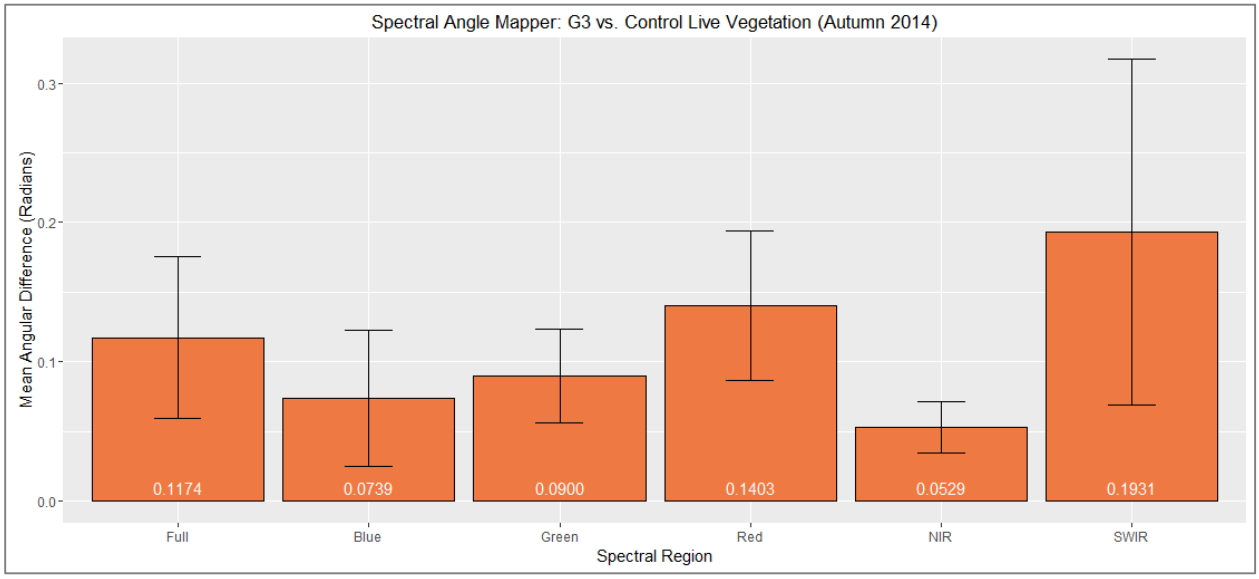

Figure A.10: Spectral Angle Mapper (SAM) results; Autumn FieldSpec samples; all individual G3 spectra (n=8) vs. Control spectral mean (derived from n=5) mean; comparisons of full spectrum and regions (left to right).

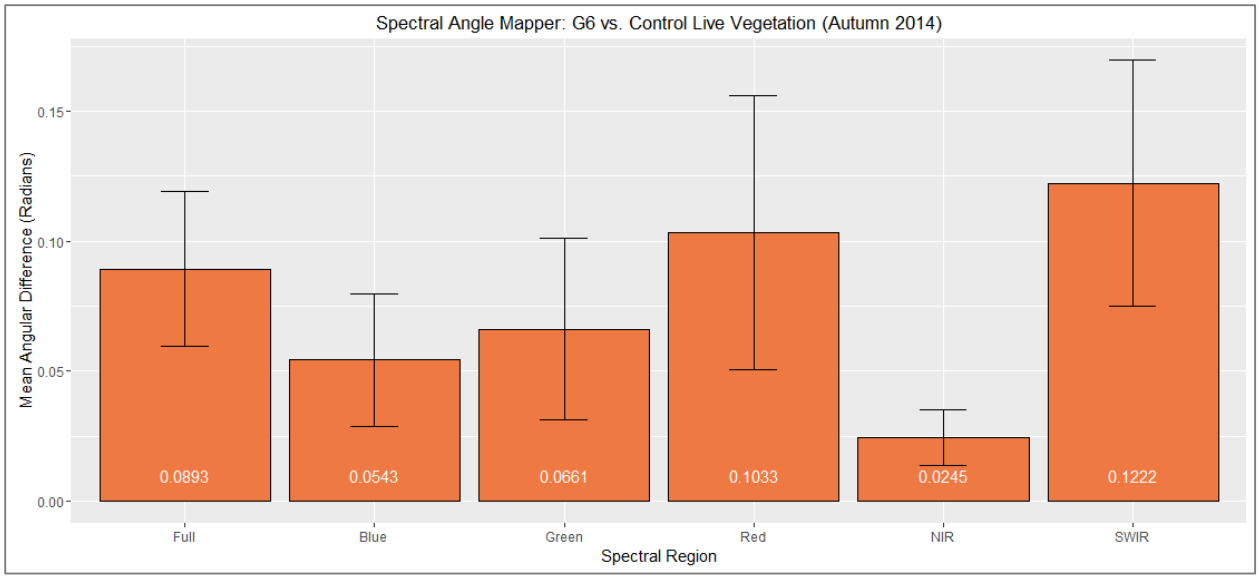

Figure A.11: Spectral Angle Mapper (SAM) results; Autumn FieldSpec samples; all individual G6 spectra (n=30) vs. Control spectral mean (derived from n=5) mean; analyses by full spectrum and by region (left to right).

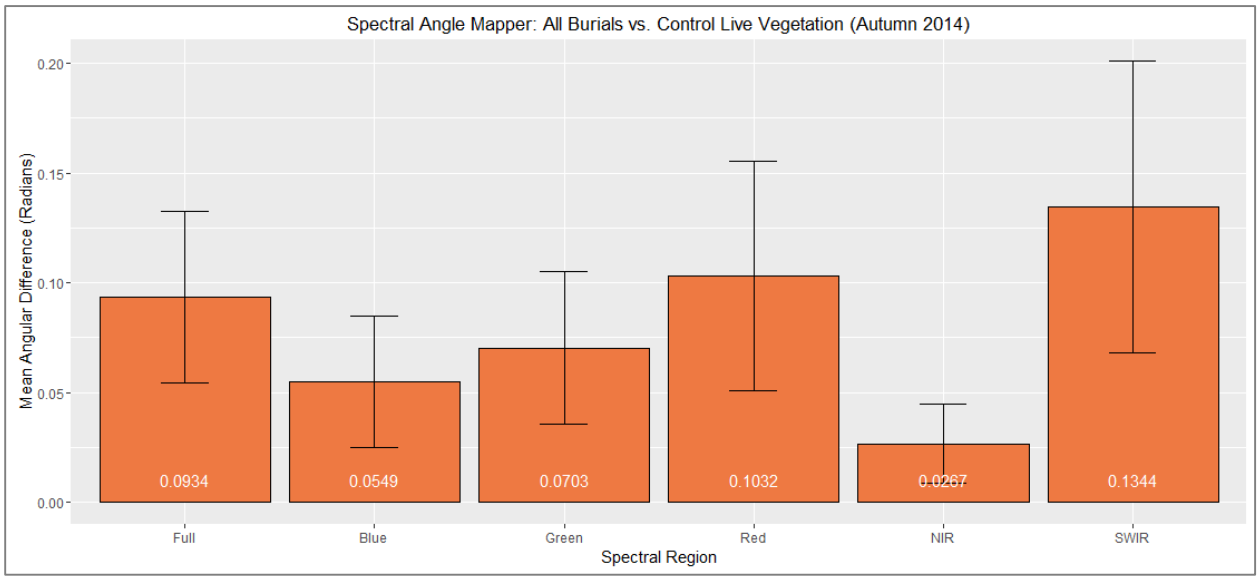

Figure A.12: Spectral Angle Mapper (SAM) results; Autumn FieldSpec samples; all individual human Burial spectra (n=49) vs. Control spectral mean (derived from n=5) mean; comparisons of full spectrum and regions (left to right).

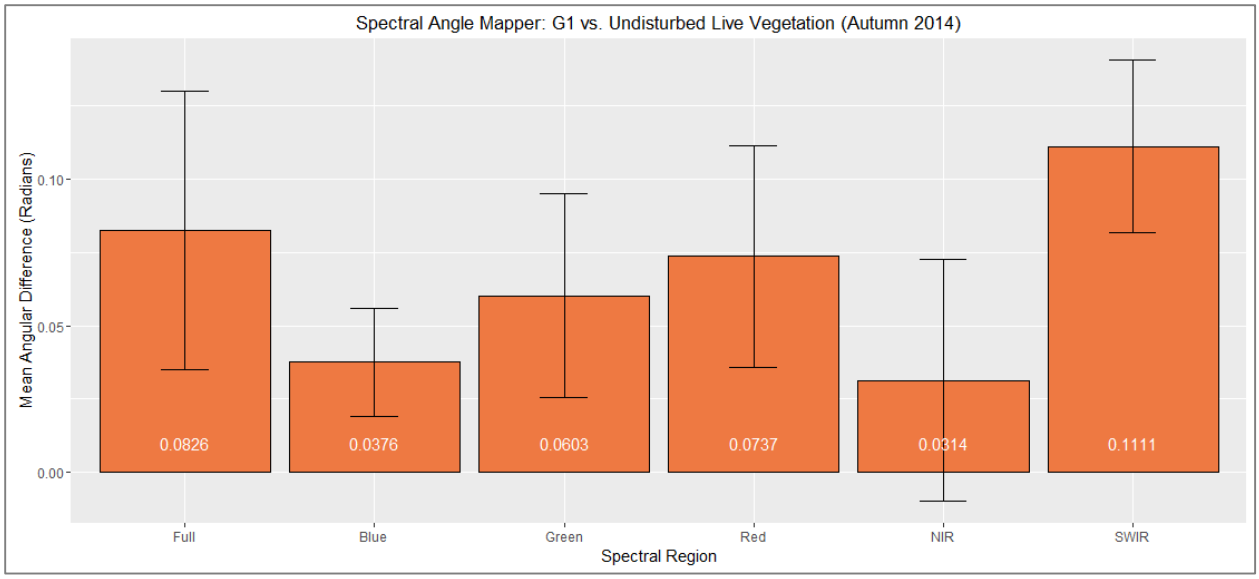

Figure A.13: Spectral Angle Mapper (SAM) results; Autumn FieldSpec samples; all individual G1 spectra (n=11) vs. Undisturbed spectral mean (derived from n=79) mean; comparisons of full spectrum and regions (left to right).

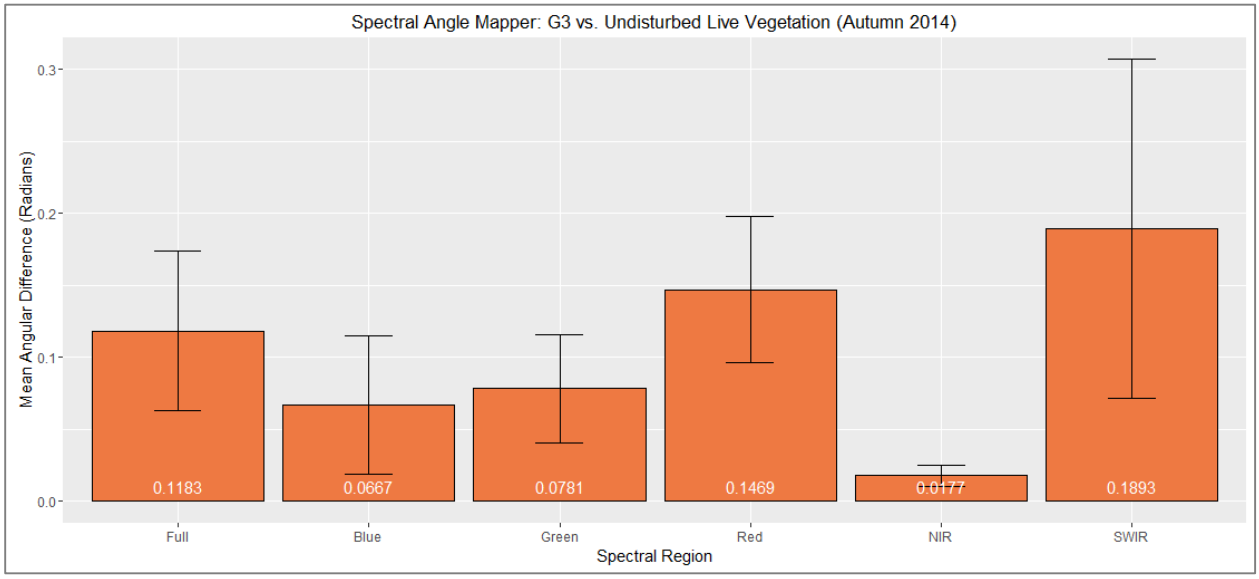

Figure A.14: Spectral Angle Mapper (SAM) results; Autumn FieldSpec samples; all individual G3 spectra (n=8) vs. Undisturbed spectral mean (derived from n=79) mean; comparisons of full spectrum and regions (left to right).

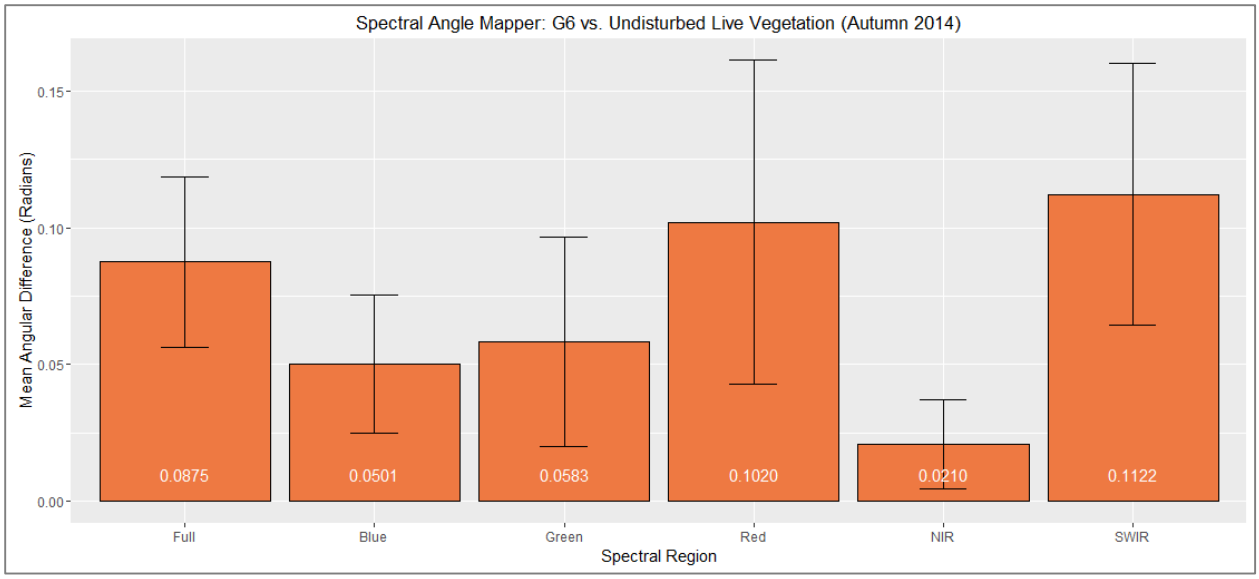

Figure A.15: Spectral Angle Mapper (SAM) results; Autumn FieldSpec samples; all individual G6 spectra (n=30) vs. Undisturbed spectral mean (derived from n=79) mean; comparisons of full spectrum and regions (left to right).

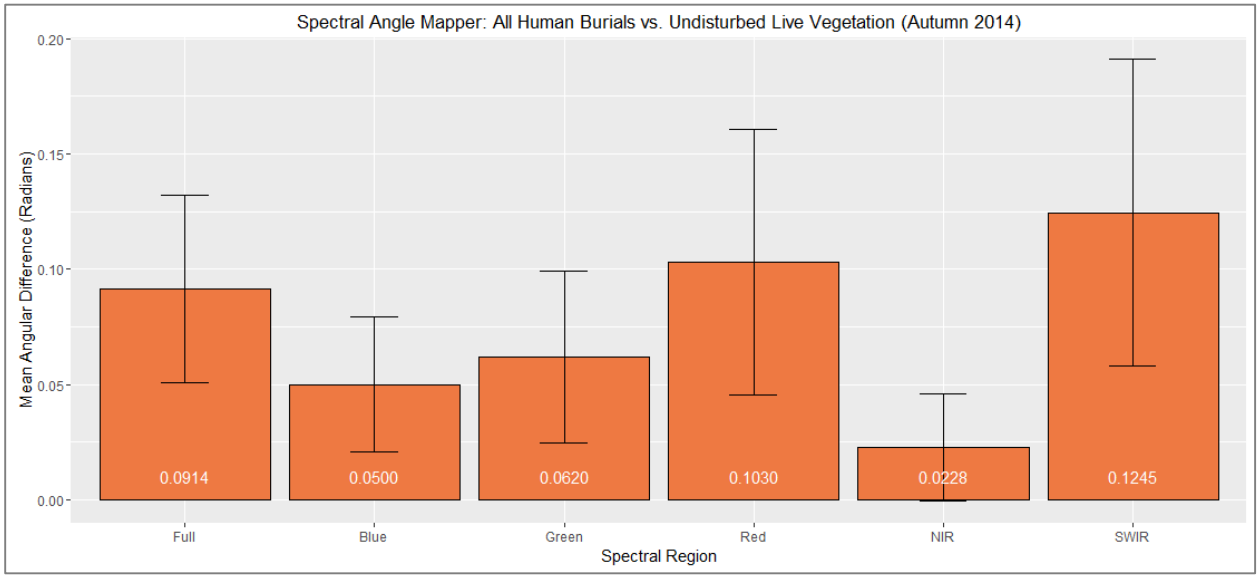

Figure A.16: Spectral Angle Mapper (SAM) results; Autumn FieldSpec samples; all individual human Burial spectra (n=49) vs. Undisturbed spectral mean (derived from n=79) mean; comparisons of full spectrum and regions (left to right).

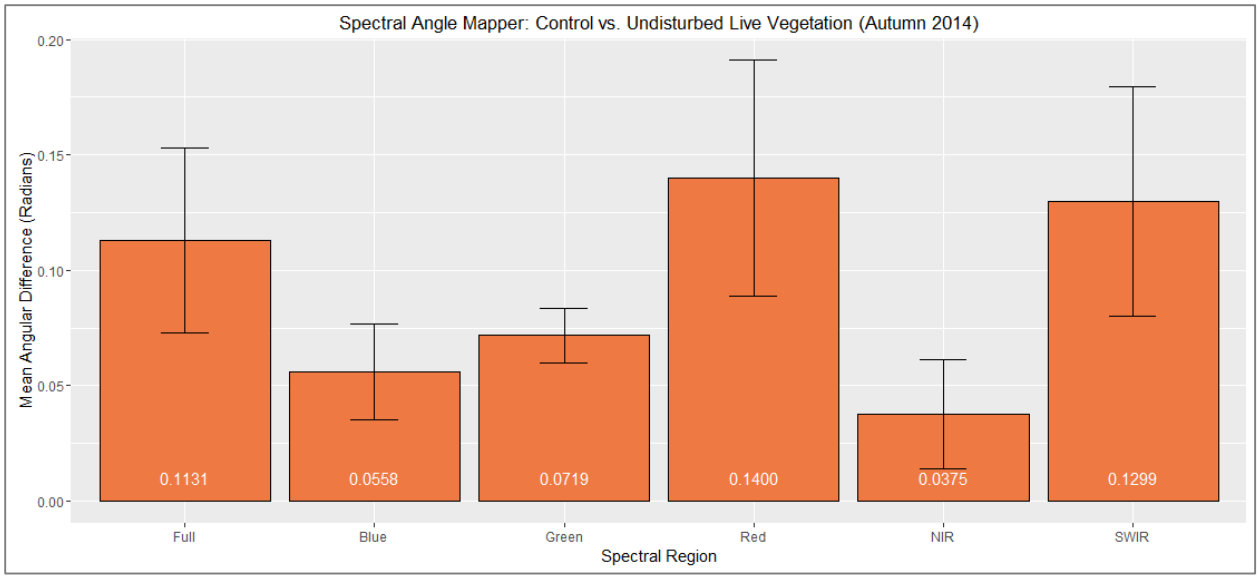

Figure A.17: Spectral Angle Mapper (SAM) results; Autumn FieldSpec samples; all individual Control spectra (n=5) vs. Undisturbed spectral mean (derived from n=79) mean; comparisons of full spectrum and regions (left to right).

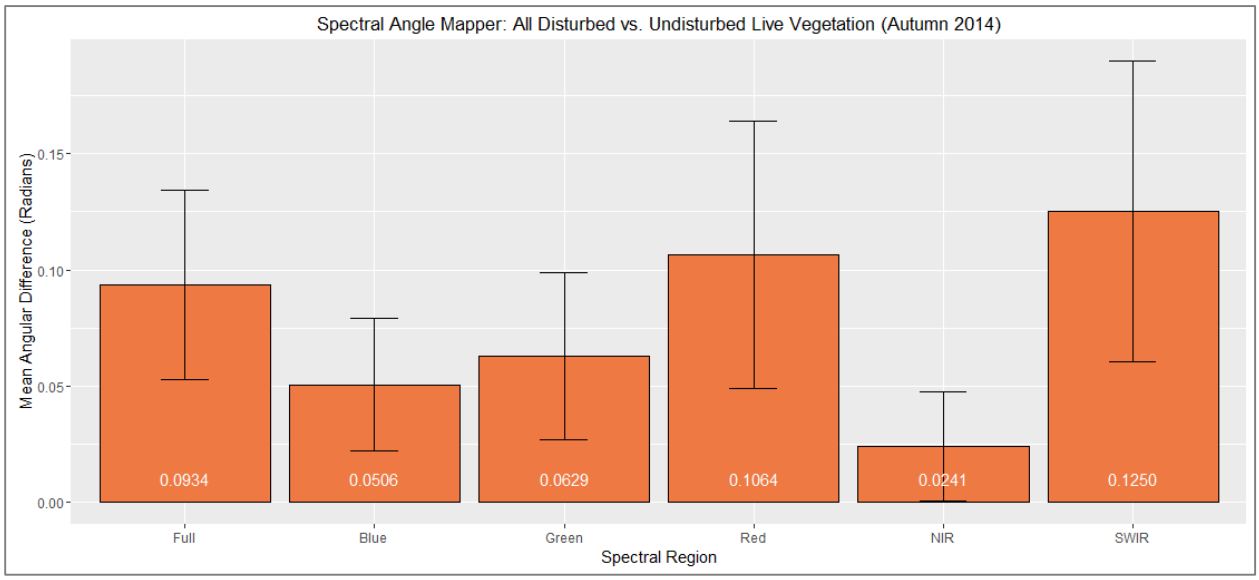

Figure A.18: Spectral Angle Mapper (SAM) results; Autumn FieldSpec samples; all individual human burial and control ('Disturbed') spectra (n=54) vs. Undisturbed spectral mean (derived from n=79) mean; comparisons of full spectrum and regions (left to right).

Spectral Information Divergence (SID)

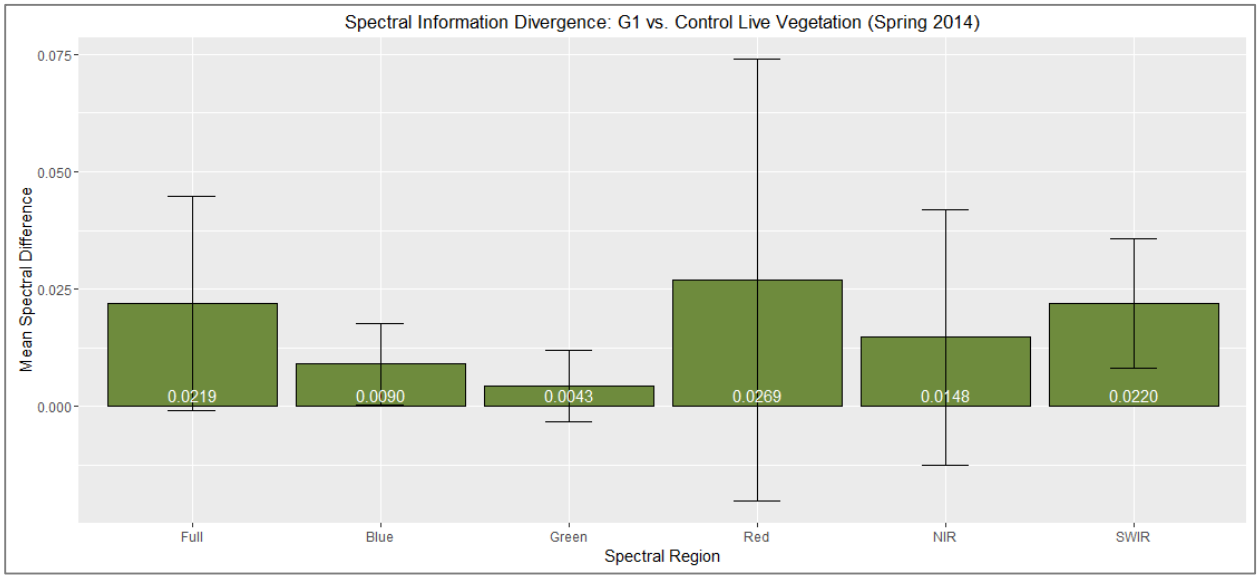

Figure A.19: Spectral Information Divergence (SID) results; Spring FieldSpec samples; all individual G1 spectra (n=16) vs. Control spectral mean (derived from n=17) mean; comparisons of full spectrum and regions (left to right).

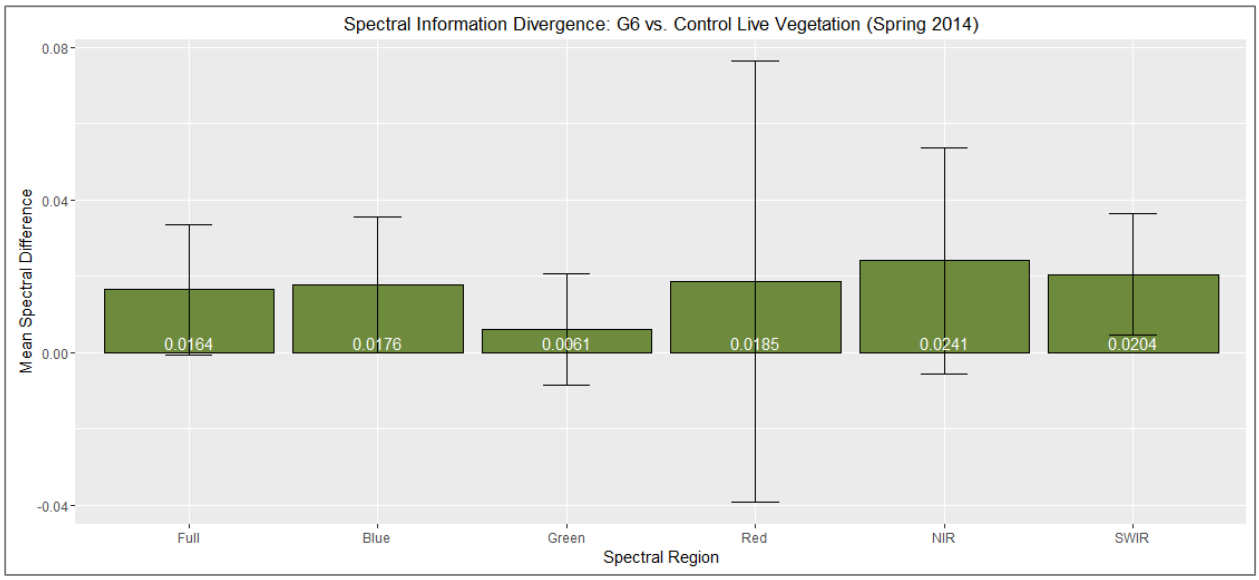

Figure A.20: Spectral Information Divergence (SID) results; Spring FieldSpec samples; all individual G6 spectra (n=36) vs. Control spectral mean (derived from n=17) mean; comparisons of full spectrum and regions (left to right).

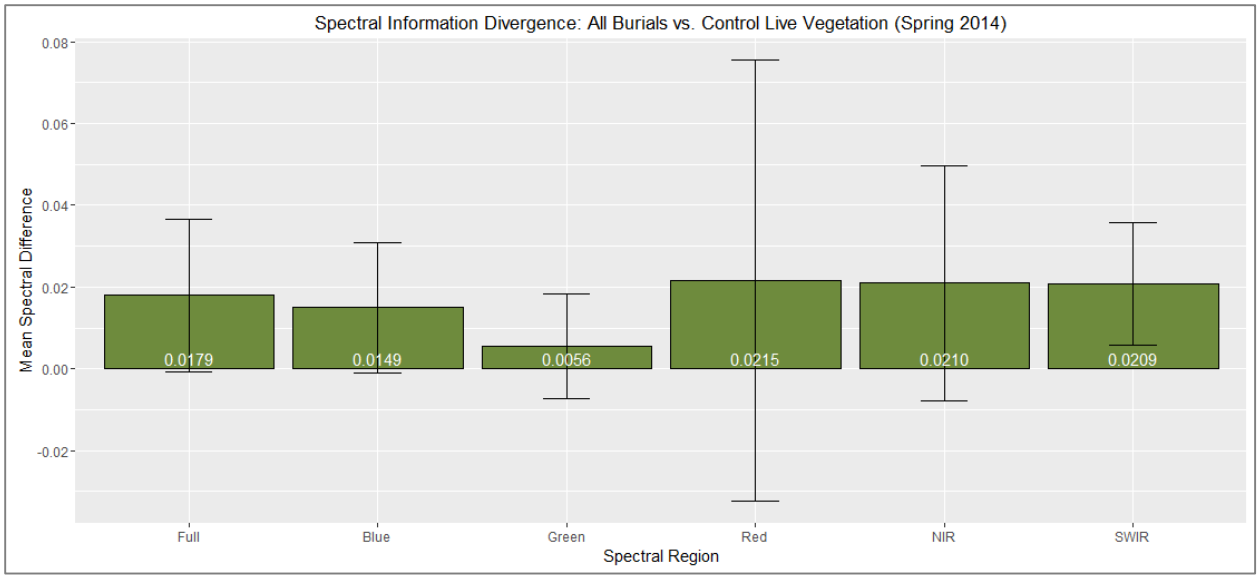

Figure A.21: Spectral Information Divergence (SID) results; Spring FieldSpec samples; all individual human Burial spectra (n=53) vs. Control spectral mean (derived from n=17) mean; comparisons of full spectrum and regions (left to right).

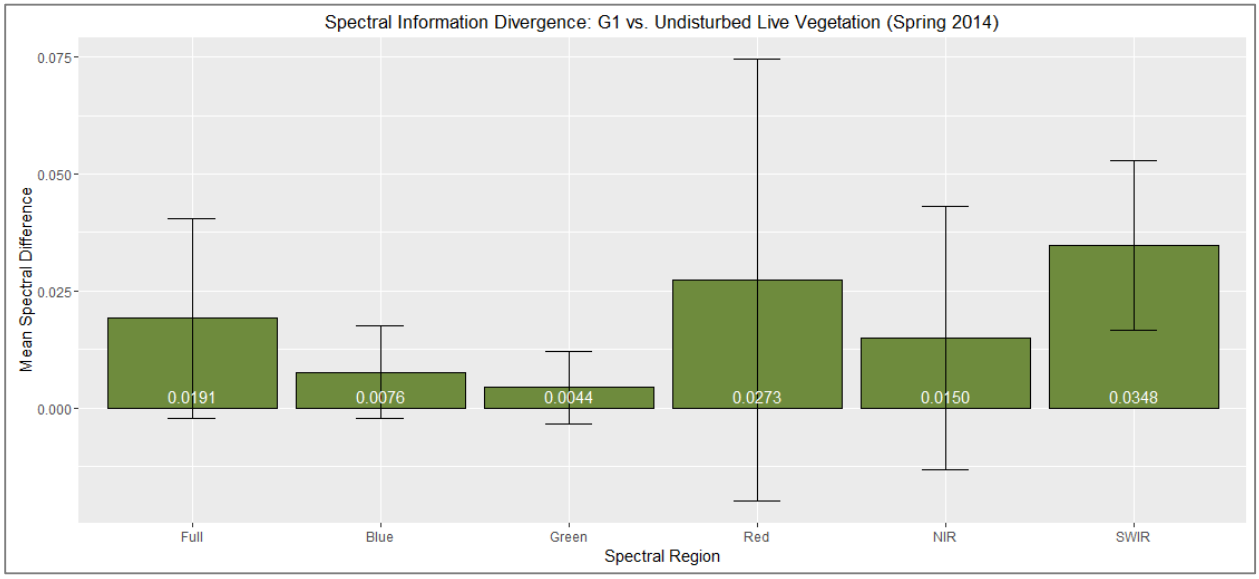

Figure A.22: Spectral Information Divergence (SID) results; Spring FieldSpec samples; all individual G1 spectra (n=16) vs. Undisturbed spectral mean (derived from n=84) mean; comparisons of full spectrum and regions (left to right).

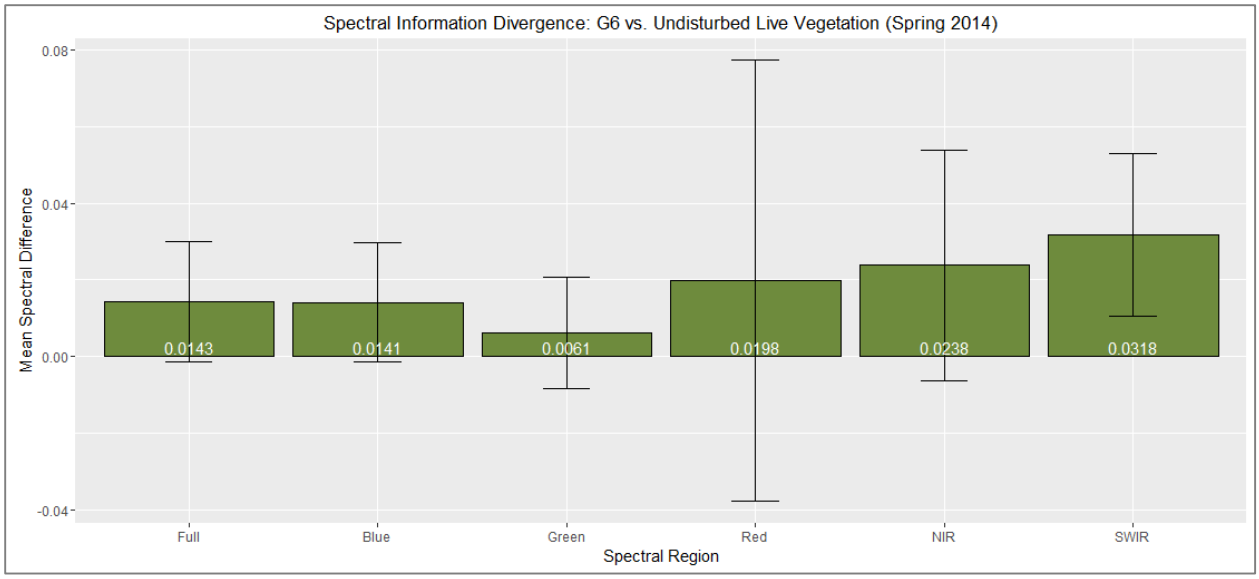

Figure A.23: Spectral Information Divergence (SID) results; Spring FieldSpec samples; all individual G6 spectra (n=36) vs. Undisturbed spectral mean (derived from n=84) mean; comparisons of full spectrum and regions (left to right).

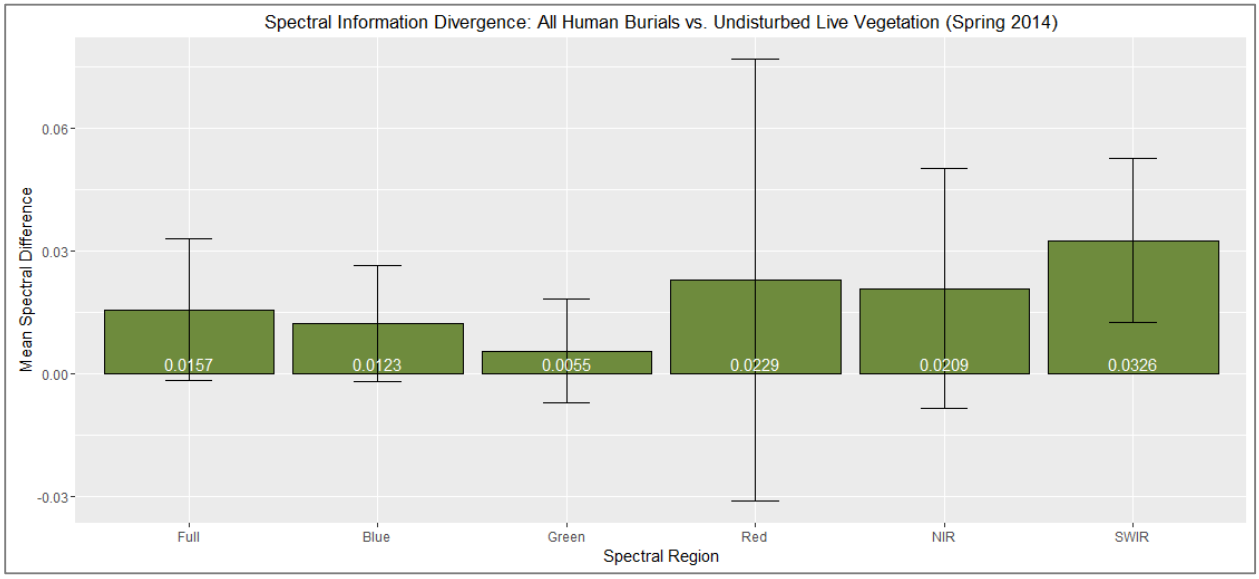

Figure A.24: Spectral Information Divergence (SID) results; Spring FieldSpec samples; all individual human Burial spectra (n=53) vs. Undisturbed spectral mean (derived from n=84) mean; comparisons of full spectrum and regions (left to right).

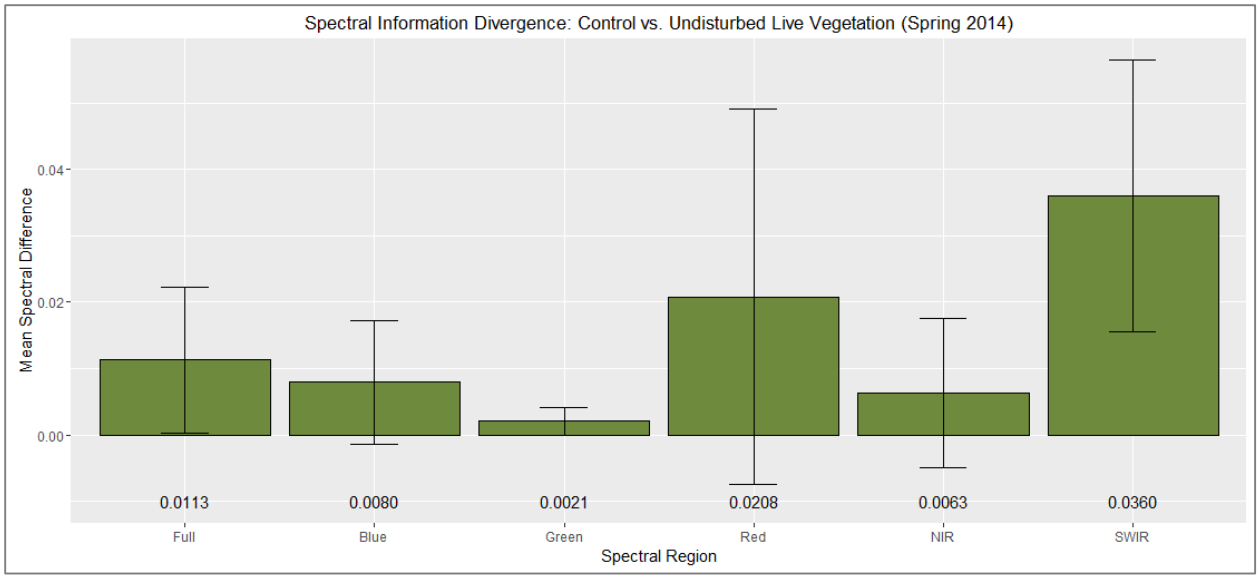

Figure A.25: Spectral Information Divergence (SID) results; Spring FieldSpec samples; all individual Control spectra (n=17) vs. Undisturbed spectral mean (derived from n=84) mean; comparisons of full spectrum and regions (left to right).

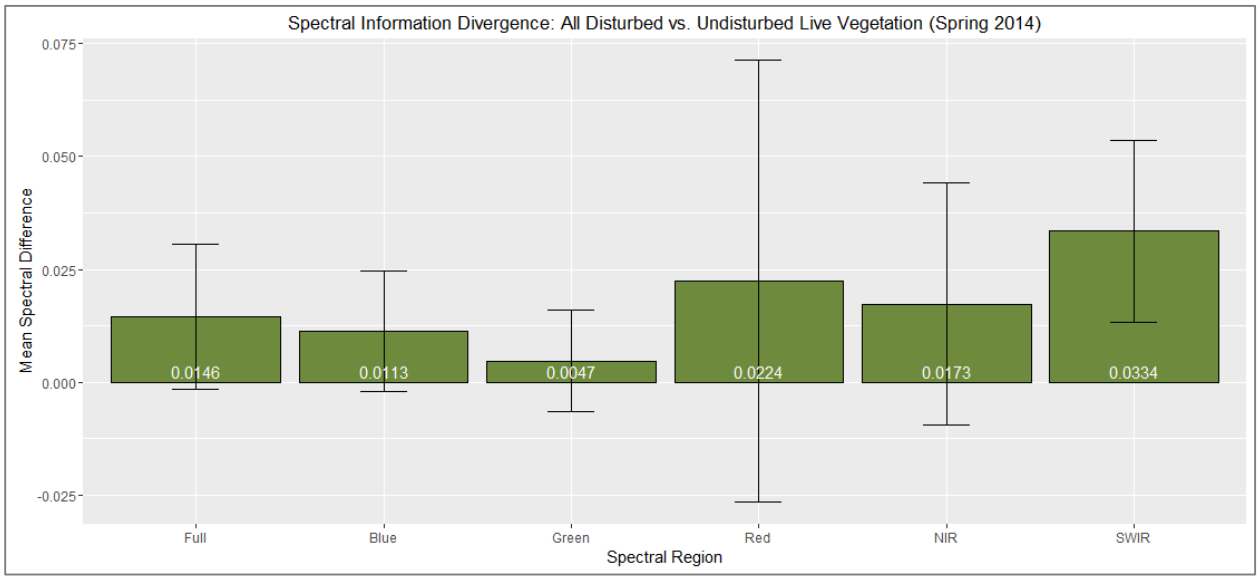

Figure A.26: Spectral Information Divergence (SID) results; Spring FieldSpec samples; all individual human burial and control ('Disturbed') spectra (n=70) vs. Undisturbed spectral mean (derived from n=84) mean; comparisons of full spectrum and regions (left to right).

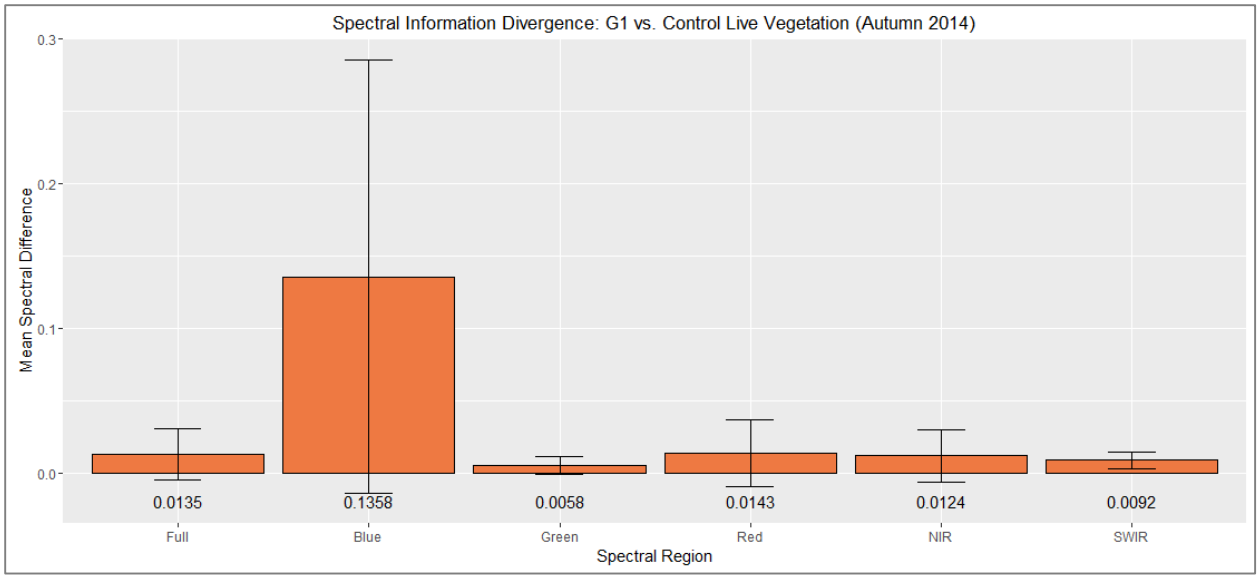

Figure A.27: Spectral Information Divergence (SID) results; Autumn FieldSpec samples; all individual G1 spectra (n=11) vs. Control spectral mean (derived from n=5) mean; comparisons of full spectrum and regions (left to right).

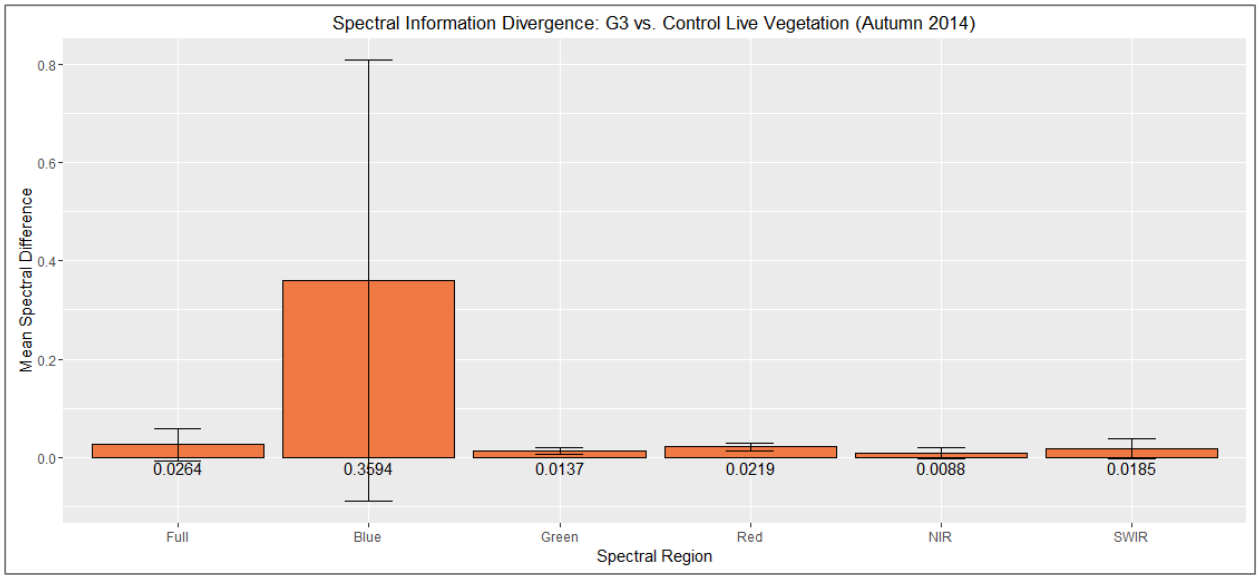

Figure A.28: Spectral Information Divergence (SID) results; Autumn FieldSpec samples; all individual G3 spectra (n=8) vs. Control spectral mean (derived from n=5) mean; comparisons of full spectrum and regions (left to right).

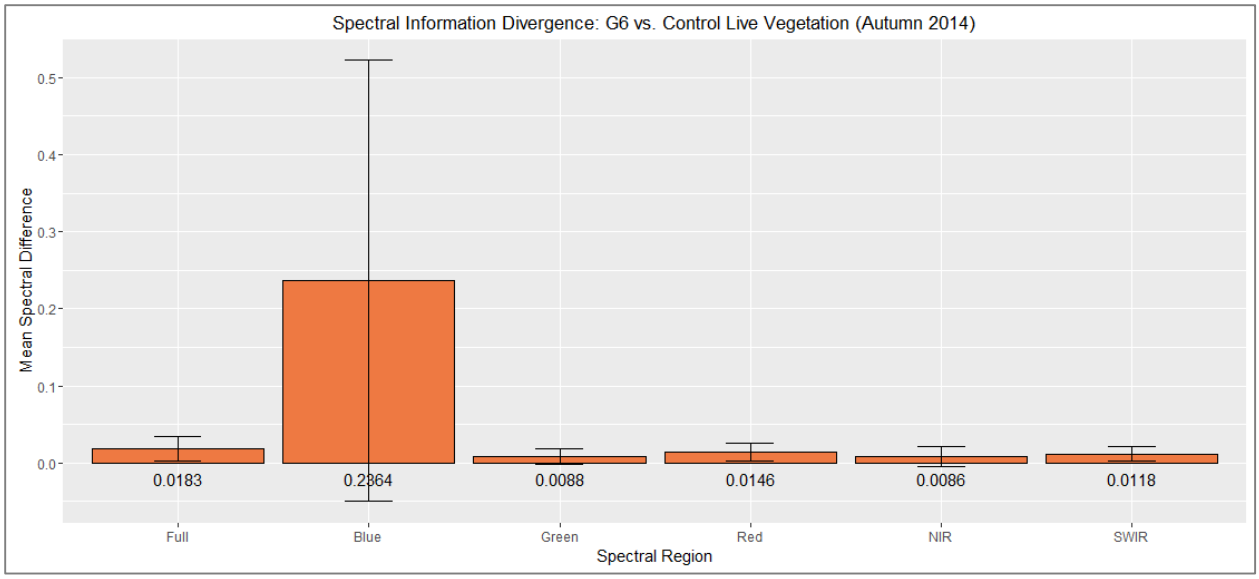

Figure A.29: Spectral Information Divergence (SID) results; Autumn FieldSpec samples; all individual G6 spectra (n=30) vs. Control spectral mean (derived from n=5) mean; comparisons of full spectrum and regions (left to right).

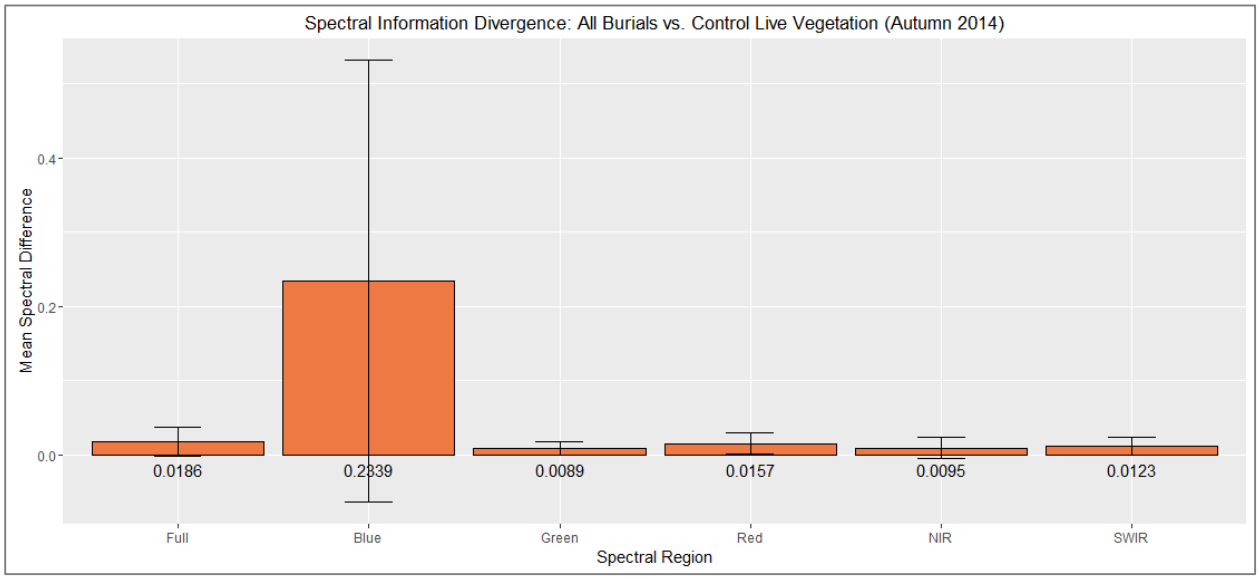

Figure A.30: Spectral Information Divergence (SID) results; Autumn FieldSpec samples; all individual human Burial spectra (n=49) vs. Control spectral mean (derived from n=5) mean; comparisons of full spectrum and regions (left to right).

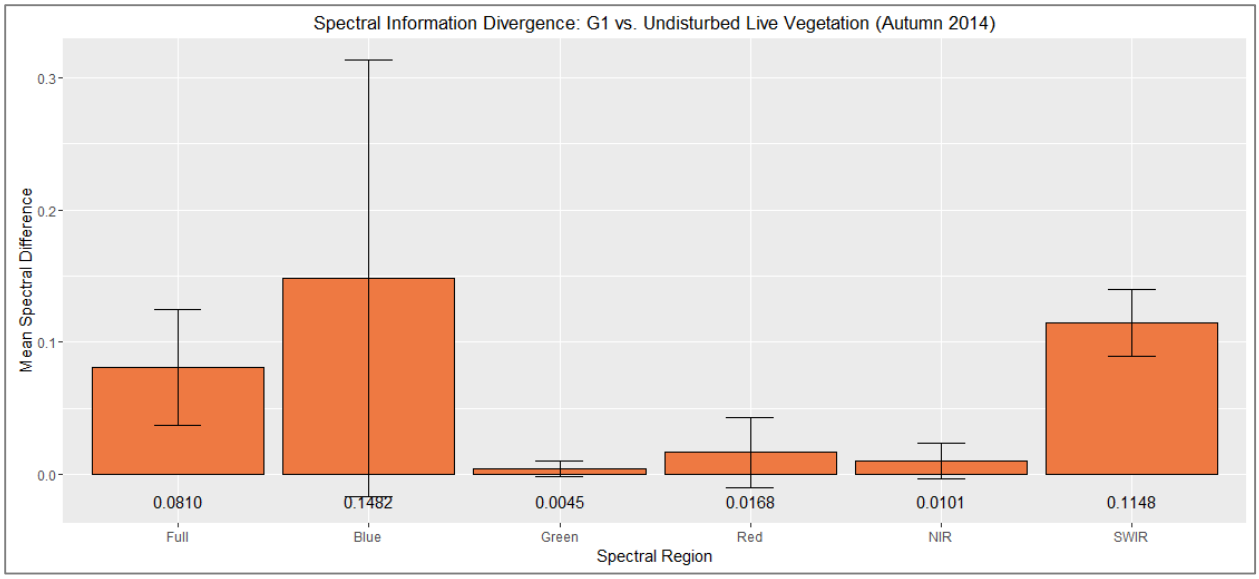

Figure A.31: Spectral Information Divergence (SID) results; Autumn FieldSpec samples; all individual G1 spectra (n=11) vs. Undisturbed spectral mean (derived from n=79) mean; comparisons of full spectrum and regions (left to right).

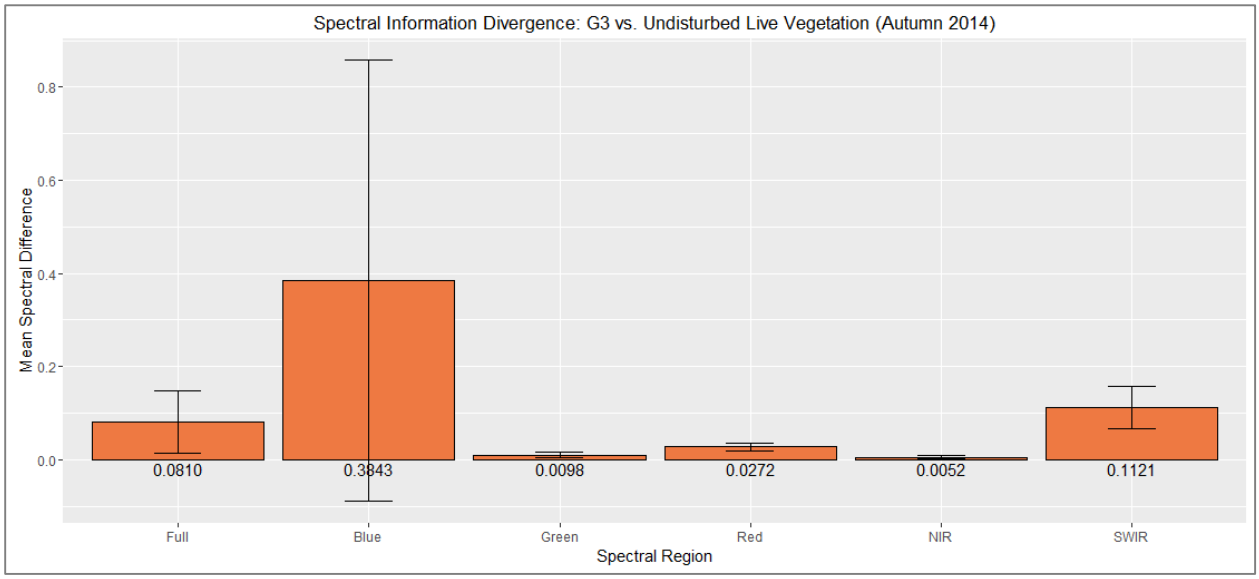

Figure A.32: Spectral Information Divergence (SID) results; Autumn FieldSpec samples; all individual G3 spectra (n=8) vs. Undisturbed spectral mean (derived from n=79) mean; comparisons of full spectrum and regions (left to right).

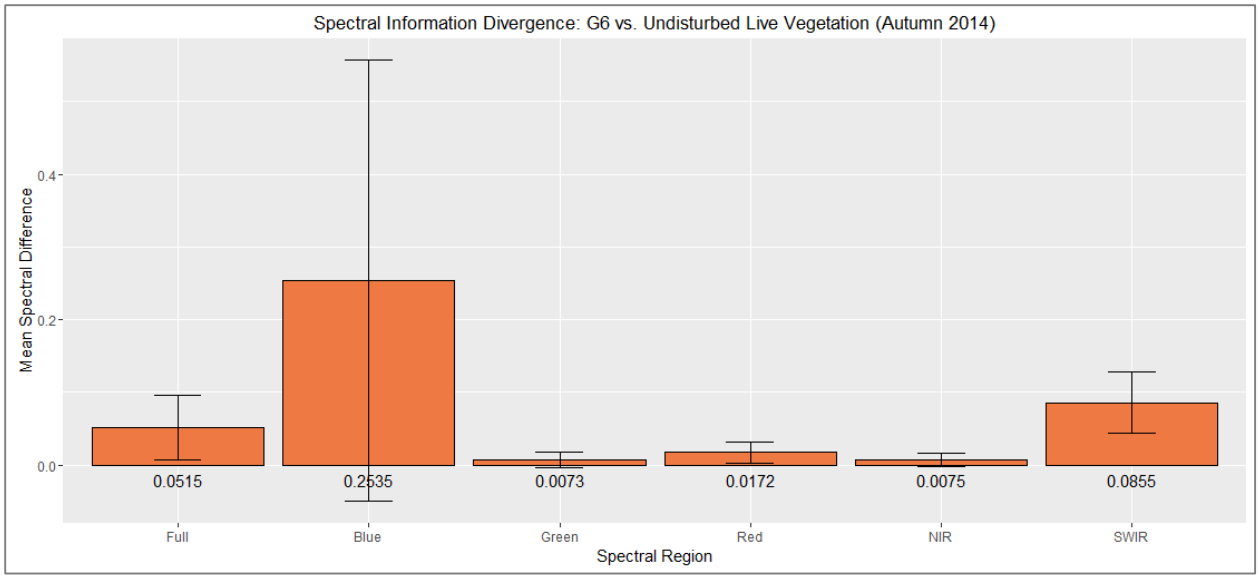

Figure A.33: Spectral Information Divergence (SID) results; Autumn FieldSpec samples; all individual G6 spectra (n=30) vs. Undisturbed spectral mean (derived from n=79) mean; comparisons of full spectrum and regions (left to right).

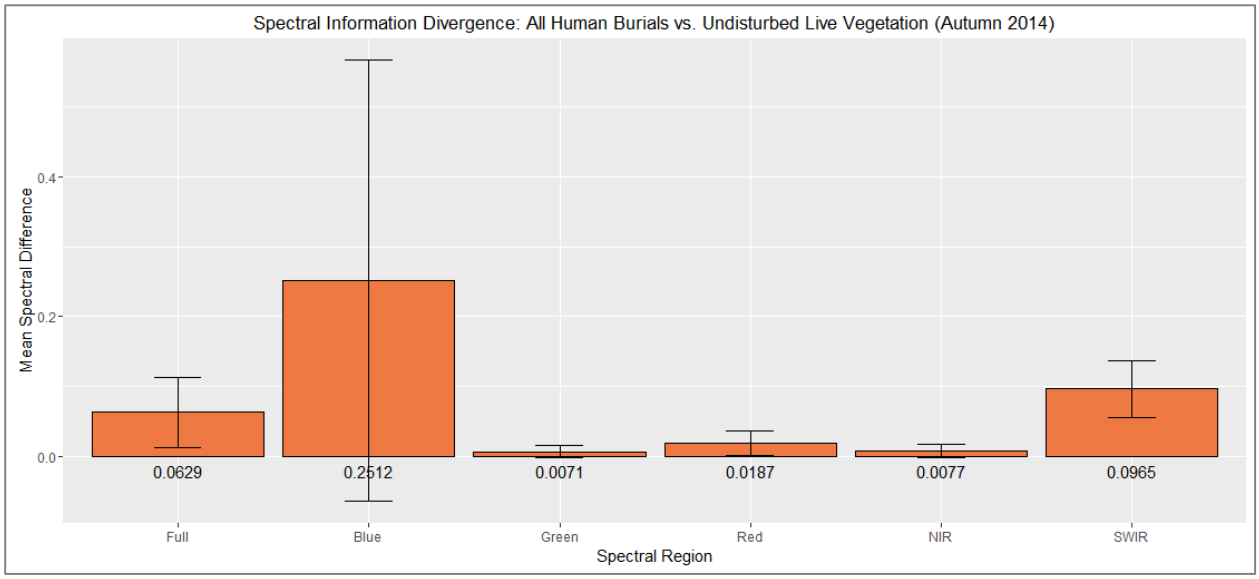

Figure A.34: Spectral Information Divergence (SID) results; Autumn FieldSpec samples; all individual human Burial spectra (n=49) vs. Undisturbed spectral mean (derived from n=79) mean; comparisons of full spectrum and regions (left to right).

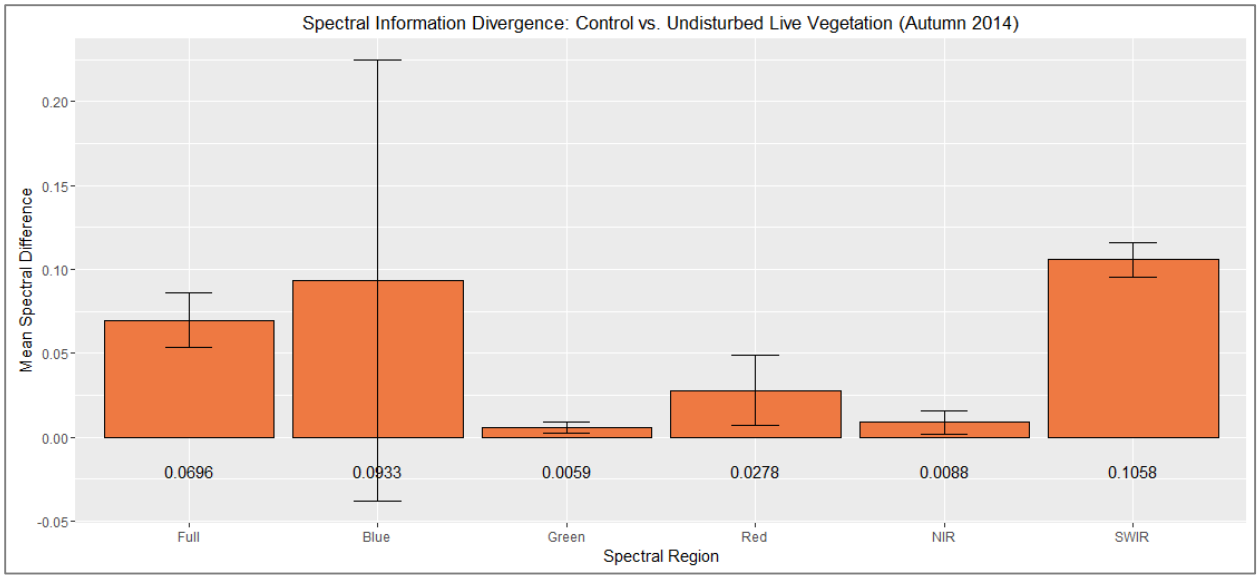

Figure A.35: Spectral Information Divergence (SID) results; Autumn FieldSpec samples; all individual Control spectra (n=5) vs. Undisturbed spectral mean (derived from n=79) mean; comparisons of full spectrum and regions (left to right).

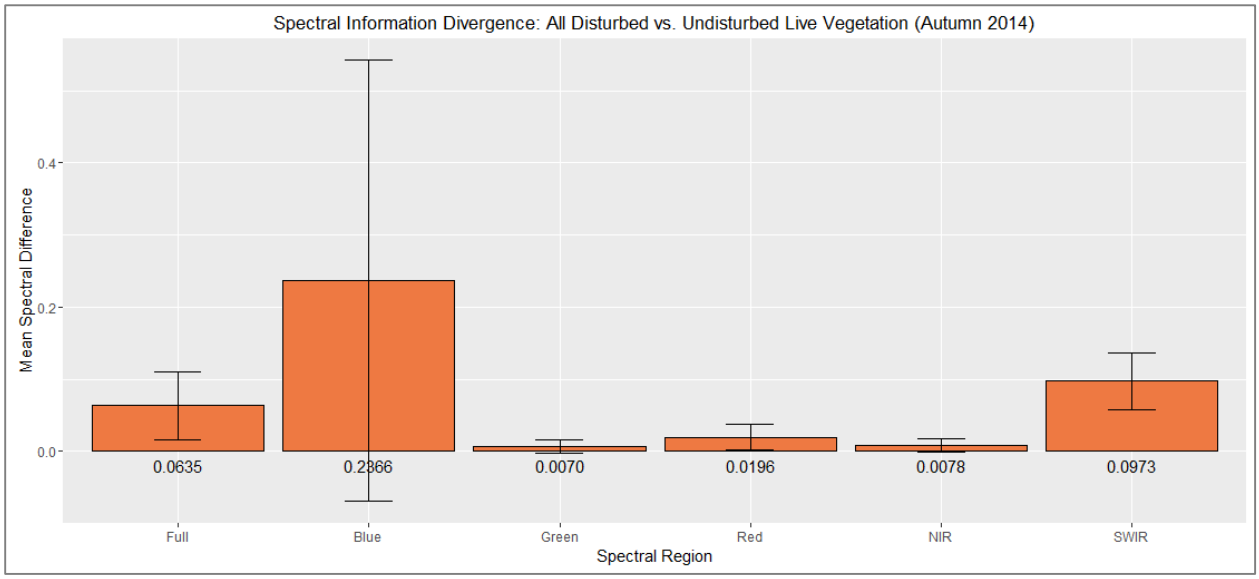

Figure A.36: Spectral Information Divergence (SID) results; Autumn FieldSpec samples; all individual human burial and control ('Disturbed') spectra (n=54) vs. Undisturbed spectral mean (derived from n=79) mean; comparisons of full spectrum and regions (left to right).

Appendix B: Detailed Statistical Model Development Process

Logistic Regression

Table B.1: Logistic regression **training** results summary; 70% training data; **full spectral range** (400 – 1330, 1440 – 1800, 1990 – 2500 nm). Green indicates models advanced to validation where correct classification of *both* groups ≥ 50.0%. Detailed results presented in **Tables B.3 – A.14**.

Model: Season	Known Group	n=	Wavelengths (nm)	Chi-square	Sig.	% Overall Correct
1: Spring	Burial	37	761, 764	15.273	0.000	65.6
	Undisturbed	59				
2: Autumn	Burial	34	707, 2423	37.663	0.000	76.7
	Undisturbed	56				
3: Spring	Control	12	2492	11.458	0.001	84.5
	Undisturbed	59				
4: Autumn	Control	3	2492	5.522	0.019	93.2
	Undisturbed	56				
5: Spring	Disturbed	49	554	11.263	0.001	60.2
	Undisturbed	59				
6: Autumn	Disturbed	37	708, 1993	34.434	0.000	71.0
	Undisturbed	56				

Table B.2: Logistic regression **validation** results summary; 30% test data; **full spectral range (**400 – 1330, 1440 – 1800, 1990 – 2500 nm). Green indicates models advanced to imagery where correct classification of *both* groups ≥ 50.0%. Detailed results presented in **Tables B.15 – B.17**.

Model: Season	Known Group	n=	% Correct	% Overall Correct
1: Spring	Burial	16	-	-
	Undisturbed	25		
2: Autumn	Burial	15	60.0	71.1
	Undisturbed	23	78.3	
3: Spring	Control	5	-	-
	Undisturbed	25		
4: Autumn	Control	2	-	-
	Undisturbed	23		
5: Spring	Disturbed	21	52.3	50.0
	Undisturbed	25	48.0	
6: Autumn	Disturbed	17	52.9	67.5
	Undisturbed	23	78.3	

Training Model #1: Spring 2014 – FieldSpec Data (2-groups: *Undisturbed* vs. *Burials*)

- Advancement criterion: Correct classification ≥ 50.0% across all categories
  - Model **NOT** advanced to validation

Table B.3: BLR training results using full resolution Spring FieldSpec reflectance spectra; 2-group analysis; overall 65.6% correct classification of training cases. Regression equation values are listed in **Table B.4.**

N=96			Predicted Membership		Total
		State	**Undisturbed**	**Burial**	
Known Membership	(Count)	**Undisturbed**	48	11	59
		Burial	22	15	37
	(%)	**Undisturbed**	**81.4**	18.6	100.0
		Burial	59.5	**40.5**	100.0

Table B.4: Logistic regression equation values.

Variable	**Coefficient**
Constant	1.803
761 nm	-452.641
764 nm	444.948

Training Model #2: Autumn 2014 – FieldSpec Data (2-groups: *Undisturbed* vs. *Burials*)

- Advancement criterion: Correct classification ≥ 50.0% across all categories
  - Model **ADVANCED** to validation

Table B.5: BLR training results using full resolution Autumn FieldSpec reflectance spectra; 2-group analysis; overall 76.7% correct classification of training cases. Regression equation values and validation results are listed in **Tables B.6** and **B.15.**

N=90			Predicted Membership		Total
		State	**Undisturbed**	**Burial**	
Known Membership	(Count)	**Undisturbed**	48	8	56
		Burial	13	21	34
	(%)	**Undisturbed**	**85.7**	14.3	100.0
		Burial	38.2	**61.8**	100.0

Table B.6: Logistic regression equation values.

Variable	**Coefficient**
Constant	3.027
707 nm	-42.345
2423 nm	37.510

Training Model #3: Spring 2014 – FieldSpec Data (2-groups: *Undisturbed* vs. *Control*)

- Advancement criterion: Correct classification ≥ 50.0% across all categories
  - Model **NOT** advanced to validation

Table B.7: BLR training results using full resolution Spring FieldSpec reflectance spectra; 2-group analysis; overall 84.5% correct classification of training cases. Regression equation values are listed in **Table B.8.**

N=71			Predicted Membership		Total
		State	**Undisturbed**	**Control**	
Known Membership	(Count)	**Undisturbed**	58	1	59
		Control	10	2	12
	(%)	**Undisturbed**	**98.3**	1.7	100.0
		Control	83.3	**16.7**	100.0

Table B.8: Logistic regression equation values.

Variable	**Coefficient**
Constant	0.375
2492 nm	-33.503

Training Model #4: Autumn 2014 – FieldSpec Data (2-groups: *Undisturbed* vs. *Control*)

- Advancement criterion: Correct classification ≥ 50.0% across all categories
  - Model **NOT** advanced to validation

Table B.9: BLR training results using full resolution Autumn FieldSpec reflectance spectra; 2-group analysis; overall 93.2% correct classification of training cases. Regression equation values are listed in **Table B.10.**

N=59			Predicted Membership		Total
		State	**Undisturbed**	**Control**	
Known Membership	(Count)	**Undisturbed**	55	1	56
		Control	3	0	3
	(%)	**Undisturbed**	**98.2**	1.8	100.0
		Control	100.0	**0.0**	100.0

Table B.10: Logistic regression equation values.

Variable	**Coefficient**
Constant	-2.935
2492	-11.044

Training Model #5: Spring 2014 – FieldSpec Data (2-groups: *Undisturbed* vs. *Disturbed*)

- Advancement criterion: Correct classification ≥ 50.0% across all categories
  - Model **ADVANCED** to validation

Table B.11: BLR training results using full resolution Spring FieldSpec reflectance spectra; 2-group analysis; overall 60.2% correct classification of training cases. Regression equation values and validation results are listed in **Tables B.12** and **B.16.**

N=108			Predicted Membership		Total
		State	**Undisturbed**	**Disturbed**	
Known Membership	(Count)	**Undisturbed**	40	19	59
		Disturbed	24	25	49
	(%)	**Undisturbed**	**67.8**	32.2	100.0
		Disturbed	49.0	**51.0**	100.0

Table B.12: Logistic regression equation values.

Variable	**Coefficient**
Constant	1.623
554 (nm)	-18.007

Training Model #6: Autumn 2014 – FieldSpec Data (2-groups: *Undisturbed* vs. *Disturbed*)

- Advancement criterion: Correct classification ≥ 50.0% across all categories
  - Model **ADVANCED** to validation

Table B.13: BLR training results using full resolution Autumn FieldSpec reflectance spectra; 2-group analysis; overall 71.0% correct classification of training cases. Regression equation values and validation results are listed in **Tables B.14** and **B.17.**

N=93			Predicted Membership		Total
		State	**Undisturbed**	**Disturbed**	
Known Membership	(Count)	**Undisturbed**	43	13	56
		Disturbed	14	23	37
	(%)	**Undisturbed**	**76.8**	23.2	100.0
		Disturbed	37.8	**62.2**	100.0

Table B.14: Logistic regression equation values.

Variable	**Coefficient**
Constant	2.591
708 nm	-33.417
1993 nm	36.306

VALIDATION – Training Model #2

- Advancement criterion: Correct classification ≥ 50.0% across all categories
  - Model **ADVANCED** to imagery test

Table B.15: BLR validation results using full range Autumn FieldSpec reflectance spectra; 2-group analysis; overall 71.1% correct classification of test cases.

N=38			Predicted Membership		Total
		State	**Undisturbed**	**Burial**	
Known Membership	(Count)	**Undisturbed**	18	5	23
		Burial	6	9	15
	(%)	**Undisturbed**	**78.3**	21.7	100.0
		Burial	40.0	**60.0**	100.0

VALIDATION – Training Model #5

- Advancement criterion: Correct classification ≥ 50.0% across all categories
  - Model **NOT** advanced to imagery test

Table B.16: BLR validation results using full range Spring FieldSpec reflectance spectra; 2-group analysis; overall 50.0% correct classification of test cases.

N=46			Predicted Membership		Total
		State	**Undisturbed**	**Disturbed**	
Known Membership	(Count)	**Undisturbed**	12	13	25
		Disturbed	10	11	21
	(%)	**Undisturbed**	**48.0**	52.0	100.0
		Disturbed	47.6	**52.3**	100.0

VALIDATION – Training Model #6

- Advancement criterion: Correct classification ≥ 50.0% across all categories
  - Model **ADVANCED** to imagery test

Table B.17: BLR validation results using full range Autumn FieldSpec reflectance spectra; 2-group analysis; overall 67.5% correct classification of test cases.

N=40			Predicted Membership		Total
		State	**Undisturbed**	**Disturbed**	
Known Membership	(Count)	**Undisturbed**	18	5	23
		Disturbed	8	9	17
	(%)	**Undisturbed**	**78.3**	21.7	100.0
		Disturbed	47.1	**52.9**	100.0

Table B.18: Logistic regression training results summary; 70% training data; spectral subset (418 – 919 nm) to match spectral range of the Headwall Hyperspec data. Gray indicates redundant models already presented in **Tables B.1** and **B.2**. Green indicates models advanced to validation where correct classification of *both* groups ≥ 50.0%. Detailed results presented in **Tables B.20 – B.25.**

Model: Season	Group	n=	Wavelengths (nm)	Chi-square	Sig.	% Overall Correct
1: Spring	Burial	37	761, 764	15.273	0.000	65.6
	Undisturbed	59				
7: Autumn	Burial	34	707	29.580	0.000	71.1
	Undisturbed	56				
8: Spring	Control	12	545, 546, 551, 895, 900, 909, 912, 913, 917	64.513	0.000	100.0
	Undisturbed	59				
N/A: Autumn	Control	3	No viable model	-	-	-
	Undisturbed	56				
5: Spring	Disturbed	49	554	11.263	0.001	60.2
	Undisturbed	59				
9: Autumn	Disturbed	37	708	25.251	0.000	67.7
	Undisturbed	56				

Table B.19: Logistic regression validation results summary; 30% test data; spectral subset (418 – 919 nm) to match spectral range of the Headwall Hyperspec data. Gray indicates redundant models already presented in **Tables B.1** and **B.2**. Green indicates models advanced to imagery where correct classification of ***both*** groups ≥ 50.0% (none are advanced). Detailed results presented in **Tables B.26 – B.27.**

Season	Known Group	n=	% Correct	% Overall Correct
1: Spring	Human	16	-	-
	Undisturbed	25		
7: Autumn	Human	15	46.7	63.2
	Undisturbed	23	73.9	
8: Spring	Control	5	40.0	86.7
	Undisturbed	25	96.0	
4: Autumn	Control	2	-	-
	Undisturbed	23		
5: Spring	Disturbed	21	-	-
	Undisturbed	25		
9: Autumn	Disturbed	17	-	-
	Undisturbed	23		

Training Model #7: **Autumn 2014 – FieldSpec Data (2-groups: *Undisturbed* vs. *Burials*)**

- Advancement criterion: Correct classification ≥ 50.0% across all categories
  - Model **ADVANCED** to validation

Table B.20: BLR training results using 418 – 919 nm Autumn FieldSpec reflectance spectra; 2-group analysis; overall 71.1% correct classification of training cases. Regression equation values and validation results are listed in **Tables B.21** and **B.26.**

N=90			Predicted Membership		Total
		State	**Undisturbed**	**Burial**	
Known Membership	(Count)	**Undisturbed**	46	10	56
		Burial	16	18	34
	(%)	**Undisturbed**	**82.1**	17.9	100.0
		Burial	47.1	**52.9**	100.0

Table B.21: Logistic regression equation values.

Variable	**Coefficient**
Constant	2.702
707 nm	-20.189

Training Model #8: Spring 2014 – FieldSpec Data (2-groups: *Undisturbed* vs. C*ontrol*)

- Advancement criterion: Correct classification ≥ 50.0% across all categories
  - Model **ADVANCED** to validation

Table B.22: BLR training results using 418 – 919 nm Spring FieldSpec reflectance spectra; 2-group analysis; overall 100.0% correct classification of training cases. Regression equation values and hold-out sample validation results are listed in **Tables B.23 and B.27.**

N=71			Predicted Membership		Total
		State	**Undisturbed**	**Control**	
Known Membership	(Count)	**Undisturbed**	59	0	59
		Control	0	12	12
	(%)	**Undisturbed**	**100.0**	0.0	100.0
		Control	0.0	**100.0**	100.0

Table B.23: Logistic regression equation values.

Variable	**Coefficient**		**Variable**	**Coefficient**
Constant	-42.510		900 nm	-58878.891
545 nm	503375.665		909 nm	-38235.606
546 nm	-587359.907		912 nm	-217993.189
551 nm	83508.731		913 nm	231044.990
895 nm	71120.327		917 nm	13075.695

Training Model #9:Autumn 2014 – FieldSpec Data (2-groups: *Undisturbed* vs. *Disturbed*)

- Advancement criterion: Correct classification ≥ 50.0% across all categories
  - Model **NOT** advanced to validation

Table B.24: BLR training results using 418 – 919 nm Autumn FieldSpec reflectance spectra; 2-group analysis; overall 67.7% correct classification of training cases. Regression equation values are listed in **Table B.25.**

N=93			Predicted Membership		Total
		State	**Undisturbed**	**Disturbed**	
Known Membership	(Count)	**Undisturbed**	45	11	56
		Disturbed	19	18	37
	(%)	**Undisturbed**	**80.4**	19.6	100.0
		Disturbed	51.4	**48.6**	100.0

Table B.25: Logistic regression equation values.

Variable	**Coefficient**
Constant	2.323
708 nm	-16.086

VALIDATION – Training Model #7

- Advancement criterion: Correct classification ≥ 50.0% across all categories
  - Model **NOT** advanced to imagery test

Table B.26: BLR validation results using 418 – 919 nm Autumn FieldSpec reflectance spectra; 2-group analysis; overall 63.2% correct classification of test cases.

N=38			Predicted Membership		Total
		State	**Undisturbed**	**Burial**	
Known Membership	(Count)	**Undisturbed**	17	6	23
		Burial	8	7	15
	(%)	**Undisturbed**	**73.9**	26.1	100.0
		Burial	53.3	**46.7**	100.0

VALIDATION – Training Model #8

- Advancement criterion: Correct classification ≥ 50.0% across all categories
  - Model **NOT** advanced to imagery test

Table B.27: BLR validation results using 418 – 919 nm Spring FieldSpec reflectance spectra; 2-group analysis; overall 86.7% correct classification of test cases.

N=30			Predicted Membership		Total
		State	**Undisturbed**	**Control**	
Known Membership	(Count)	**Undisturbed**	24	1	25
		Control	3	2	5
	(%)	**Undisturbed**	**96.0**	4.0	100.0
		Control	60.0	**40.0**	100.0

Discriminant Function Analysis (DFA)

Table B.28: DFA **training** results summary; 70% training data; **full spectral range** (400 – 1330, 1440 – 1800, 1990 – 2500 nm). Green indicates models advanced to validation where correct classification of 2 groups ≥ 50.0% or 3 groups at ≥ 33.3%. Detailed results presented in **Tables B.30 – B.47.**

Season	Group	n=	Wavelengths (nm)	Wilk's Lambda	Sig.	% Overall Correct
1: Spr.	Human	37	551	0.895	0.003	50.9
	Control	12				
	Undist.	59				
2: Aut.	Human	34	708, 2053, 2407, 2445, 2498	(1) 0.475	0.000	80.6
	Control	3		(2) 0.748	0.000	
	Undist.	56				
3: Spr.	Human	37	761, 1440, 2015, 2291, 2355, 2401, 2405, 2417, 2448, 2459, 2467, 2480	0.371	0.000	88.5
	Undist.	59				
4: Aut.	Human	34	707	0.753	0.000	75.6
	Undist.	56				
5: Spr.	Dist.	49	554	0.904	0.001	60.2
	Undist.	59				
6: Aut.	Dist.	37	708, 2006, 2412	0.706	0.000	72.0
	Undist.	56				

Table B.29: DFA validation results summary; 30% test data; full spectral range (400 – 1330, 1440 – 1800, 1990 – 2500 nm). Green indicates models advanced to imagery where correct classification of 2 groups ≥ 50.0% or 3 groups at ≥ 33.3%. Detailed results presented in **Tables B.48 – B.53.**

Season/Model	Known Group	n=	% Correct	% Overall Correct
1: Spring 3-groups	Human	16	12.5	32.6
	Control	5	60.0	
	Undisturbed	25	40.0	
2: Autumn 3-groups	Human	15	73.3	62.5
	Control	2	0.0	65.8
	Undisturbed	23	60.9	
3: Spring 2-groups	Human	16	68.8	58.5
	Undisturbed	25	52.0	
4: Autumn 2-groups	Human	15	66.7	63.2
	Undisturbed	23	60.9	
5: Spring 2-groups	Disturbed	21	57.1	47.8
	Undisturbed	25	40.0	
6: Autumn 2-groups	Disturbed	17	52.9	62.5
	Undisturbed	23	69.6	

Training Model #1: Spring 2014 – FieldSpec Data (3-groups: *Undist.* vs. *Burial* vs. *Control*)

- Advancement criterion: Correct classification ≥ 33.3% across all categories
  - Model **ADVANCED** to validation

Table B.30: DFA training results using full resolution Spring FieldSpec reflectance spectra; 3-group analysis; overall 50.9% correct classification of training cases. Classification function coefficients and validation results are listed in **Tables B.31, B.32** and **B.48**.

N=108			Predicted Membership			
		State	**Undisturbed**	**Burial**	**Control**	Total
Known Membership	(Count)	**Undisturbed**	32	9	18	59
		Burial	9	15	13	37
		Control	4	0	8	12
	(%)	**Undisturbed**	**54.2**	15.3	30.5	100.0
		Burial	24.3	**40.5**	35.1	100.0
		Control	33.3	0.0	**66.7**	100.0

Table B.31: Model #1 Unstandardized Discriminant Function Coefficients**.**

Variable	**D_1 Coefficient**
Constant	-2.641
551 nm	25.925

Table B.32: Model #1 Fisher's Classification Function Coefficients.

Variable	**(U) Coefficient**	**(H) Coefficient**	**(C) Coefficient**
Constant	-5.407	-3.906	-3.116
551 (nm)	76.099	61.431	52.722

Training Model #2: Autumn 2014 – FieldSpec (3-groups: *Undist.* vs. *Burial* vs. *Control*)

- Advancement criterion: Correct classification ≥ 33.3% across all categories
  - Model **ADVANCED** to validation

Table B.33: DFA training results using full resolution Autumn FieldSpec reflectance spectra: 3-group analysis; overall 80.6% correct classification of training cases. Classification function coefficients and validation results are listed in **Tables B.34, B.35** and **B.49.**

N=93			Predicted Membership			
		State	**Undisturbed**	**Burial**	**Control**	Total
Known Membership	(Count)	**Undisturbed**	38	18	0	56
		Burial	0	34	0	34
		Control	0	0	3	3
	(%)	**Undisturbed**	**67.9**	32.1	0.0	100.0
		Burial	0.0	**100.0**	0.0	100.0
		Control	0.0	0.0	**100.0**	100.0

Table B.34: Model #2 Unstandardized Discriminant Function Coefficients.

Variable	**D_1 Coefficient**	**D_2 Coefficient**		**Variable**	**D_1 Coefficient**	**D_2 Coefficient**
Constant	-1.282	-1.487		2407	-117.585	76.992
708 (nm)	8.653	15.627		2445	43.777	-21.515
2053	63.955	-63.538		2498	5.235	-0.692

Table B.35: Model #2 Fisher's Classification Function Coefficients.

Variable	(U) Coefficient	(H) Coefficient	(C) Coefficient
Constant	-4.883	-2.546	-12.925
708 (nm)	29.896	6.821	23.758
2053	33.399	41.962	374.836
2407	-24.752	-0.652	-566.458
2445	-10.314	-26.439	175.919
2498	3.159	-0.651	21.366

Training Model #3: Spring 2014 – FieldSpec Data (2-groups: *Undisturbed* vs. *Burial*)

- Advancement criterion: Correct classification ≥ 33.3% across all categories
  - Model **ADVANCED** to validation

Table B.36: DFA training results using full resolution Spring FieldSpec reflectance spectra; 2-group analysis; overall 88.5% correct classification of training cases. Classification function coefficients and validation results are listed in **Tables B.37, B.38, and B.50.**

N=96			Predicted Membership		Total
		State	**Undisturbed**	**Burial**	
Known Membership	(Count)	**Undisturbed**	53	6	59
		Burial	5	32	37
	(%)	**Undisturbed**	**89.8**	10.2	100.0
		Burial	13.5	**86.5**	100.0

Table B.37: Model #3 Unstandardized Discriminant Function Coefficients.

Variable	**D_1 Coefficient**	**Variable**	**D_1 Coefficient**	**Variable**	**D_1 Coefficient**
Constant	-1.723	2355	244.397	2459	72.732
761 (nm)	16.672	2401	126.695	2467	48.846
1440	159.929	2405	-185.989	2480	27.198
2015	-146.723	2417	-83.318		
2291	-318.063	2448	57.457		

Table B.38: Model #3 Fisher's Classification Function Coefficients.

Variable	(U) Coefficient	(H) Coefficient		Variable	(U) Coefficient	(H) Coefficient
Constant	-10.577	-6.820		2405	-160.127	332.210
761 (nm)	80.630	36.497		2417	-193.261	27.292
1440	306.794	-116.559		2448	214.378	62.280
2015	-173.959	214.436		2459	257.155	64.624
2291	-441.858	400.097		2467	50.646	-78.656
2355	73.052	-573.899		2480	-5.480	-77.477
2401	61.779	-273.600				

Training Model #4: Autumn 2014 – FieldSpec Data (2-groups: *Undisturbed* vs. *Burial*)

- Advancement criterion: Correct classification ≥ 33.3% across all categories
  - Model **ADVANCED** to validation

Table B.39: DFA training results using full resolution Autumn FieldSpec reflectance spectra; 2-group analysis; overall 75.6% correct classification of training cases. Classification function coefficients and validation results are listed in **Tables B.40, B.41,** and **B.51**.

N=90			Predicted Membership		Total
		State	**Undisturbed**	**Burial**	
Known Membership	(Count)	**Undisturbed**	38	18	56
		Burial	4	30	34
	(%)	**Undisturbed**	**67.9**	32.1	100.0
		Burial	11.8	**88.2**	100.0

Table B.40: Model #4 Unstandardized Discriminant Function Coefficients.

Variable	**D_1 Coefficient**
Constant	-2.258
707 nm	12.570

Table B.41: Model #4 Fisher's Classification Function Coefficients.

Variable	**(U) Coefficient**	**(H) Coefficient**
Constant	-4.335	-1.866
707 (nm)	33.926	19.252

Training Model #5: Spring 2014 – FieldSpec Data (2-groups: *Undisturbed* vs. *Disturbed*)

- Advancement criterion: Correct classification ≥ 33.3% across all categories
  - Model **ADVANCED** to validation

Table B.42: DFA training results using full resolution Spring FieldSpec reflectance spectra; 2-group analysis; overall 60.2% correct classification of training cases. Classification function coefficients and validation results are listed in **Tables B.43, B.44, and B.52.**

N=108			Predicted Membership		Total
		State	**Undisturbed**	**Disturbed**	
Known Membership	(Count)	**Undisturbed**	32	27	59
		Disturbed	16	33	49
	(%)	**Undisturbed**	**54.2**	45.8	100.0
		Disturbed	32.7	**67.3**	100.0

Table B.43: Model #5 Unstandardized Discriminant Function Coefficients.

Variable	**D_1 Coefficient**
Constant	-2.641
554 nm	25.702

Table B.44: Model #5 Fisher's Classification Function Coefficients.

Variable	**(U) Coefficient**	**(D) Coefficient**
Constant	-5.000	-3.307
554 (nm)	75.430	58.766

Training Model #6: Autumn 2014 – FieldSpec Data (2-groups: *Undisturbed* vs. *Disturbed*)

- Advancement criterion: Correct classification ≥ 33.3% across all categories
  - Model **ADVANCED** to validation

Table B.45: DFA training results using full resolution Autumn FieldSpec reflectance spectra; 2-group analysis; overall 72.0% correct classification of training cases. Classification function coefficients and validation results are listed in **Tables B.46, B.47,** and **B.53.**

N=93			Predicted Membership		Total
		State	**Undisturbed**	**Disturbed**	
Known Membership	(Count)	**Undisturbed**	37	19	56
		Disturbed	7	30	37
	(%)	**Undisturbed**	**66.1**	33.9	100.0
		Disturbed	18.9	**81.1**	100.0

Table B.46: Model #6 Unstandardized Discriminant Function Coefficients.

Variable	**D_1 Coefficient**		**Variable**	**D_1 Coefficient**
Constant	-1.878		2006	-53.329
708 (nm)	12.796		2412	41.692

Table B.47: Model #6 Fisher's Classification Function Coefficients.

Variable	**(U) Coefficient**	**(D) Coefficient**		**Variable**	**(U) Coefficient**	**(D) Coefficient**
Constant	-4.419	-2.142		2006	-49.066	20.546
708 (nm)	28.427	11.724		2412	52.454	-1.968

VALIDATION – Training Model #1

- Advancement criterion: Correct classification ≥ 33.3% across all categories
  - Model **NOT** advanced to imagery test

Table B.48: DFA validation results using full range Spring FieldSpec reflectance spectra; 3-group analysis; overall 32.6% correct classification of test cases.

N=46			Predicted Membership			
		State	**Undisturbed**	**Burial**	**Control**	Total
Known Membership	(Count)	**Undisturbed**	10	2	13	25
		Burial	6	2	8	16
		Control	2	0	3	5
	(%)	**Undisturbed**	**40.0**	8.0	52.0	100.0
		Burial	37.5	**12.5**	50.0	100.0
		Control	40.0	0.0	**60.0**	100.0

VALIDATION – Training Model #2

- Advancement criterion: Correct classification ≥ 33.3% across 3 categories or ≥ 50.0% across 2 categories
    - Model **ADVANCED** to imagery test

Table B.49: DFA validation results using full range Autumn FieldSpec reflectance spectra; 3-group analysis; overall 62.5% correct classification of test cases.

N=40			Predicted Membership			Total
		State	**Undisturbed**	**Burial**	**Control**	
Known Membership	(Count)	**Undisturbed**	14	8	1	23
		Burial	4	11	0	15
		Control	1	1	0	2
	(%)	**Undisturbed**	**60.9**	34.8	4.3	100.0
		Burial	26.7	**73.3**	0.0	100.0
		Control	50.0	50.0	**0.0**	100.0

VALIDATION – Training Model #3

- Advancement criterion: Correct classification ≥ 50.0% across all categories
  - Model **ADVANCED** to imagery test

Table B.50: DFA validation results using full range Spring FieldSpec reflectance spectra; 2-group analysis; overall 58.5% correct classification of test cases.

N=41			Predicted Membership		Total
		State	**Undisturbed**	**Burial**	
Known Membership	(Count)	**Undisturbed**	13	12	25
		Burial	5	11	16
	(%)	**Undisturbed**	**52.0**	48.0	100.0
		Burial	31.2	**68.8**	100.0

VALIDATION – Training Model #4

- Advancement criterion: Correct classification ≥ 50.0% across all categories
  - Model **ADVANCED** to imagery test

Table B.51: DFA validation results using full range Autumn FieldSpec reflectance spectra; 2-group analysis; overall 63.2% correct classification of test cases.

N=38			Predicted Membership		Total
		State	**Undisturbed**	**Burial**	
Known Membership	(Count)	**Undisturbed**	14	9	23
		Burial	5	10	15
	(%)	**Undisturbed**	**60.9**	39.1	100.0
		Burial	33.3	**66.7**	100.0

VALIDATION – Training Model #5

- Advancement criterion: Correct classification ≥ 50.0% across all categories
  - Model **NOT** advanced to imagery test

Table B.52: DFA validation results using full range Spring FieldSpec reflectance spectra; 2-group analysis; overall 47.8% correct classification of test cases.

N=46			Predicted Membership		Total
		State	**Undisturbed**	**Disturbed**	
Known Membership	(Count)	**Undisturbed**	10	15	25
		Disturbed	9	12	21
	(%)	**Undisturbed**	**40.0**	60.0	100.0
		Disturbed	42.9	**57.1**	100.0

VALIDATION – Training Model #6

- Advancement criterion: Correct classification ≥ 50.0% across all categories
  - Model **ADVANCED** to imagery test

Table B.53: DFA validation results using full range Autumn FieldSpec reflectance spectra; 2-group analysis; overall 62.5% correct classification of test cases.

N=40			Predicted Membership		Total
		State	**Undisturbed**	**Disturbed**	
Known Membership	(Count)	**Undisturbed**	16	7	23
		Disturbed	8	9	17
	(%)	**Undisturbed**	**69.6**	30.4	100.0
		Disturbed	47.1	**52.9**	100.0

Table B.54: DFA **training** results summary, 70% training data; **spectral subset** (418 – 919 nm) to match spectral range of the Headwall Hyperspec data. Gray indicates redundant models already presented in **Tables B.28** and **B.29.** Green indicates models advanced to validation where correct classification of 2 groups ≥ 50.0% or 3 groups at ≥ 33.3%. Detailed results presented in **Tables B.56 – B.64.**

Season	Group	n=	Wavelengths (nm)	Wilk's Lambda	Sig.	% Overall Correct
1: Spring	Human	37	551	0.895	0.003	50.9
	Control	12				
	Undist.	59				
7:	Human	34	708	0.755	0.000	61.3
	Control	3				
	Undist.	56				
8: Spring	Human	37	761	0.906	0.002	59.4
	Undist.	59				
4:	Human	34	707	0.753	0.000	75.6
	Undist.	56				
5: Spring	Dist.	49	554	0.904	0.001	60.2
	Undist.	59				
9:	Dist.	37	708	0.783	0.000	72.0
	Undist.	56				

Table B.55: DFA **validation** results summary; 30% test data; **spectral subset** (418 – 919 nm) to match spectral range of the Headwall Hyperspec data. Gray indicates redundant models already presented in **Tables B.28** and **B.29**. Green indicates models advanced to validation where correct classification of 2 groups ≥ 50.0% or 3 groups at ≥ 33.3%. Detailed results presented in **Tables B.65 – B.67.**

Season/Model	Known Group	n=	% Correct	% Overall Correct
1: Spring 3-groups	Human	16	12.5	32.6
	Control	5	60.0	
	Undisturbed	25	40.0	
7: Autumn 3-groups	Human	15	58.8	52.5
	Control	2	0.0	
	Undisturbed	23	47.8	
8: Spring 2-groups	Human	16	75.0	58.5
	Undisturbed	25	48.0	
4: Autumn 2-groups	Human	15	66.7	63.2
	Undisturbed	23	60.9	
5: Spring 2-groups	Disturbed	21	57.1	47.8
	Undisturbed	25	40.0	
9: Autumn 2-groups	Disturbed	17	70.6	62.5
	Undisturbed	23	56.5	

Training Model #7: Autumn– FieldSpec Data (3-groups: *Undist.* vs. *Burials* vs. *Control*)

- Advancement criterion: Correct classification ≥ 33.3% across all categories
  - Model **ADVANCED** to validation

Table B.56: DFA training results using 418 – 919 nm Autumn FieldSpec reflectance spectra; 3-group analysis; overall 61.3% correct classification of training cases. Classification function coefficients and validation results are listed in **Tables B.57, B.58,** and **B.65**.

N=93			Predicted Membership			
		State	**Undisturbed**	**Burial**	**Control**	Total
Known Membership	(Count)	**Undisturbed**	26	17	13	56
		Burial	0	30	4	34
		Control	1	1	1	3
	(%)	**Undisturbed**	**46.4**	30.4	23.2	100.0
		Burial	0.0	**88.2**	11.8	100.0
		Control	33.3	33.3	**33.3**	100.0

Table B.57: Model #7 Unstandardized Discriminant Function Coefficients.

Variable	**D_1 Coefficient**
Constant	-2.289
708 nm	12.233

Table B.58: Model #7 Fisher's Classification Function Coefficients.

Variable	**(U) Coefficient**	**(H) Coefficient**	**(C) Coefficient**
Constant	-4.792	-2.301	-4.615
708 (nm)	33.247	18.966	32.442

Training Model #8: Spring 2014 – FieldSpec Data (2-groups: *Undisturbed* vs. *Burials*)

- Advancement criterion: Correct classification ≥ 50.0% across all categories
  - Model **ADVANCED** to validation

Table B.59: DFA training results using 418 – 919 nm Spring FieldSpec reflectance spectra; 2-group analysis; overall 59.4% correct classification of training cases. Classification function coefficients and validation results are listed in **Tables B.60, B.61,** and **B.66.**

N=96			Predicted Membership		Total
		State	**Undisturbed**	**Burial**	
Known Membership	(Count)	**Undisturbed**	33	26	59
		Burial	13	24	37
	(%)	**Undisturbed**	**55.9**	44.1	100.0
		Burial	35.1	**64.9**	100.0

Table B.60: Model #8 Unstandardized Discriminant Function Coefficients.

Variable	**D_1 Coefficient**
Constant	-3.462
761 (nm)	9.731

Table B.61: Model #8 Fisher's Classification Function Coefficients.

Variable	**(U) Coefficient**	**(H) Coefficient**
Constant	-7.590	-5.377
761 (nm)	36.139	29.781

Training Model #9: Autumn 2014 – FieldSpec Data (2-groups: *Undisturbed* vs. *Disturbed*)

- Advancement criterion: Correct classification ≥ 50.0% across all categories
  - Model **ADVANCED** to validation

Table B.62: DFA training results using 418 – 919 nm Autumn FieldSpec reflectance spectra; 2-group analysis; overall 72.0% correct classification of training cases. Classification function coefficients and validation results are listed in **Tables B.63, B.64,** and **B.67.**

N=93			Predicted Membership		Total
		State	**Undisturbed**	**Disturbed**	
Known Membership	(Count)	**Undisturbed**	36	20	56
		Disturbed	6	31	37
	(%)	**Undisturbed**	**64.3**	35.7	100.0
		Disturbed	16.2	**83.8**	100.0

Table B.63: Model #9 Unstandardized Discriminant Function Coefficients.

Variable	**D_1 Coefficient**
Constant	-2.260
708 (nm)	12.078

Table B.64: Model #9 Fisher's Classification Function Coefficients.

Variable	**(U) Coefficient**	**(D) Coefficient**
Constant	-4.294	-2.004
708 (nm)	32.412	19.555

VALIDATION – Training Model #7

- Advancement criterion: Correct classification ≥ 33.3% across 3 categories or ≥ 50.0% across 2 categories
    - Model **NOT** advanced to imagery test

Table B.65: DFA validation results using 418 – 919 nm Autumn FieldSpec reflectance spectra; 3-group analysis; overall 52.5% correct classification of test cases.

N=40			Predicted Membership			
		State	**Undisturbed**	**Burial**	**Control**	Total
Known Membership	(Count)	**Undisturbed**	11	9	3	23
		Burial	3	10	2	15
		Control	0	2	0	2
	(%)	**Undisturbed**	**47.8**	39.1	13.1	100.0
		Burial	20.0	**66.7**	13.3	100.0
		Control	0.0	100.0	**0.0**	100.0

VALIDATION – Training Model #8

- Advancement criterion: Correct classification ≥ 50.0% across all categories
  - Model **NOT** advanced to imagery test

Table B.66: DFA validation results using 418 – 919 nm Spring FieldSpec reflectance spectra; 2-group analysis; overall 58.5% correct classification of test cases.

N=41			Predicted Membership		Total
		State	**Undisturbed**	**Burial**	
Known Membership	(Count)	**Undisturbed**	12	13	25
		Burial	4	12	16
	(%)	**Undisturbed**	**48.0**	52.0	100.0
		Burial	25.0	**75.0**	100.0

VALIDATION – Training Model #9

- Advancement criterion: Correct classification ≥ 50.0% across all categories
  - Model **ADVANCED** to imagery test

Table B.67: DFA validation results using 418 – 919 nm Autumn FieldSpec reflectance spectra; 2-group analysis; overall 62.5% correct classification of test cases.

N=40			Predicted Membership		Total
		State	**Undisturbed**	**Disturbed**	
Known Membership	(Count)	**Undisturbed**	13	10	23
		Disturbed	5	12	17
	(%)	**Undisturbed**	**56.5**	43.5	100.0
		Disturbed	29.4	**70.6**	100.0

Appendix C: Partial Least Squares, Comparisons Unmatched to Models

Partial Least Squares Regression (PLS)

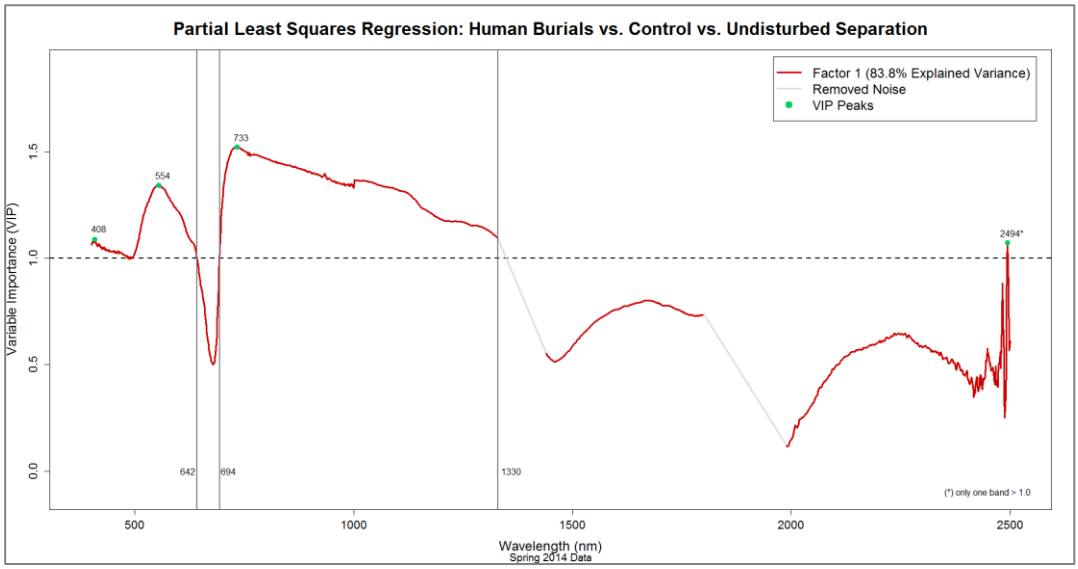

Figure C.1: PLS first factor variable importance (VIP) to group separation, Spring data (n=154); test for separation of Burials vs. Control vs. Undisturbed vegetation groups; VIP ≥ 1.0 intercepts as indicated by vertical lines; VIP peaks at 408, 554, 733, and 2494 nm.

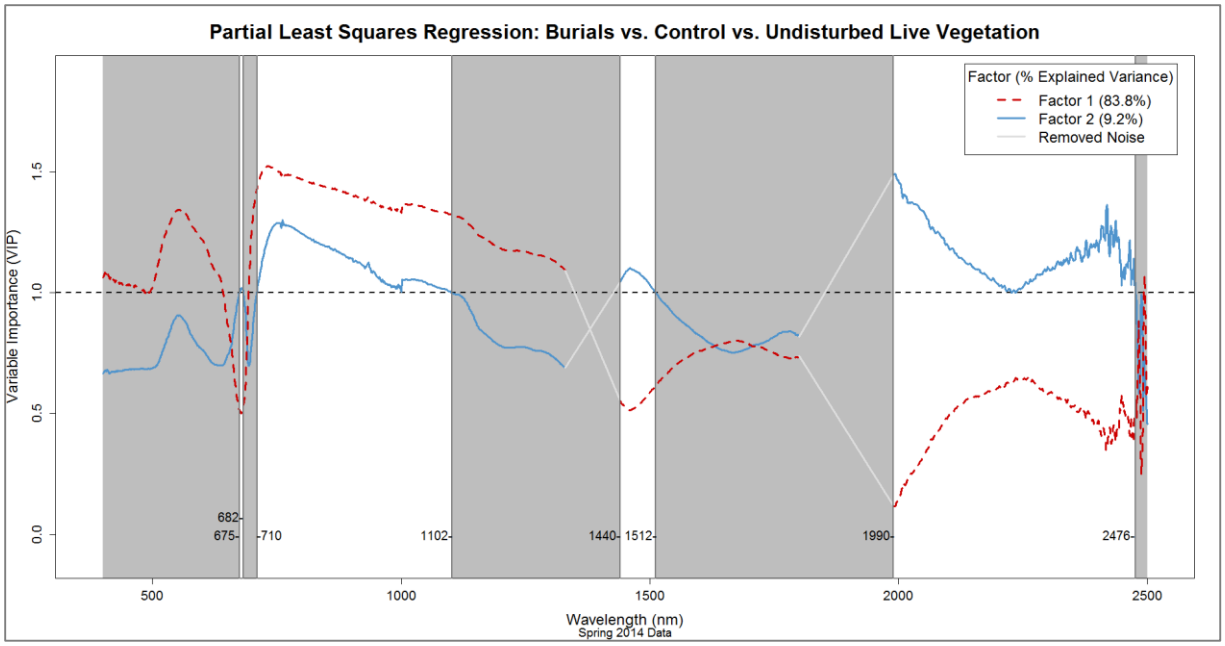

Figure C.2: PLS second factor VIP; Spring data (n=154); test for separation of Burial vs. Control vs. Undisturbed vegetation groups, 93.0% cumulative variance of the independent variables explained by the first two latent factors; graphical emphasis on Factor 2 ≥ 1.0 VIP wavelengths. Factor 1 highlighted in **Figure C.1.**

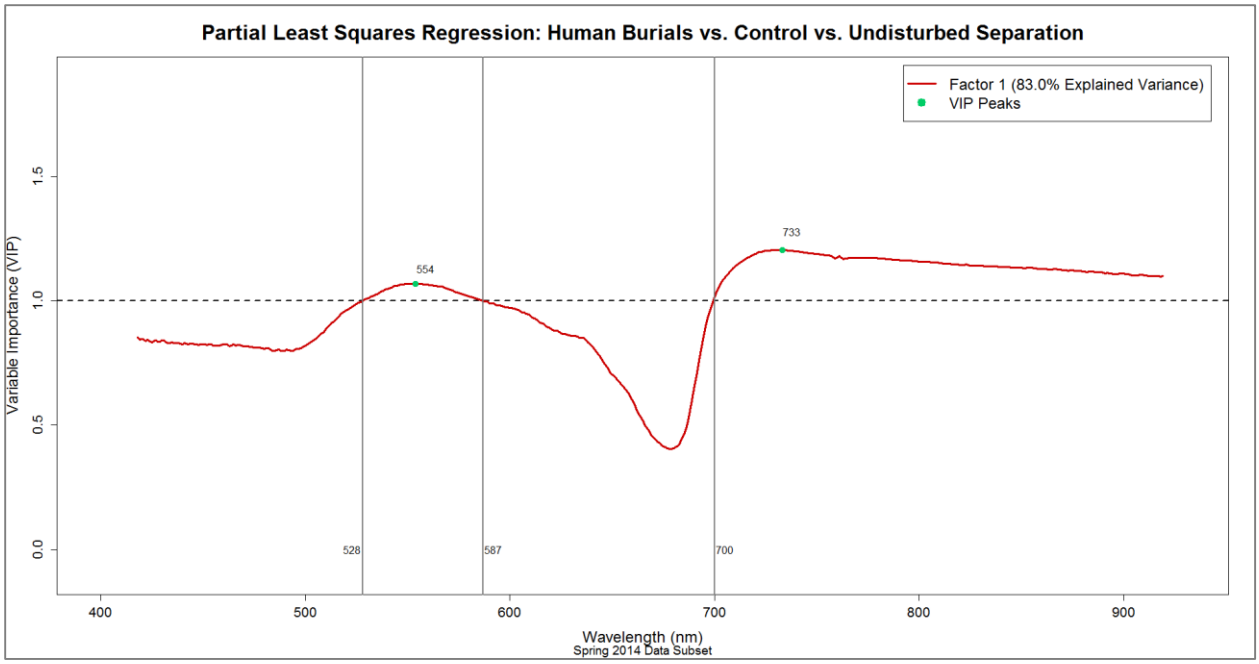

Figure C.3: PLS first factor variable importance (VIP) to group separation, Spring data (n=154); test for separation of Burials vs. Control vs. Undisturbed vegetation groups; VIP ≥ 1.0 intercepts as indicated by vertical lines; VIP peaks at 554 and 733 nm.

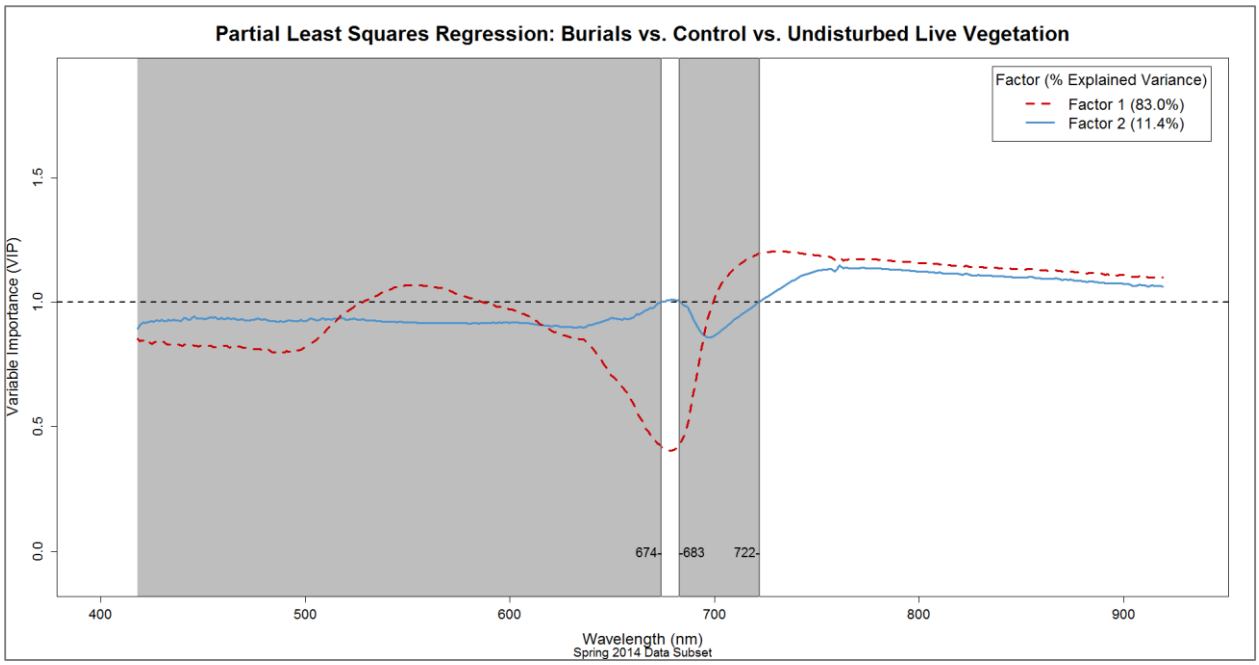

Figure C.4: PLS second factor VIP, Spring data (n=154); test for separation of Burial vs. Control vs. Undisturbed vegetation groups, 94.4% cumulative variance of the independent variables explained by the first two latent factor; graphical emphasis on Factor 2 ≥ 1.0 VIP wavelengths. Factor 1 highlighted in **Figure C.3.**

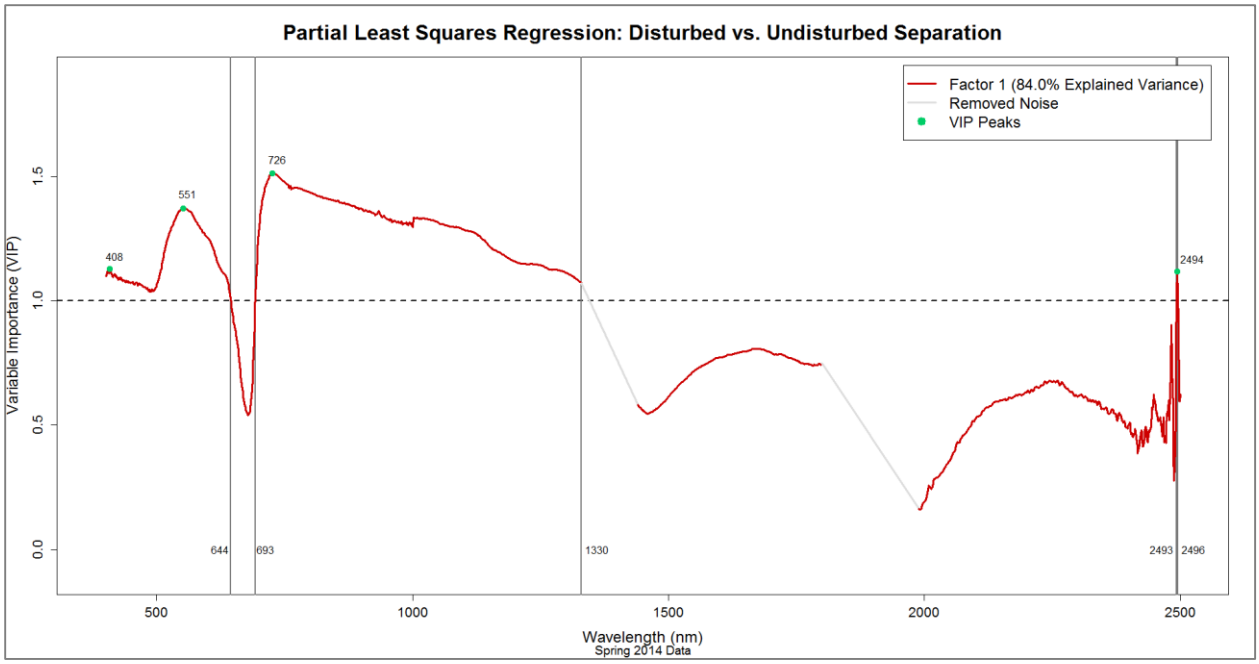

Figure C.5: PLS first factor variable importance (VIP) to group separation, Spring data (n=154); test for separation of Disturbed vs. Undisturbed vegetation groups; VIP ≥ 1.0 intercepts as indicated by vertical lines; VIP peaks at 408, 551, 726, and 2494 nm.

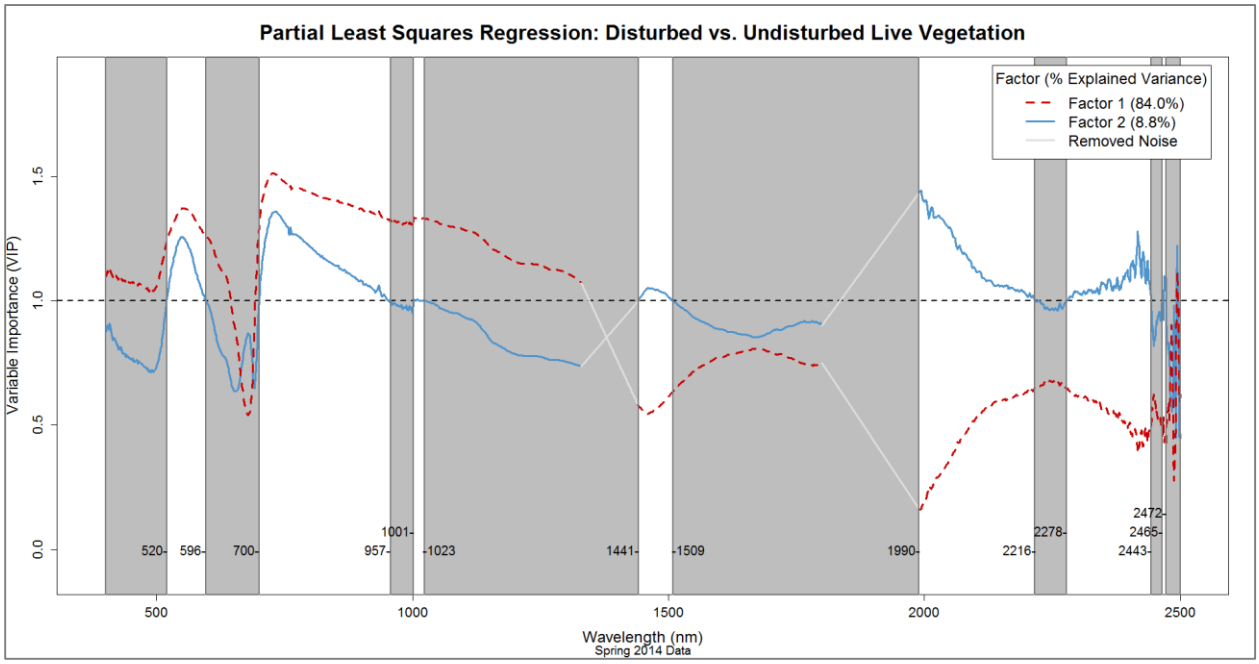

Figure C.6: PLS second factor VIP, Spring data (n=154); test for separation of Disturbed vs. Undisturbed groups, 92.8% cumulative variance of the independent variables explained by the first two latent factors; graphical emphasis on Factor 2 ≥ 1.0 VIP wavelengths. Factor 1 highlighted in **Figure C.5.**

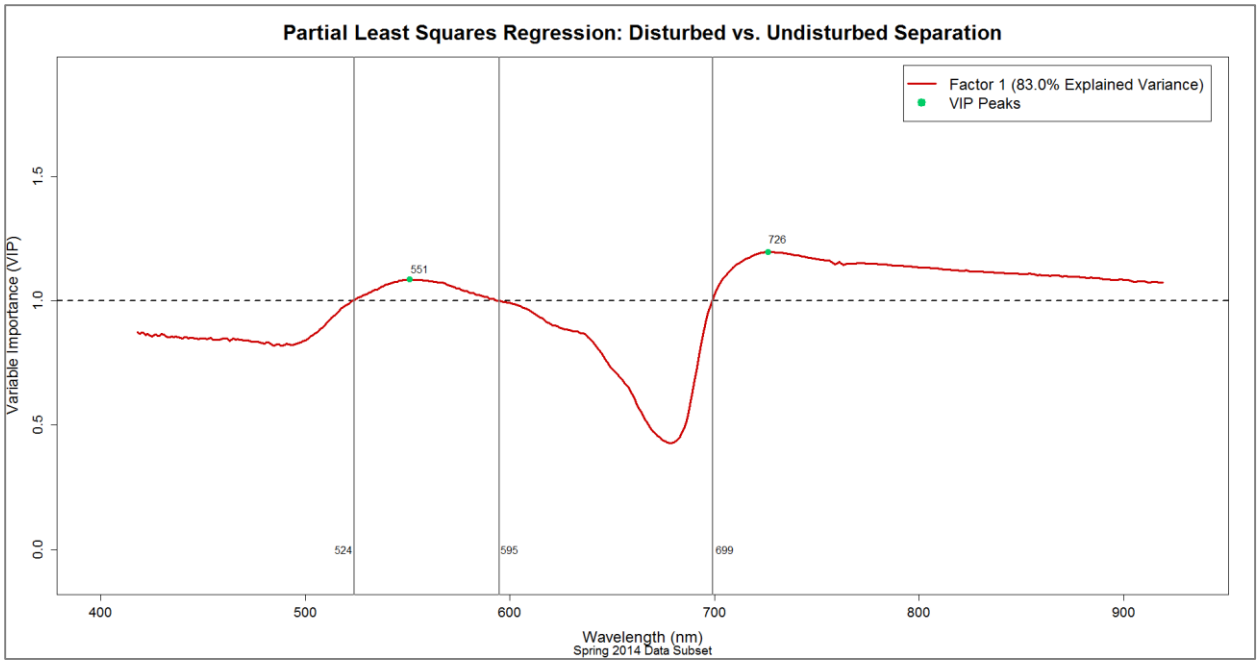

Figure C.7: PLS first factor variable importance (VIP) to group separation, Spring data (n=154); test for separation of Disturbed vs. Undisturbed vegetation groups; VIP ≥ 1.0 intercepts as indicated by vertical lines; VIP peaks at 551 and 726 nm.

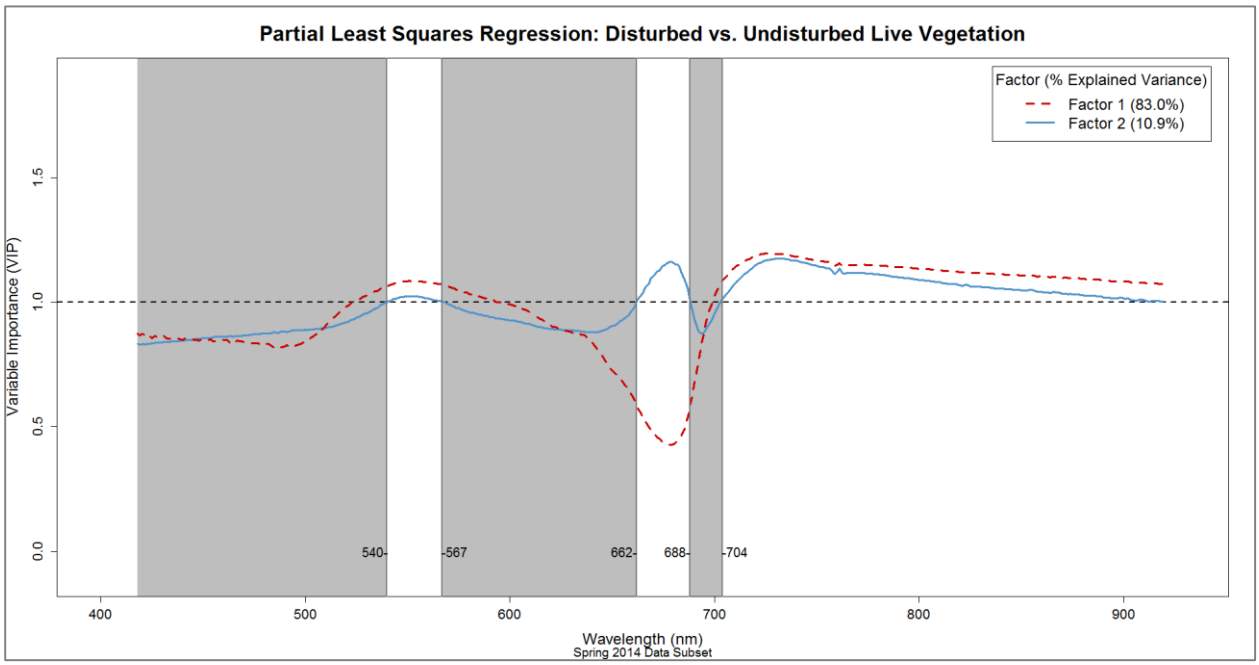

Figure C.8: PLS second factor VIP, Spring data (n=154); test for separation of Disturbed vs. Undisturbed vegetation groups, 93.9% cumulative variance of the independent variables explained by the first two latent factors; graphical emphasis on Factor 2 ≥ 1.0 VIP wavelengths. Factor 1 highlighted in **Figure C.7.**

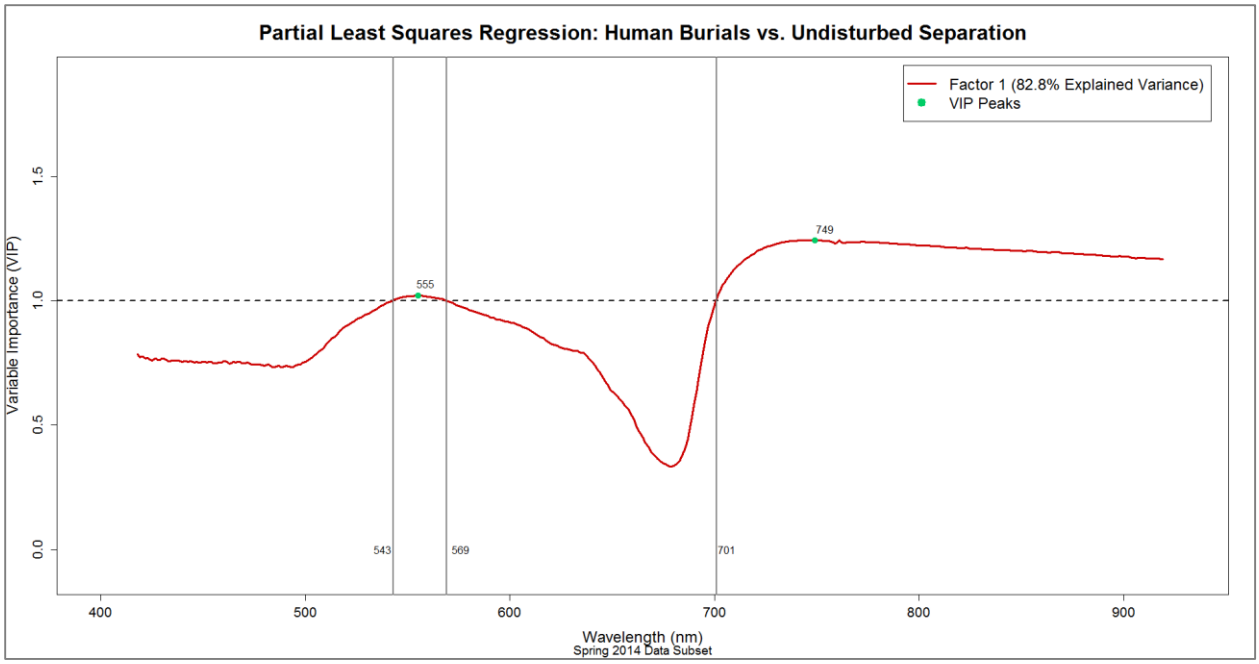

Figure C.9: PLS first factor variable importance (VIP) to group separation, Spring data (n=137); test for separation of Burial vs. Undisturbed vegetation groups; VIP ≥ 1.0 intercepts as indicated by vertical lines; VIP peaks at 555 and 749 nm.

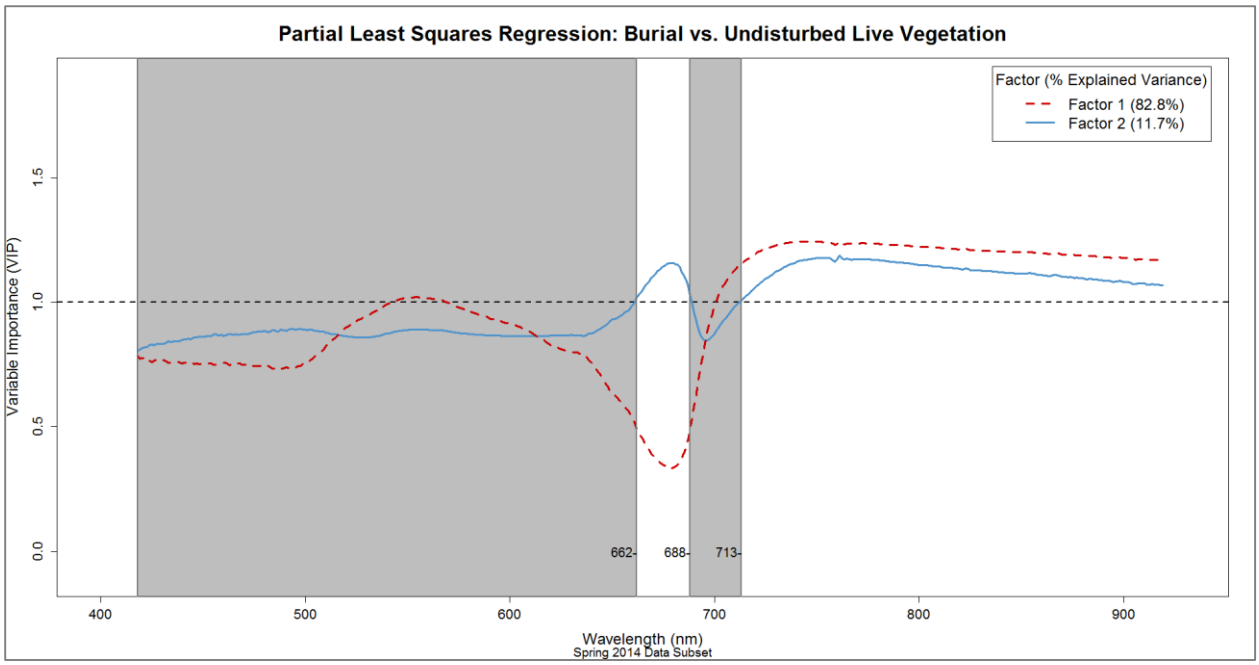

Figure C.10: PLS second factor VIP, Spring data (n=137); test for separation of Burial vs. Undisturbed groups, 94.5% cumulative variance of the independent variables explained by the first two latent factors; graphical emphasis on Factor 2 ≥ 1.0 VIP wavelengths. Factor 1 highlighted in **Figure C.9.**

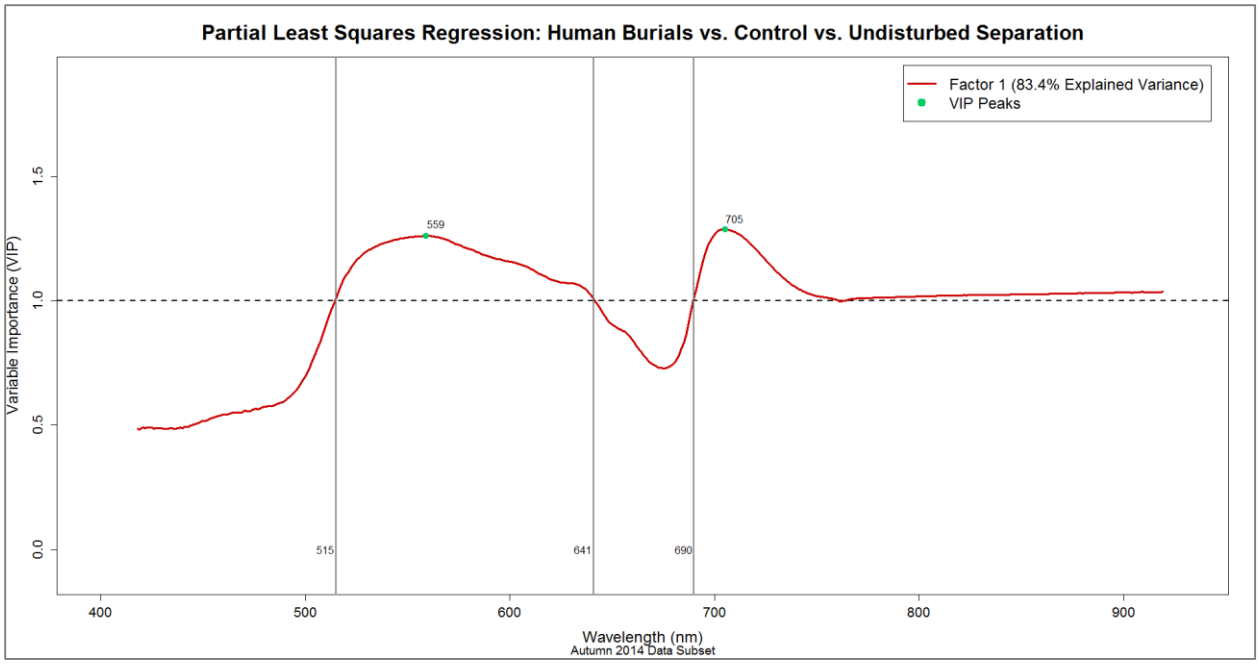

Figure C.11: PLS first factor variable importance (VIP) to group separation, Autumn data (n=133); test for separation of Burial vs. Control vs. Undisturbed vegetation groups; VIP ≥ 1.0 intercepts as indicated by vertical lines; VIP peaks at 559 and 705 nm.

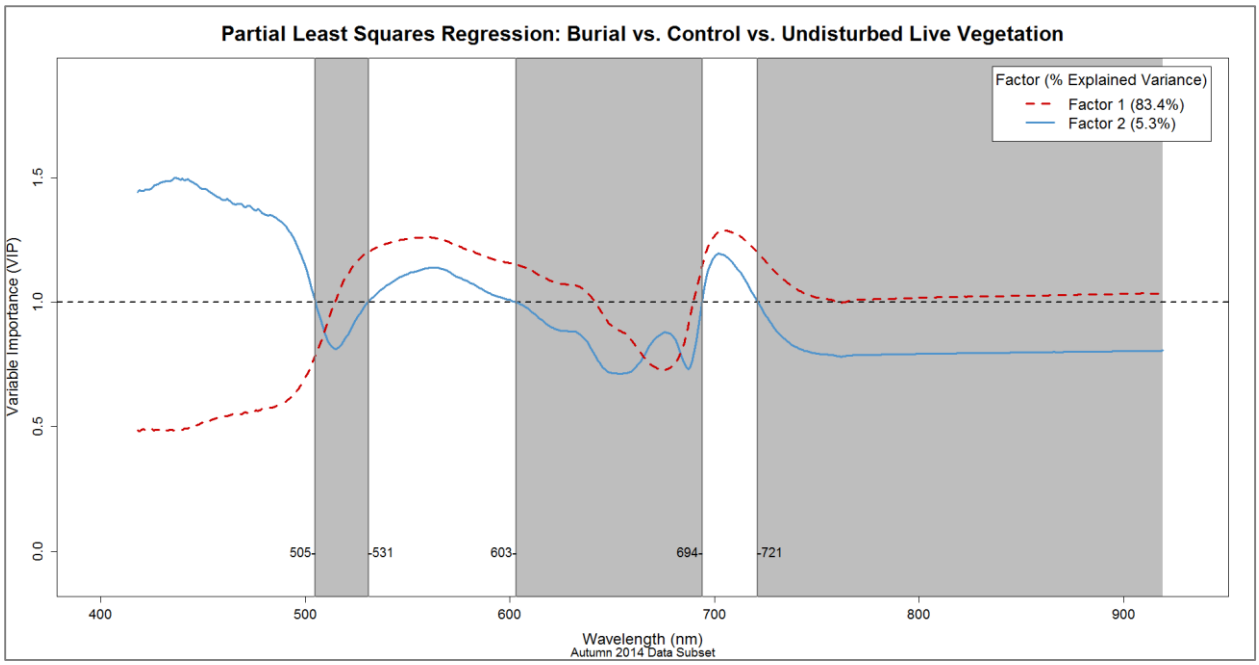

Figure C.12: PLS second factor VIP, Autumn data (n=133); test for separation of Burial vs. Control vs. Undisturbed vegetation groups,88.7% cumulative variance of the independent variables explained by the first two latent factors; graphical emphasis on Factor 2 ≥ 1.0 VIP wavelengths. Factor 1 highlighted in **Figure C.11.**

Appendix D: Spectral Index Calculations

Table D.1: Formulas for calculating vegetation indices from reflectance spectra, R, at certain wavelengths; (*) indicates indices used by LeBlanc et al. (2014). Sub-calculations, including which wavelengths are used for 'NIR,' 'Red,' or 'Blue' values in general formulas, are available in **Tables D.2 and D.3.**

Index	Calculation
NDVI*	(NIR – Red) ÷ (NIR + Red)
RENDVI	($R750 – R705$) ÷ ($R750 + R705$)
MRESRI	($R750 – R445$) ÷ ($R705 – R445$)
MRENDVI	($R750 – R705$) ÷ ($R750 + R705 – 2* R445$)
SGI*	Mean of all bands 500 – 600 nm
REPI	Wavelength of the maximum derivative of reflectance in 690 – 740 nm
SIPI*	($R800 – R445$) ÷ ($R800 – R680$)

Table D.2: ENVI definitions for each wavelength range used for calculating spectral indices.

Region	Min (nm)	Center (nm)	Max (nm)
Blue	400	470	500
Green	500	550	600
Red	600	650	700
NIR	760	860	960
SWIR1	1550	1650	1750
SWIR2	2080	2220	2350

Table D.3: Default ENVI logic for selecting wavelengths used in spectral index calculations

Step	Condition
1:	Find the center wavelength for each input file band
2:	Determine if the center wavelength falls within the ranges in **Table D.2**
3:	If more than one band meets Step 2 condition, ENVI chooses the band nearest the relevant band center listed **Table D.2**

Appendix E: Elevation Surface Changes per Burial

Table E.1: Minimum, mean, and maximum elevation changes at burial surfaces between 12 Feb. 2013 and 15 Feb. 2013 using elevation change data from ROIs depicted in **Figure 6.4-9**. Gray indicates data from the G6 burial before it was completely backfilled.

15 Feb. 2013 vs. Baseline	Min (m)	Mean (m)	Max (m)
2 x 4 m (Control)	-0.024399	0.066561	0.189835
2 x 4 m (Burial, 6)	-0.627548	-0.214229	0.104797
2 x 2 m (Burial, 3)	-0.130157	0.041221	0.167236
1 x 2 m (Burial, 1)	-0.015884	0.039124	0.339127

Table E.2: Minimum, mean, and maximum elevation changes at burial surfaces between 12 Feb. 2013 and 03 June 2013 using elevation change data from ROIs depicted in **Figure 6.4-9**.

03 June 2013 vs. Baseline	Min (m)	Mean (m)	Max (m)
2 x 4 m (Control)	-0.074402	0.003205	0.192825
2 x 4 m (Burial, 6)	-0.125595	-0.049756	0.079102
2 x 2 m (Burial, 3)	-0.094223	-0.015283	0.488342
1 x 2 m (Burial, 1)	-0.058685	-0.016381	0.048172

Table E.3: Minimum, mean, and maximum elevation changes at burial surfaces between 12 Feb. 2013 and 20 Nov. 2014 using elevation change data from ROIs depicted in **Figure 6.4-9**.

20 Nov. 2014 vs. Baseline	Min (m)	Mean (m)	Max (m)
2 x 4 m (Control)	-0.040421	0.05884	0.185181
2 x 4 m (Burial, 6)	-0.093796	-0.022477	0.085419
2 x 2 m (Burial, 3)	-0.057739	0.032038	0.260101
1 x 2 m (Burial, 1)	0.001038	0.041151	0.134689

Table E.4: Minimum, mean, and maximum elevation changes at burial surfaces between 15 Feb. 2013 and 03 June 2013 using elevation change data from ROIs depicted in **Figure 6.4-9**. Gray indicates data from the G6 burial before it was completely backfilled.

03 June vs. 15 Feb.	Min (m)	Mean (m)	Max (m)
2 x 4 m (Control)	-0.120773	-0.063356	0.101486
2 x 4 m (Burial, 6)	-0.147507	0.164474	0.623871
2 x 2 m (Burial, 3)	-0.146042	-0.056505	0.453262
1 x 2 m (Burial, 1)	-0.371094	-0.055505	0.009369

Table E.5: Minimum, mean, and maximum elevation changes at burial surfaces between 15 Feb. 2013 and 20 Nov. 2014, using elevation change data from ROIs depicted in **Figure 6.4-9**. Gray indicates data from the G6 burial before it was completely backfilled.

20 Nov. vs. 15 Feb.	Min (m)	Mean (m)	Max (m)
2 x 4 m (Control)	-0.078827	-0.005065	0.127686
2 x 4 m (Burial, 6)	-0.132233	0.196748	0.638397
2 x 2 m (Burial, 3)	-0.132187	-0.004755	0.228455
1 x 2 m (Burial, 1)	-0.321686	0.005541	0.115112

Table E.6: Minimum, mean, and maximum elevation changes at burial surfaces between 03 June 2013 and 20 Nov. 2014, using elevation change data from ROIs depicted in **Figure 6.4-9.**

20 Nov. vs. 03 June	Min (m)	Mean (m)	Max (m)
2 x 4 m (Control)	-0.153595	0.054696	0.172150
2 x 4 m (Burial, 6)	-0.058029	0.027295	0.103745
2 x 2 m (Burial, 3)	-0.397125	0.046957	0.241394
1 x 2 m (Burial, 1)	0.002228	0.057402	0.152573

Appendix F: Low Resolution Elevation Change Images, Terrestrial LIDAR

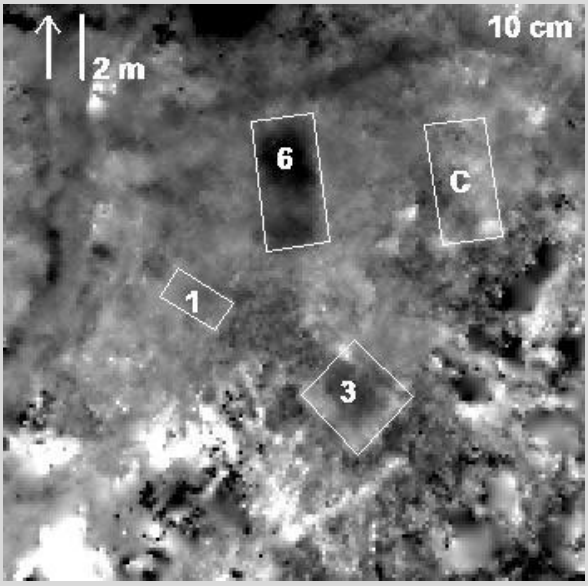

Figure F.1: ROI overlays shown here for referencing burial locations in **Figures F.2 – F.4** (no new data).

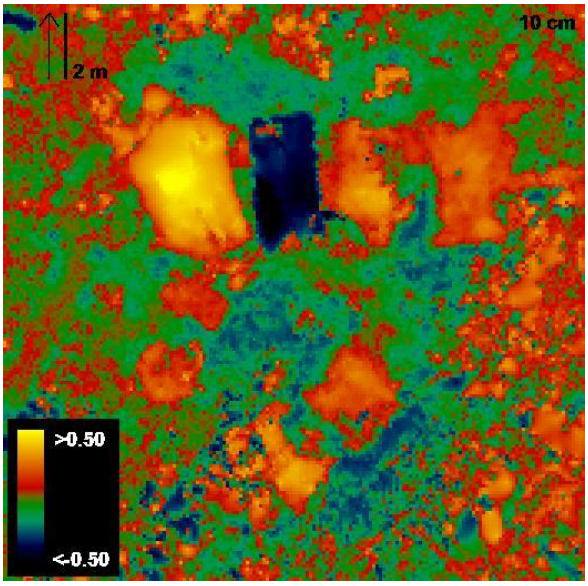

Figure F.2: Elevation changes of study area between 12 Feb. – 15 Feb. 2013; values indicate net elevation change (m).

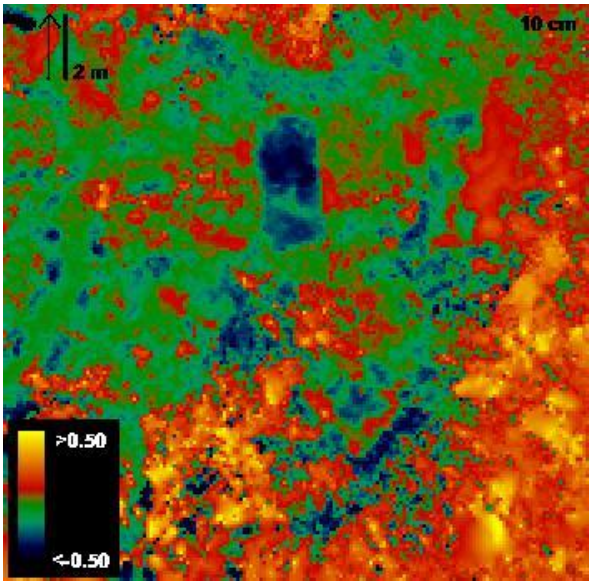

Figure F.3: Elevation changes of study area between 12 Feb. – 03 June 2013.

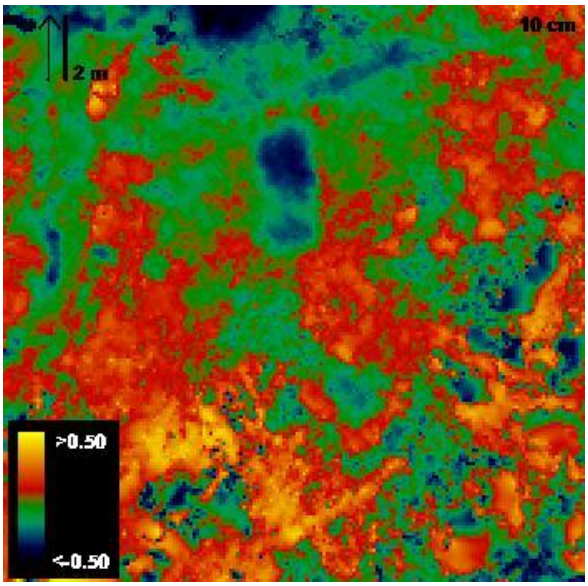

Figure F.4: Elevation changes of study area between 12 Feb. 2013 – 20 Nov. 2014.

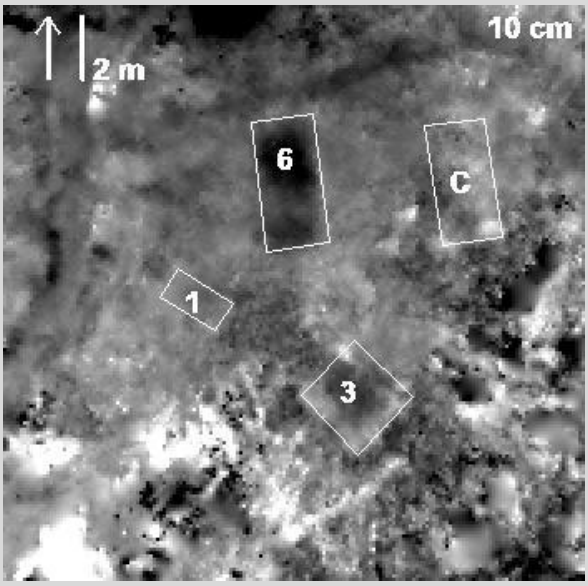

Figure F.1*: ROI overlays shown here for referencing burial locations in **Figures F.5 – F.7** (no new data).

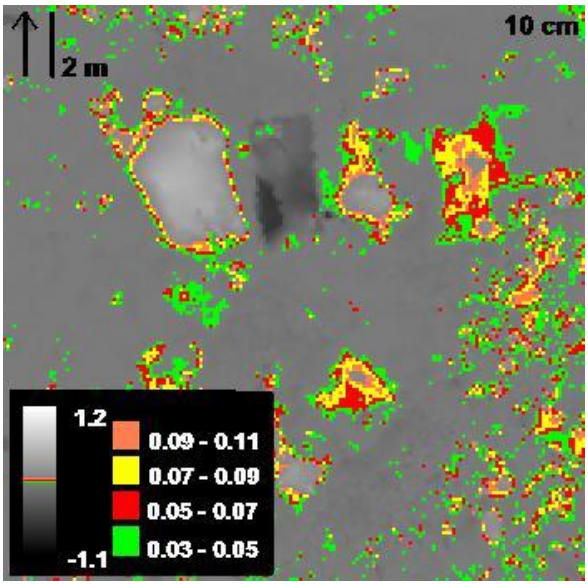

Figure F.5: Elevation changes of study area between 12 Feb. – 15 Feb. 2013; 2 cm density slices added to emphasize elevation change clustering at 3.0 – 11.0 cm; values follow means from **Figures 4.4-16 – 4.4-19**.

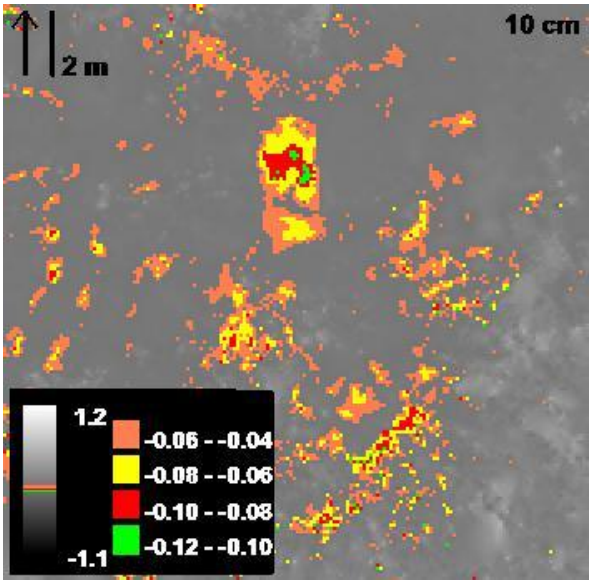

Figure F.6: Elevation changes of study area between 12 Feb. – 03 June 2013; 2 cm density slices added for -12 - -4.0 cm.

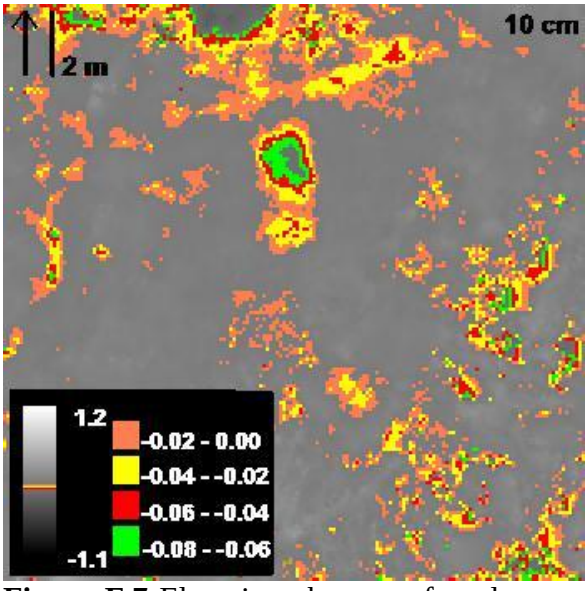

Figure F.7 Elevation changes of study area between 12 Feb. 2013 – 20 Nov. 2014; 2 cm density slices added for -8.0 – 0.0 cm.

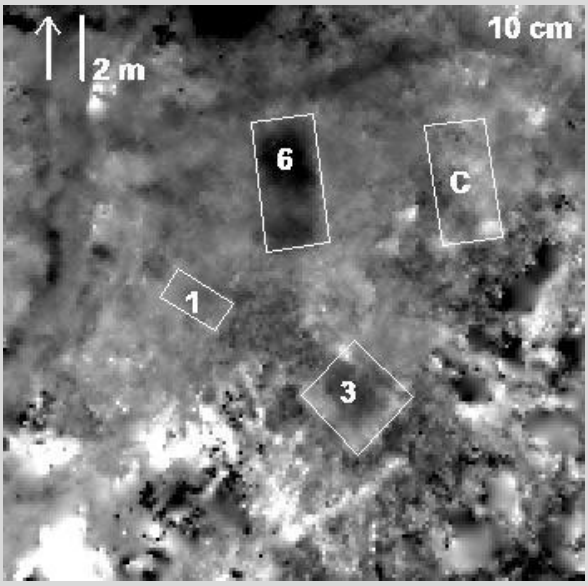

Figure F.1*: ROI overlays shown here for referencing burial locations in **Figures F.8 – F.10** (no new data).

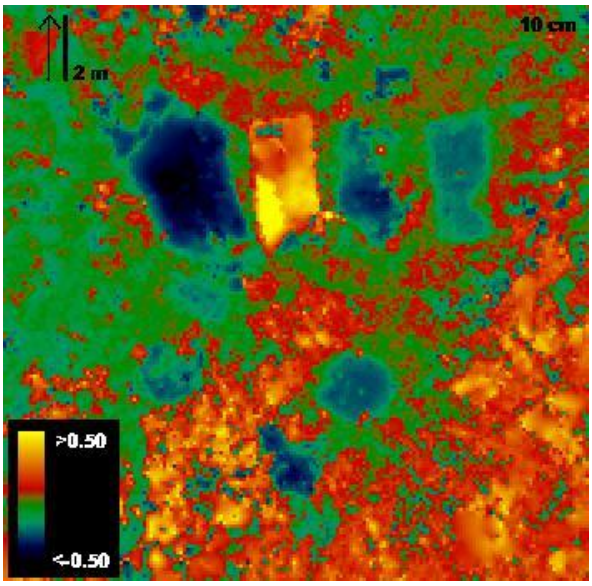

Figure F.8: Elevation changes of study area between 15 Feb. – 03 June 2013; values indicate net elevation change (m).

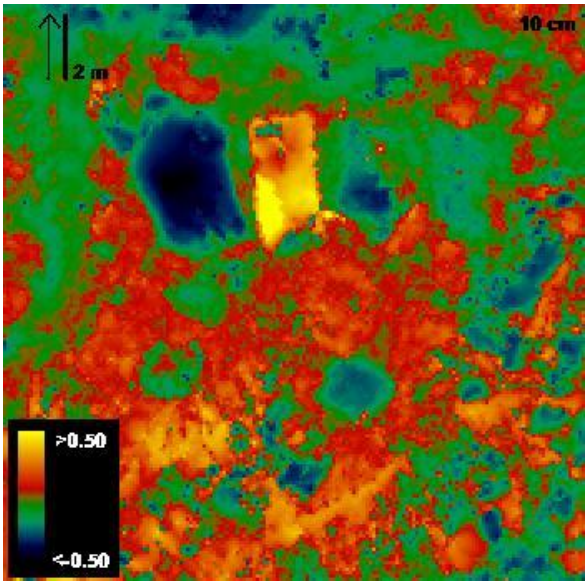

Figure F.9: Elevation changes of study area between 15 Feb. 2013 – 20 Nov. 2014.

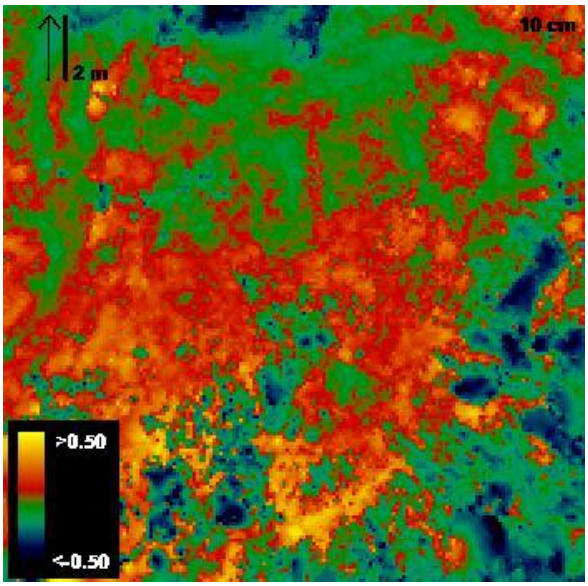

Figure F.10: Elevation changes of study area between 03 June 2013 – 20 Nov. 2014.

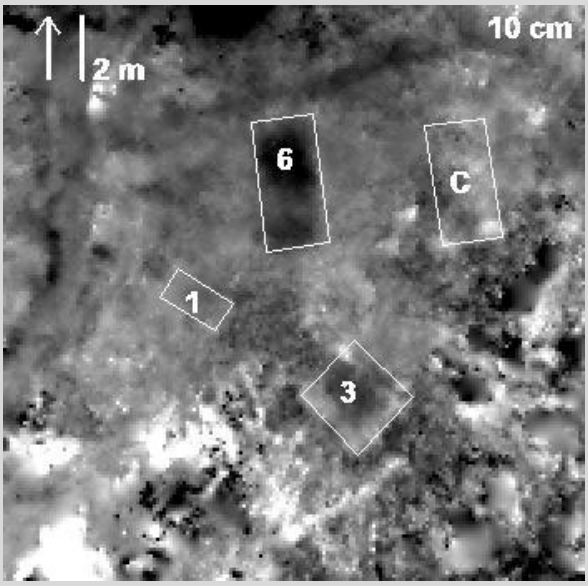

Figure F.1*: ROI overlays shown here for referencing burial locations in **Figures F.11 – F.13** (no new data).

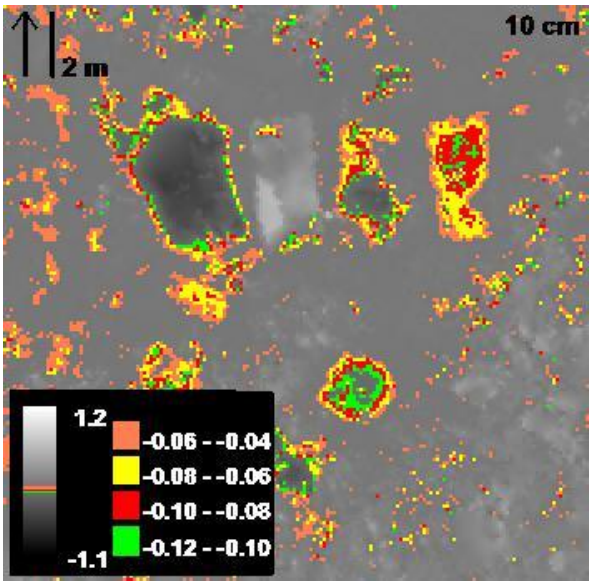

Figure F.11: Elevation changes of study area between 15 Feb. – 03 June 2013; 2 cm density slices added to emphasize elevation change clustering at -12.0 - -4.0 cm; values follow means from **Figures E.4 – E.6**.

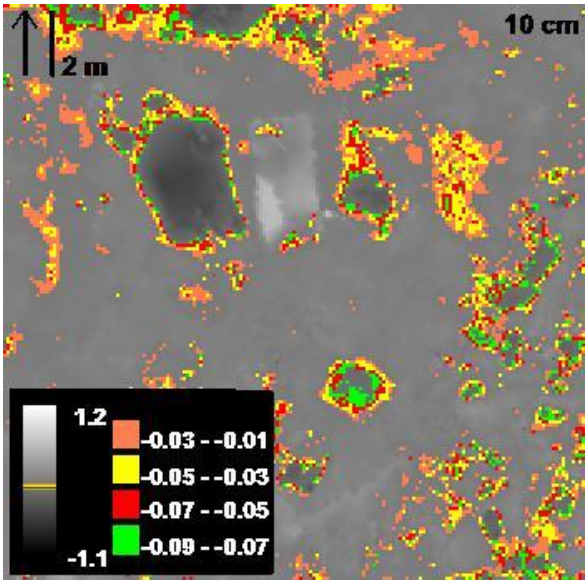

Figure F.12: Elevation changes of study area between 15 Feb. 2013 – 20 Nov. 2014; 2 cm density slices added for -9.0 - -1.0 cm.

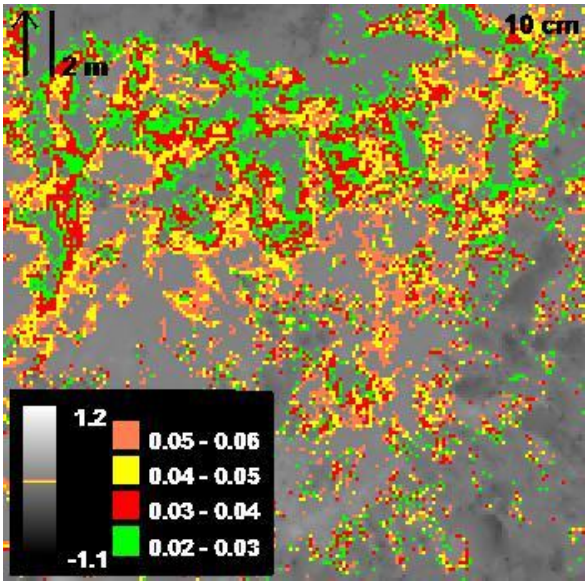

Figure F.13: Elevation changes of study area between 03 June 2013 – 20 Nov. 2014; 1 cm density slices for 2.0 – 6.0 cm.

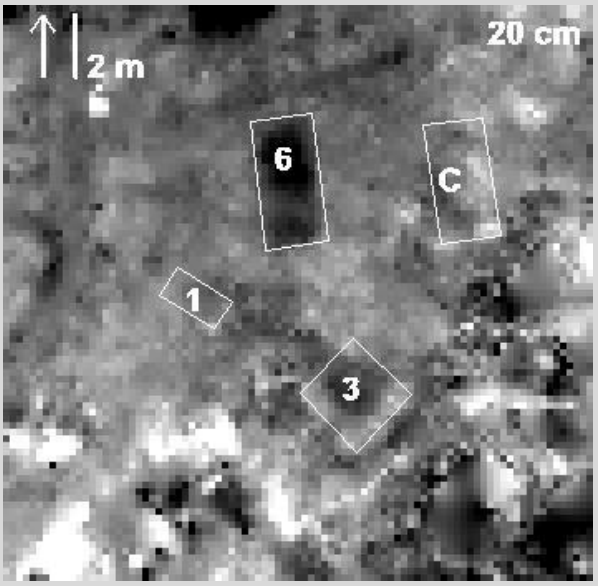

Figure F.14: ROI overlays shown here for referencing burial locations in **Figures F.15 – F.17** (no new data).

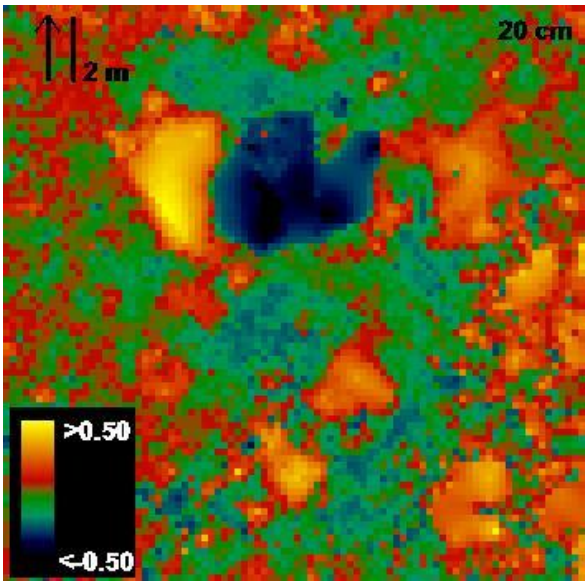

Figure F.15: Elevation changes of study area between 12 Feb. 15 Feb. 2013; values indicate net elevation change (m).

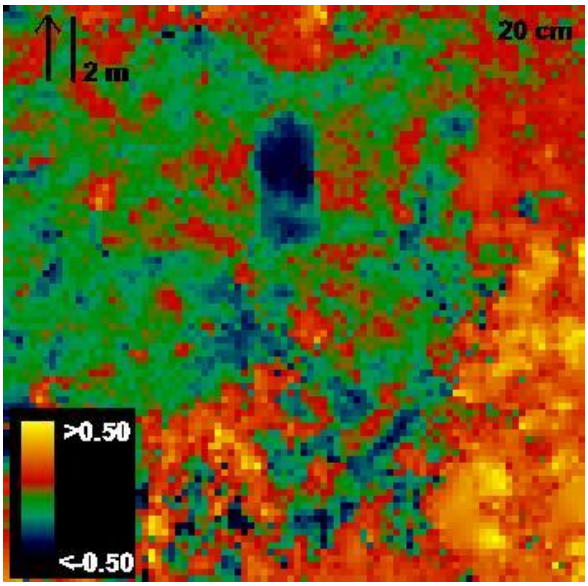

Figure F.16: Elevation changes of study area between 12 Feb. – 03 June 2013.

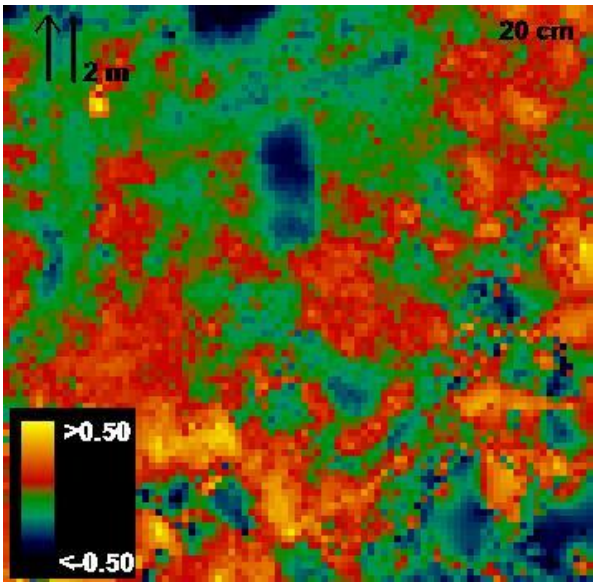

Figure F.17: Elevation changes of study area between 12 Feb. 2013 – 20 Nov. 2014.

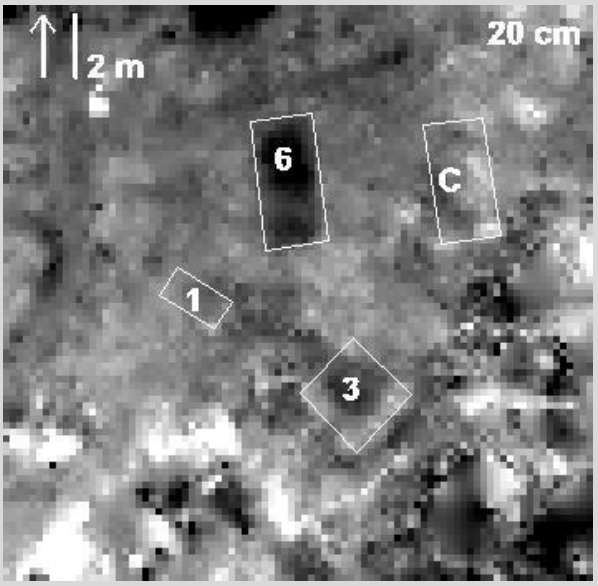

Figure F.14*: ROI overlays shown here for referencing burial locations in **Figures F.18 – F.20** (no new data).

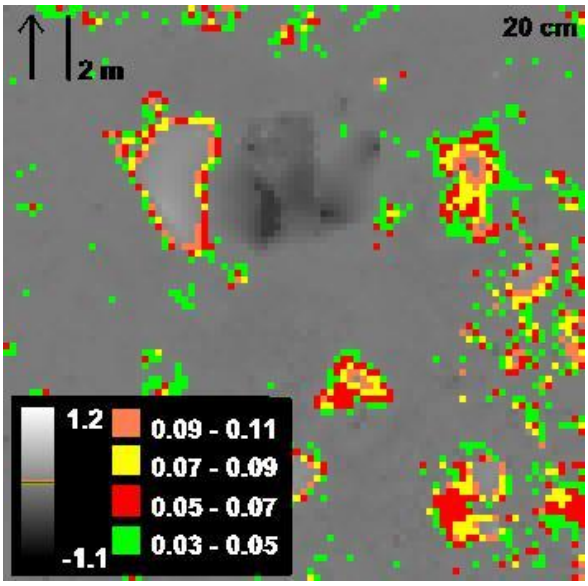

Figure F.18: Elevation changes of study area between 12 Feb. – 15 Feb. 2013; 2 cm density slices added to emphasize elevation change clustering at 3.0 – 11.0 cm; values follow means from **Figures 4.4-16 – 4.4-19**.

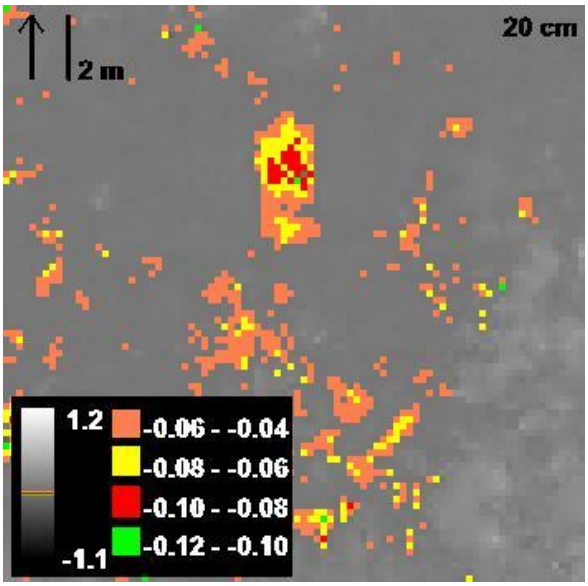

Figure F.19: Elevation changes of study area between 12 Feb. – 03 June 2013; 2 cm density slices added for -12.0 - -4.0 cm.

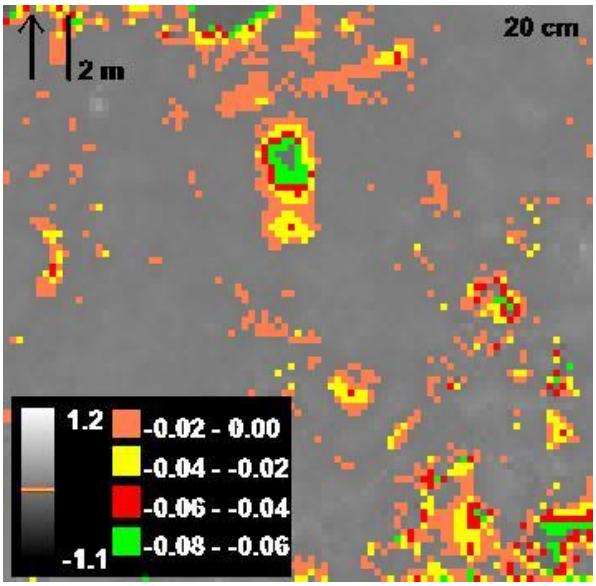

Figure F.20: Elevation changes of study area between 12 Feb. 2013 – 20 Nov. 2014; 2 cm density slices added for -8.0 – 0.0 cm.

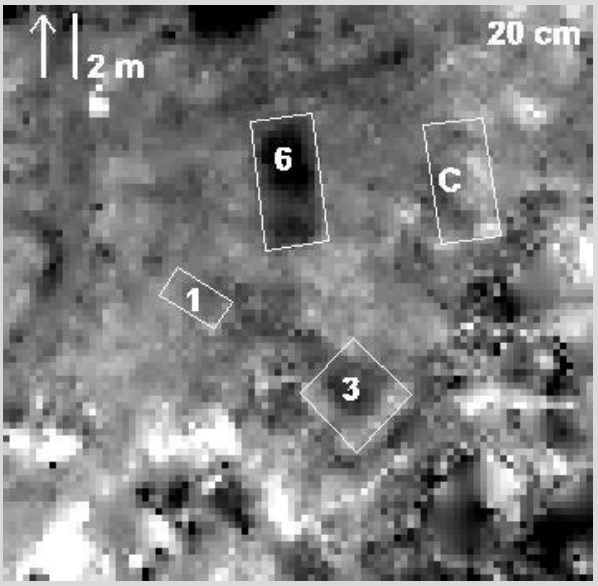

Figure F.14*: ROI overlays shown here for referencing burial locations in **Figures F.21 – F.23** (no new data).

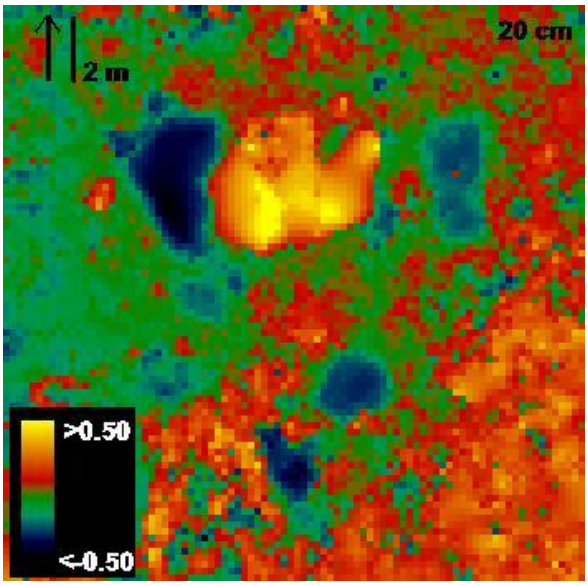

Figure F.21: Elevation changes of study area between 15 Feb. – 03 June 2013; values indicate net elevation change (m).

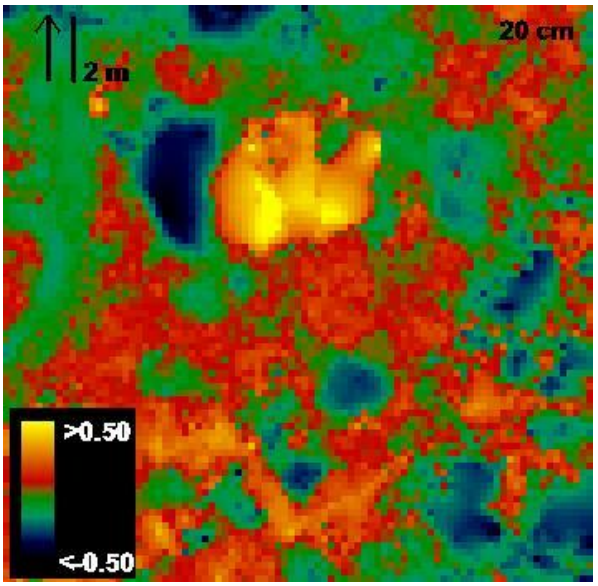

Figure F.22: Elevation changes of study area between 15 Feb. – 20 Nov. 2014.

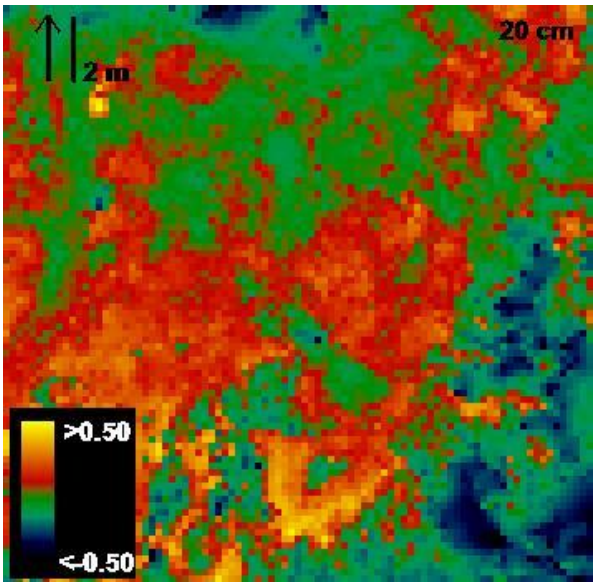

Figure F.23: Elevation changes of study area between 03 June 2013 – 20 Nov. 2014.

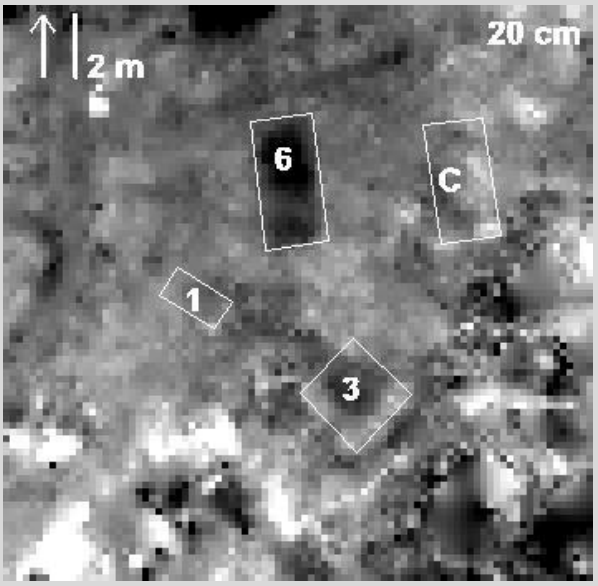

Figure F.14*: ROI overlays shown here for referencing burial locations in **Figures F.24 – F.26** (no new data).

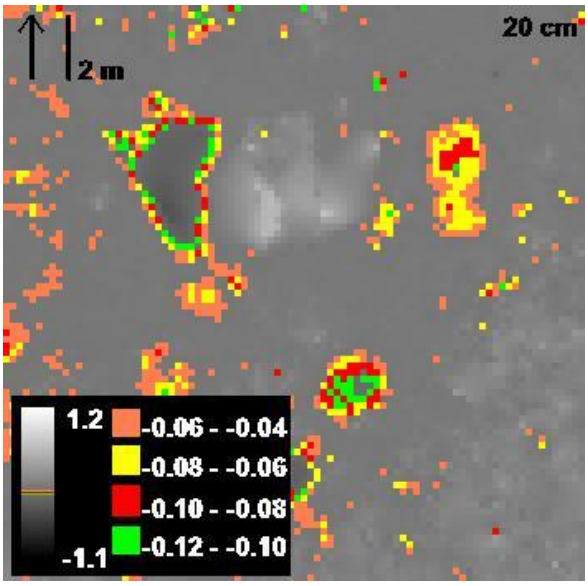

Figure F.24: Elevation changes of study area between 15 Feb. – 03 June 2013; 2 cm density slices added to emphasize elevation change clustering at -12.0 - -4.0 cm; values follow means from **Figures E.4 – E.6**.

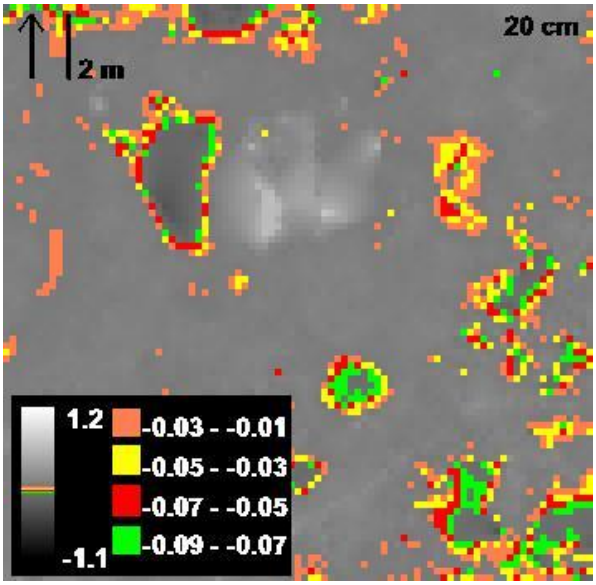

Figure F.25: Elevation changes of study area between 15 Feb. 2013 – 20 Nov. 2014; 2 cm density slices added for -9.0 - -1.0 cm.

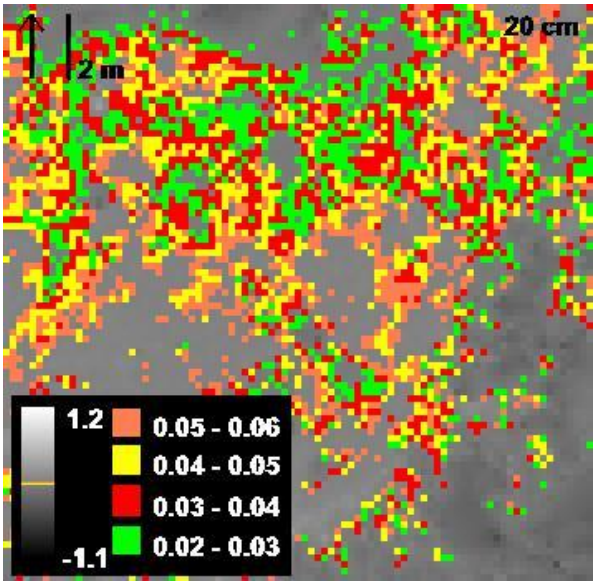

Figure F.26: Elevation changes of study area between 03 June 2013 – 20 Nov. 2014; 1 cm density slices for 2.0 – 6.0 cm.

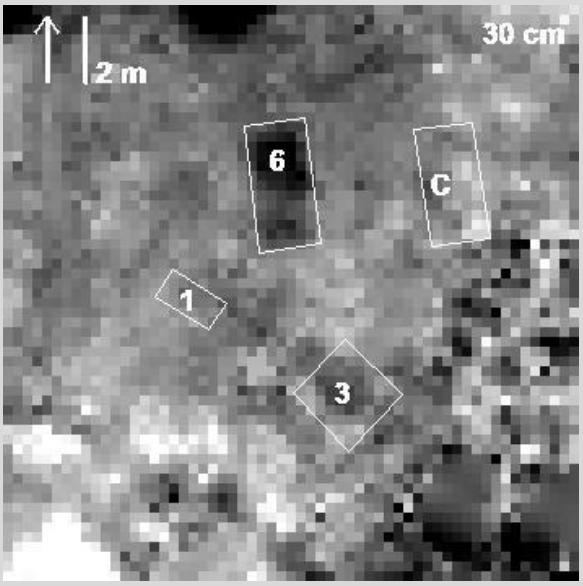

Figure F.27: ROI overlays shown here for referencing burial locations in **Figures F.28 – F.30** (no new data).

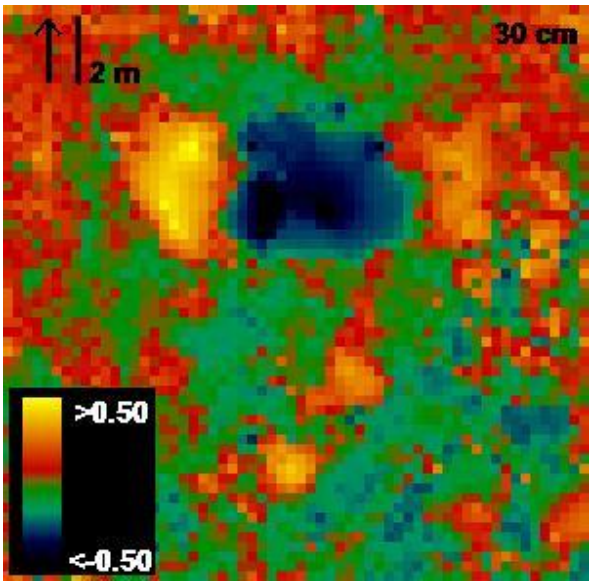

Figure F.28: Elevation changes of study area between 12 Feb. – 15 Feb. 2013; values indicate net elevation change (m).

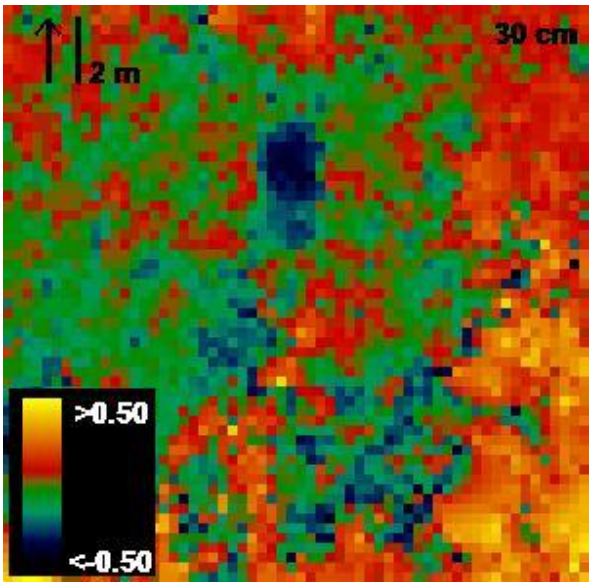

Figure F.29: Elevation changes of study area between 12 Feb. – 03 June 2013.

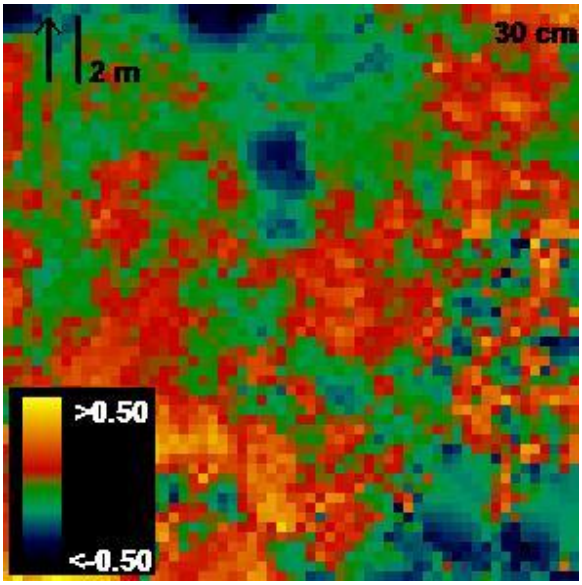

Figure F.30: Elevation changes of study area between 12 Feb. 2013 – 20 Nov. 2014.

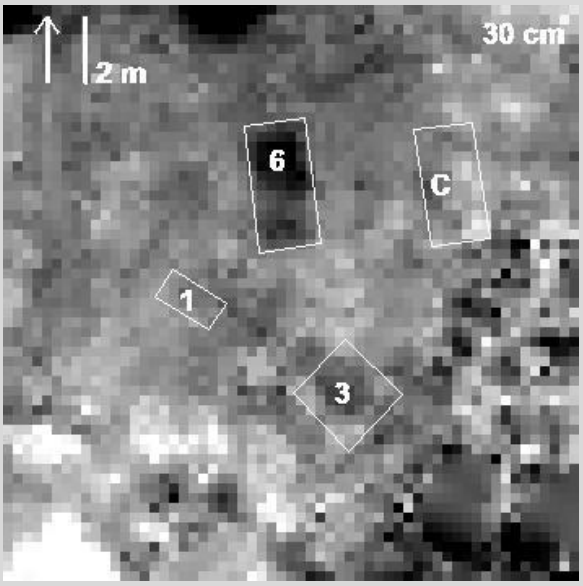

Figure F.27*: ROI overlays shown here for referencing burial locations in **Figures F.31 – F.33** (no new data).

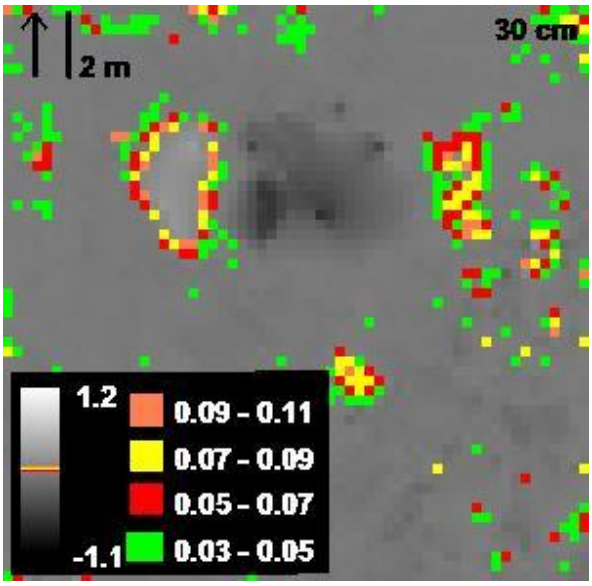

Figure F.31: Elevation changes of study area between 12 Feb. – 15 Feb. 2013; 2 cm density slices added to emphasize elevation change clustering at 3.0 – 11.0 cm; values follow means from **Figures 4.4-16 – 4.4-19**.

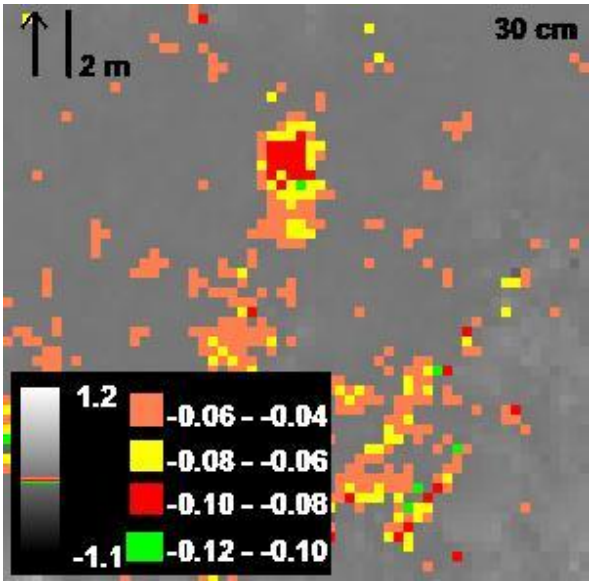

Figure F.32: Elevation changes of study area between 12 Feb. – 03 June 2013; density slices added for -12.0 - -4.0 cm.

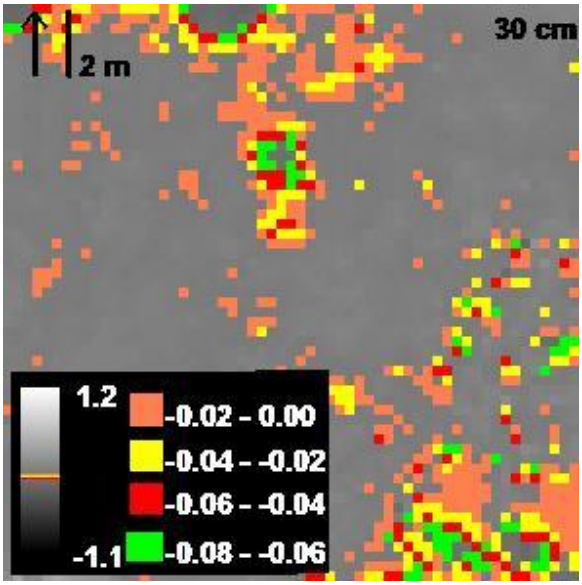

Figure F.33: Elevation changes of study area between 12 Feb. 2013 – 20 Nov. 2014; 2 cm density slices added for -8.0 – 0.0 cm.

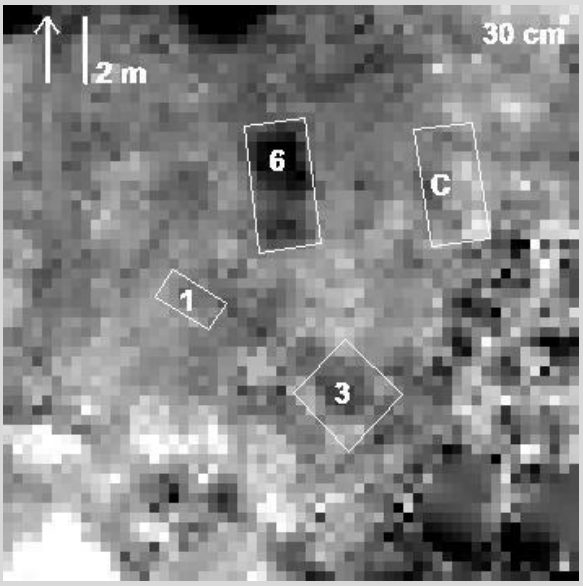

Figure F.27*: ROI overlays shown here for referencing burial locations in **Figures F.34 – F.36** (no new data).

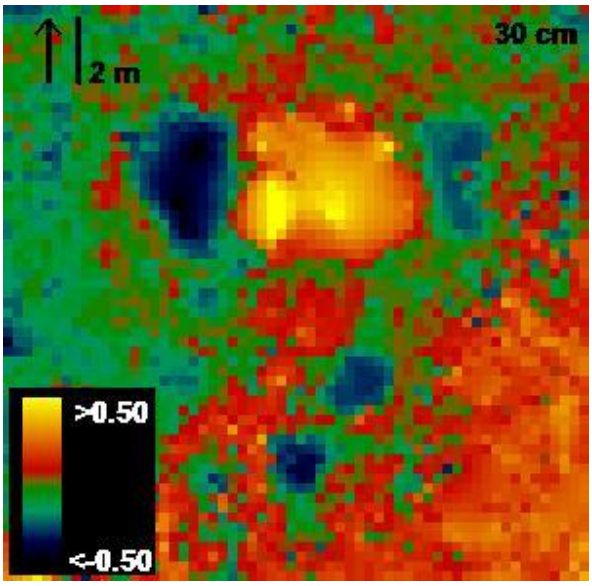

Figure F.34: Elevation changes of study area between 15 Feb. – 03 June 2013; values indicate net elevation change (m).

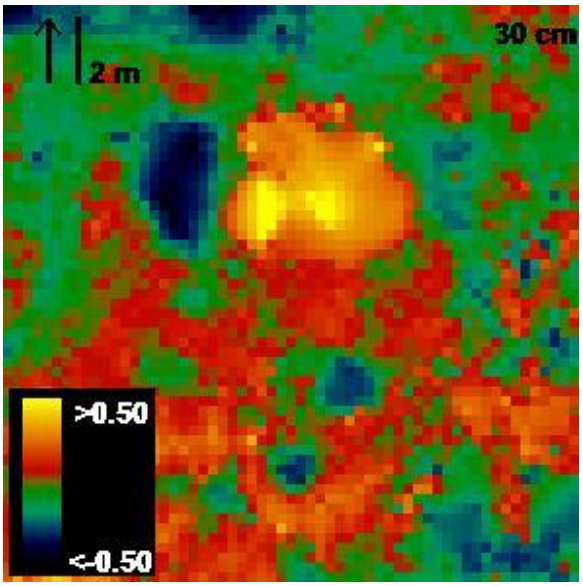

Figure F.35: Elevation changes of study area between 15 Feb. 2013 – 20 Nov. 2014.

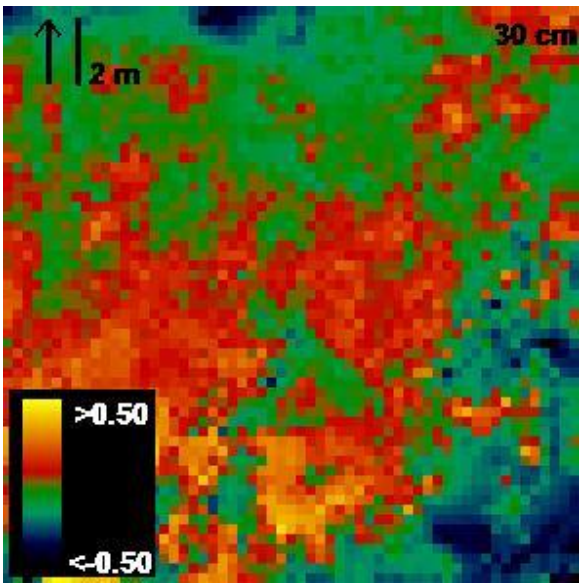

Figure F.36: Elevation changes of study area between 03 June 2013 – 20 Nov. 2014.

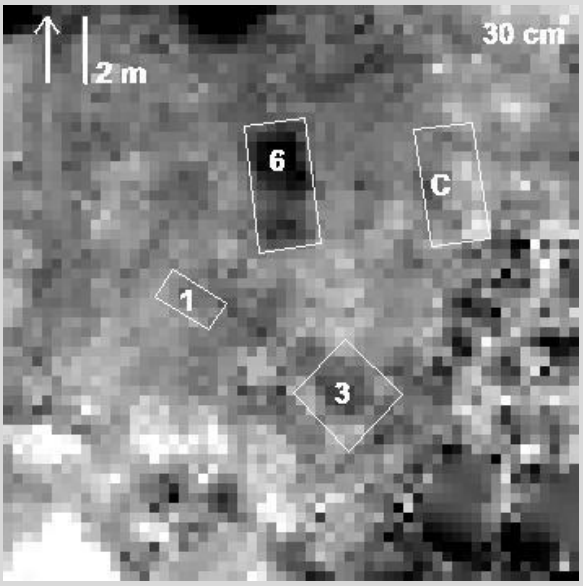

Figure F.27*: ROI overlays shown here for referencing burial locations in **Figures F.37 – F.39** (no new data).

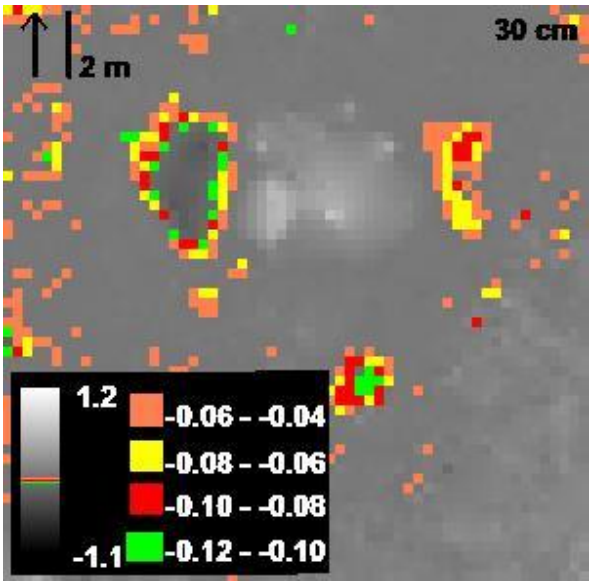

Figure F.37: Elevation changes of study area between 15 Feb. – 03 June 2013; 2 cm density slices added to emphasize elevation change clustering at -12.0 - -4.0 cm; values follow means from **Figures E.4 – E.6**.

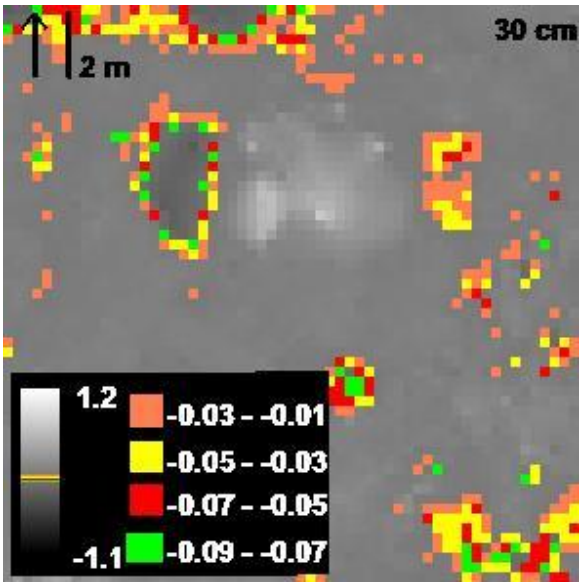

Figure F.38: Elevation changes of study area between 15 Feb. 2013 – 20 Nov. 2014; 2 cm density slices added for -9.0 - -1.0 cm.

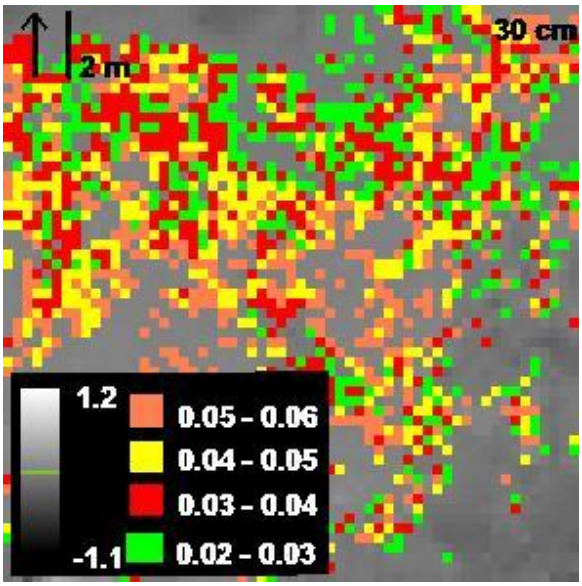

Figure F.39: Elevation changes of study area between 03 June 2013 – 20 Nov. 2014; 1 cm density slices for 2.0 – 6.0 cm.

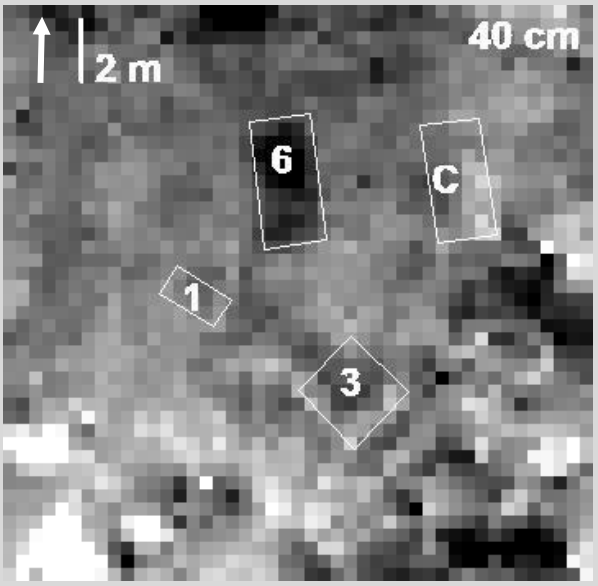

Figure F.40: ROI overlays shown here for referencing burial locations in **Figures F.41 – F.43** (no new data).

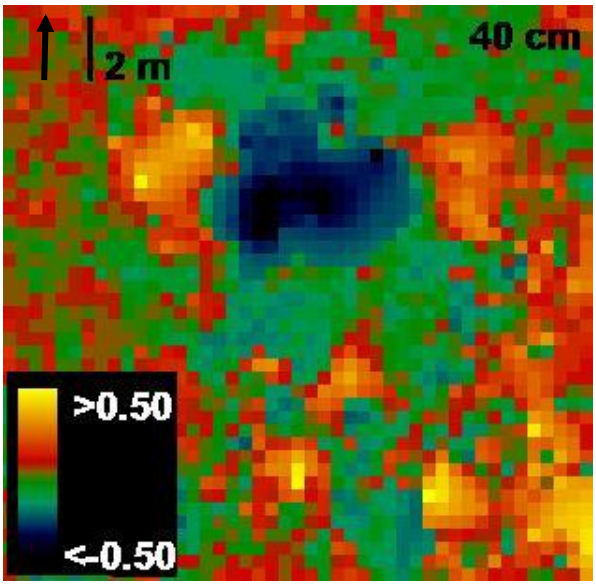

Figure F.41: Elevation changes of study area between 12 Feb. – 15 Feb. 2013; values indicate net elevation change (m).

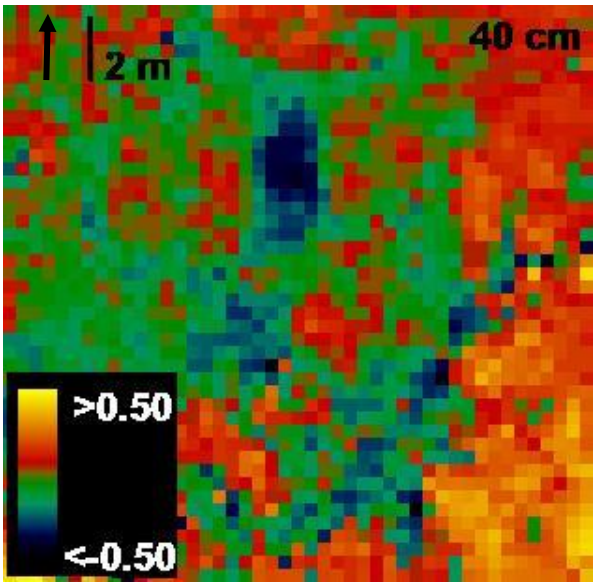

Figure F.42: Elevation changes of study area between 12 Feb. – 03 June 2013.

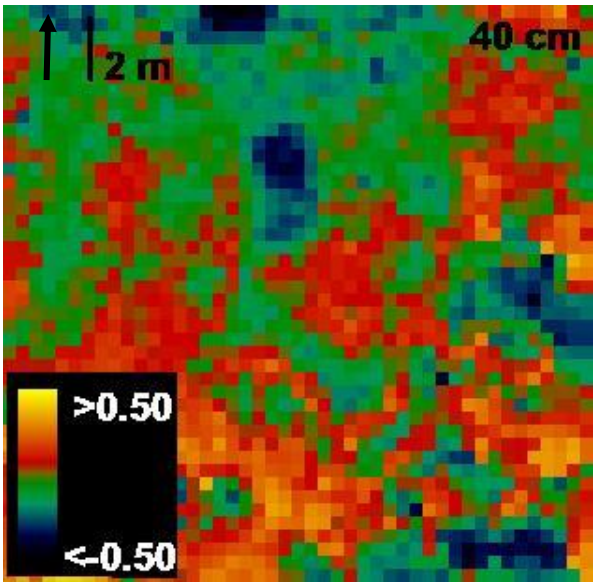

Figure F.43: Elevation changes of study area between 12 Feb. 2013 – 20 Nov. 2014.

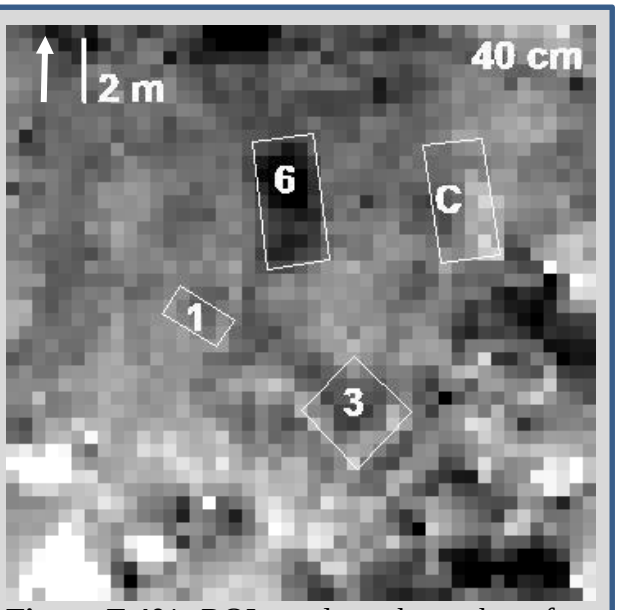

Figure F.40*: ROI overlays shown here for referencing burial locations in **Figures F.44 – F.46** (no new data).

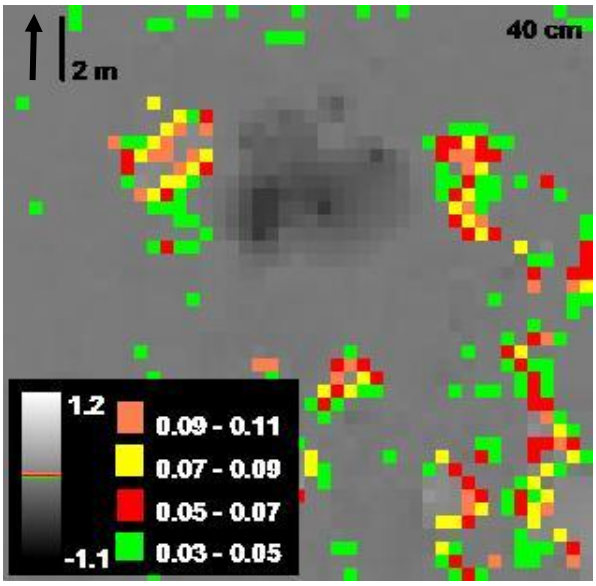

Figure F.44: Elevation changes of study area between 12 Feb. – 15 Feb. 2013; 2 cm density slices added to emphasize elevation change clustering at 3.0 – 11.0 cm; values follow means from **Figures 4.4-16 – 4.4-19**.

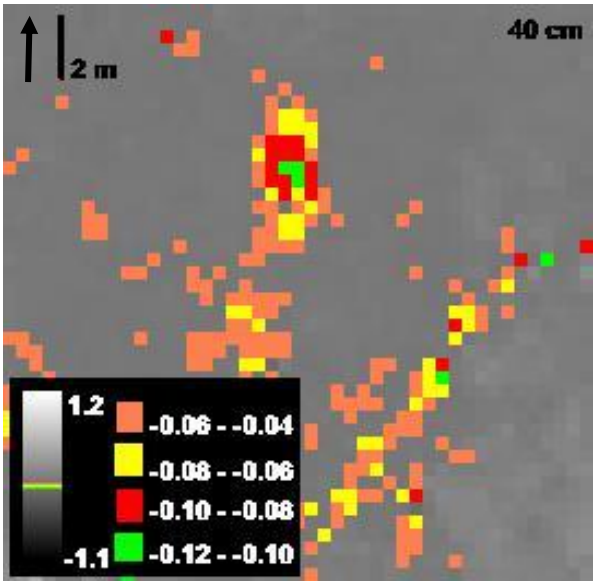

Figure F.45: Elevation changes of study area between 12 Feb. – 03 June 2013; 2 cm density slices added for -12.0 - -4.0 cm.

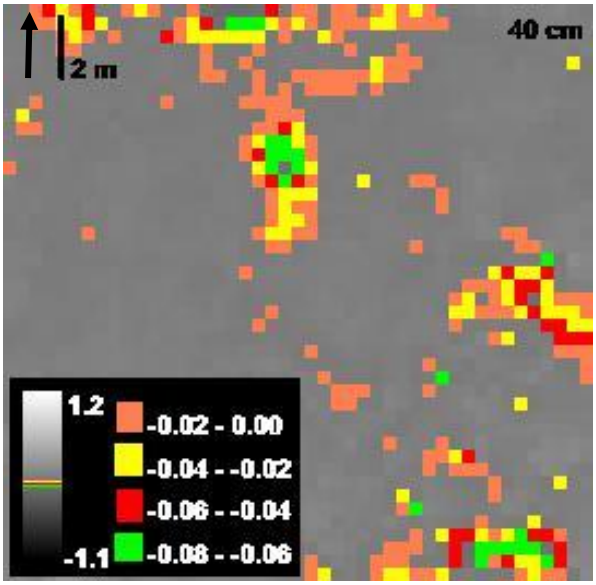

Figure F.46: Elevation changes of study area between 12 Feb. 2013 – 20 Nov. 2014; 2 cm density slices added for -8.0 – 0.0 cm.

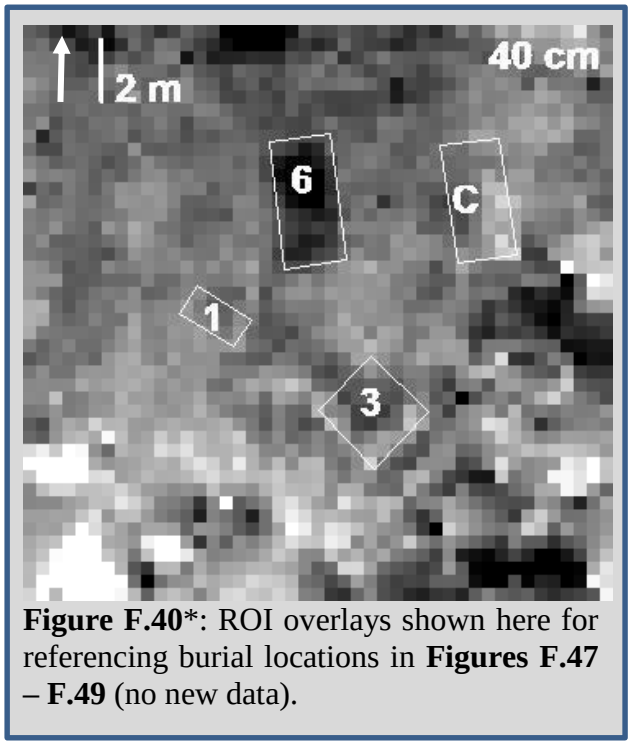

Figure F.40*: ROI overlays shown here for referencing burial locations in **Figures F.47 – F.49** (no new data).

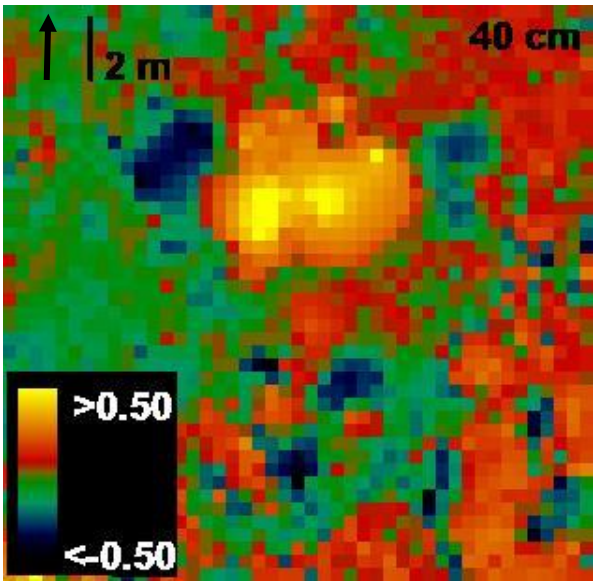

Figure F.47: Elevation changes of study area between 15 Feb. – 03 June 2013; values indicate net elevation change (m).

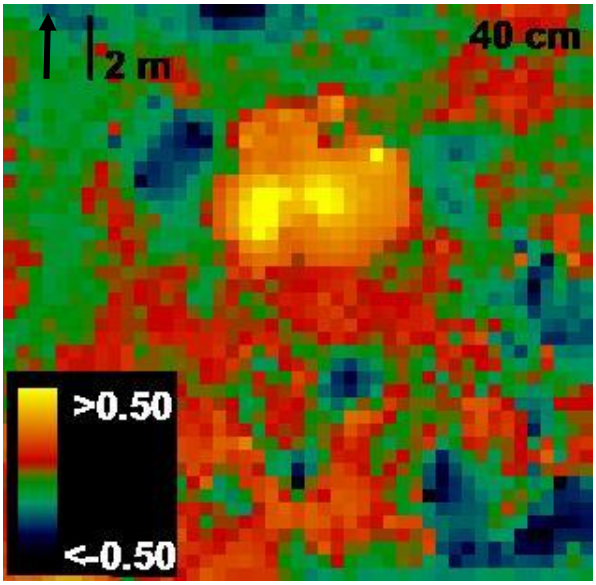

Figure F.48: Elevation changes of study area between 15 Feb. 2013 – 20 Nov. 2014.

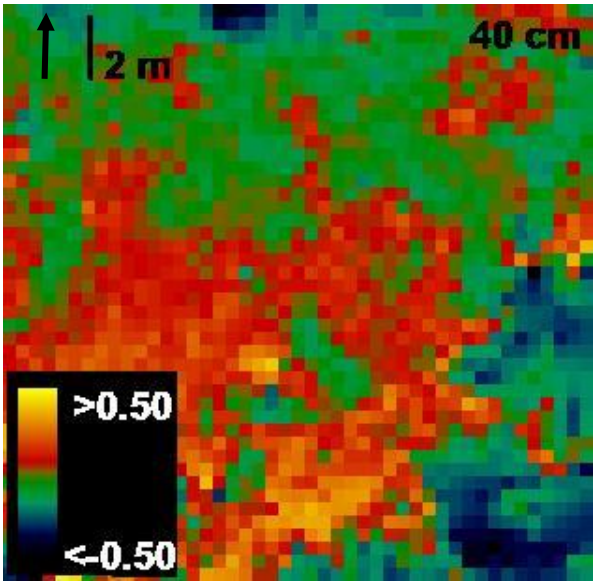

Figure F.49: Elevation changes of study area between 03 June 2013 – 20 Nov. 2014.

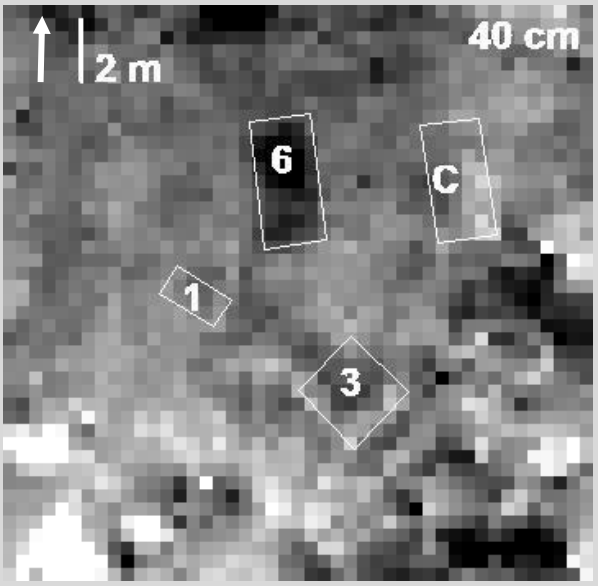

Figure F.40*: ROI overlays shown here for referencing burial locations in **Figures F.50 – F.52** (no new data).

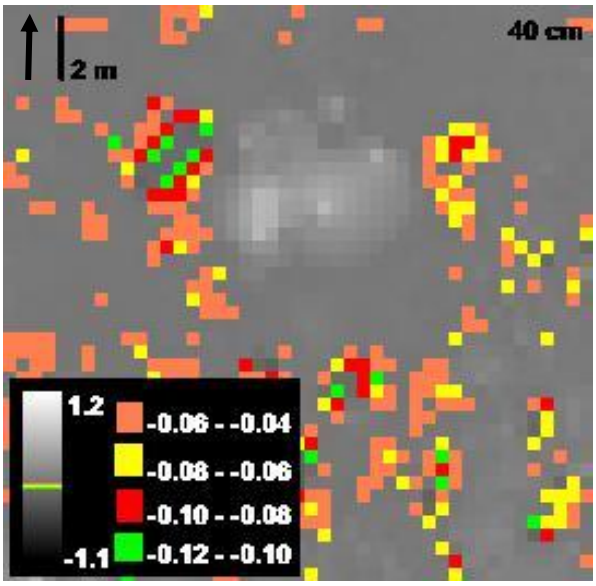

Figure F.50: Elevation changes of study area between 15 Feb. – 03 June 2013; 2 cm density slices added to emphasize elevation change clustering at -12.0 - -4.0 cm; values follow means from **Figures E.4 – E.6**.

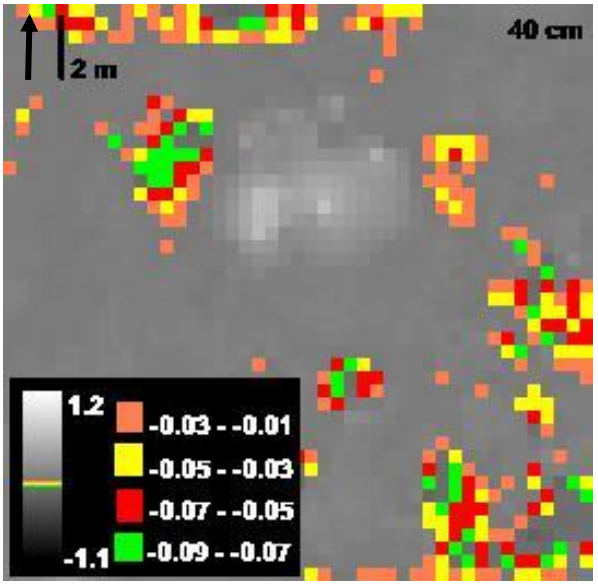

Figure F.51: Elevation changes of study area between 15 Feb. 2013 – 20 Nov. 2014; 2 cm density slices added for -9.0 - -1.0 cm.

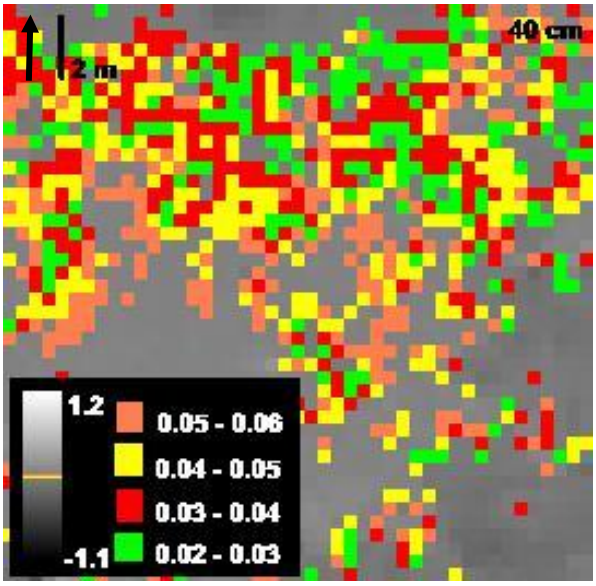

Figure F.52: Elevation changes of study area between 03 June 2013 – 20 Nov. 2014; 1 cm density slices added for 2.0 – 6.0 cm.

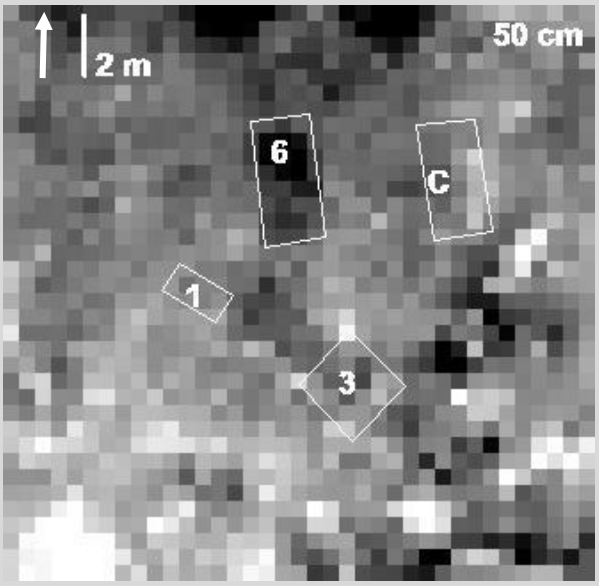

Figure F.53: ROI overlays shown here for referencing burial locations in **Figures F.54 – F.56** (no new data).

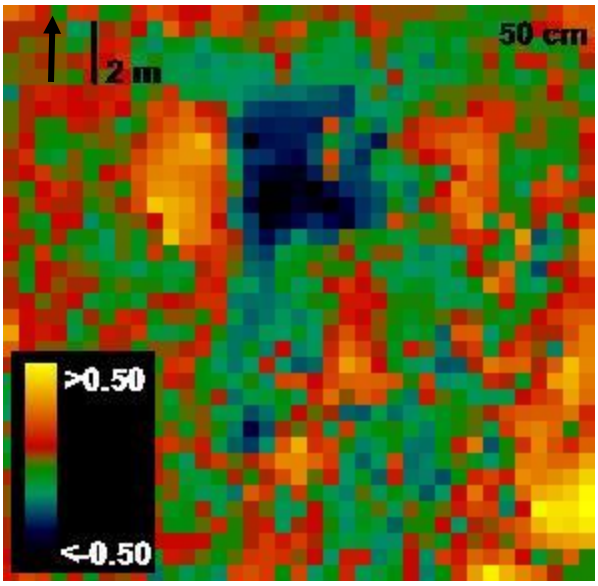

Figure F.54: Elevation changes of study area between 12 Feb. – 15 Feb. 2013; values indicate net elevation change (m).

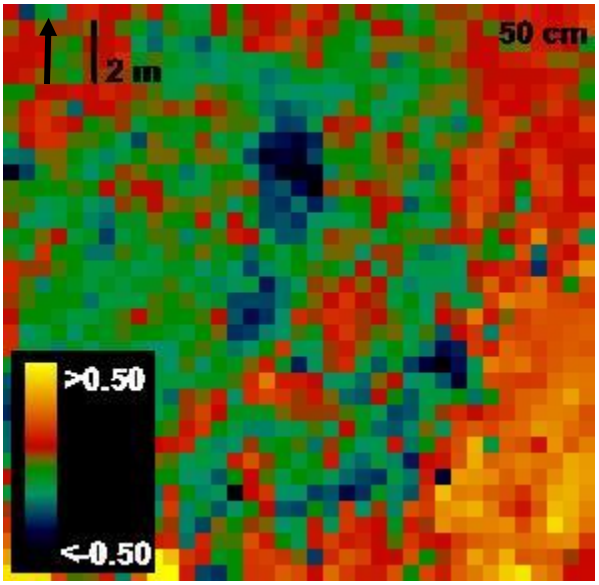

Figure F.55: Elevation changes of study area between 12 Feb. – 03 June 2013.

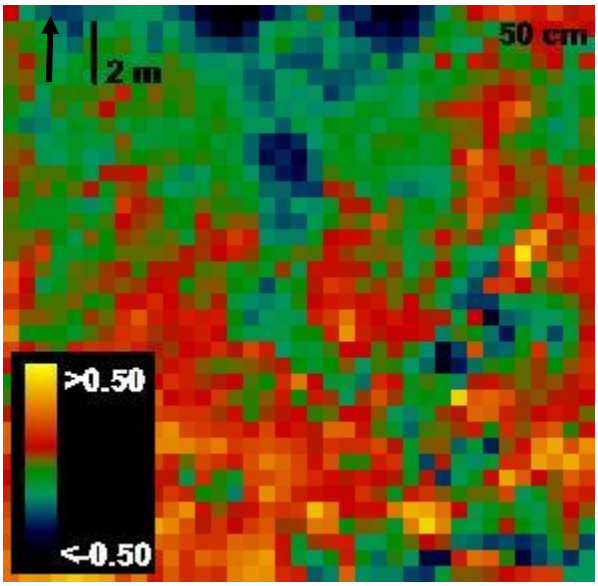

Figure F.56: Elevation changes of study area between 12 Feb. 2013 – 20 Nov. 2014.

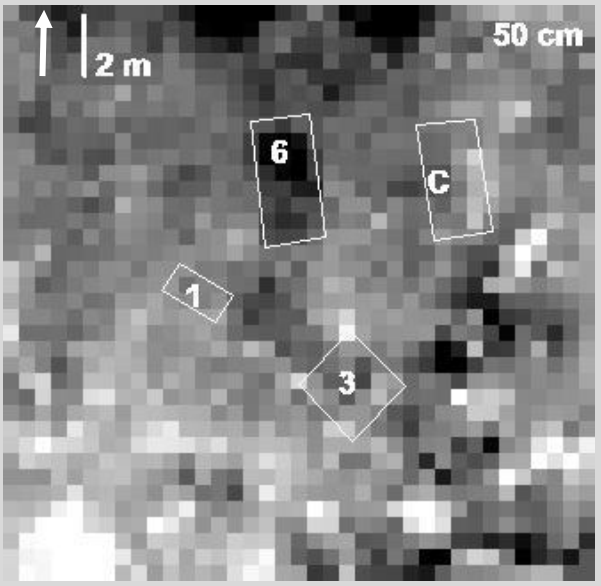

Figure F.53*: ROI overlays shown here for referencing burial locations in **Figures F.57 – F.59** (no new data).

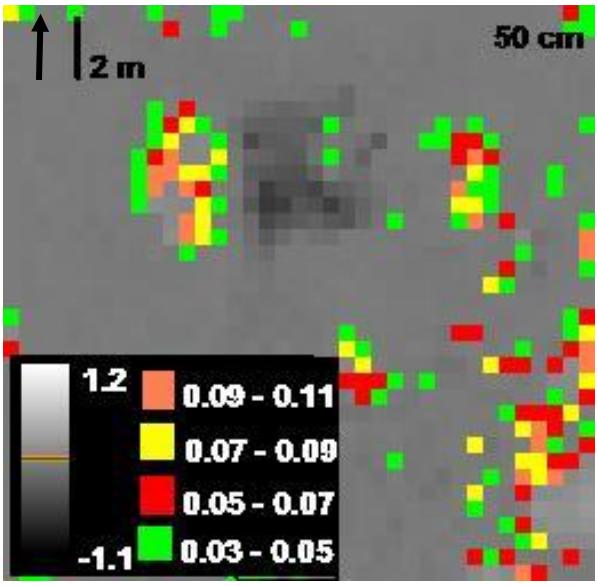

Figure F.57: Elevation changes of study area between 12 Feb. – 15 Feb. 2013; 2 cm density slices added to emphasize elevation change clustering at 3.0 – 11.0 cm; values follow means from **Figures 4.4-16 – 4.4-19**.

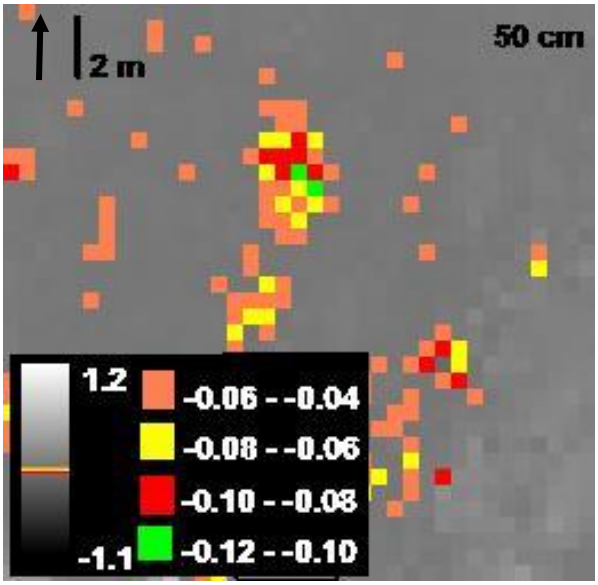

Figure F.58: Elevation changes of study area between 12 Feb. – 03 June 2013; 2 cm density slices added for -12.0 - -4.0 cm.

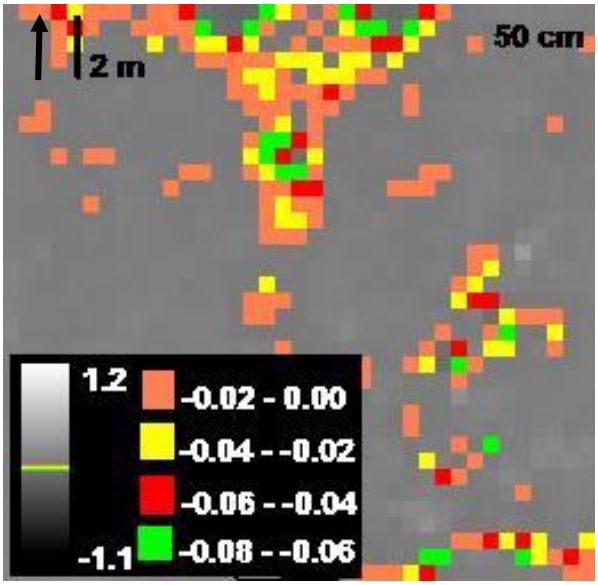

Figure F.59: Elevation changes of study area between 12 Feb. 2013 – 20 Nov. 2014; 2 cm density slices added for -8.0 – 0.0 cm.

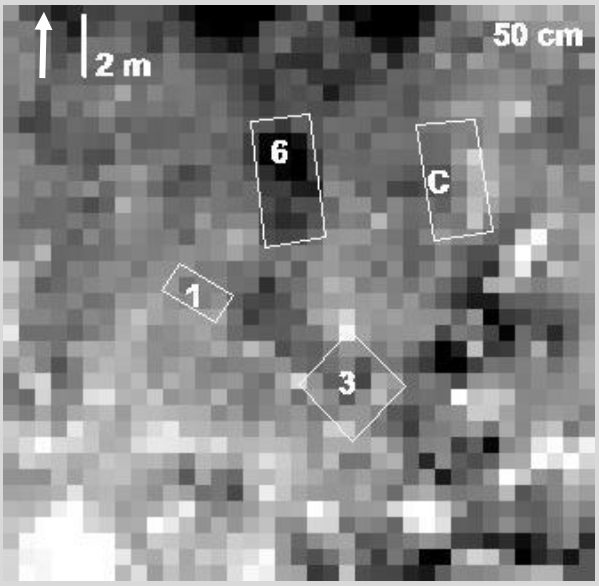

Figure F.53*: ROI overlays shown here for referencing burial locations in **Figures F.60 – F.62** (no new data).

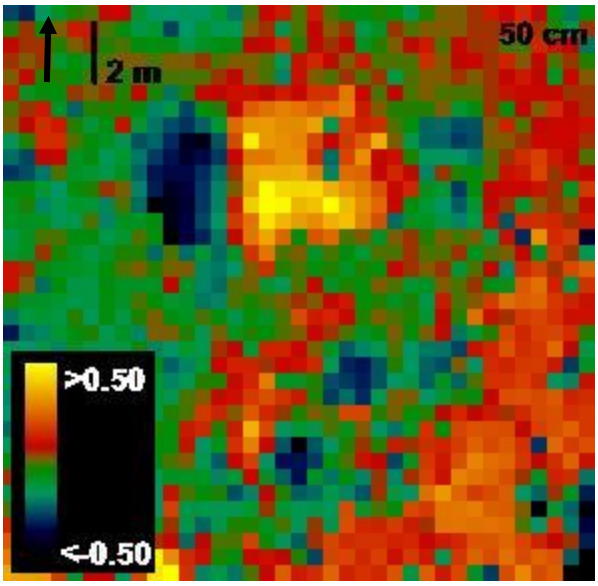

Figure F.60: Elevation changes of study area between 15 Feb. – 03 June 2013; values indicate net elevation change (m).

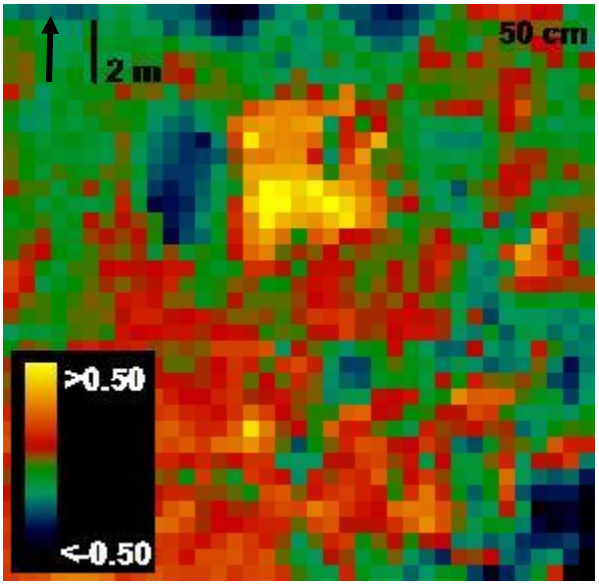

Figure F.61: Elevation changes of study area between 15 Feb. 2013 – 20 Nov. 2014.

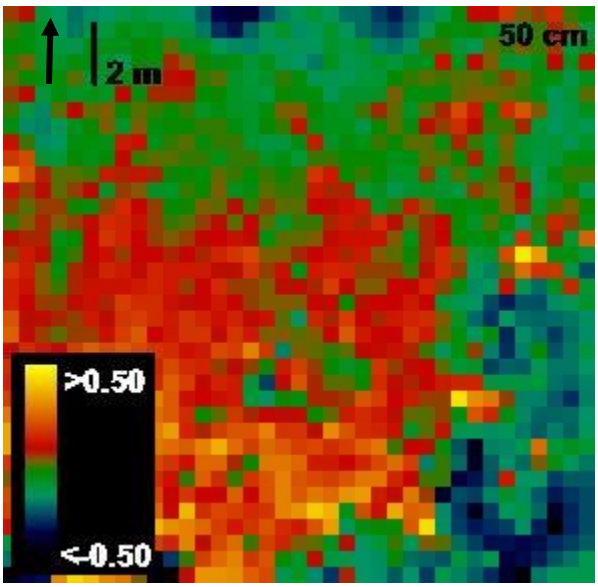

Figure F.62: Elevation changes of study area between 03 June 2013 – 20 Nov. 2014.

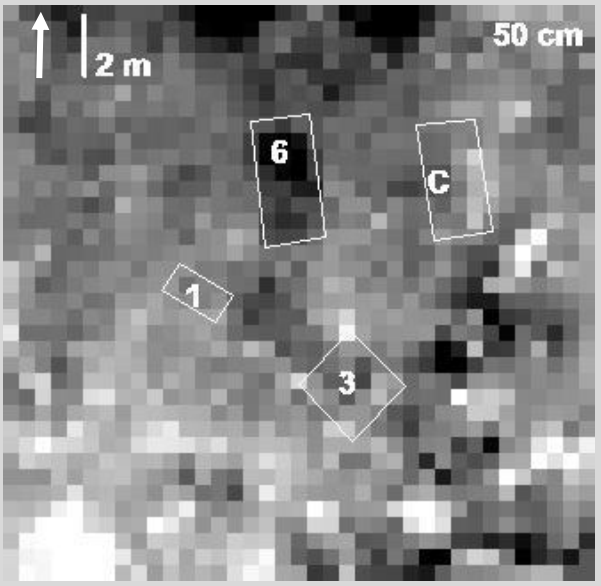

Figure F.53*: ROI overlays shown here for referencing burial locations in **Figures F.63 – F.65** (no new data).

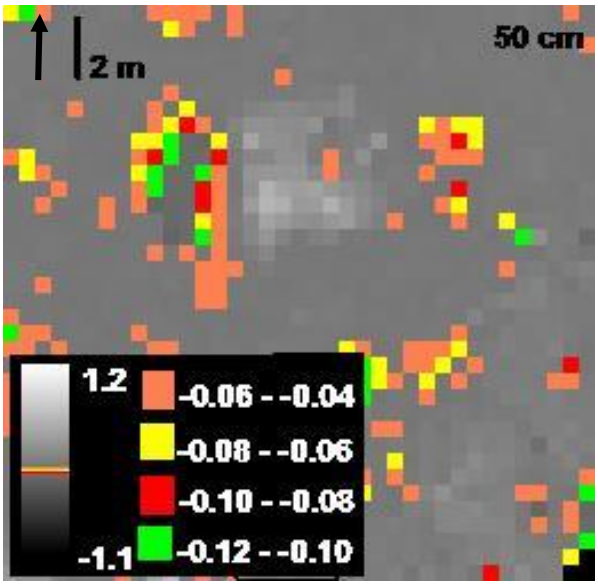

Figure F.63: Elevation changes of study area between 15 Feb. – 03 June 2013; 2 cm density slices added to emphasize elevation change clustering at -12.0 - -4.0 cm; values follow means from **Figures E.4 – E.6**.

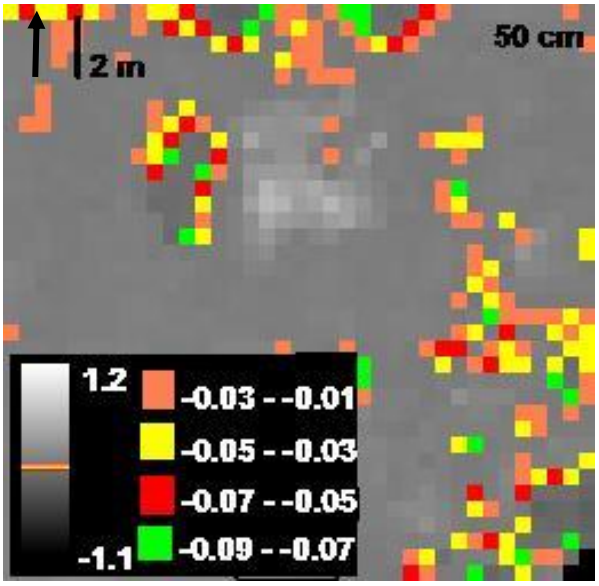

Figure F.64: Elevation changes of study area between 15 Feb. 2013 – 20 Nov. 2014; 2 cm density slices added for -9.0 - -1.0 cm.

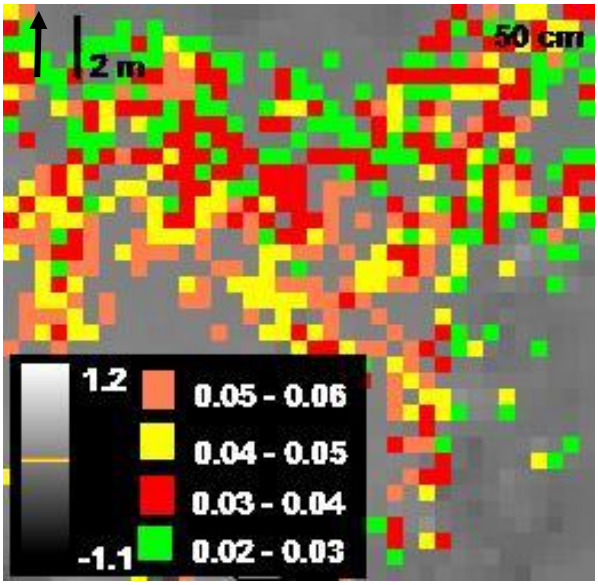

Figure F.65: Elevation changes of study area between 03 June 2013 – 20 Nov. 2014; 1 cm density slices added for 2.0 – 6.0 cm.

VITA

Katie Corcoran was born in New England where she lived until absconding to Florida with the help of a band of traveling hippies at the age of seven. Under the tutelage of Bernard the Junior, Katie learned the way of the flip flop, of alligator avoidance, and of "fixin'" to do things. These important skills prepared her for the rigors of life at the Florida Academy of Not-Quite Capable Youths, where she studied the ancient human arts, eventually earning a degree in humaning. Acclimated to the unforgiving Florida heat, Katie embarked on the journey of journeys and spent two years digging precisely 14,385,921 holes in the Florida sand until, with a stroke of luck and minimal skill, famed anthropologist Dorothy Block hit her in the face with a shovel handle. The impact rattled Katie's brain, and the circling stars spelled out a fateful message: "Graduate student offices sometimes have air conditioning." With that revelation, she bequeathed her trowel to the earth and traveled north to Tennessee, which proved a welcome change for Katie. While avoiding her studies, she frequented all four corners of Knoxville and could be seen scampering to and fro across those Great Smoky Mountains.